

Phenotype Variability Determination using Airy Disc Analysis

Submitted by Lynsey Ann Penwill to the University of Exeter as a thesis for the
degree of Doctor of Philosophy in Biological Sciences in December 2013

This thesis is available for Library use on the understanding that it is copyright material and that no
quotation from the thesis may be published without proper acknowledgement.

I certify that all material in this thesis which is not my own work has been identified and that no
material has previously been submitted and approved for the award of a degree by this or any other
University.

Signature:

ABSTRACT

Rapid phenotype identification and screening is a relatively unexplored field compared with genotype screening probably owing to a lack of appropriate technology. The Lensless microscope has a large field of view and allows the capture of the diffraction pattern from a large number of cells simultaneously, its potential to screen growth phenotypes will be evaluated in this thesis. A simple algorithm has been developed to measure intensity changes in the Airy Disc First Fringe (ADFF) from which length and width dimensions can be derived from scattering objects with an accuracy of 5%, except for those lengths below 6 microns which have diffraction-limited measurements. A low refractive index growth medium was developed to allow growth phenotypes under normal and silver-stressed conditions to be measured for the three model organisms, *S. pombe*, *E. coli* and *S. aureus*. Phenotype classification parameters were derived from the growth curve of these organisms from which a total of 18 growth phenotypes were identified. All three cell populations exhibit survival phenotypes for both transitions from planktonic to surface growth, typically 98%, and from natural to stressed growth conditions at sub-lethal concentrations of silver. In *S. pombe* growth phenotypes of interest involve the movement into a possible G₀ growth phase of the cell cycle on exposure to silver and a skewed ratio of monopolar to bipolar growth rate increase not previously observed. *S. aureus* growth under silver stress displayed asymmetric growth of the colonies under silver stress. Analysis of the lag period parameter in the normal growth population of *S. aureus* identified 4% of the population which have the characteristics of a known growth phenotype, Small Colony Variants. The lag period parameter also identified two cell populations of *E. coli* under normal conditions, with 20% of the colonies demonstrating a significantly shorter lag period length than the remaining 80%. More importantly, a high sub-lethal dose of silver ions induces two growth phenotypes in *E. coli*, called here 'sub-bug' with parameters indicating an increased resistance to the silver stress growing slowly and a second sub-population with similar enhanced silver resistance that grew rapidly, a 'super-bug', which has a shorter lag period, a faster growth rate and reaches a much larger colony size. Genomic analysis demonstrated that these two growth types were genetically identical and are therefore a silver resistant growth phenotype.

ACKNOWLEDGEMENTS

I would like to thank the many people who have helped and supported me throughout the duration of this Ph.D. Firstly I would like thank my supervisor Andrew Shaw for supervising me both industrially and academically over the last 8 years. I would like to thank Howard Slater and all of my EvanesCo colleagues for inspiring me and guiding me down this route.

I would like to thank the Royal Commission for the Exhibition of 1851 for not only the funding, but the flexibility during the transition from industry and the University of Exeter for academic support.

I would like to thank Konrad Paszkiewicz and Karen Moore for providing the genome sequencing service and for their hard work and advice. Special thanks go to Jonathan McQuillan for his continuing support and advice, from my first day until the very last.

I would like to thank Stefania Castagnetti for her help and collaboration with all things *S. pombe*, and special thanks to Gwen Batten who has helped me, supported me and assisted me over the last two years.

I am constantly reminded that I couldn't have done any of this without my amazing parents and sisters and I thank them for being the most caring, supportive and positive family anyone could ever hope to have on their side.

Table of Contents

1	Introduction	14
1.1	The Determination and Classification of a Phenotype	14
1.2	Influencing the Phenotype.....	23
1.2.1	Inheritable Reduction in Sensitivity Towards Antibiotics	23
1.2.2	Silver stress	25
1.3	Pathogenic Bacteria and Hospital Acquired Infections.....	28
1.3.1	The Evolution of Rapid Unicellular Identification at the Point of Care (POC).....	30
1.4	The Technique of Lensless Microscopy.....	33
1.5	Aims and Objectives.....	35
1.6	References	38
2	Lensless Microscope Technique Development and Analysis for Growth Phenotype Screening using the model organism <i>Schizosaccharomyces pombe</i>	46
2.1	Introduction	46
2.2	Aims and Objectives.....	49
2.3	Lensless Microscope	49
2.4	Diffraction and the formation of the Airy Disc	49
2.4.1	Diffraction	50
2.4.2	Young's Double Slit	51
2.4.3	Diffraction Limit	54
2.4.4	Lensless Microscope Configuration	55
2.5	Image Processing	58
2.6	Dimension Calibration.....	64
2.7	<i>Schizosaccharomyces pombe</i>	69
2.7.1	Experimental Setup.....	70
2.7.2	Results.....	70

2.8	Distribution Analysis – The Classification of a Phenotype	75
2.8.1	Phenotype Classification Parameter Analysis	76
2.8.2	Describing a Distribution as ‘Normal’	77
2.8.3	Graphical Representation	78
2.8.4	Distribution Shape Parameters	80
2.8.5	Tests for Normality.....	81
2.8.6	Distribution <i>N</i> -bias	83
2.9	Discussion.....	85
2.10	Conclusions	87
2.11	References	89
3	Eukaryotic cell response to sub lethal silver stress – <i>Schizosaccharomyces pombe</i>	92
3.1	Introduction	92
3.1.1	<i>S. pombe</i> cell cycle	93
3.1.2	Aims and Objectives.....	97
3.2	Materials and Methods.....	97
3.3	Results.....	99
3.3.1	Growth Curves	101
3.3.2	Phenotype Classification Parameter Screening	102
3.3.3	New End Take Off and Sub Population Correlations	117
3.4	Discussion.....	121
3.5	Conclusion.....	128
3.6	References	130
4	<i>Escherichia coli</i> Colony Growth Phenotypes under Optimal and sub lethal silver stress conditions.....	133
4.1	Introduction	133
4.2	<i>E. coli</i> Cell Cycle.....	134
4.3	<i>E. coli</i> colonies as a multicellular organism.....	136
4.4	Response to Silver Stress	137

4.5	Aims and Objectives.....	137
4.6	Materials and Experimental Methods	138
4.6.1	Growth Media	138
4.6.2	Illumina DNA Genome Sequencing.....	140
4.7	Results.....	140
4.8	Discussion.....	161
4.8.1	Growth Phenotypes under normal growth conditions.....	161
4.8.2	Silver-Stress <i>E. coli</i> Growth Phenotypes,	164
4.8.3	Super-bug and Sub-bug Growth Phenotypes	165
4.9	Conclusion.....	169
4.10	References	170
5	Growth Phenotypes in Colonies of <i>Staphylococcus aureus</i> under normal and silver stressed Growth Conditions.....	173
5.1	Introduction	173
5.1.1	<i>S. aureus</i> Growth Phenotype and Structure.....	174
5.1.2	Antibiotic Resistance and the Effect of Silver	175
5.1.3	Small Colony Variants	176
5.1.4	Aims and Objectives.....	177
5.2	Materials and Methods.....	177
5.3	Results.....	178
5.4	Discussion.....	189
5.5	Conclusion.....	193
5.6	References	195
6	Conclusions and Future Work.....	198

Table of Figures

Figure 1.1. A typical bacterial growth curve	15
Figure 1.2 A. The up and down regulation of 4,619 genes of <i>S. typhimurium</i>	17
Figure 1.3 Two phenotypic morphologies of the <i>Candida albicans</i> strain WO-1	20
Figure 1.4 The percentage of proteins containing one or more cysteine residues compared with the percentage of cysteine free proteins encoded in the genome of 5 organisms, Humans, <i>Drosophila</i> , <i>Saccharomyces cerevisiae</i> , <i>Escherichia coli</i> and <i>Haloarcula marismortui</i>	27
Figure 1.5 A demonstration of the images which can be reconstructed holographically	35
Figure 2.1. A typical Airy disc pattern of a sphere 30 μm in diameter and the horizontal cross section of this sphere plotted as an intensity distribution curve	50
Figure 2.2. (A) the basic properties of a monochromatic light wave.	51
Figure 2.3 Young's double slit setup.	52
Figure 2.4. The fringe pattern projected on the screen from the Young's double slit setup.	53
Figure 2.5 The basic Lensless microscope flow-cell configuration	55
Figure 2.6A Technical drawing of the Lensless Microscope setup. A complete component list is included in Appendix 1.....	56
Figure 2.7. The stability of the temperature within the device housing at both 25°C and 37°C over a time course of 600 minutes.	58
Figure 2.8 (A) The calculation of ΔI	60
Figure 2.9. The plots created by the ADFF models of one quarter in size, one eighth in size and one eighth averaged with the opposite eighth using the simple model data.	61
Figure 2.10 The plots created by the ADFF models of one quarter in size, one eighth in size and one eighth averaged with the opposite eighth using the simple model data	62
Figure 2.11 The effect mask width and mask misalignment/jitter have on the ΔI	63
Figure 2.12 The measured ΔI of a 30 μm sphere over a time course of 600 minutes.....	64
Figure 2.13 A raw diffraction pattern of a thirty micrometre sphere and the same sphere after the images have been averaged 255 times.....	65
Figure 2.14 The reduction in error between size measurements of 20, 30 μm spheres when frames are averaged over a range of 4 to 225 images.	66
Figure 2.15. The largest error associated with each sphere diameter	67
Figure 2.16. Calibration curve for averaging of 225 images for the whole annulus averaged ADFF....	68
Figure 2.17 The correlation between the optically measured image size and the corresponding ADFF calculation using the calibration curve.	68

Figure 2.18 A comparison between 18 <i>S. pombe</i> microscope images and the corresponding Airy Discs	71
Figure 2.19. A typical <i>S. pombe</i> growth curve displaying some of the growth parameters which may be extracted from the data.....	72
Figure 2.20 The histogram distributions of all 11 parameters extracted and calculated from the growth curve of <i>S. pombe</i>	73
Figure 2.21 The normalised histograms and Box plots for the distributions of A + B major axis at t_0 mins and C + D minor axis at t_0 mins for $N=100$ <i>S. pombe</i>	74
Figure 2.22 Selection of output from the Normality Program on model, randomly generated 'normal' data of $N=100$ samples	80
Figure 2.23 The evolution of the QQ plot as the difference between the mean of two bimodal normal distributions	83
Figure 2.24 The convergence of the median of the distribution of the Width t_0 minutes parameter and the bootstrapped 95% confidence limits.....	85
Figure 3.1 Schematic representation of <i>S. pombe</i> cell cycle	94
Figure 3.4 The experimental set up for the control and silver stress growth chambers.....	98
Figure 3.5. The planktonic growth curve, measured in optical density, for <i>S.pombe</i>	100
Figure 3.6 Typical growth curves, recorded by the Lensless microscope, for <i>S. pombe</i>	101
Figure 3.7. The growth parameters extracted from all cell growth observations.....	102
Figure 3.8. The graphical representations of the length at t_0 mins distributions for both the control sample and the silver stressed sample	104
Figure 3.9. The Box plot and Beeswarm plots of the raw data for Length at t_0 minutes	106
Figure 3.10 The Box plot and Beeswarm plots of the raw data for Width at t_0 minutes	108
Figure 3.11 The Box plot and Beeswarm plots of the raw data for length of lag period.....	110
Figure 3.12 The Box plot and Beeswarm plots of the raw data for L_B	112
Figure 3.13 The Box plot and Beeswarm plots of the raw data for t_{cell}	114
Figure 3.14 The Box plot and Beeswarm plots of the raw data for average growth rate	116
Figure 3.15 The mirror plot of the median shifted distributions of the widths at t_0 mins for both the control and silver stressed samples.....	117
Figure 3.16 A comparison mirror plot of the length at t_0 of all the cells on the surface in the control sample and those cells which later went on to display NETO	119
Figure 3.17 A comparison mirror plot of the calculated L_B of all the cells on the surface in the control sample and those cells which later went on to display NETO	120
Figure 4.1 A simplified representation of the <i>E. coli</i> cell cycle	134

Figure 4.2 Chromosome replication in <i>E. coli</i>	135
Figure 4.3 The basic flow cell set up for the experiments with <i>E.coli</i> cells.....	139
Figure 4.4. A typical growth curve for <i>E. coli</i> K-12 MG1655 on a Matrigel surface	141
Figure 4.5 The determination of the MIC of silver ions on planktonic <i>E. coli</i> growth displaying growth curves under varying levels of silver stress.....	142
Figure 4.6 A typical <i>E. coli</i> growth curve indicating the growth parameters which can be extracted	143
Figure 4.7 Comparison of viable cells lengths at t_0 mins distributions.....	148
Figure 4.8 Comparison of cell width distributions of the viable cells at t_0 mins.	150
Figure 4.9 Distribution of lag periods of the three <i>E. coli</i> populations.....	152
Figure 4.10 Comparison of the maximum growth rate of <i>E. coli</i> grown under three silver concentrations	154
Figure 4.11 Comparison of the maximum lengths reached.....	156
Figure 4.12. The typical growth curve for the growth along the maximum axis for the control <i>E.coli</i> sample and the two populations observed during growth under a silver concentration of 3 $\mu\text{g}/\text{mL}$: the sub-bug population and the ‘super-bug’ population	158
Figure 4.13 The percentage of each genome sequenced.....	159
Figure 4.15. A comparison between the correlation between the maximum growth rate of an <i>E. coli</i> colony.....	166
Figure 4.16 A comparison between the correlation between the maximum growth rate of an <i>E.coli</i> colony and the lag period length	167
Figure 5.1 Gram stains and scanning electron micrographs at low resolution and high resolution of <i>S. aureus</i> SCVs.....	176
Figure 5.2 The determination of the MIC of silver ions on planktonic <i>S. aureus</i> growth.....	179
Figure 5.3 Comparison of viable cells lengths at t_0 mins of the three <i>S. aureus</i> populations	182
Figure 5.4 Comparison of viable cells width at t_0 mins of the three <i>S. aureus</i> populations.....	184
Figure 5.5 Distribution of lag periods of the three <i>S. aureus</i> populations of the three <i>S. aureus</i> populations	186
Figure 5.6 Comparison of average growth rate of the three <i>S. aureus</i> populations	188
Figure 6.1 The evolution of individual cell phenotypes through various distributions	201

Table of Tables

Table 1.1. The ASSURED criteria for the ideal rapid POC test.	30
Table 1.2 A review of devices developed for sub 24hr detection of HAIs.....	32
Table 2.1. The process of creating a correlation coefficient matrix	76
Table 2.2 The output moment statistics of the randomly generated model data.	82
Table 3.1. The published values for the key wild type <i>S. pombe</i> growth parameters when grown at 25°C.....	96
Table 3.2 The correlation coefficient table for the control <i>S. pombe</i> sample.	103
Table 3.3 The correlation coefficient table for the sample of <i>S. pombe</i> cells which have been grown in silver stress conditions.....	103
Table 3.4 The measured distribution parameters of the length at t_0 mins parameter for three classes of cells	105
Table 3.5 The measured distributions parameters of the width at t_0 mins parameter for three classes of cells	107
Table 3.6 The measured distributions parameters of the lag period parameter for two classes of cells	109
Table 3.7 The measured distributions parameters of the birth length (L_B) parameter for two classes of cells s.....	111
Table 3.8 The measured distributions of the cell cycle length (t_{cell}) parameter for two classes of cells	113
Table 3.9 The measured distributions of the average growth rate parameter for two classes of cells	115
Table 3.10 The measured distributions of the growth rate parameters for the cells which undergo NETO, μ_1 , the rate of growth before NETO and μ_2 , the rate of growth after NETO.	118
Table 3.11. The parameters of the distributions of length at t_0 mins for the whole control sample and the distribution just of the cells which contain a RCP during the growth period.....	119
Table 3.12 The parameters of the distributions of the calculated L_B for the whole control sample and the distribution just of the cells which contain a RCP during the growth period.....	120
Table 3.13 A summary of some published growth parameters compared with the parameters calculated here and the parameters observed when <i>S. pombe</i> is grown under silver stress conditions.	121
Table 4.1 The table of correlation coefficients for the control sample of <i>E.coli</i>	145

Table 4.2 The table of correlation coefficients for <i>E. coli</i> k-12 MG1655 when grown in the presence of a low level, 1 µg/mL, of AgNO ₃ ,	146
Table 4.3 The table of correlation coefficients for <i>E. coli</i> k-12 MG1655 when grown in the presence of a higher level, 3 µg/mL, of AgNO ₃	146
Table 4.4 The parameters of the three length distributions of viable cells.....	147
Table 4.5 The parameters of the three distributions of widths at t ₀ mins of viable cells.	151
Table 4.6. The parameters of the three distributions of lengths of lag period in all of viable colonies.	152
Table 4.7 The parameters of the three distributions of the maximum growth rates of the viable colonies.....	155
Table 4.8 The normality-testing parameters of the three distributions of maximum lengths of viable colonies.....	157
Table 4.9 The nature of each SNP detected from the comparative Illumina sequencing	160
Table 4.10 A comparison of colony size types of the viable colonies in all three experimental conditions, the control, and the silver concentrations of 1 µg/mL and 3 µg/mL.....	164
Table 4.11 The main growth phenotypes identified from both control and silver stressed <i>E. coli</i> growth.....	168
Table 5.1 The correlation coefficient table for the control <i>S. aureus</i> sample	180
Table 5.2 The correlation coefficient table for the growth of <i>S. aureus</i> under silver stress conditions of 1 µg/mL.....	180
Table 5.3 The correlation coefficient table for <i>S. aureus</i> under silver stress conditions of 2 µg/mL.	180
Table 5.4 The distribution parameters for the length at t ₀ of <i>S. aureus</i> grown at all three silver concentrations, the control, 1 µg/mL and 3 µg/mL.....	183
Table 5.5 The distribution parameters for the width at t ₀ of <i>S. aureus</i> grown at all three silver concentrations, the control, 1 µg/mL and 3 µg/mL.....	185
Table 5.6 The distribution parameters for the length of the lag period of <i>S. aureus</i> grown at all three silver concentrations, the control, 1 µg/mL and 3 µg/mL.	186
Table 5.7 The distribution parameters for average colony growth rate of <i>S. aureus</i> grown at all three silver concentrations, the control, 1 µg/mL and 3 µg/mL..	187
Table 5.8 A comparison of colony size types of the viable colonies grown at all three silver concentrations, the control, 1 µg/mL and 3 µg/mL.....	189
Table 6.1 A table of all the growth phenotypes identified in this thesis.	202

Table of Abbreviations

A-D	Anderson-Darling
ADFF	Airy Disc First Fringe
AR	Aspect Ratio
CCD	Charge Coupled Device
CFU	Colony Forming Units
CI	Confidence Intervals
ΔI	Delta Intensity
ePDF	empirical Probability Density Function
EPS	Extracellular polymeric substances
FDA	Food and Drug Administration
FOV	Field of View
HAIs	Hospital Acquired Infections
LTA	Lipoteichoic Acid
LB	Lysogeny Broth
MIC	Minimum Inhibitory Concentration
MRSA	Methicillin Resistant <i>Staphylococcus aureus</i>
NASBA	Nucleic acid sequence based amplification
NETO	New End Take Off
PCR	Polymerase Chain Reaction
POC	Point of Care
Q-Q plot	Quantile-Quantile plot
RCP	Rate Changing Point

RI	Refractive Index
Rpm	revolutions per minute
SCVs	Small Colony Variants
S-W	Shapiro-Wilk
WTA	Wall Teichoic Acid
YE5S	Yeast Extract plus 5 Supplements

1 Introduction

Cell populations contain a degree of cell-to-cell differences, there is said to be heterogeneity amongst the sample^[1]. Within a planktonic clonal solution the cells will have an identical genotype but the individual behaviour of the cell may be masked by the overall bulk behaviours of the population.

The profiling and classification of the phenotype remains significantly miss-understood and the incidence of discovery of pathogens and groups of cells displaying unique phenotypes while having identical genomes is increasing^[2-4]. Linking the genotype to the phenotype as now become a method of determining the function of genes which have been sequenced but currently have no known function^[5]. Detailed knowledge of the phenotype may lead to new understanding of pathology such as the mechanisms of drug action^[6]. The relationship between genotype, phenotype and environment, their ability to determine disease states and the subsequent approach to therapy is now an emerging field of research^[7, 8]. There is no defined method for the classification of a phenotype, which individual characteristics of growth determine one phenotype from another or how different two characteristics must be before they are considered to be a new phenotype.

1.1 The Determination and Classification of a Phenotype

Genotype is defined as the genetic complement of an organism^[9]. Humans and Chimpanzees evolved from a common ancestor between 5 and 7 million years ago, and it is reported that they differ by ~35 million single nucleotides and ~90 Mb of insertions and deletions^[10]. This difference equates to only 4% of the genome and strains of *Staphylococcus aureus* have been shown to differ by 6%. A phenotype is conventionally described as the sum of the observable properties of an organism resulting from the interaction of the environment with the genotype^[11]. The characteristics of an organism observable by experimental means^[9] are those of its phenotype. The phenotypic expression of a given genotypic constitution is governed by environmental factors and conditions^[12]. Typically then, an organism phenotype is classified by the interaction of its genotype with the environment in which it is exposed. If a phenotype is a reaction of the genome to the environmental stress, then the phenotype definition must go beyond what can be observed, and to what can be measured.

More recently the definition of phenotype, while remaining the observable characteristics, has extended to the mRNA level, as this is immediate the molecular response of the organism to the environment^[13]. Analysis of the mRNA level of the cell quantifies the expression levels of genes at individual time points, this has even been shown to be possible for individual cells^[14]. While this

molecular method of phenotype analysis is now the most-used approach, studying the growth phenotype remains paramount in the science of classification (taxonomy), in determining the functions of unknown genes and to understand the processing of proteins, from the primary structure encoded by the genome to the tertiary or quaternary structure in which they are functional. For example, the human genome has 26,588 genes^[15] but a number of these genes code for more than one protein^[16], and the peptide chains encoded undergo varying degrees of post-translational modifications yielding different protein products^[17] leading to a human proteome that consists of approximately 1 million proteins^[18]. An increasing knowledge of the genotype has led to the interest in the genome-phenome interaction, to establish the function of an unknown gene^[19],^[5],^[6], the phenome being the sum of an organisms phenotypic data^[20]. Phenotype will change with the environment of the organism, gene expression changing in response to stress or overall culture age.

The conventional growth phenotype for a population of organisms in solution is called planktonic growth. Observation of planktonic bacterial growth shows a characteristic growth curve with 5 distinct growth phases: the lag period, exponential growth phase, stationary phase, death phase and finally long term stationary phase, Figure 1.1. At each of these stages the bacteria are expressing a different subset of genes dependent on the task required.

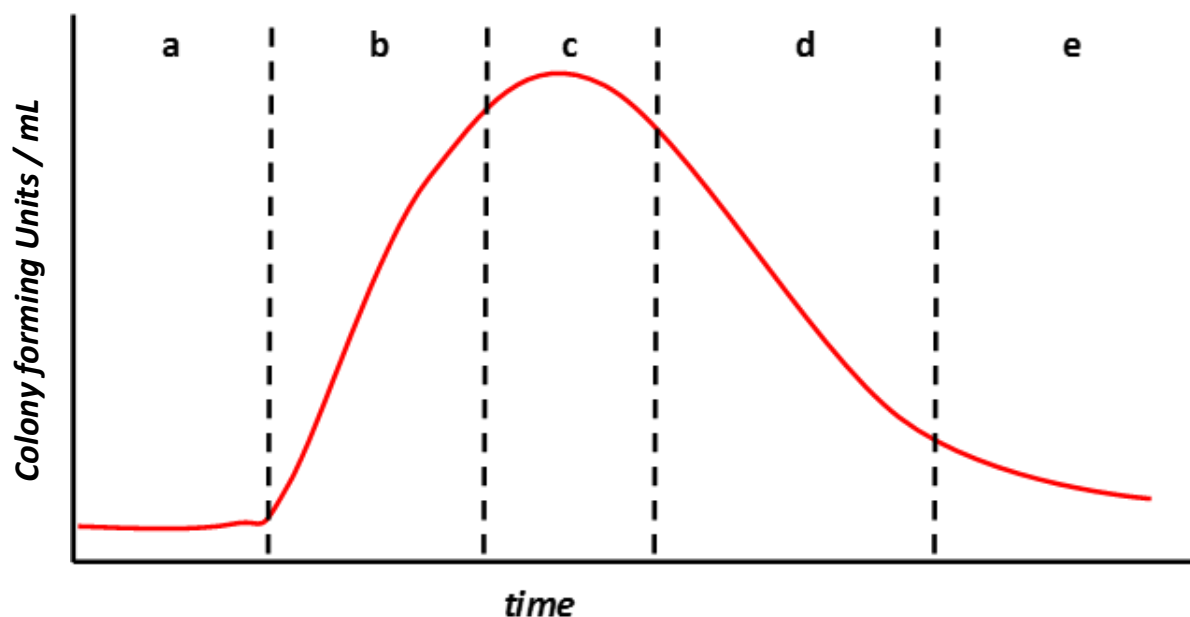


Figure 1.1. A typical bacterial growth curve, highlighting the five main growth phases: the lag period (a), the exponential growth phase (b), the stationary phase (c), the death phase (d) and the long term stationary phase (e).

The initial phase of the growth curve is the lag period. This is the period between inoculation of cells from one growth environment to another up to the point at which physical growth is detected, i.e. a change in dimension. During the lag phase microbes will not increase along any physical dimension,

however they are metabolically active, preparing for the exponential phase, repair of oxidative damage and the development of intracellular macromolecular stores^[21]. Gene expression studies in the yeast *Saccharomyces cerevisiae*^[22] show that in the early lag period, almost immediately post transfer to new growth conditions, there is an up-regulation in genes related to the synthesis and processing of RNA and proteins. The expression of these genes peaks early in the lag period and then falls, followed by a peak in the expression of genes encoding proteins required for chromosome structure, towards the end of the lag period^[22]. Comparative studies conducted using the lactic acid bacterium, *Lactococcus lactis*^[23], highlight the up-regulation of genes related to the purine and pyrimidine biosynthetic pathways, the enzymes of carbohydrate metabolic pathways and the genes involved in amino acid synthesis. Further studies analyse the global expression patterns during the lag and exponential phases of the Gram-negative pathogen *Salmonella typhimurium* growth (Figure 1.2), and show the up and down regulation of more than half the genes observed^[24]. Figure 1.2 shows, in A, the full gene set of *S. typhimurium*, the areas highlighted in yellow show no change at each time point post inoculation, the areas in red indicated genes which are up-regulated and those in blue are down regulated. The table in Figure 1.2 B displays this data quantitatively.

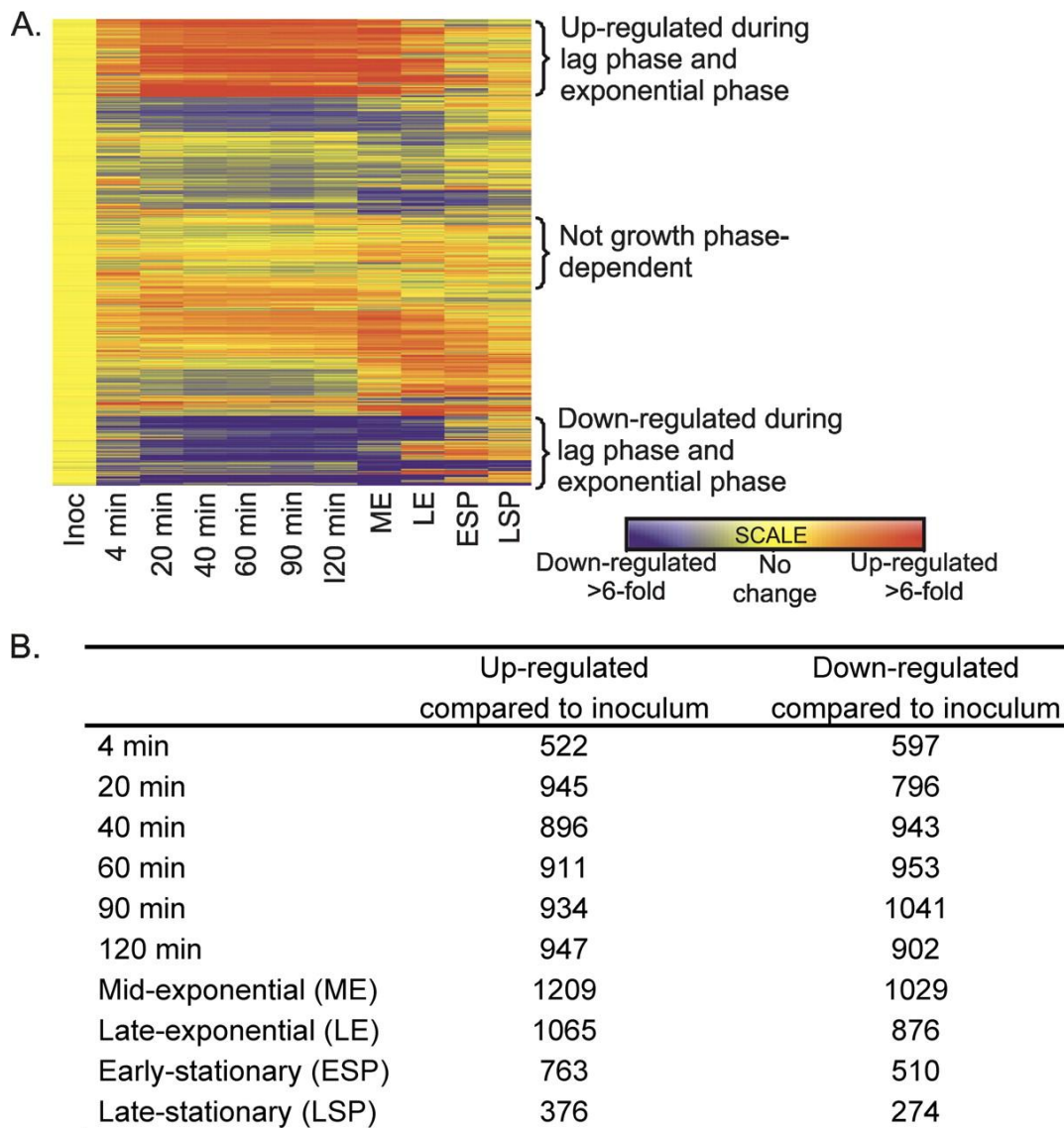


Figure 1.2 A. The up and down regulation of 4,619 genes relative to the expression state in the original inoculum during the early growth phases of *S. typhimurium*. B. The number of genes which change in expression at each time point, with a cut off of $P < 0.05$ and an expression change of a minimum of 2-fold [Reproduced with permission from reference ^[24]].

These changes are consistent with the idea that during the microbial lag period the cell is assessing and adapting to the new nutrient surroundings. Once the assessment and preparation to growth has been completed, physical enlargement begins.

During the exponential growth phase there is the up and down regulation of over half the genes (Figure 1.2), double the number with changed expression in the lag period of this organism. *E. coli* under nutrient stress, as is typical at the end of the exponential growth phase, down-regulates genes related to both transcription and translation, consistent with cell elongation halting^[25]. When the bacteria move into the stationary phase they enter into a state that allows them to survive in a nutrient hostile environment; this stationary stage state is consistent with the cells developing a resistance to chemical and physical stresses^[26]. Approximately 1000 genes in *E. coli* which are

expressed during the exponential phase are either entirely switched off or predominantly down regulated and instead a set of between 50 and 100 genes, down regulated in growth, begin to be expressed. The new set of up-regulated genes control production of storage products, gene regulation, energy metabolism and stress resistance, consistent with preparation for prolonged survival in a stress environment.

Bacteria which grow as a culture in solution display the phenotype which is associated with the strain, the growth characteristics by which it is characterised. Studies of bacteria growing in the environments in which they are naturally occurring, infected tissues for example, are known to show different growth characteristics, a different phenotype^[27]. One well-studied example of advantageous adaptation to environment is the formation of a bacterial biofilm^[28-30]. Bacteria growing in an aquatic environment have a tendency to interact with solid surfaces, initially with reversible adherence, eventually becoming irreversible^[31], these initiate the formation of biofilms. Biofilms are matrix enclosed microbial layers which adhere to surfaces, bacterial or otherwise^[32]. It has been shown^[33, 34] that biofilms are not simply groups of microbes assembled together at the solid-liquid interface but complex biological systems, both structurally and dynamically^[32].

Biofilms are protected by a self-secreted matrix of hydrated extracellular polymeric substances (EPS)[35], consisting of glycoproteins, glycolipids, proteins, polysaccharides and in cases extracellular DNA[36]. It is currently thought that bacteria form biofilms for one, or both, of two main reasons:

- The surfaces provide a degree of stability. Cells stabilised close to each other may have a catalytic advantage, extracellular enzymes are kept close to cells by the EPS^[35];
- Biofilms have been shown to provide a degree of physical protection against many environmental challenges.

Within a biofilm of *E. coli* K-12 MG1655, 206 genes are up-regulated in comparison to cells of the same strain growing in planktonic growth during the exponential growth phase^[37]. The genes of note here are related to energy metabolism, transport and binding. Biofilms are known to have a phenotype different to that of the planktonic cells of which it consists^[37], the bacteria within the EPS matrix behaving as a multicellular organism. Biofilms are adaptations of bacterial populations to survive in unfavourable environments. It is of note that the phenotype of the biofilm can be induced by sublethal concentrations of antibiotic^[38, 39] and that the biofilm EPS layer acts as a protective layer against any environmental attack. The bacteria within a biofilm act as a community, and parallels have been drawn between a biofilm and a multicellular organism or indeed a city of micro-organisms^[40, 41]. This way of thinking about the bacterial community is exploring the concept of

extended phenotype, the idea that a gene has extended phenotypic effects beyond the cell in which it is expressed^[42, 43].

The extended phenotype has been described in relation to viruses and their hosts, a baculovirus infects the caterpillar of the gypsy moth, inducing a behaviour of climbing to the top of trees, dying and essentially raining the virus on the organisms below^[44]. The causation of this phenomenon was previously unknown with no obvious mechanistic process, but a viral gene has been identified, *egt*, which induces this behaviour in Gypsy moth larvae. Hoover *et al.*^[44] conclude that there is a genetic basis for the extended phenotype, whereby the genes of one organism affect the phenotype of another. A similar example of the extended phenotype is that of *Camponotus leonardi* ants colonised with *Ophiocordyceps unilateralis* fungus, the ants displaying behaviour unfavourable to them but favourable to the colonisation of the fungi^[45]. The parasites in both these situations express genes which affect their host in order to make the environment more favourable to them, inducing a phenotype with their hosts. Other micro-organisms, instead of influencing their host, phenotypically change themselves in order to better survive in hostile environments. Phenotype switching is a phenotypic survival technique.

Homogeneous populations can display more than one phenotype. Phenotypic switching, or phenotypic dimorphism, is the commutation between phenotypic states^[46]. This is displayed by the yeast *Candida albicans*, which has the ability of switching between a number of phenotypes, displayed as different colony structural features^[47], Figure 1.3.

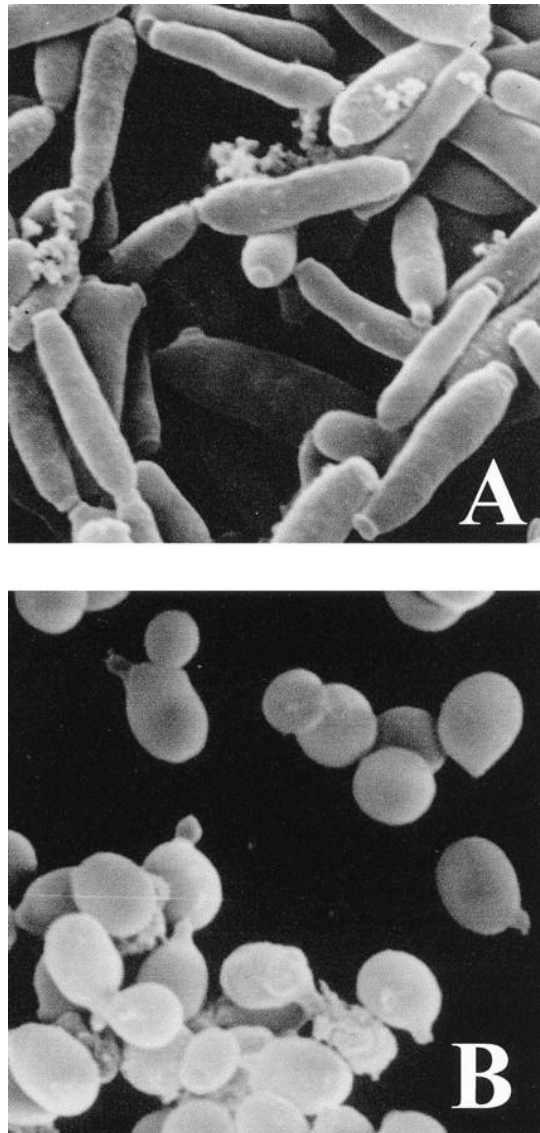


Figure 1.3 Two phenotypic morphologies of the *Candida albicans* strain WO-1, A) Flat grey and rod-like and B) Smooth, white and coccal, photographs represent images of 20 by 20 μm . [reproduced with permission from reference^[48]].

These cells, the daughters of a single cell, are able to display a number of different phenotypes, which are inheritable; they are passed on to subsequent offspring. Many of the switches appear random and are thought to occur in order to evade threatening environmental changes. In one switching strain, 3153A, the gene *SIR2* has been identified as being involved with the switching, a gene involved in chromosomal silencing^[49], the implication being that the genes for all different phenotypes are hidden in silenced regions. This phenotypic change is a change in morphology detectable at the micron level, a distinct change in size and shape, the change in gene expression, also part of the phenotype, is detectable at the molecular level. There will be no change in the genome. The phenotypical switching of the cell to evade unfavourable environmental change is detected in other micro-organisms although the change in morphology not so pronounced.

The Gram positive coccus *Staphylococcus aureus* has developed a method of phenotypic switching which aids cell survival in both antibiotic stress and antibiotic deficient conditions^[50], favourable for the organism as genotypic antibacterial resistance often associated with poor survival in a 'non-stress' environment^[51]. As discussed later in this chapter, antibiotic resistance in bacteria is brought about by a favourable genetic mutation which confers protection or resistance against the antibiotic mechanism^[52]. *S. aureus* has developed a method of resistance to antibiotics which is displayed in a small subsection of the population, known as Small Colony Variants (SCVs). SCVs are typically defined as having a slow growing phenotype, forming micro-colonies up to 10 times smaller than expected^[53]. It has been observed that SCVs emerging from a population exposed to the antibiotic gentamicin were able to switch phenotype depending on the subsequent stress environment. The SCVs displayed phenotypic resistance to gentamicin, when exposed to it, and then switched phenotype to promote better survival when the environment is gentamicin free^[50]. This is an example of a subset displaying different characteristic from the bulk of the population. Does a single cell in a population display an advantageous growth phenotype? These individuals are often not detected when analysed with the bulk concentration and it is these which are of interest in this thesis. Within a population of isogenetic individuals, those with the same genotype, there is a variation in the expression patterns across the sample^[54]. This is commonly known as phenotypic variation^[55], the dynamic nature of the bacterial phenotype depending largely on selective gene expression. Even under the most uniform of environmental conditions variations in rates of development, morphology and molecule concentrations have been observed between clonal members of the same population^[56]. Recognition of this population heterogeneity is only resolved in transfer from the bulk solution to a surface where a single cell or individual may be monitored. It is known that there is a fraction of cells, displaying a different growth phenotype, that survive on exposure to stress but on re-growth and re-exposure to the same stress they remain sensitive to it^[3]. One population of these cells is known as persister cells.

Persister cells are those cells, which are believed to form randomly in a microbial population, that become dormant and highly resistant to antibiotics^[4, 57]. Persister cells, phenotypic variants of the wildtype^[58], occur in a maximum of 1% of the population, and whilst tolerant of antibiotics it is perhaps more accurate to state that, while persister cells do not die in high antibiotic concentrations, they will not grow either^[59]. Persister cell populations have arisen in eukaryotic and prokaryotic cells alike with examples seen in the yeast *Candida albicans*, the Gram-negative bacterium *E. coli*^[4] and the Gram-positive bacterium *S. aureus*^[60]. The bacteria in a persister cell population appear to have developed a tolerance to antibiotics via a phenotypic mechanism unlike conventional resistance^[4]. The cell appears to enter a dormant state so that all potential antibiotic

targets are essentially turned off^[4]. The validity of this statement has been confirmed by a gene expression profile of *E. coli* persister cells which show a down regulation of biosynthetic pathways^[61]. *E. coli* cells were grown on media containing 10× Minimum Inhibitory Concentration (MIC) of various antibiotics, ensuring only the persister cells would survive on the plate. It was these survivors which were analysed for their gene expression. While persister cells form via a random process in any microbial culture, the prevalence of persister cells arising from two other phenotypes discussed here, cells in the stationary phase and cells in a biofilm, can be up to 100 fold higher^[59]. It has been shown that microbes at different stages of growth display different growth phenotypes, cells growing slowly may be at the beginning of the growth curve or at the end, bacteria growing in association with other may be part of a phenotype which work together to form a protective layer^[32].

We have been developing the concept of phenotype as the sum of the observable properties of an organism resulting from the interaction of the environment with the genotype^[62]; changing the growth environment of the cells induces a change in the transcriptome, the complement of RNA molecules, of the organism. Consequently, a phenotype can be defined as the set of protein/enzyme concentrations of a cell, theoretically identifying a continuous distribution of phenotypes at any given time point, equation (1):

$$[E]_{i,j} = \rho_i \tag{1}$$

Where E is proteins and so $[E]_i$ is the compliment of enzymes within a cell giving rise to a specific phenotype ρ_i at any given time/cell cycle stage, j . A cell arrives on the surface of the flow cell as its own unique phenotype, each cell, at each cell cycle stage will have differing levels of cell wall proteins and regulatory proteins, including the enzymes that control the metabolism and so the rate of growth. Therefore a phenotype is defined as the metabolome plus the transcriptome of the organism, the metabolites plus the gene expression set present in the cell. The description of the phenotype in such a way indicates that the phenotype is fluid, constantly evolving, at any given time a cell may have a phenotype more favourable to the environment than the others around it. Bacteria grown planktonically in a rich growth media may display growth and physiological phenotypes which make them distinguishable as a strain from others and can be classified into groups according to how they look, grow and behave in different environments.

The initial classification of bacteria into the current genera involved observation of growth phenotype and morphology^[63]. In the Final Report of the Committee of the Society of American

Bacteriologists on Characterization and Classification of Bacterial Types in 1919, Winslow *et al.*^[64] outlined classifications into classes initially using basic morphology, size and shape, then further classification into orders depending on either growth characteristics, the ability to metabolise certain substrates, or both. The incidence of bacterial phenotype variation, as described here, is correlated in many circumstances to the number of other bacteria in the vicinity. The transcriptome of an organism can be influenced by other environmental factors, typically those associated with stress.

1.2 Influencing the Phenotype.

The phenotype of an organism is strongly influenced by the growth conditions suggesting the hypothesis: genotype + environment = phenotype. The phenotype observed in a laboratory setting and used to classify the organism is that of an organism grown in optimum growth conditions. It is known that infections are often caused by opportunistic pathogens, that is those bacteria, present in the environment or the host's natural flora, which take the opportunity to grow in a less than favourable environment^[65]. Bacteria have adapted mechanisms by which they survive in hostile environments, often changing phenotype rapidly to cope with a dramatic shift in conditions:

- Heat shock^[66]
- Nutrient starvation^[67]
- Silver Stress^[68]
- Antibiotic Stress^[69]

While all of the above conditions involve a rapid change in expression patterns of a vast number of genes, as a study based on the rapid detection of Hospital Acquired Infections, Here we discuss the known effects of two major stress conditions used as antimicrobial measures in the health care industry and how they can subsequently induce resistance.

1.2.1 Inheritable Reduction in Sensitivity Towards Antibiotics

The World Health Organisation^[70] describe antimicrobial resistance as the resistance of a microorganism to an antimicrobial medicine to which it was originally sensitive. Bacteria typically infer a reduction in sensitivity to antibiotics via a change such as chromosomal rearrangements^[71] (deletions, inversions, duplications or translocations^[72]) or the acquisition of genetic components, plasmids, transposons and bacteriophage^[52]. These genetic changes enable the bacteria to demonstrate a tolerance to the antibiotic attack by one of three ways^[71, 73]:

1. Chemically modifying the antibiotic via enzyme interaction^[73];
2. Altering the bacterial antibiotic target site^[74];

3. Altering bacterial membrane permeability and antibiotic efflux^[75].

The β -lactam antibiotics are broad spectrum antibiotics which are grouped together because they share the common structure of a β -lactam ring. The antibiotics inhibit bacterial growth by inactivating between 4 and 8 enzymes involved in cell wall synthesis^[76]. β -lactamases are enzymes produced by antibiotic resistant bacteria which attacks the β -lactam ring of the β -lactam antibiotics, hydrolytically cleaving it^[77]. While the first of these enzymes, penicillinase, was isolated from *E. coli* these enzymes are now present in a wide range of bacteria which display a reduced sensitivity to antibiotics^[73].

The macrolide family of antibiotics, Erythromycin for example, inhibit bacterial protein synthesis by binding to and inhibiting the formation of the 50s ribosomal subunit^[78]. Resistant bacteria secrete an enzyme which methylates an adenine residue in its ribosomal RNA (rRNA), it is thought that this modification induces a conformational change in the ribosome of the bacteria, the ribosome is still able to function but the antibiotic is unable to bind^[79].

Membrane bound efflux proteins are transport proteins involved in the removal of toxic molecules to outside of the cell^[80]. The drug-specific efflux by Gram-negative bacteria is known to be the key component of the resistance mechanism to the antibiotic tetracycline^[81]. Tetracycline inhibits protein synthesis by preventing the binding of tRNA to the ribosomal acceptor site^[82] and while genes for the tetracycline efflux proteins have been found in both Gram positive and Gram negative bacteria and some eukaryotic cells, Gram negative bacteria are intrinsically more resistant to antibiotics due to the activity of their drug efflux systems^[80]. Drug specific efflux systems are associated with mobile genetic elements, the acquisition of which is enough to confer antibiotic resistance^[83].

As discussed above certain bacteria have an inherent resistance to certain antibiotics. However, the emergence of antibiotic resistance has shown that within a clonal bacterial population there is a subset of bacteria which display antibiotic resistance. Bacteria can gain genetic antibiotic tolerance in one of two main ways:

1. acquisition of genetic material from another bacterium (lateral gene transfer)^[84];
2. a random genetic mutation^[85].

Horizontal (or lateral) gene transfer is a mechanism of inheritance of genetic information, from another organism via a recombination event which does not require sequence homology^[86]. Horizontal gene transfer describes the movement of transposable genetic material from one genome to a related genome or one genome to an unrelated genome. Moveable genetic elements

within cells are genetically discrete and structurally separate from the organism chromosome^[87], such as plasmids, and can be inserted into other organisms at several insertion sites. Enterococci have two plasmids conferring antibiotic resistance, one providing erythromycin resistance and another tetracycline resistance^[88] and these plasmids can be transferred to other bacteria.

A favourable mutation in the bacterial DNA, which may result in the formation of any of the three resistant mechanisms described above, will lead to survival where others do not and will then be passed onto subsequent generations. Mutations in the genes coding for efflux pumps have been discovered in a diverse range of bacteria resistant to tetracycline, chloramphenicol, and quinolones^[85]. These bacteria, including *Neisseria gonorrhoeae*^[89], *Burkholderia cepacia*^[90] and *Campylobacter jejuni*^[91], over-express the genes for efflux proteins, meaning they are better equipped to clear the cell of toxins. These methods of antibiotic resistance have seen the incidence of antibiotic resistance has now reached a point where there are resistant strains of the bacteria which cause diarrhoea, sepsis, urinary infections and respiratory infections to name but a few^[71], the percentage of ventilator-associated pneumonia infections caused by Methicillin Resistant *Staphylococcus aureus* (MRSA) increasing from 40% to 60% in a three year period^[92]. While the major mechanisms of antibiotic resistance are genotype change related and so therefore out of the scope of this thesis, there are incidences of bacterial tolerance to antibiotics which have been identified as phenotypic only.

Previously in this chapter, I have described four examples of bacteria displaying a resistance to antibiotics, the switching phenotype of *S. aureus*, antibiotic resistance in biofilms, the emergence of a resistant phenotype during the extended stationary phase of the bacterial growth curve and the phenomenon of persister cells^[93]. Phenotypic tolerance to antibiotics tends to be a transient reversible change as opposed to the permanent change brought about by the genetic mutations of typical antibacterial resistance^[93]. Phenotypic tolerance may be one of the reasons for failures in antibiotic treatments of infection and researching the mechanisms of phenotypic tolerance is key in moving forward in infection control, although the incidence of this phenomenon is not reported^[93]. An example which does induce a quantifiable phenotypical change when introduced into the environment of both eukaryotic and prokaryotic cells is silver. The use of silver ions in wound care as a broad spectrum antimicrobial agent is widespread in the western world.

1.2.2 Silver stress

In a move to reduce the use of antibiotics to treat infection, silver was introduced^[94] as bactericidal measure in wound dressings^[95] and as coating for medical devices^[96]. Although previously silver was

first introduced as part of a sulphonamide antibiotic in burn management^[95] and eventually the merit of silver as an antimicrobial agent was extended to the width it is currently used.

The silver (I) ion is thought to disrupt biological processes via the following mechanisms:

1. Reactivity of the silver ion with sulphur containing elements within the cell^[94, 97, 98].
2. Displacement of native metal ions from their natural binding sites^[99].

Sulphur is present in the cell in two of the 20 amino acids, methionine and cysteine. The methionine amino acid has a methyl group attached to the sulphur ion, whereas the cysteine amino acid sulphur is bound to hydrogen. The methyl group in methionine results in this amino acid being less reactive, more hydrophobic and physically larger^[100]. The disulphide bridges formed between two cysteine residues aid stabilisation of both the tertiary and quaternary structures of proteins^[101], the thiol groups of cysteine residues (-SH) are present in the active sites of enzymes, reversible oxidation leading to reaction catalysis^[102] and the redox potential of cells has been linked to the reversible formation of disulphide bridges within proteins^[103].

The proteins of various species contain between 0.5 and 2.5%^[104] cysteine. Figure 1.4 shows how many proteins encoded by the genomes of Humans, *Drosophila*, *Saccharomyces cerevisiae*, *E. coli* and *Haloarcula marismortui* contain at least one cysteine residue.

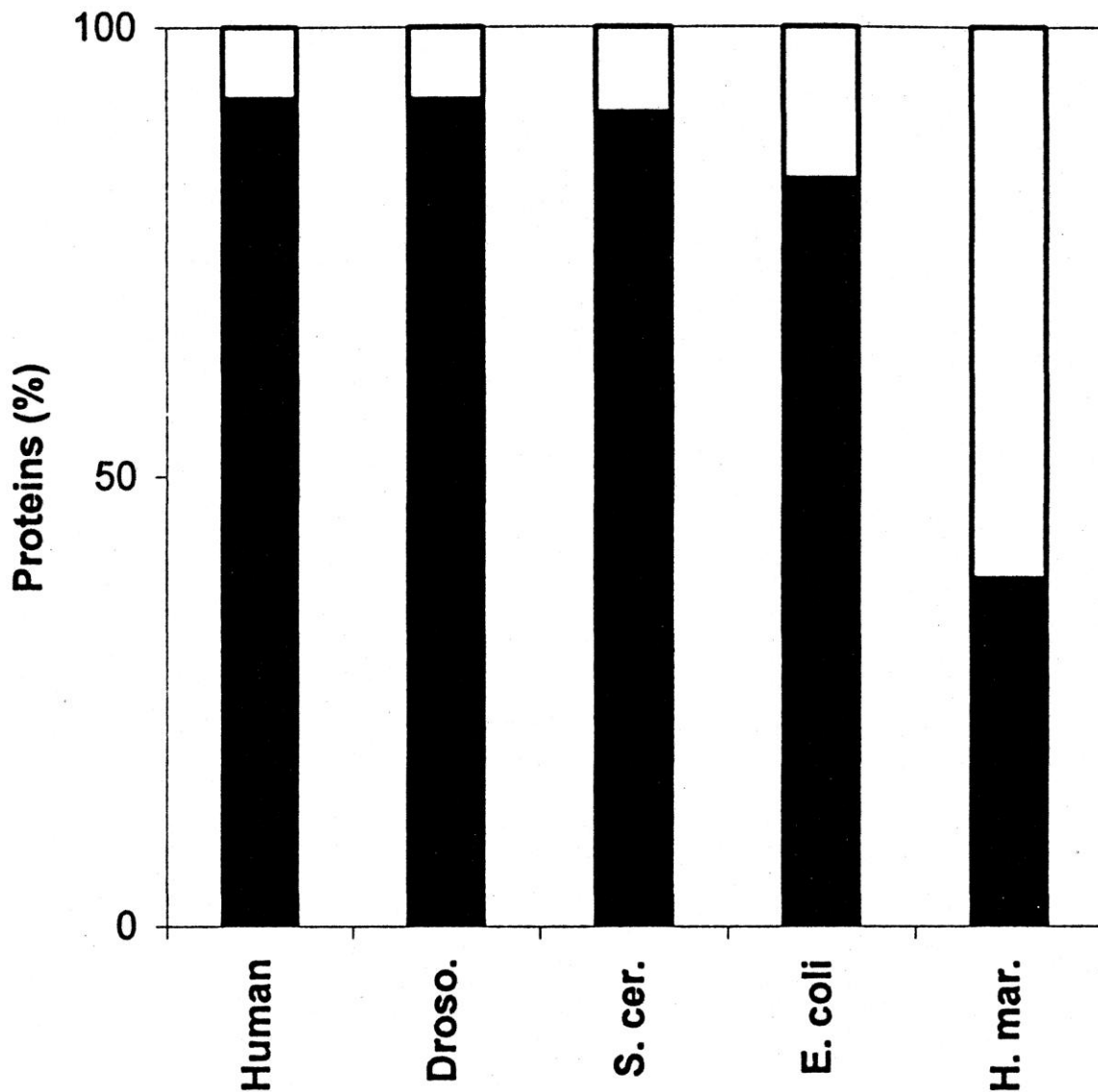


Figure 1.4 The percentage of proteins containing one or more cysteine residues (black) compared with the percentage of cysteine free proteins (white) encoded in the genome of 5 organisms, Humans, *Drosophila*, *Saccharomyces cerevisiae*, *Escherichia coli* and *Haloarcula marismortui* [With permission from reference ^[104]].

Over 80% of proteins in *E. coli* contain at least one cysteine molecule, Figure 1.4, the percentage of proteins containing cysteine being even higher for eukaryotic cells. Silver(I) will covalently bind to any sulphur complex, the strongest interaction being with a thiol group^[105], the group present on the cysteine side chain. From these two facts we can conclude that the presence of silver ions in the cell growth environment can lead to the potential disruption of upwards of 80% of the proteins within a cell. *H. marismortui* is a member of the Archaea, which thrives in the Dead Sea. It is used to conditions of high light intensity, low oxygen availability and high salinity. It is these facts which verify the lack of cysteine residues in the genome of this bacterium.

Silver can further disrupt the tertiary structure of proteins by covalently bonding two thiol groups together to form additional disulphide bridges^[106], the silver catalysing reactions between the thiol

groups on cysteine residues and oxygen molecules present in the cell; both these scenarios leading to irreversible conformational changes in protein structure, either changing the function or denaturing it completely.

It is hypothesised that the binding of Ag^+ to an iron-sulphur cluster^[107] may inhibit the activity of succinate dehydrogenase, an enzyme involved in both the electron transport chain and the citric acid cycle^[108]. Further to this hypothesis it was demonstrated that silver competes for sites which should be bound to copper and so silver presence in a cell may lead to copper deficiency^[107]. Copper concentration is tightly homeostatically controlled within a cell, too high and it can cause the oxidation of proteins but it is required as a cofactor of redox enzymes^[109]. It has been shown that following treatment with silver ions cells experience iron leakage, corroborated by transcriptome analysis which demonstrates the up regulation of a number of iron transport genes in *Staphylococcus epidermis*^[110]. The displacement mechanism can therefore disrupt the respiratory chain and lead to the formation of reactive oxygen species^[99]. When the cell cannot detoxify the number of reactive oxygen species as quickly as they accumulate, the build up of reactive oxygen species leads to oxidative stress. The reactive oxygen species target DNA, RNA, proteins and lipids, altering membrane permeability, creating lesions in DNA which block replication, protein-protein cross linking and peptide fragmentation^[111].

As with any hostile environment, when in the presence of silver, a stress response will be initiated in the microbes. Analysis of the transcriptome of *E. coli* K-12 after exposure to silver ions showed the up-regulation of 273 genes and the down-regulation of 224 genes^[112]. It was revealed that the groups of genes up-regulated included those involved in protein unfolding, iron uptake, sulphur metabolism and iron sulphur cluster assembly. The gene sets down-regulated included those involved in RNA processing, aerobic respiration and translation.

Incidences of silver resistance have been reported, arising in a number of environmental conditions. In silver contaminated environments a number of resistant bacteria have been discovered and more importantly there have been silver resistant transposable elements discovered in *E. coli*^[113]. Both silver and antibiotics are used in the treatment and prevention of infection in hospital but increasing levels of resistance to both has led to the increase in Hospital Acquired Infections (HAIs).

1.3 Pathogenic Bacteria and Hospital Acquired Infections

Pathogenic microorganisms are present in the environment in a great many settings^[114], the food industry^[115], the medical industry^[116], the water purity industry^[117] and in potential bioterrorism^[118] events to name a few. Therefore the identification of pathogenic organisms is an ongoing field of research because the conventional methods of bacterial identification tend to be complex, lengthy

and expensive^[119-121]. The rapid identification of pathogenic microorganisms usually starts with a genome-level analysis made possible by a set of new rapid sequencing technologies^[122]. The complete genome of 7407 organisms has been sequenced^[123] following the development of this technology and has brought about a sudden decrease in cost associated with whole genome sequencing; the National Human Genome Research Institute (NHGRI) reporting a reduction on cost from \$95,263,072 in 2001 to \$5,826 in 2013^[124]. Organisms are classified by their genetic relatedness^[125], their genotype, further down the dendrogram of classification the number of clusters of closely related species increases. Genera of the same family may be related by 50% homology, species within a genus related by 70% and individual strains related by 90%. Complete genomic analysis of *Staphylococcus aureus* has shown a 6% difference between a methicillin resistant and a methicillin susceptible strain^[126].

HAIs are those which have been acquired by the patient after admission to hospital^[127], are usually antibiotic resistant and acquired as the result of a healthcare intervention. Statistics from the World Health Organisation state that for every 100 patients hospitalised in developed countries, 7 of them will develop an infection secondary to the cause of admission^[128]. The Health Protection Agency cites the environment, the patient's own flora and other infectious patients as the main three sources of infection and lists the following measures which can help prevent the further spread of infection^[129]:

- Patient isolation
- Regular cleaning
- Healthcare professionals wearing Personal Protection Equipment and adhering to correct hand washing procedures
- Careful use of antibiotics to minimise the increase in antibiotic resistance^[130].

I have discussed the resistance of bacteria to antibiotics as a consequence of the over-use of broad spectrum antibiotics, treating an infection before the specific bacterial cause has been identified, promoting the possible incidence of favourable point mutations. Treating or targeting the specific infecting bacteria with a narrow spectrum antibiotic can only be carried out once it has been identified and classified. Clinical hospital laboratory classification of bacteria employs traditional culture-based identification methods, which require extended growth periods for a successful identification lasting several days, such as the Gram stain, identification of biochemical markers unique to species and growth culture^[131]. Further to the conventional culture based methods described here Hospital Acquired Infections are diagnosed in laboratories using molecular analysis techniques including Polymerase Chain Reaction (PCR) and Nucleic Acid Sequence-Based Amplification (NASBA)^[132]. Sequencing of a whole genome is not required to determine the presence

of a specific organism. In the case of MRSA, for example, the organism is detected by the presence of the specific methicillin resistance gene *mecA* and one other, Staphylococcus specific gene^[133]. While these methods have reduced the time to positive identification of microbe of choice and have the ability to detect bacterial concentrations as low as 10 complete cells^[133], these techniques still require trained individuals, a laboratory setting and do not distinguish between viable and non-viable cells^[132]. An infection cannot be left without medical intervention while the cause of infection is identified, so contributing to leading to the over use of a broad spectrum antibiotic, an antibiotic which will inhibit the growth of a wide range of bacteria. One method of reducing the over prescription of the incorrect/non-specific antibiotic is to know what is being treated before it is treated. This has lead to an increase in the area of research of rapid identification of pathogens, specifically as a point of care device to further reduce time between test and diagnosis.

1.3.1 The Evolution of Rapid Unicellular Identification at the Point of Care (POC)

A point of care device is a device for analysis which can be operated outside of a laboratory setting and is such that it can be transported to the vicinity of the patient^[134]. A POC device needs to be accurate, rapid, affordable, simple to operate and generate results within the same health-care visit^[119, 135], up to 3 hours after the appointment. Peeling *et al*^[120] outline these requirements for an 'ideal test' as the ASSURED scale (Table 1.1), the test should be affordable, sensitive and specific. The test should be user friendly, i.e. requiring minimal training to carry out a few simple steps; robust and rapid, meaning results are available in sub 30 minutes and all tests can be stored at room temperature; equipment minimal; and easy to make available to all that require it.

Table 1.1. The ASSURED criteria for the ideal rapid POC test [adapted from reference^[120]].

A	Affordable
S	Sensitive
S	Specific
U	User Friendly
R	Robust and Rapid
E	Equipment Minimal
D	Deliverable to those who need them

An example of a simple point of care test which appears to meet all of the criteria in Table 1.1 is the pregnancy test; it is affordable, requires no prior training to operate, sensitive enough for the

application, requires no extra equipment to operate and provides a rapid result. This test however, is qualitative, i.e. the data can be observed but not measured^[136]. The pregnancy test also has an incidence of false negative result (up to 33%)^[137], more likely in very early pregnancy as there is a threshold level of hormone required for a positive test and certain medications can skew the results of the test^[138]. Point-of-Care devices for highly infectious diseases or bioterrorism events cannot afford to wait for a threshold level of pathogen before they detect it, neither is it advisable to know whether it is present in the sample or not without knowing at what level it is.

Recently the development of devices for the rapid detection of HAIs has increased significantly and a volume of work has been performed focused on the rapid detection of Multi-Resistant *Staphylococcus aureus*^[139]. The basic platform of these devices can, theoretically, be applied to the detection of any pathogenic bacteria and so the rapid quantitative detection methods of MRSA are reviewed in Table 1.2.

Table 1.3 A review of devices developed for sub 24hr detection of HAIs. Sensitivity is the true positive rate, the proportion of positives measured as positives and specificity is the true negative rate, the number of negative results measured as negatives. The table also highlights the potential advantages and disadvantages of each of the methods.

Test	How it works	Sensitivity	Advantages	Disadvantages	Test Duration	References
BacLite Rapid MRSA	After growth in selective media, cells are lysed and the level of the housekeeping enzyme adenylate kinase are detected using bioluminescence.	90.4%	Detects only viable cells	Requires 45 minutes of technician time A result takes 5 hours to achieve	6 hours	[139-141]
StaphyloResist	Multiplex PCR assay with results within 24 hours.	98%	Result in 2.5-4 hours is possible.	Not a point of care device, requires a laboratory setting with significant levels of specialised equipment.	4 hours	[142]
Xpert MRSA	Purification and concentration of target organism followed by PCR amplification of the SCCmec cassette	90%	On demand results in 66 minutes or less Early assay termination leading to faster results Hands on time of 1 hour only	<ul style="list-style-type: none"> • SCCmec cassette has proven to be unstable • Moderately complex test to be performed by lab personnel. 	Sub 2 hours	[143-145]
BD GeneOhm MRSA	Real time PCR assay, detecting half a unique <i>S.aureus</i> sequence and half the SCCmec cassette	89%	<ul style="list-style-type: none"> • Results in two hours directly from a nasal sample 	<ul style="list-style-type: none"> • SCCmec cassette has proven to be unstable • Requires a degree of laboratory processing prior to the PCR. 	2 hours	[146-148]

Current rapid identification of pathogenic microorganisms is distinctly split into two groups, culture/growth based methods and Nucleic Acid Amplification Tests (NAATs). None of the tests here are 100 % sensitive, 100 % specific or able to detect a single pathogenic cell within a sample. A

comparison of all tests has been performed extensively elsewhere^[149]. Rapid identification will decrease the requirement for antimicrobial therapy and improve patient care^[150].

These technologies are the current solution and a compromise between the POC device described in Table 1.1 and the current limit to technology. Recently there have emerged new technologies which have concentrated on the specific issues relating to rapid detection. The Verigene Gram-Positive Blood Culture (BC-GP) nucleic acid test^[151], for example, detects a number of pathogens directly from a blood sample^[152] using gold-nanoparticle labelled probes. The rapid identification of pathogens directly from blood can reduce mortality rates by reducing the overall test time significantly.

These methods of single cell detection are restricted by cost limitations, initial cell numbers and the requirement of trained healthcare professionals. Results take hours to be obtained and any further information about the sample is lost as it has first been purified to increase the concentration of the target molecules. A method of rapidly screening microbial growth phenotype is required. As discussed above the bacterial stress response is very rapid, the up-regulation of numerous genes occurring almost immediately after exposure^[112]. The ability to detect this change in bacterial expression is potentially quicker than current genomic and growth methods. The Lensless Microscope is proposed for this application.

1.4 The Technique of Lensless Microscopy

Conventional imaging of objects which cannot be seen by the naked eye is performed using the light microscope with a number of limitations:

1. Limited depth of field^[153];
2. Relatively small Field of View^[154];
3. The accurate size measurement of images is limited by the diffraction limit.
4. Need for focussing fluid for high magnification

A light microscope has a short focusing lens in close proximity to the sample to be imaged and a long focusing lens in the eye-piece. The depth of field is related to the magnification factor used in the eye-piece, decreasing as the magnification increases^[153]. At a magnification of 40x on a light microscope it is estimated that the field of view is 0.036mm^2 , and so the capability to observe simultaneously only a small number of cells^[155]. By using the Lensless microscope we seek to address some of the limitations of the light microscope while also creating a device which is cost effective, simple to operate and possible to operate at the POC. The Lensless microscope has previously been

applied to measure the lengths and morphologies of nematode worms^[156] and to discriminate between cell types in a blood plasma sample^[157].

The Lensless microscope as a device to image cell diffraction patterns was first described both theoretically and practically by Ozcan & Demirci in 2008^[158]. This initial Lensless microscope has a CCD chip with pixels of 9.2 μm , a field of view of 37.25 mm \times 25.70 mm and has the potential to image the diffraction patterns of between 11 and 35 microparticles per square mm. In this case this is a field of view of over 2 orders of magnitude larger than conventional light microscopy. Ozcan's device is a proof-of-principle system which demonstrates that a primitive form of the Lensless microscope and simple counting software is able to count the number of diffracting objects, of a particular size, in a sample. Development of this idea by 'The Ozcan Research Group'^[159] has explored the extent to which this simple idea can be exploited. Further publications^[160, 161] demonstrate that with improvements to experimental set up and digital recording the Lensless microscope and related processing software has the ability to determine between different cell types from the variation in diffraction signatures^[162]. The diffraction pattern can be holographically reconstructed into a 3D image of the object, replacing the complex optics with the signal processing^{[163, 164], [157, 165]} and producing images which one would expect to see from a light microscope.

The process of holographic reconstruction involves the raw diffraction pattern image being rebuilt into the image of the scattering object. There are a number of methods of achieving this, each having their own benefits^[154]. Here we describe one method used by The Ozcan Research Group^[159], an Interferometric Phase-Retrieval Technique. The steps of this process involve iterating the image back and forth between the initial hologram image, located at the screen, and a virtual image plane. This process gradually focuses the hologram, producing an image recognisable as a light microscope image. The typical images produced by this process are shown in Figure 1.5. The figure further demonstrates how this method is able to distinguish between cell types in a mixed sample. Even without holographic reconstruction, the diffraction patterns appear different, the cells produce diffraction patterns dependent on their size, position, shape and physical components. These differences will be discussed further in chapter 2.

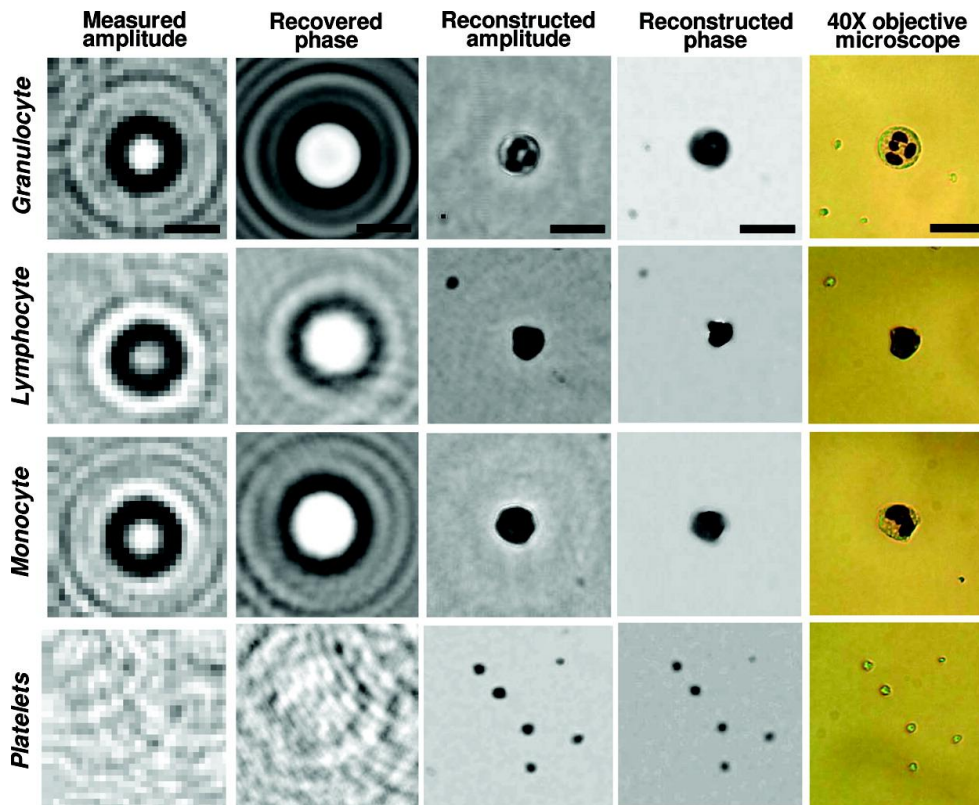


Figure 1.5 A demonstration of the images which can be reconstructed holographically from the corresponding diffraction patterns [reproduced with permission from reference ^[157]]. These cells were individually identified, by their diffraction pattern, from a mixed cell sample.

The group^[159] has shown that the identification of cells in an environment which is not conducive to growth can be done very successfully, they have demonstrated that diffraction patterns, and subsequent holographic reconstruction, is enough to identify cell types in a mixed solution of cells, and have developed complex algorithms to extract data of the highest quality from small poor scattering objects such as bacterial cells. They show that this technology can be refined to work on the most common of platforms, a basic mobile telephone^[166, 167]. A further cellphone device acts as both optofluidic device and a cell imager, recording movies of fluorescent labelled cells flowing through the microfluidic channel^[168]. The software on the cell phone has the capability to rapidly process the movie stills to count the number of cells and the cell density. The benefits of these cell phone systems are that the experimental chamber is disposable, light weight^[169] and can be attached to a device already owned by the operator^[170]. This method collects the size and shape data from individual cells, and we propose that the Lensless microscope technology can be adapted to record the phenotypic data from single cells over time.

1.5 Aims and Objectives

The rapid detection of organisms beyond the genotype is important as there are increasing cases of pathogens adapting to their environment phenotypically^[3, 21, 48, 57]. A great deal is known about the

genome of organisms, with 7407 full genomes sequenced and the cost of sequencing a genome reducing by 99% in 22 years^[123]. Understanding the phenotype will lead to better understanding of the functions of unknown genes and the way in which bacteria work together synergistically to form a stronger multicellular organism.

The Aim of the thesis is:

To design a Lensless microscope device and to assess the performance of this Lensless microscope to perform rapid phenotype screening. The device will be tested for a potential application in rapid identification of organisms.

Thesis objectives are:

- 1) Development of the Lensless microscope technology and a new analysis algorithm.
- 2) To use the Lensless microscope to accurately measure growth phenotypes;
- 3) Derive a potential set of growth phenotype classification parameters and interrogate their distributions;
- 4) Investigate phenotype adaptation in response to a silver-stress induced growth phenotypes to classify:
 - a. Single cellular behaviours of eukaryotic *Schizosaccharomyces pombe*;
 - b. Phenotypes of single cells and small colonies of the Gram-negative prokaryote *Escherichia coli*;
 - c. Phenotypes of single cells and small colonies of the Gram-positive prokaryote *Staphylococcus aureus*;
- 5) Perform genetic validation of the presence of a phenotype over genetic conferred tolerance where required.

Initially I will demonstrate modification of the lensless microscope technology for the measurement of eukaryotic and prokaryotic growth and analyse the diffraction patterns of single cells grown on surfaces. The diffraction patterns recorded by the Lensless Microscope will be interrogated with a new, simple algorithm which negates the requirement for current holographic image reconstruction methods, while not discarding any useful information, and converts this information into useful, tangible size calibration. Chapter 2 explains the theory behind the Lensless microscope, the development of the device and the analysis of the diffraction patterns. This chapter takes an initial look at the calculation of the length and width of a model eukaryotic unicellular organism, *S. pombe* as confirmation of the analysis and calibration methods.

In Chapter 3 I aim to apply this analysis method to study the phenotypic growth of a single eukaryotic cell, *S. pombe*, producing growth curves for $N = 100$ single cells and extracting 11 growth parameters. The parameters of this growth will be compared to the same parameters when $N = 100$ cells are grown under silver stress (AgNO_3). The distributions of these growth parameters will be analysed using tests of normality and non-parametric distribution comparison methods, to determine whether, within the growth parameters, phenotypic variability can be determined and to explore the new phenotype induced by the silver stress.

Chapter 4 aims to explore the growth phenotype of single cells and small colonies of the model Gram negative organism *E. coli* K-12 MG1655 under controlled growth conditions and silver stress conditions. The growth parameters will be extracted and phenotypes, which arise in both the normal growth conditions and as a result of growth in the presence of silver ions, will be identified using the same distribution analysis techniques. Colonies displaying different growth phenotypes will be sequenced and the genotype compared to the known genomic sequence of *E. coli* K-12 MG1655. The genotype validation attempts to show the favourable changes in growth are genotypic or phenotypic.

The growth phenotype of the Gram positive organism *S. aureus* with and without the presence of a sub-lethal concentration of silver ions is the aim of chapter 5. As with chapter 4 this chapter will analyse the growth phenotype of colonies which arise from single cells and small colonies. The chapter will study the effect of Gram positive cell wall on the ability to survive hostile environmental conditions and the known ability of small colony variants to switch phenotype.

Prior to collection of growth data, extraction of growth parameters, analysis of parameter distributions or challenging microbial growth with environmental stress conditions the use of the Lensless microscope for this application must be assessed. In chapter 2 I aim to develop the Lensless Microscope device, develop a simple method of analysing the collected diffraction patterns and to prove that this method provides credible data with the use of calibration spheres and the model eukaryotic rod shaped organism, *S. pombe*.

1.6 References

1. Altschuler, S.J. and L.F. Wu, *Cellular Heterogeneity: Do Differences Make a Difference?* Cell. **141**(4): p. 559-563.
2. Stewart, P.S. and J. William Costerton, *Antibiotic resistance of bacteria in biofilms*. The Lancet, 2001. **358**(9276): p. 135-138.
3. Balaban, N.Q., et al., *Bacterial Persistence as a Phenotypic Switch*. Science, 2004. **305**(5690): p. 1622-1625.
4. Lewis, K., *Persister Cells*. Annual Review of Microbiology, 2010. **64**: p. 357.
5. *Bacterial genomics: Connecting genotypes and phenotypes*. Nat Rev Micro, 2012. **10**(9): p. 595-595.
6. Nichols, R.J., et al., *Phenotypic Landscape of a Bacterial Cell*. Cell, 2011. **144**(1): p. 143-156.
7. Thorisson, G.A., J. Muilu, and A.J. Brookes, *Genotype-phenotype databases: challenges and solutions for the post-genomic era*. Nat Rev Genet, 2009. **10**(1): p. 9-18.
8. GEN2PEN. *Project Summary and Objectives*. 2011 [cited 2013 2nd December]; Available from: <http://www.gen2phen.org/about-gen2phen/project-summary-and-objectives>.
9. Brock, T.D., D.W. Smith, and M.T. Madigan, *Biology of Microorganisms*. 1984, USA: Prentice-Hall International.
10. Varki, A. and T.K. Altheide, *Comparing the human and chimpanzee genomes: Searching for needles in a haystack*. Genome Research, 2005. **15**: p. 1746-1758.
11. Nester, E.W., et al., *Microbiology*. 2nd ed. 1978, USA: Holt, Rinehart and Winston.
12. Schlegel, H.G. and K. Schmidt, *General Microbiology*. 6th ed. 1988, Cambridge: Cambridge University Press.
13. Bochner, B.R., *Global Phenotypic Characterization of Bacteria*. FEMS Microbiol. Rev., 2009. **33**(1): p. 191.
14. Ramskold, D., et al., *Full-length mRNA-Seq from single-cell levels of RNA and individual circulating tumor cells*. Nat Biotech, 2012. **30**(8): p. 777-782.
15. Venter, J.C., et al., *The sequence of the human genome*. Science, 2001. **291**(5507): p. 1304-1351.
16. Brodsky, G., et al., *The human GARS-AIRS-GART gene encodes two proteins which are differentially expressed during human brain development and temporally overexpressed in cerebellum of individuals with Down syndrome*. Human Molecular Genetics, 1997. **6**(12): p. 2043-2050.
17. Boulter, D., B. Parthier, and L. Beevers, *Post-Translational Modifications, in Nucleic Acids and Proteins in Plants I*. 1982, Springer Berlin Heidelberg. p. 136-168.
18. MÅ¼ller, A., R.M. MacCallum, and M.J.E. Sternberg, *Structural Characterization of the Human Proteome*. Genome Research, 2002. **12**(11): p. 1625-1641.
19. Dutilh, B.E., et al., *Explaining microbial phenotypes on a genomic scale: GWAS for microbes*. Briefings in Functional Genomics, 2013.
20. Freimer, N. and C. Sabatti, *The human phenome project*. Nature genetics, 2003. **34**(1): p. 15-21.
21. Rolfe, M.D., et al., *Lag phase is a distinct growth phase that prepares bacteria for exponential growth and involves transient metal accumulation*. Journal of Bacteriology, 2012. **194**(3): p. 686.
22. Brejning, J., L. Jespersen, and N. Arneborg, *Genome-wide Transcriptional Changes During the Lag Phase of Saccharomyces cerevisiae*. Archives of Microbiology, 2003. **179**(278).
23. Larsen, N., et al., *Differential Expression of Proteins and Genes in the Lag Phase of Lactococcus lactis subsp. lactis Grown in Synthetic Medium and Reconstituted Skim Milk*. Applied Environmental Microbiology, 2006. **72**(2): p. 1173.

24. Rolfe, M.D., et al., *Lag Phase Is a Distinct Growth Phase That Prepares Bacteria for Exponential Growth and Involves Transient Metal Accumulation*. Journal of Bacteriology, 2011. **194**(3): p. 686-701.
25. Chang, D.E., D.J. Smalley, and T. Conway, *Gene expression profiling of Escherichia coli growth transitions: an expanded stringent response model*. Molecular Microbiology, 2002. **45**(2): p. 289-306.
26. Ishihama, A., *Adaptation of gene expression in stationary phase bacteria*. Current Opinion in Genetics & Development, 1997. **7**(5): p. 582-588.
27. Costerton, J.W., et al., *Bacterial Biofilms in Nature and Disease*. Annual Review of Microbiology, 1987. **41**: p. 435.
28. Davies, D.G., et al., *The Involvement of Cell-to-Cell Signals in the Development of a Bacterial Biofilm*. Science, 1998. **280**(5361): p. 295-298.
29. Hoffman, L.R., et al., *Aminoglycoside antibiotics induce bacterial biofilm formation*. Nature, 2005. **436**(7054): p. 1171-1175.
30. O'Toole, G., H.B. Kaplan, and R. Kolter, *Biofilm Formation as Microbial Development*. Annual Review of Microbiology, 2000. **54**: p. 49-79.
31. Zobell, C.E., *The Effect of Solid Surfaces upon Bacterial Activity*. Journal of Bacteriology, 1943. **46**(1): p. 39.
32. Hall-Stoodley, L., J.W. Costerton, and P. Stoodley, *Bacterial biofilms: from the Natural environment to infectious diseases*. Nat Rev Micro, 2004. **2**(2): p. 95-108.
33. Doyle, R., ed. *Microbial Growth in Biofilms, Part A: Developmental and Molecular Biological Aspects*. Methods in Enzymology. 2001, Academic Press: Kentucky. 469.
34. Doyle, R., ed. *Microbial Growth in Biofilms, part B: Special Environments and Physiochemical aspects*. Methods in Enzymology. 2001, Academic Press: Kentucky. 337.
35. Flemming, H.-C. and J. Wingender, *The Biofilm Matrix*. Nature Reviews: Microbiology, 2010. **8**: p. 623.
36. Flemming, H.-C., T.R. Neu, and D.J. Wozniak, *The EPS Matrix: The "House of Biofilm Cells"*. Journal of Bacteriology, 2007. **189**(22): p. 7945.
37. Schembri, M.A., K. Kjærsgaard, and P. Klemm, *Global gene expression in Escherichia coli biofilms*. Molecular Microbiology, 2003. **48**(1): p. 253-267.
38. Hoffman, L.R., et al., *Aminoglycoside antibiotics induce bacterial biofilm formation*. Nature, 2005. **436**: p. 1171.
39. Linares, J.F., et al., *Antibiotics as intermicrobial signaling agents instead of weapons*. Proceedings of the National Academy of Sciences of the United States of America, 2006. **103**: p. 19484.
40. Nikolaev, Y.A. and V.K. Plakunov, *Biofilm-"City of microbes" or an Analogue of multicellular organisms*. Microbiology and Molecular Biology Reviews, 2007. **76**(2): p. 125-138.
41. Shapiro, J.A., *Thinking about bacteria as multicellular organisms*. Annual Review of Microbiology, 1998. **52**: p. 81-104.
42. Dawkins, R., *The Extended Phenotype: The Long Reach of the Gene*. 1999: Oxford University Press.
43. Whitham, T.G., et al., *COMMUNITY AND ECOSYSTEM GENETICS: A CONSEQUENCE OF THE EXTENDED PHENOTYPE*. Ecology, 2003. **84**(3): p. 559-573.
44. Hoover, K., et al., *A Gene for an Extended Phenotype*. Science, 2011. **333**: p. 1401.
45. Sandra B. Andersen, et al., *The Life of a Dead Ant: The Expression of an Adaptive Extended Phenotype*. 2009, The University of Chicago Press for The American Society of Naturalists. p. 424-433.
46. Sousan, A.M., I. Machado, and M.O. Pereira, eds. *Phenotypic Switching: An opportunity to bacteria thrive*. Science Against Microbial Pathogens: Communicating Current Research and Technological Advances, ed. A. Mendez-Vilas. 2011.

47. Soll, D.R., *High-Frequency Switching on Candida albicans*. Clinical Microbiology Reviews, 1992. **5**(2): p. 183-203.
48. Sonneborn, A., B. Tebarth, and J.F. Ernst, *Control of White-Opaque Phenotypic Switching in Candida albicans by the Efg1p Morphogenetic Regulator*. Infection and Immunity, 1999. **67**(9): p. 4655-4660.
49. Dean, L. and J. McEntyre, eds. *How Candida albicans switches phenotype-and back again*. Coffee Break: Tutorials for NCBI Tools. 1999, National Centre for Biotechnology Information (US).
50. Massey, R.C., A. Buckling, and S.J. Peacock, *Phenotypic switching of antibiotic resistance circumvents permanent costs in Staphylococcus aureus*. Current Biology, 2001. **11**(22): p. 1810-1814.
51. Angst, D.C. and A.R. Hall, *The Cost of Antibiotic Resistance Depends on Evolutionary History in Escherichia coli*. BMC Evolutionary Biology, 2013. **13**(163): p. 1.
52. Silva, J., *Mechanisms of antibiotic resistance*. Current Therapeutic Research, 1996. **57**(13): p. 30-35.
53. von Eiff, C., *Staphylococcus aureus small colony variants: a challenge to microbiologists and clinicians*. International Journal of Antimicrobial Agents, 2008. **31**(6): p. 507-510.
54. Rocco, A., A.M. Kierzek, and J. McFadden, *Slow Protein Fluctuations Explain the Emergence of Growth Phenotypes and Persistence in Clonal Bacterial Populations*. PLoS ONE, 2013. **8**(1): p. e54272.
55. Smits, W.K., O.P. Kuipers, and J.-W. Veening, *Phenotypic Variation in Bacteria: the role of feedback variation*. Nature Reviews: Microbiology, 2006. **4**: p. 259.
56. McAdams, H.H. and A. Arkin, *It's a noisy business! Genetic regulation at the nanomolar scale*. Trends in Genetics, 1999. **15**(2): p. 65-69.
57. Keren, I., et al., *Persister cells and tolerance to antimicrobials*. FEMS Microbiology Letters, 2004. **230**(1): p. 13-18.
58. Spoering, A., M. Vulic, and K. Lewis, *GlpD and PlsB Participate in Persister Cell Formation in Escherichia coli*. Journal of Bacteriology, 2006. **188**(14): p. 5136.
59. Wood, T.K., S.J. Knabel, and B.W. Kwan, *Bacterial Persister Cell Formation and Dormancy*. Applied and Environmental Microbiology, 2013.
60. Allison, K.R., M.P. Brynidsen, and J.J. Collins, *Metabolite-enables eradication of bacterial persisters by aminoglycosides*. Nature, 2011. **473**: p. 216.
61. Keren, I., et al., *Specialized Persister Cells and the Mechanism of Multidrug Tolerance in Escherichia coli*. Journal of Bacteriology, 2004. **186**(24): p. 8172-8180.
62. Nester, E.W., et al., *Microbiology*. 2nd ed. 1978, USA: Holt, Rinehart and Winston.
63. Chang-Li, X., et al., *Microcalorimetric study of bacterial growth*. Thermochimica Acta, 1988. **123**(0): p. 33-41.
64. Winslow, C.-E.A., et al., *The Families and Genera of the Bacteria: Final Report of the Committee of the Society of American Bacteriologists on Characterization and Classification of Bacterial Types*. Journal of Bacteriology, 1919. **5**(3): p. 191.
65. Casadevall, A. and L.-a. Pirofski, *Host-Pathogen Interactions: Redefining the Basic Concepts of Virulence and Pathogenicity*. Infection and Immunity, 1999. **67**(8): p. 3703-3713.
66. Feder, M.E. and G.E. Hofmann, *HEAT-SHOCK PROTEINS, MOLECULAR CHAPERONES, AND THE STRESS RESPONSE: Evolutionary and Ecological Physiology*. Annual Review of Physiology, 1999. **61**(1): p. 243-282.
67. Kjelleberg, S., et al., *How do non-differentiating bacteria adapt to starvation?* Antonie van Leeuwenhoek, 1993. **63**(3-4): p. 333-341.
68. Percival, S.L., P.G. Bowler, and D. Russell, *Bacterial resistance to silver in wound care*. Journal of Hospital Infection, 2005. **60**(1): p. 1-7.
69. Gefen, O. and N.Q. Balaban, *The importance of being persistent: heterogeneity of bacterial populations under antibiotic stress*. FEMS Microbiology Reviews, 2009. **33**(4): p. 704-717.

70. WorldHealthOrganisation. *Antimicrobial resistance* 2013 [cited 2013 15th November]; Available from: <http://www.who.int/mediacentre/factsheets/fs194/en/>.
71. Neu, H.C., *The Crisis in Antibiotic Resistance*. Science, 1992. **257**(5073): p. 1064-1073.
72. Griffiths, A.J.F., et al., *Modern Genetic Analysis*. 1999, New York: W. H. Freeman.
73. Wright, G.D., *Bacterial resistance to antibiotics: Enzymatic degradation and modification*. Advanced Drug Delivery Reviews, 2005. **57**(10): p. 1451-1470.
74. Lambert, P.A., *Bacterial Resistance to ANTibiotics: modified target sites*. Advanced Drug Delivery Reviews, 2005. **57**(10): p. 1471.
75. Poole, K., *Efflux pumps as antimicrobial resistance mechanisms*. Annals of Medicine, 2007. **39**(3): p. 162-176.
76. Spratt, B.G. and K.D. Cromie, *Penicillin-Binding Proteins of Gram-Negative Bacteria*. Reviews of Infectious Diseases, 1988. **10**(4): p. 699.
77. Bush, K., *Characterization of B-lactamases*. Antimicrobial Agents and Chemotherapy, 1989. **33**(3): p. 259.
78. Champney, W.S. and R. Burdine, *Macrolide antibiotics inhibit 50s ribosomal subunit assembly in Bacillus subtilis and Staphylococcus aureus*. Antimicrobial Agents and Chemotherapy, 1995. **39**(9): p. 2141.
79. Leclercq, R. and P. Courvalin, *Bacterial Resistance to Macrolide, Lincosamide, and Streptogramin Antibiotics by Target Modification*. American Society for Microbiology, 1991. **35**(7): p. 1267.
80. Webber, M.A. and L.J.V. Piddock, *The importance of efflux pumps in bacterial antibiotic resistance*. Journal of Antimicrobial Chemotherapy, 2003. **51**(1): p. 9-11.
81. Li, X.-Z. and H. Nikaido, *Efflux-Mediated Drug Resistance in Bacteria*. Drugs, 2004. **64**(2): p. 159.
82. *Tetracycline Resistance*. ARDB-Antibiotic Resistance Genes Database 2013 [cited 2013 14th November]; Available from: <http://ardb.cbcb.umd.edu/browse/tetracycline.shtml>.
83. Poole, K., *Efflux-mediated antimicrobial resistance*. Journal of Antimicrobial Chemotherapy, 2005. **56**(1): p. 20-51.
84. Davison, J., *Genetic Exchange between Bacteria in the Environment*. Plasmid, 1999. **42**(2): p. 73-91.
85. Chopra, I. and M. Roberts, *Tetracycline Antibiotics: Mode of Action, Applications, Molecular Biology, and Epidemiology of Bacterial Resistance*. Microbiology and Molecular Biology Reviews, 2001. **65**(2): p. 232-260.
86. Krishnapillai, V., *Horizontal Gene Transfer*. Journal of Genetics, 1996. **75**(2): p. 219.
87. Cohen, S.N., *Transposable Genetic Elements and Plasmid Evolution*. Nature, 1976. **263**: p. 731.
88. Clewell, D.B., *Movable genetic elements and antibiotic resistance in enterococci*. European Journal of Clinical Microbiology and Infectious Diseases, 1990. **9**(2): p. 90-102.
89. Lucas, C.E., et al., *The MtrR repressor binds the DNA sequence between the mtrR and the mtrC genes in Neisseria gonorrhoeae*. Journal of Bacteriology, 1997. **179**: p. 4123.
90. Burns, J.L., et al., *Nucleotide sequence analysis of a gene from Burkholderia(Pseudomonas) cepacia encoding an outer membrane lipoprotein involved in multiple antibiotic resistance*. Antimicrobial Agents and Chemotherapy, 1996. **40**: p. 307.
91. Charvalos, E., et al., *Evidence for an efflux pump in multidrug-resistant Campylobacter jejuni*. Antimicrobial Agents and Chemotherapy, 1995. **39**: p. 2019.
92. Gruson, D., et al., *Rotation and Restricted Use of Antibiotics in a Medical Intensive Care Unit*. American Journal of Respiratory and Critical Care Medicine, 2000. **162**(3): p. 837-843.
93. Corona, F. and J. Martinez, *Phenotypic Resistance to Antibiotics*. Antibiotics, 2013. **2**(2): p. 237-255.
94. Morones, J.R., et al., *The Bacterial Effect of Silver Nanoparticles*. Nanotechnology, 2005. **16**: p. 2346.

95. Leaper, D.J., *Silver dressings: their role in wound management*. International Wound Journal, 2006. **3**(4): p. 282-294.
96. Rupp, M.E., et al., *Effect of silver-coated urinary catheters: Efficacy, cost-effectiveness, and antimicrobial resistance*. American Journal of Infection Control, 2004. **32**(8): p. 445-450.
97. Matsumura, Y., et al., *Mode of Bactericidal Action of Silver Zeolite and Its Comparison with That of Silver Nitrate*. Applied and Environmental Microbiology, 2003. **69**(7): p. 4278-4281.
98. Gupta, A., M. Maynes, and S. Silver, *Effects of Halides on Plasmid-Mediated Silver Resistance in Escherichia coli*. Applied and Environmental Microbiology, 1998. **64**(12): p. 5042-5045.
99. Leung, B.O., et al., *Silver(I) Complex Formation with Cysteine, Penicillamine, and Glutathione*. Inorganic Chemistry, 2013. **52**(8): p. 4593-4602.
100. Brosnan, J.T. and M.E. Brosnan, *The Sulfur-Containing Amino Acids: An Overview*. The Journal of Nutrition, 2006. **136**(6): p. 1636S-1640S.
101. Wirtz, M. and M. Droux, *Synthesis of the sulfur amino acids: cysteine and methionine*. Photosynthesis Research, 2005. **86**(3): p. 345-362.
102. van Montfort, R.L.M., et al., *Oxidation state of the active-site cysteine in protein tyrosine phosphatase 1B*. Nature, 2003. **423**(6941): p. 773-777.
103. Wouters, M.A., S.W. Fan, and N.L. Haworth, *Disulphides as Redox Switches: from Molecular Mechanisms to Functional Significance*. Antioxidants & Redox Signalling, 2010. **12**(1): p. 53.
104. Miseta, A. and P. Csutora, *Relationship Between the Occurrence of Cysteine in Proteins and the Complexity of Organisms*. Molecular Biology and Evolution, 2000. **17**(8): p. 1232-1239.
105. Bell, R.A. and J.R. Kramer, *Structural chemistry and geochemistry of silver-sulfur compounds: Critical review*. Environmental Toxicology and Chemistry, 1999. **18**(1): p. 9-22.
106. Davis, R.L. and S.F. Etris, *The development and functions of silver in water purification and disease control*. Catalysis Today, 1997. **36**: p. 107.
107. Ghandour, W., et al., *The uptake of silver ions by Escherichia coli K12: toxic effects and interaction with copper ions*. Applied Microbiology and Biotechnology, 1988. **28**(6): p. 559-565.
108. Oyedotun, K.S. and B.D. Lemire, *The Quaternary Structure of the Saccharomyces cerevisiae Succinate Dehydrogenase: HOMOLOGUE MODELING, COFACTOR DOCKING, AND MOLECULAR DYNAMICS SIMULATION STUDIES*. Journal of Biological Chemistry, 2004. **279**(10): p. 9424-9431.
109. Florianczyk, B., *Copper in the organism: Transport and Storage in the cells*. Annales Universitatis Mariae Curie Skłodowska Sectio D Medicina, 2003. **58**(1): p. 85.
110. Gordon, O., et al., *Silver Coordination Polymers for Prevention of Implant Infection: Thiol Interaction, Impact on Respiratory Chain Enzymes, and Hydroxyl Radical Induction*. Antimicrobial Agents and Chemotherapy, 2010. **54**(10): p. 4208-4218.
111. Cabisco, E., J. Tamarit, and J. Ros, *Oxidative Stress in Bacteria and Protein Damage by Reactive Oxygen Species*. International Microbiology, 2000. **3**: p. 3.
112. McQuillan, J., *Bacterial-Nanoparticle Interactions*. 2010, University of Exeter. p. 250.
113. Summers, A.O., et al., *Metal cation and oxyanion resistances in plasmids of gram-negative bacteria*. Microbiology, ed. D. Schlessinger. 1978: American Society of Microbiology.
114. Jones, K.E., et al., *Global trends in emerging infectious diseases*. Nature, 2008. **451**(7181): p. 990-993.
115. Gracias, K.S. and J.L. McKillip, *A review of conventional detection and enumeration methods for pathogenic bacteria in food*. Canadian Journal of Microbiology, 2004. **50**(11): p. 883-890.
116. Jarvis, W.R. and W.J. Martone, *Predominant pathogens in hospital infections*. Journal of Antimicrobial Chemotherapy, 1992. **29**(suppl A): p. 19-24.
117. Levine, A.D. and T. Asano, *Peer Reviewed: Recovering Sustainable Water from Wastewater*. Environmental Science & Technology, 2004. **38**(11): p. 201A-208A.
118. Hodge, J.G., *Bioterrorism Law and Policy: Critical Choices in Public Health*. The Journal of Law, Medicine & Ethics, 2002. **30**(2): p. 254-261.

119. Dheda, K., et al., *Point-of-care diagnosis of tuberculosis: Past, present and future*. *Respirology*, 2013. **18**(2): p. 217-232.
120. Peeling, R.W. and D. Mabey, *Point-of-care tests for diagnosing infections in the developing world*. *Clinical Microbiology and Infection*, 2010. **16**(8): p. 1062-1069.
121. Vickerman, P., et al., *Detection of gonococcal infection: pros and cons of a rapid test*. *Molecular Diagnosis*, 2005. **9**(4): p. 175.
122. Pass, M.A., R. Odedra, and R.M. Batt, *Multiplex PCRs for Identification of Escherichia coli Virulence Genes*. *Journal of Clinical Microbiology*, 2000. **38**(5): p. 2001-2004.
123. Genomes_Online_Database. *Complete Genome Projects*. 2013 [cited 2013 2nd December]; Available from: http://www.genomesonline.org/cgi-bin/GOLD/index.cgi?page_requested=Complete+Genome+Projects.
124. Wetterstrand, K.A. *DNA Sequencing Costs: Data from the NHGRI Genome Sequencing Program (GSP)*. 2013 [cited 2013 2nd December]; Available from: <http://www.genome.gov/sequencingcosts/>.
125. Baron, E.J., *Classification*, in *Medical Microbiology*. 1996, University of Texas Medical Branch: Galveston.
126. Holden, M.T.G., et al., *Complete genomes of two clinical Staphylococcus aureus strains: Evidence for the rapid evolution of virulence and drug resistance*. *Proceedings of the National Academy of Sciences of the United States of America*, 2004. **101**(26): p. 9786-9791.
127. Plowman, R., et al., *The rate and cost of hospital-acquired infections occurring in patients admitted to selected specialties of a district general hospital in England and the national burden imposed*. *Journal of Hospital Infection*, 2001. **47**(3): p. 198-209.
128. WorldHealthOrganisation. *Health Care-Associated Infections: FACT SHEET*. Patient Safety - A World Alliance for Safer Health Care 2013 [cited 2013 20th November]; Available from: http://www.who.int/gpsc/country_work/gpsc_ccisc_fact_sheet_en.pdf.
129. PublicHealthEngland. *General Information on Healthcare associated infections (HCAI)*. 2013 [cited 2013 18th November]; Available from: <http://www.hpa.org.uk/Topics/InfectiousDiseases/InfectionsAZ/HCAI/GeneralInformationOnHCAI/#type>.
130. Schrag, S.J., V.r. Perrot, and B.R. Levin, *Adaptation to the fitness costs of antibiotic resistance in Escherichia coli*. *Proceedings of the Royal Society of London. Series B: Biological Sciences*, 1997. **264**(1386): p. 1287-1291.
131. Kaleta, E. and D.M. Wolk, *Bacterial Identification: Where Mass Spectrometry Meets Microbiology*. *Clinical Laboratory News*, 2012. **38**(5).
132. Keer, J.T. and L. Birch, *Molecular methods for the assessment of bacterial viability*. *Journal of Microbiological methods*, 2003. **53**: p. 175-183.
133. Struelens, M. and O. Denis, *Rapid molecular detection of methicillin-resistant Staphylococcus aureus: a cost-effective tool for infection control in critical care?* *Critical Care*, 2006. **10**(2): p. 128.
134. Park, S., et al., *Advances in microfluidic PCR for point-of-care infectious disease diagnostics*. *Biotechnology Advances*, 2011. **29**(6): p. 830-839.
135. Yager, P., G.J. Domingo, and J. Gerdes, *Point-of-Care Diagnostics for Global Health*. *Annual Review of Biomedical Engineering*, 2008. **10**: p. 107.
136. Patton, M.Q., *Qualitative Research*, in *Encyclopedia of Statistics in Behavioral Science*. 2005, John Wiley & Sons, Ltd.
137. Valanis, B.G. and C.S. Perlman, *Home Pregnancy testing kits: prevalence of use, false-negative rates, and compliance with instructions*. *American Journal of Public Health*, 1982. **72**(9): p. 1034-1036.
138. NHS. *How Accurate are Home Pregnancy Tests*. 2012 [cited 2013 27th November]; Available from: <http://www.nhs.uk/chq/pages/2308.aspx?categoryid=54>.

139. Sturenbury, E., *Rapid detection of methicillin-resistant Staphylococcus aureus directly from clinical samples: methods, effectiveness and cost considerations*. German Medical Science, 2009. **7**: p. 1.
140. Brown, D., et al., *Joint Working Party of the British Society for Antimicrobial Chemotherapy; Hospital Infection Society; Infection Control Nurses Association. Guidelines for the laboratory diagnosis and susceptibility testing of methicillin-resistant Staphylococcus aureus (MRSA)*. J Antimicrob Chemother, 2005. **56**: p. 1000 - 18.
141. OHara, S., *Novel Rapid Culture-Based Detection Method for Methicillin-Resistant Streptococcus aureus*. Journal of Clinical Microbiology, 2008. **46**(9): p. 3181-3182.
142. Leven, M., et al., *Evaluation of a real-time PCR assay and an multiplex-reverse hybridisation system for the detection of methicillin-resistant Staphylococcus aureus*, in *17th European Congress of Clinical Microbiology and Infectious Diseases (ECCMID) & 25th International Congress of Chemotherapy (ICC)*, B.E. Edegem, Editor. 2007.
143. Rossney, A.S., et al., *Evaluation of the Xpert Methicillin-Resistant Staphylococcus aureus (MRSA) Assay Using the GeneXpert Real-Time PCR Platform for Rapid Detection of MRSA from Screening Specimens*. Journal of Clinical Microbiology, 2008. **46**(10): p. 3285.
144. Wolk, D.M., et al., *Multicenter Evaluation of the Cepheid Xpert Methicillin-Resistant Staphylococcus aureus (MRSA) Test as a Rapid Screening Method for Detection of MRSA in Nares*. Journal of Clinical Microbiology, 2009. **47**(3): p. 758-764.
145. Wolk, D.M., et al., *Rapid Detection of Staphylococcus aureus and Methicillin-Resistant S. aureus (MRSA) in Wound Specimens and Blood Cultures: Multicenter Preclinical Evaluation of the Cepheid Xpert MRSA/SA Skin and Soft Tissue and Blood Culture Assays*. Journal of Clinical Microbiology, 2009. **47**(3): p. 823-826.
146. Farley, J.E., et al., *Comparison of the BD GeneOhm Methicillin-Resistant Staphylococcus aureus (MRSA) PCR Assay to Culture by Use of BBL CHROMagar MRSA for Detection of MRSA in Nasal Surveillance Cultures from an At-Risk Community Population*. Journal of Clinical Microbiology, 2008. **46**(2): p. 743-746.
147. Boyce, J.M. and N.L. Havill, *Comparison of BD GeneOhm Methicillin-Resistant Staphylococcus aureus (MRSA) PCR versus the CHROMagar MRSA Assay for Screening Patients for the Presence of MRSA Strains*. Journal of Clinical Microbiology, 2008. **46**(1): p. 350-351.
148. Paule, S.M., et al., *Performance of the BD GeneOhm Methicillin-Resistant Staphylococcus aureus Test before and during High-Volume Clinical Use*. Journal of Clinical Microbiology, 2007. **45**(9): p. 2993-2998.
149. Luteijn, J.M., et al., *Diagnostic accuracy of culture-based and PCR-based detection tests for methicillin-resistant Staphylococcus aureus: a meta-analysis*. Clinical Microbiology and Infection, 2010. **17**(2): p. 146-154.
150. Fothergill, A., et al., *Rapid Identification of Bacteria and Yeasts from Positive-Blood-Culture Bottles by Using a Lysis-Filtration Method and Matrix-Assisted Laser Desorption Ionization-Time of Flight Mass Spectrum Analysis with the SARAMIS Database*. Journal of Clinical Microbiology, 2013. **51**(3): p. 805-809.
151. Samuel, L.P., et al., *Evaluation of a Microarray-Based Assay for Rapid Identification of Gram-Positive Organisms and Resistance Markers in Positive Blood Cultures*. Journal of Clinical Microbiology, 2013. **51**(4): p. 1188-1192.
152. Scott, L., *Verigene[®] Gram-Positive Blood Culture Nucleic Acid Test*. Molecular Diagnosis & Therapy. **17**(2): p. 117-122.
153. Forster, B., et al., *Complex wavelets for extended depth-of-field: A new method for the fusion of multichannel microscopy images*. Microscopy Research and Technique, 2004. **65**(1-2): p. 33-42.
154. Mudanyali, O., et al., *Compact, light-weight and cost-effective microscop based on lensless incoherent holography for telemedicine applications*. Lab on a Chip, 2010. **10**: p. 1417-1428.

155. Penwill, L.A., et al., *Growth phenotype screening of Schizosaccharomyces pombe using a Lensless microscope*. Biosensors and Bioelectronics, 2014. **54**(0): p. 345-350.
156. Cui, X., et al., *Lensless high-resolution on-chip optofluidic microscopes for Caenorhabditis elegans and cell imaging*. Proceedings of the National Academy of Sciences, 2008. **105**(31): p. 10670-10675.
157. Seo, S., et al., *High-Throughput Lens-Free Blood Analysis on a Chip*. Analytical Chemistry, 2010. **82**(11): p. 4621-4627.
158. Ozcan, A. and U. Demirci, *Ultra wide-field lens-free monitoring of cells on-chip*. Lab on a Chip, 2008. **8**(1): p. 98-106.
159. Ozcan, A. *The Ozcan Research Group: Innovation Through Photonics*. 2009 [cited 2013 26th November]; Available from: <http://innovate.ee.ucla.edu/>.
160. Seo, S., et al., *Multi-color LUCAS: Lensfree On-chip Cytometry Using Tunable Monochromatic Illumination and Digital Noise Reduction*. Cellular and Molecular Bioengineering, 2008. **1**(2-3): p. 146-156.
161. Su, T.-w., et al., *Towards Wireless Health: Lensless On-Chip Cytometry*. Opt. Photon. News, 2008. **19**(12): p. 24-24.
162. Mudanyali, O., et al., *Lensless On-chip Imaging of Cells Provides a New Tool for High-throughput Cell-Biology and Medical Diagnostics*. Journal of Visualised Experiments, 2009. **34**: p. e1650.
163. Mudanyali, O., et al., *Compact, light-weight and cost-effective microscope based on lensless incoherent holography for telemedicine applications*. Lab on a Chip, 2010. **10**(11): p. 1417-1428.
164. Moon, S., et al., *Integrating microfluidics and lensless imaging for point-of-care testing*. Biosensors and Bioelectronics, 2009. **24**(11): p. 3208-3214.
165. Tseng, D., et al., *Lensfree Microscopy on a Cellphone*. Lab on a Chip, 2010. **10**(14): p. 1.
166. Zhu, H., et al., *Cost-effective and compact wide-field fluorescent imaging on a cell-phone*. Lab on a Chip, 2011. **11**(2): p. 315-322.
167. Isikman, S.O., et al., *Lensfree On-Chip Microscopy and Tomography for Biomedical Applications*. Selected Topics in Quantum Electronics, IEEE Journal of, 2012. **18**(3): p. 1059-1072.
168. Zhu, H., et al., *Optofluidic Fluorescent Imaging Cytometry on a Cell Phone*. Analytical Chemistry, 2011. **83**(17): p. 6641-6647.
169. Mudanyali, O., et al., *Integrated rapid-diagnostic-test reader platform on a cellphone*. Lab on a Chip, 2012. **12**(15): p. 2678-2686.
170. Zhu, H., U. Sikora, and A. Ozcan, *Quantum dot enabled detection of Escherichia coli using a cell-phone*. Analyst, 2012. **137**(11): p. 2541-2544.

2 Lensless Microscope Technique Development and Analysis for Growth Phenotype Screening using the model organism *Schizosaccharomyces pombe*

2.1 Introduction

Rapid detection techniques are generally targeted at the detection of a specific known pathogen, for example MRSA, *C. difficile* or gentamicin-resistant *E. coli*^[1] bacteria which have a genetic resistance to a treatment method. It has been discussed in the Chapter **Error! Reference source not found.** that the incidence of phenotypic resistance is on the increase, demonstrated in populations such as biofilms^[2], persister cells^[3] and Small Colony Variants (SCVs)^[4]. Individuals from these populations infer no genotypic resistance, they are genetically identical to the non-resistant wildtype but have growth phenotypes. By monitoring and extracting the cell phenotypes, the populations containing these will be separated simply from the bulk, using their individual growth parameters as discriminating factors.

Extracting phenotypic growth data from the individual growth curves of single-celled organisms can be a lengthy procedure:

- Bacterial growth curves are recorded over time courses of several hours;
- Analysis of single cell growth characteristics is conventionally performed using a light microscope, collecting time-lapse photography images;
- Many bacteria are motile, moving out of field of view and focal plane rapidly.

To image successfully a bacterium which has a diameter of 1 μm the optical microscope will have to be operated using high magnification, it has been calculated for a light microscope with a 40x magnification that the Field Of View (FOV) is only 0.036 mm^2 . Empirically it has been noted that during time lapse imaging of non-motile eukaryotic cells they often move out of the field of view and the focal plane changes especially in the early phase of the time course experiments where thermal equilibration is not complete. *E. coli* is known to be able to swim up to 50 times its diameter per second^[5]. The Lensless microscope however does not suffer from the thermal variations of the focal plane and has a significantly larger FOV. Hence large numbers of cells may be observed growing simultaneously from which rapid growth phenotype populations can be derived. The Lensless

Microscope^[6, 7], as discussed previously, has a FOV limited only by the size of the detection sensor CCD chip. Even for the simplest cameras this can produce a FOV of two orders of magnitude greater than the conventional light microscope. As a result, the Lensless microscope can monitor a cell as it moves through a flow cell or large numbers of organisms simultaneously. Vertical movement of a particle along the focal plane, the plane in which the object image is in focus, is a limitation for both the Light microscope and the Lensless Microscope, particles leaving the focal plane change the apparent size in both instruments. However, the Lensless microscope is able to still monitor these cells and adjust size measurements accordingly. The Lensless microscope can image through a flow cell of more than 4 mm deep, all cells throughout this depth can be recorded and monitored^[8]. In contrast to this the phase contrast microscope has a much narrower depth of field, ranging from 1.0 μm at a 40x magnification to 0.2 μm at 100x magnification. Further to this the detection of an organism rapidly is limited by the length of time it takes to grow (length of lag period, rate of growth etc, Chapter 1). The concept of 'Phenotype Fingerprinting' has been devised to address this limitation and preliminary investigations presented in this thesis.

The presentation of protein on the cell surface varies with organism type. At the most simple level of phenotype distinction, a Gram positive organism presents the polysaccharide teichoic acid on its surface^[9, 10] while the Gram negative organism does not. These surface structures can be detected rapidly with fluorescence labelled antibodies or a stain, at this level conferring immediate distinction between Gram positive and Gram negative. Sub-lethal levels of silver stress have been shown to up-regulate the genes related to a number of surface-presenting proteins in *E. coli*^[11] within 10 minutes^[12]. The level of these proteins on the cell surface following exposure to silver ions will increase, changing the cell surface presentation, potentially displaying a different, identifiable surface phenotype. Coupled with the phenotypic growth behaviour in the early stages of the growth curve, the identification of surface proteins by labelled antibodies can be described as the 'phenotype fingerprint' and has the potential to be unique to the organism. The Lensless microscope and corresponding analysis algorithm have been used to determine the difference between cells in a mixed solution^[13], to count the number of cells in a sample^[8] and to detect cells with fluorescent elements attached^[14]. The advantage of using a Lensless microscope to detect fluorescence is that the method is able to determine between fluorescence which is bound to a cell and fluorescence which is present but not associated with a cell, increasing the sensitivity and specificity of the detection. Further to this the device and the corresponding analysis algorithm will be applied here to monitor the changing parameters of microbial growth; the growth phenotype.

Optimum bacterial growth must be supported by nutrient-containing growth medium, maintained at a constant, often elevated, temperature with a moist and oxygenated environment. Lensless microscope configurations reported to date are illuminated by a single wavelength of light, to improve the image quality and to simplify the ease of image reconstruction. The total holographic reconstruction of diffraction patterns to complete cell images requires the application of a complex integral which was outlined in Chapter 1. This method requires significant (but not insurmountable) computing to reconstruct an image containing a high level of structural information but the extraction of simple dimension measurements may be considered appropriate for growth phenotype classification and indeed phenotype fingerprinting. Holographic reconstruction methods^[15, 16] are not realistic in the proposed Lensless microscope Point Of Care (POC) setting for the following further reasons:

1. White light illumination is used to prevent the detrimental effects on organism growth observed with a single wavelength^[17]
2. Single wavelength illumination provides a sharper diffraction pattern, the most detailed patterns coming from illumination in the longer wavelengths. A hologram illuminated with white light source is constructed of numerous images, one from each wavelength of light in the range. Each image will have a different set of parameters, size, angle of 1st dark fringe and distance from centre. When reconstructed these will superimpose on another, impairing the image and cancelling each other out.
3. Images are acquired through a flow cell which is 1mm thick, the medium volume chosen to ensure oxygenated growth, thus reducing associated redox stress responses which are in themselves phenotypic changes.
4. The flow cells contain a growth surface chosen for each organism; in the case of *S. pombe* the slide is lectin coated. Thin layer interference effects were observed from the top and bottom of the flow cell components but can be removed successfully using an initial background image subtraction.

Imaging the diffraction patterns of cells with relatively low refractive indices, and poor scattering properties, have been discussed previously, Chapter **Error! Reference source not found.** The *E. coli* cell images with diffraction patterns recorded by the Ozcan group are imaged in PBS, a medium with a low refractive index, with iso-osmotic properties to maintain cell integrity whilst maintaining the optical contrast of the *E. coli* cells. The construction of a Lensless microscope using existing and cost effective cell phone technologies has been demonstrated^[6]. It is proposed that the algorithm

described in this chapter can further simplify the cell phone device, making cell size analysis more robust.

2.2 Aims and Objectives

This chapter aims to construct a temperature-stable Lensless microscope device with a removable and reusable growth chamber. The analysis of the diffraction patterns recorded by the Lensless microscope will be performed with a new, simple algorithm which negates the requirement for holographic image reconstruction methods. The analysis method should be robust, stable and will extract from the diffraction pattern data the dimension information required to construct phenotype growth parameters.

The rod shaped fungus *S. pombe* will be imaged and analysed to verify that the algorithm and subsequent calibration curve can be applied to measure the length and widths of organisms with an aspect ratio. The distribution of single cell length (L_{t0}) and width (W_{t0}) collected will be compared to the distributions published in the literature to determine the validity of the measurement and further analysis of the evolution of the cell over time to determine whether growth measurement is feasible.

2.3 Lensless Microscope

The concept of the Lensless microscope^[18] will be applied to study the evolution of the Airy Disc diffraction pattern over time, as the diffracting object grows. The Lensless microscope is a device to measure the diffraction pattern cast on a sensor when a light wave encounters an object in its path. In this case, the sensor is a Charge Coupled Device (CCD) and the diffracting objects are microspheres, bacteria and fungi.

2.4 Diffraction and the formation of the Airy Disc

The Lensless microscope monitors diffraction patterns created by light scattered by small diffracting objects in its path. Circular and spherical objects cast patterns known as Airy Discs surrounded by an Airy pattern, a central bright node surrounded by concentric rings of alternating low and high intensity called fringes, Figure 2.1. The plotted cross section of the centre of the Airy Disc is called an intensity profile curve. As the object in Figure 2.1 from which the diffraction pattern is formed is spherical, any cross section of the diffraction pattern should be the same.

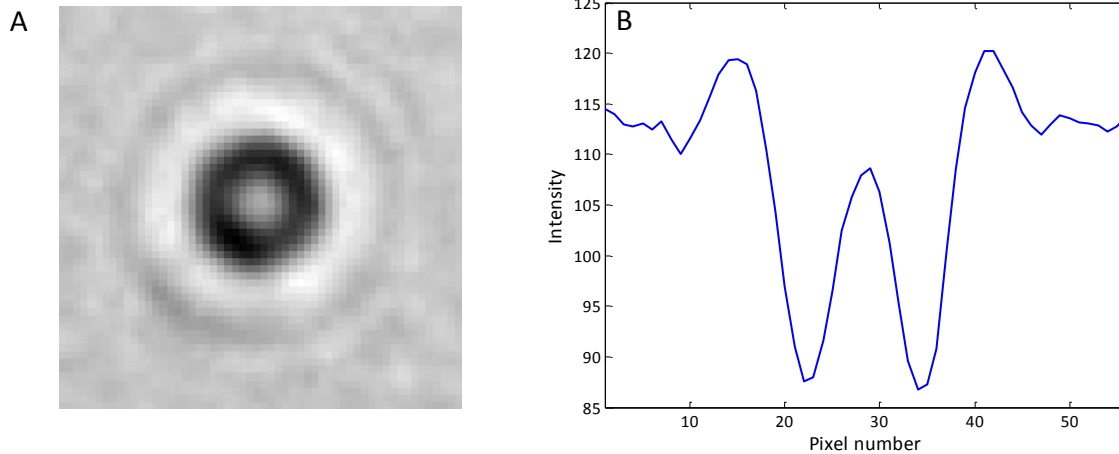


Figure 2.1. A typical Airy disc pattern (A) of a sphere 30 μm in diameter and the horizontal cross section of this sphere plotted as an intensity distribution curve (B).

The Airy disc is the bright circular spot in the centre of the diffraction pattern in Figure 2.1 A, and is surrounded by concentric dark and light rings, referred to as the Airy pattern^[19]. The formation of the Airy Disc and the surrounding Airy Pattern fringes is now discussed.

2.4.1 Diffraction

The Huygens Principle is used to describe light propagation as waves and states that when light encounters a slit or aperture in the path of travel every point along the wave of light at the slit may be considered to be a secondary light source, or a wavelet, which radiates circular waves^[20]. Plane waves diffracting around an object have a phase difference between one side of the object and the other. When the lights waves recombine in phase they show constructive interference and when they are in anti-phase they show destructive interference, Figure 2.2 B and C.

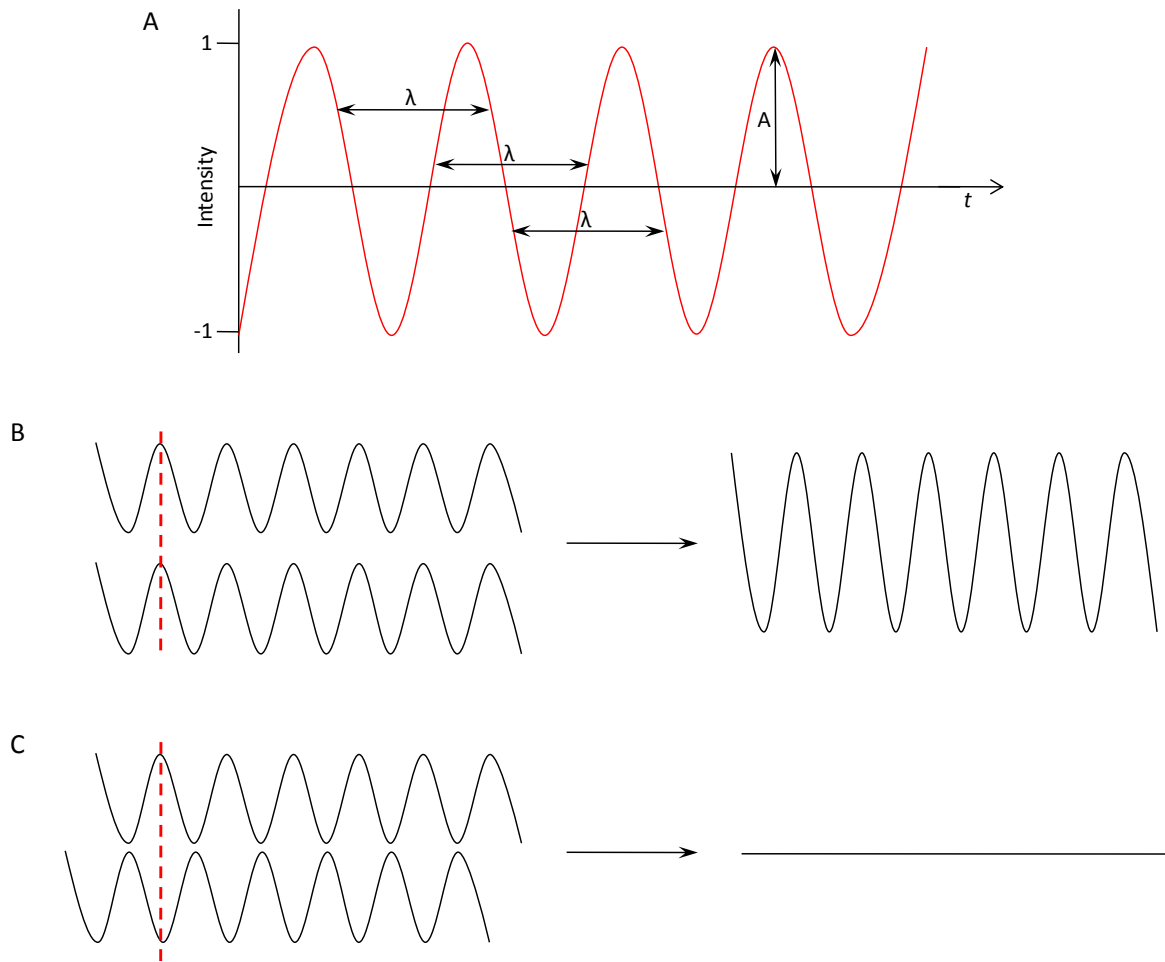


Figure 2.2. (A) the basic properties of a monochromatic light wave. In the unit time of this graph the wave has a frequency of 4.5, an amplitude, A and a wavelength, λ . When the waves in (B) interfere they have constructive interference and result in an increase in magnitude. When the waves in (C) interfere they have destructive interference and result in a decrease in magnitude.

As light diffracts around an object, the waves interfere, at some points constructively and at others destructively. The diffraction pattern that propagates to a screen, in this case a CCD chip, from the point of diffraction is dependent on the size of the diffracting object, the wavelength of the light, the working distance – the distance from the diffracting object to the screen – and the proximity of other objects to the diffracting object in question. The 2D representation of the Airy Disc, the intensity profile in Figure 2.1 can be re-created using the idea that a cross-section of a small particle, with width a , is similar to two thin slits on a screen separated by a .

2.4.2 Young's Double Slit

The theory of diffraction is exemplified in the Young's double slit experiment the findings of which were published in a paper entitled 'Experiments and Calculations Relative to Physical Optics'[21]; the concepts may be considered schematically, Figure 2.3.

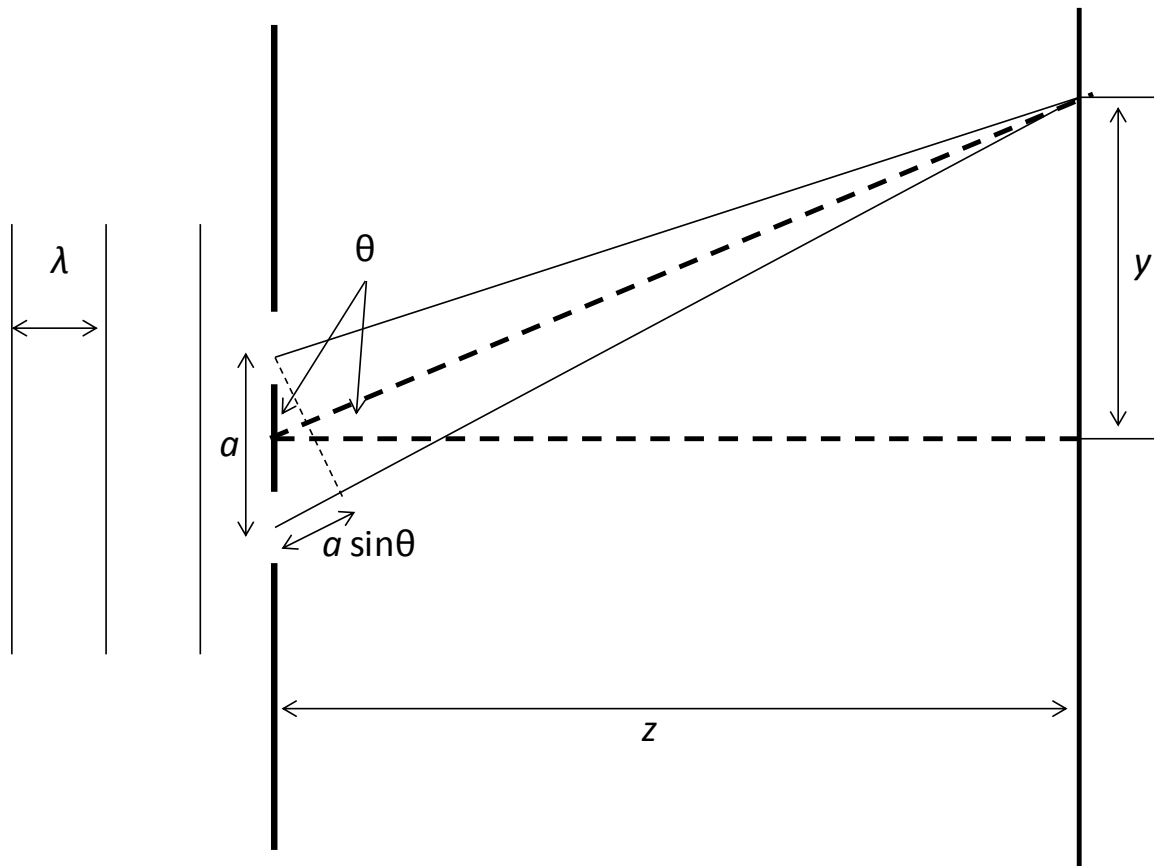


Figure 2.3 Young's double slit setup. Monochromatic coherent light propagated through two slits separated by distance a , to a screen a distance of z from the slits.

Light from a coherent light source is propagated through two slits separated by distance a . The incident, plane-wave propagating light at the slits is considered to be two point sources with circular (spherical) symmetry after the slits. Coherent superposition of the waves leads to constructive and destructive interference and the characteristic fringe patterns when projected onto a screen, shown in Figure 2.4.

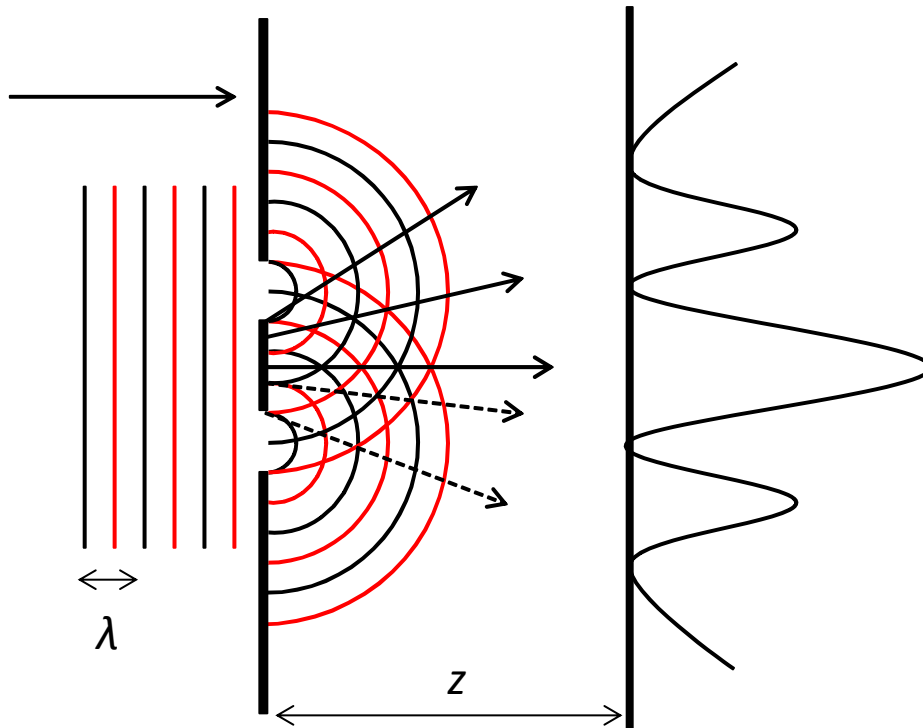


Figure 2.4. The fringe pattern projected on the screen from the Young's double slit setup, lit by monochromatic light with wavelength λ , with the slits and screen separated by distance z . The red line indicates peaks of intensity of the light wave and the black lines the troughs. The black arrows indicate areas of constructive interference and the dash arrows areas of destructive interference.

Using the parameters in Figure 2.3 the distances between the areas of bright intensity can be calculated using equation (1).

$$a \sin \theta = m\lambda \tag{1}$$

where m is an integer (the central bright peak occurs where $m = 0$). When θ is small, $\sin \theta$ can be approximated as $\frac{y}{z}$ resulting in the equation (2) for the position of the bright fringes:

$$y = \frac{\lambda z}{a} m \tag{2}$$

A comparison between the two slits and the two sides of the diffracting object may be drawn to allow and effective diameter of the sphere to be determined, a . The working distance, the distance from the point of diffraction and the screen, is the distance z and the screen is the CCD chip. The determination of object size from the diffraction pattern is dependent on other factors such as the diffraction limit and the diffractive index differences between object and surrounding medium.

2.4.3 Diffraction Limit

All imaging systems illuminated in the far-field are restricted by the diffraction limit^[22, 23] although there is a considerable field of investigation into techniques that are not confined by the diffraction limit such as those using near-field imaging^[24]. Ernst Abbe showed that whenever objects are imaged in light, those objects smaller than half of the wavelength of that light are not present in the final image^[25]. Abbe proposed the following equation (3) to determine the diffraction limit for each system^[26]:

$$DL = \frac{\lambda}{2(NA)} \quad (3)$$

where DL is the diffraction limit; λ the wavelength of diffracting light; and NA the numerical aperture of the system. For the Lensless microscope optical configuration, the NA = 1 giving a simple limit of diffraction as $\lambda/2$. The shorter the illuminating wavelength of light the smaller an object the system is able to accurately view. This explains how the electron microscope is able to image much smaller objects than a light microscope as it illuminates with wavelengths 100,000 times shorter than visible light associated with the de Broglie wavelength of the electrons. When objects are close together they cannot be distinguished separately due to the diffraction limit and the Rayleigh criterion, a continuation of the Abbe limit of diffraction.

Considering the nature of the images recorded by the CCD of a Lensless microscope, the Rayleigh criterion^[27] is the minimum resolvable distance between two objects. Rayleigh Criterion accounts for the wavelength of the illuminating light, size of diffracting object and the distance from point of diffraction to the screen. Images are said to be not resolved when the first dark fringe of one diffraction pattern overlaps with the central bright node of another^[28]. The Rayleigh Criterion for a circular aperture is given, equation (4), containing the correction factor of 1.22:

$$\sin \theta = 1.22 \frac{\lambda}{a} \quad (4)$$

The parameters here are defined in Figure 2.3. The correction factor is approximately the first zero of the Bessel function of the first kind, of order one, divided by π . Equation (4) can be adjusted to account for the refractive index of the diffracting object. An object with a larger refractive index than the medium in which it is surrounded will slow the travel of the light, adjusting the λ parameter in equation (4). The larger the refractive index contrast, the larger the retardation in λ , and subsequently the larger the angle of spread of the diffraction fringes.

2.4.4 Lensless Microscope Configuration

The conventional configuration for the Lensless microscope is shown in Figure 2.5 and has been described by others elsewhere^[6, 29]. The Lensless microscope configuration maximises the diffraction pattern stability and intensity whilst controlling the environmental parameters such as temperature, light intensity and wavelength stability, nutrient concentration and humidity. The current configuration of the Lensless microscope is designed to study microbial growth with growth medium in a flow cell and this has some significant challenges: refractive index contrast, image stability, temperature stability, turbulence and thermal lensing. Due to these varied demands we aim to develop a simple algorithm to extract the aspect ratio and therefore growth parameters of the imaged objects over time. The configuration, therefore, needs to be stable over a period of 24 hrs – 72 hrs and the flow cell must hold sufficient media volume to prevent nutrient starvation in this time and be liquid tight to avoid drying out. The proposed final device design is displayed in Figure 2.5, with a technical drawing in Figure 2.6.

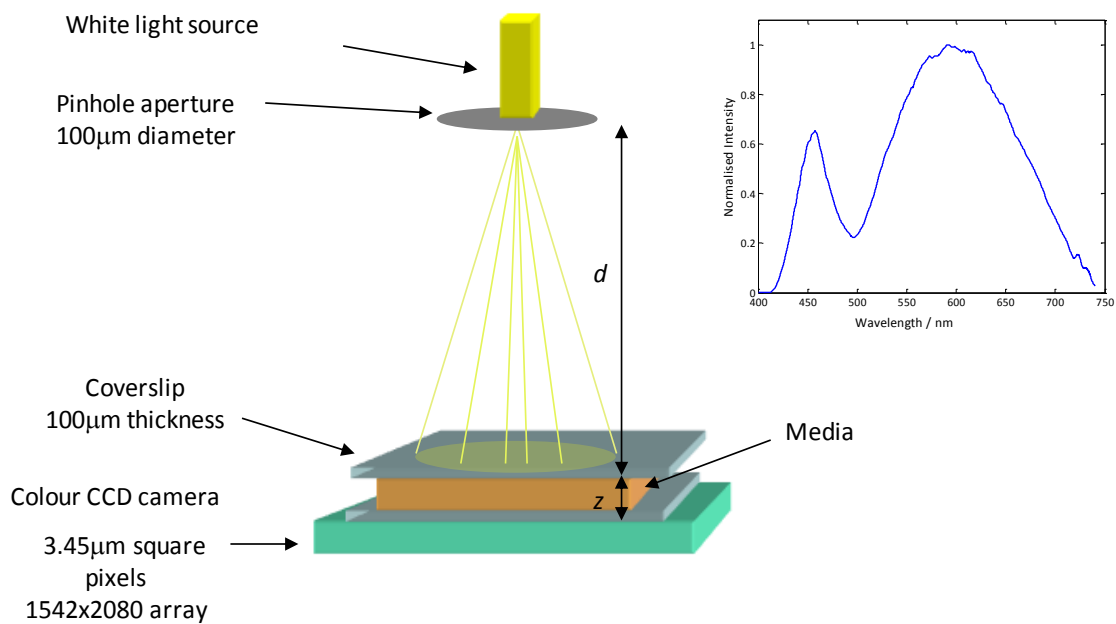


Figure 2.5 The basic Lensless microscope flow-cell configuration. For all experiments described here the distance d is 15cm and the working distance z is 1100 µm. The white light source, insert top right, has a peak intensity of 595nm and a range from 405-740nm. The CCD has 3.45mm² pixels under a Bayer colour filter.

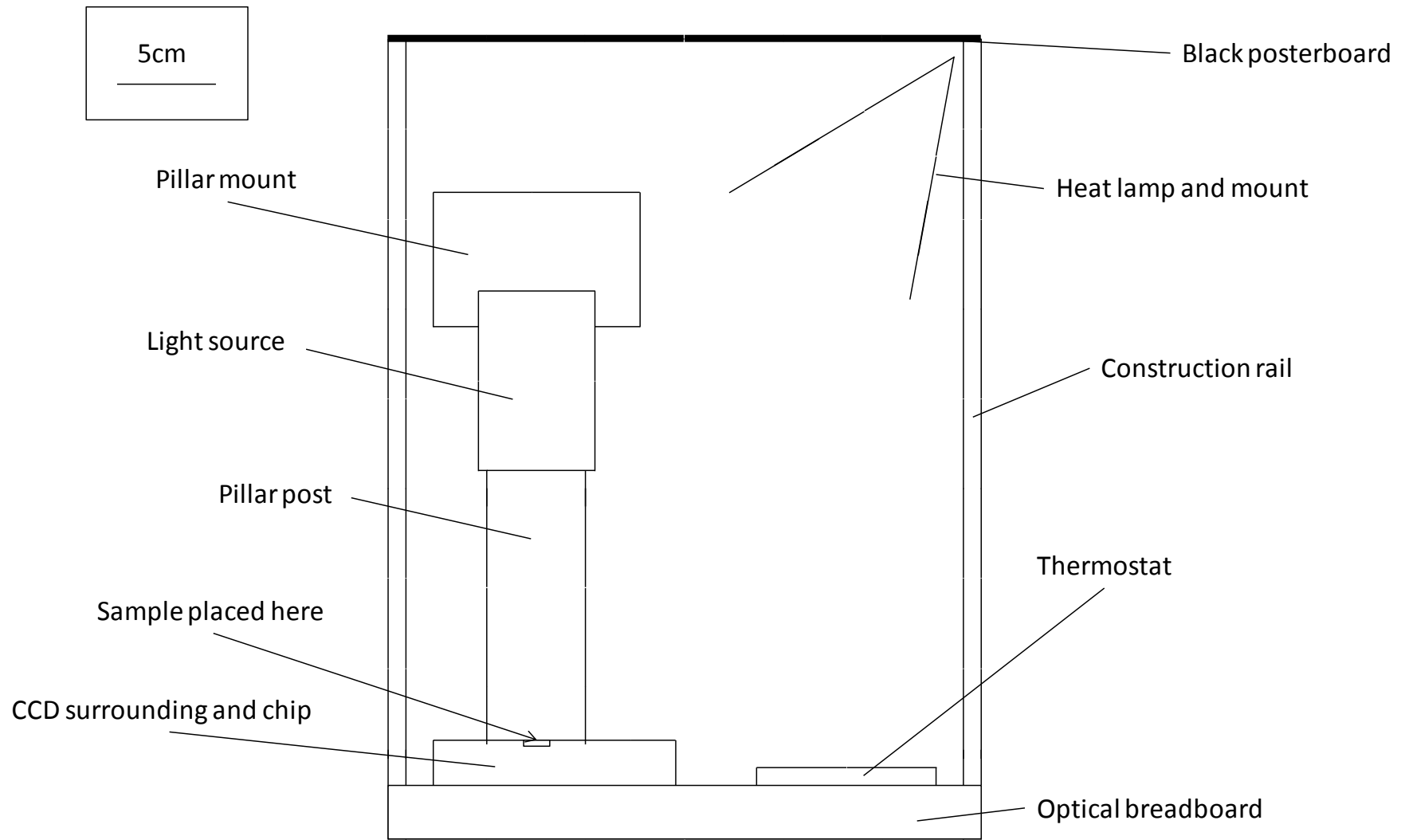


Figure 2.6 A Technical drawing of the Lensless Microscope setup. A complete component list is included in Appendix 1

The light from a white light source was chosen so as not to affect the growth of the organisms adversely. The emission spectrum of an LED is shown in the inset of Figure 2.5. Light propagates over a distance, d , of 15 cm before reaching the flow cell where it will interact with the diffracting objects of interest, microspheres and *S. pombe* cells. The resulting Airy Disc pattern is collected on a CCD camera, with pixels with an area of $3.45 \mu\text{m}^2$ and a total sensor area of 39mm^2 (IM 3.2, Jenoptik). The CCD is a colour CCD chip, a colour filter provided by a Bayer pattern filter, a checkerboard of 3 colours, red, green and blue applied to 4 pixels, twice as many pixels filtered green than red or blue. The raw colour values for each pixel are 8-bit digitised to give a value between 0 and 256 for red, for green and for blue.

The flow cell is formed from two cover slips sealed with an inert silicone gel and petroleum jelly. The flow cell has a constant thickness of $\sim 1 \text{mm}$ and a total volume of $174 \mu\text{L}$. The cell has entrance and exit flow ports to allow medium to enter and leave the flow cell: the ports remained closed in these experiments. The flow cell is tightly clamped directly to the surface, the diffracting objects set at a working distance, z , typically 1 mm from the sensor surface. The working distance is chosen to ensure the Airy disc patterns cover 20×20 pixels on the camera but not allow the patterns from nearby cells to overlap. The diffracting light waves spread out from the point of diffraction until interception by the screen (Figure 2.4); smaller z is the smaller the diffraction pattern on the screen. The physical restraint of the flow cell ensures the working distance is temperature and mechanically stable to allow signal averaging. The clamping also reduces chances of inconsistent lensing effects caused by the glass elements of the cell heating up and reduces the cell drying out, which also causes unwanted lensing effects.

The entire Lensless microscope instrument is housed in a temperature controlled, light excluding box. The temperature is thermostatically controlled to within $\pm 2 \text{ }^\circ\text{C}$ at lower temperatures and $\pm 4 \text{ }^\circ\text{C}$ at higher temperatures. Figure 2.7 shows a time course of temperature monitoring overnight from 17:00 hours for 10 hours. The mean temperature at a nominal $25 \text{ }^\circ\text{C}$ was $24.9 (+0.2 -0.1) \text{ }^\circ\text{C}$ and for the elevated growth temperature, of $37 (+0.4 -0.1) \text{ }^\circ\text{C}$ constant over a 600 minute period.

The *S. pombe* growth temperature was maintained at $25 \text{ }^\circ\text{C}$, the temperature over the period of 600 minutes had a mean of $24.9 (+0.2 -0.1) \text{ }^\circ\text{C}$ and a standard deviation of $0.7 \text{ }^\circ\text{C}$ and all other experiments were carried out at $37 \text{ }^\circ\text{C}$ and were maintained to a mean of $37 (+0.4 -0.1) \text{ }^\circ\text{C}$ with a standard deviation of $0.9 \text{ }^\circ\text{C}$. Long term temperature stability is important for the growth of unicellular organisms. A change in temperature of the growth environment of *E. coli* and *S. pombe* can change the rate of growth^[30] and induce a heat shock stress response^[31]. In the case of *E. coli* the

cell volume at division is also affected by temperature fluctuations^[32]. Now the device is stable for temperature it can be assessed for stability of images captured.

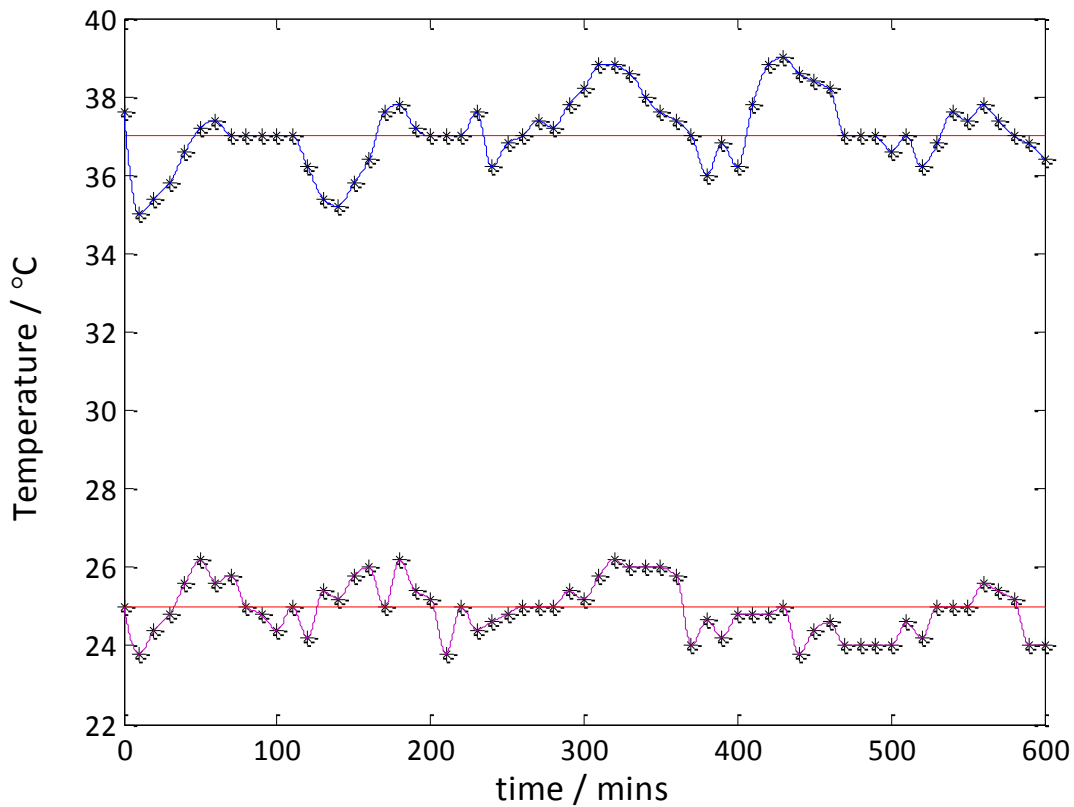


Figure 2.7. The stability of the temperature within the device housing at both 25 °C (purple) and 37 °C (blue) over a time course of 600 minutes. The temperature controlled to 25 °C has a range of 2.4 °C with a mean of 24.9 (+0.2 -0.1) °C. The temperature controlled to 37 °C has a range of 4 °C and a mean of 37 (+0.4 -0.1) °C. Red lines indicate the target, reported temperature for the setup.

2.5 Image Processing

The CCD chip is connected via IEEE 1394a FireWire to the operating computer and images were collected at a frame rate of one image every 0.6 seconds by the proprietary software ProgRes Capture Pro v.2.8.8.1. The images are collected in 8-bit vertical resolution and stored in TIFF format. The data collected by the Lensless microscope described here could be analysed using the full holographic reconstruction methods described in Chapter 1. The images contain all the information of a light microscope image but the growth phenotype analysis only requires in length and so a simple major and minor axis measurement algorithm the analysis process has been designed, rendering it more suitable for operation at the point of care.

The Lensless microscope configuration used in this thesis is shown schematically, Figure 2.5, and produces an Airy disc diffraction pattern covering $\sim 20 \times 20$ pixels, however larger objects may extend to $\sim 50 \times 50$ pixels. Extraction of the major and minor axes dimensions from the Airy disc requires a robust algorithm to measure the brightness between the fringes. The Airy disc diffraction pattern consists of a bright central spot surrounded by concentric rings of dark and bright diffraction fringes. By measuring the intensity profiles along the major and minor axis of the pattern the lengths along each axis and the aspect ratio of the diffracting object can be derived as a function of time.

Airy disc patterns are analysed using an algorithm designed here, and in Appendix 2, to determine the intensity brightness difference between the centre and first fringe of the Airy disc (Figure 2.8). The centre of the Airy Disc, the bright spot, is selected by the user manually. It is possible to select all Airy Disc patterns on the FOV of the CCD chip automatically using thresh-holding algorithms, but here it is performed manually to avoid analysing an air bubble or dust particle. The difference between the central bright spot maxima and the first dark fringe is chosen as the ΔI measurement as it was observed that poor "scatterers" such as Gram negative bacterial cells produce a diffraction pattern which has well defined central maxima and first minima only.

A virtual mask is located over the centre of the pattern and the first fringe and the intensity is then integrated as a function of the anticlockwise angle. The major axis is located as the maximum ΔI ; the minor axis is defined perpendicular to the major axis; together this forms the basis of the Airy Disc First Fringe (ADFF) analysis procedure. Figure 2.9 shows the evolution of the shape of the mask using model data as expected for a spherical object, and Figure 2.10 using model data for an object with aspect ratio of 2:1. In these preliminary experiments, elements such as mask width and mask positioning have been controlled, the variations and associated errors discussed subsequently.

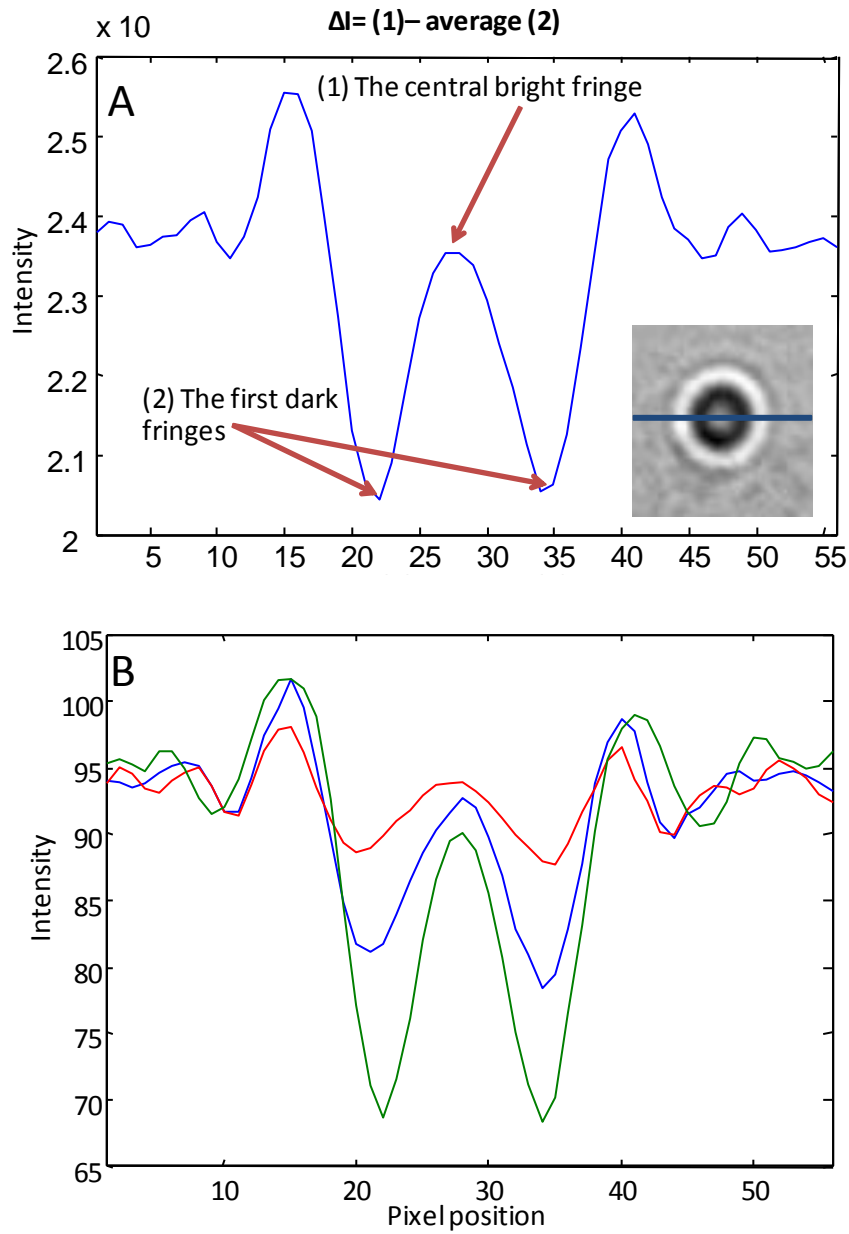


Figure 2.8 (A) The calculation of ΔI , the intensity difference between the central bright spot and the average of the first dark fringes, the initial dark ring. The graph shows an intensity cross-section of the Airy disc diffraction pattern, insert). This is the typical pattern observed for a sphere of 30 μm . (B) The intensity cross section taken at the maximum ΔI position for the sphere sizes from 12 μm (red), to 20 μm (blue) and finally 30 μm (green). It is to be noted that although this figure shows spheres of sizes larger than 12 μm in diameter, this trend is observed for all sphere diameters measured, starting at 1 μm .

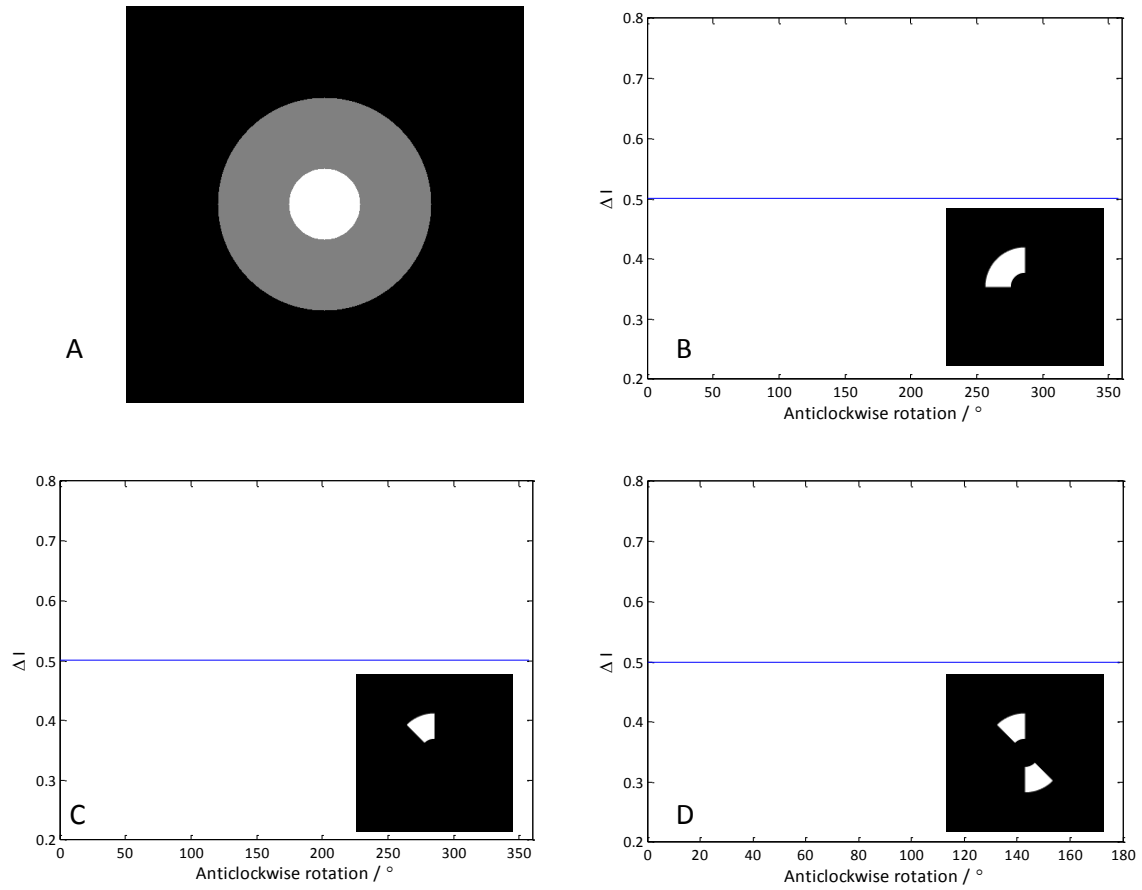


Figure 2.9. The plots created by the ADFF models of one quarter in size (B), one eighth in size (C) and one eighth averaged with the opposite eighth (D) using the simple model data (A). This data is how it would be expected that a perfect sphere central node and initial dark fringe would appear.

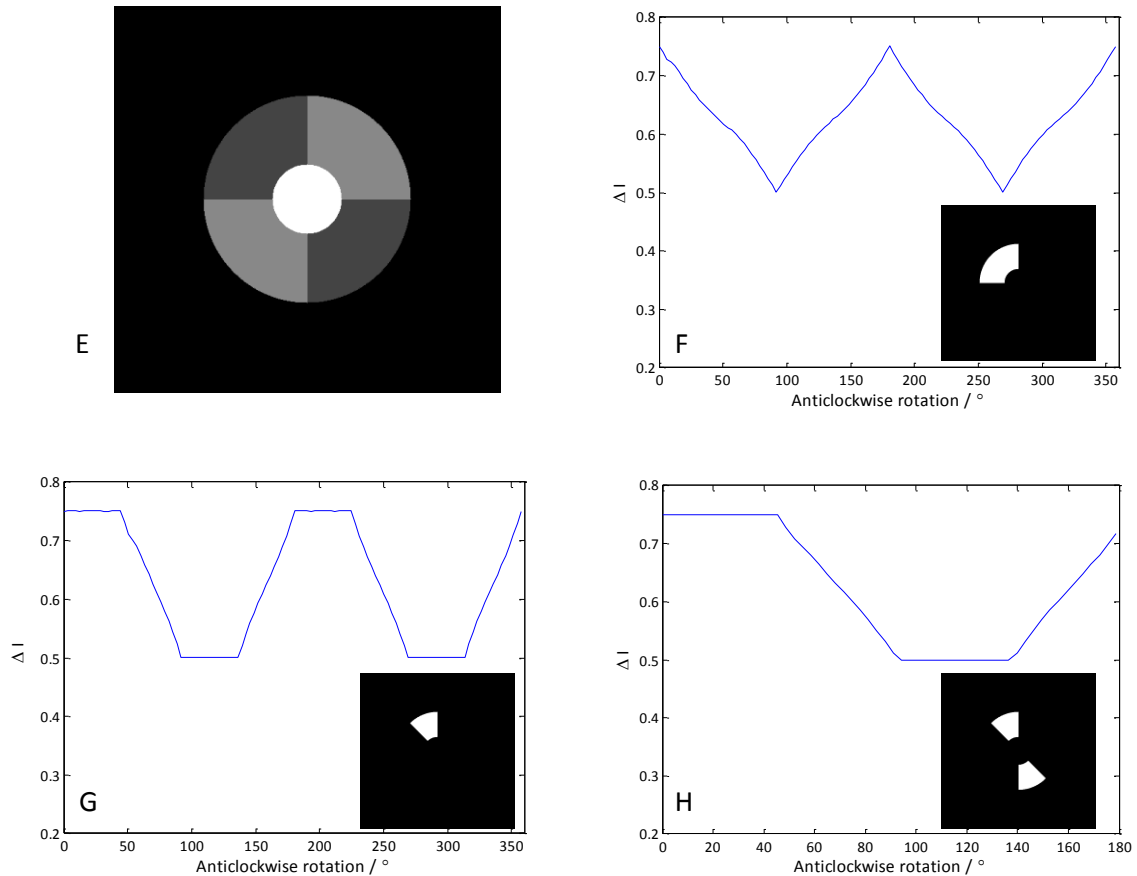


Figure 2.10 The plots created by the ADFF models of one quarter in size (F), one eighth in size (G) and one eighth averaged with the opposite eighth (H) using the simple model data (E). This data is how it would be expected that a rod shaped objects central node and initial dark fringe would appear.

Optimising the mask structure, Figure 2.10, shows the best ADFF performance occurs when the mask is smaller than a quarter of the circle to enhance the sensitivity of the location of the major axis; smaller than an eighth of the circle and the mask and high frequency noise especially from 'real' data reduces the accuracy of the measurement. Further, data are prone to noise from neighbouring diffracting objects and small local changes may enhance the ΔI erroneously. There are other errors which can be introduced into the data by this mask method, namely 'jitter' and mask misalignment.

The software mask has automated corrections for 'jitter' and mask misalignment. The Airy disc centre is not completely fixed by the mechanical configuration of the microscope and the algorithm chooses the central 3 pixels, which have the highest intensity within an area of 6×6 pixels defined by the original choice. The algorithm is set to fail if the central ΔI is calculated as lower than the average ΔI of the first dark fringes. Figure 2.11 shows what happens to the calculated ΔI of model data if the mask is not corrected for jitter and mask misalignment.

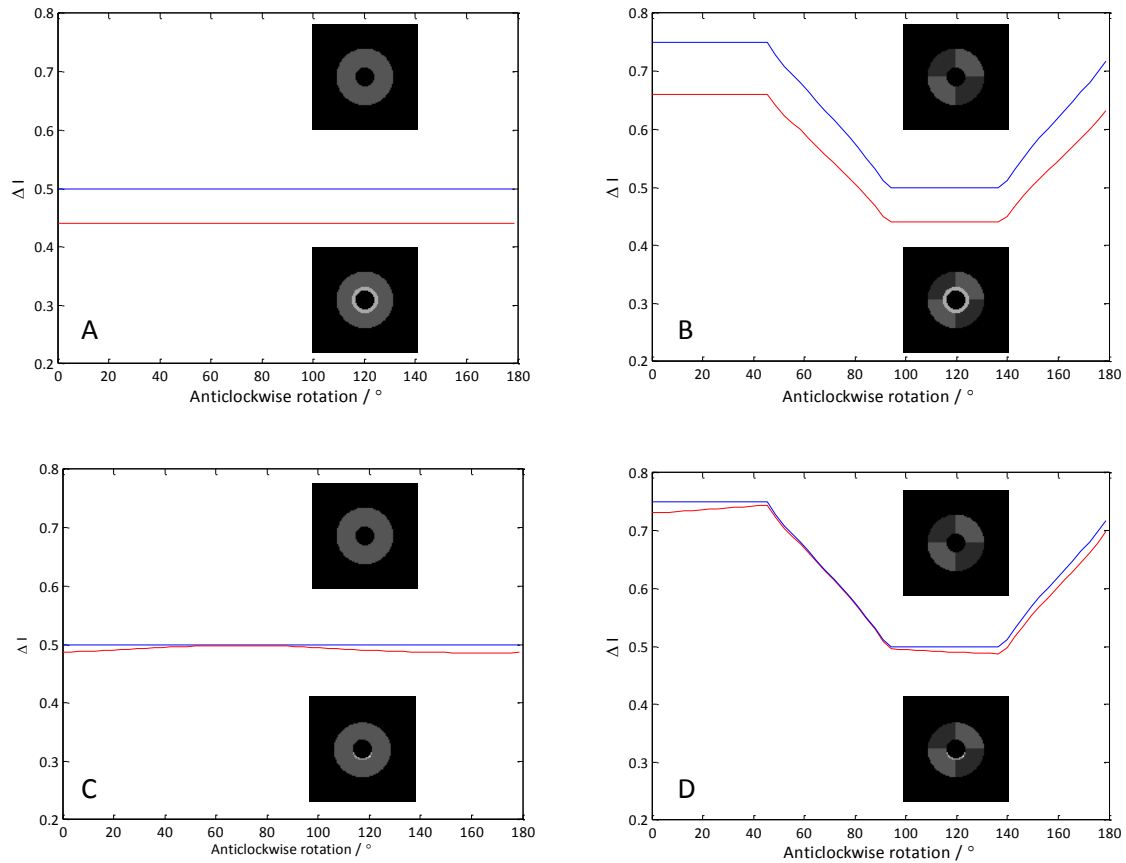


Figure 2.11 The effect mask width and mask misalignment/jitter have on the ΔI calculated by the bowtie ADF. Blue lines are the data from ideal situations, red lines from the misalignment. A and B show the effects on calculations when the masks central radius is too small, similar effects occur if the outer radius is too large. C and D show the calculation errors when the mask is misaligned, the greater the misalignment the larger the error. C in particular demonstrates how if the mask is misaligned the Airy Disc analysed could appear to have an aspect ratio of something other than 1.

The figures above demonstrate the mask optimisation and tracking procedure, showing how the calculated ΔI varies with mask thickness and positioning. The mask thickness has been set for each organism type analysed, too thick and discrete changes are not observed, too thin and the data become dominated by high frequency noise resulting in measurement error. The mask thicknesses were all optimised using spheres of known diameters with aspect ratios assumed to be 1. The full ADF software program is included as an appendix to this thesis, Appendix 2.

The stability of this method was characterised over extended time periods required for the growth phenotype monitoring.

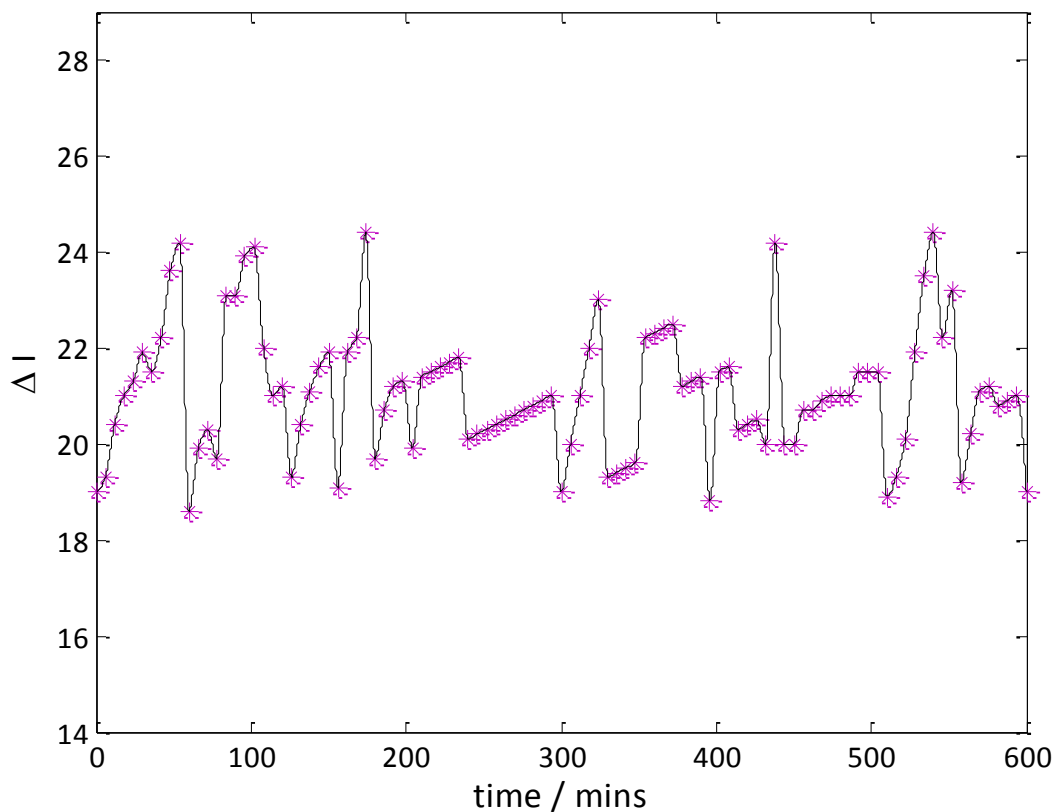


Figure 2.12 The measured ΔI of a $30\ \mu\text{m}$ sphere over a time course of 600 minutes. The range is 5.8, deviating a maximum of $\pm 13\%$ from the mean of 21.1 (+0.4 -0.2). A conversion to size is required to calculate the actual size measurement error associated with this algorithm.

Confident that errors attributed to image analysis have been reduced the calibration of ΔI with respect to size of the scattering object needs to be considered.

2.6 Dimension Calibration

The ADFP algorithm produces a size-dependent intensity difference that needs to be calibrated over the length scales required for the growth experiments, in the case of *S. pombe* the 1st cell division only is of interest, a maximum range of 3 – 20 μm . The experiments with *E. coli* (Chapter 4) require an extended range of 1 – 60 μm to account for colony growth. It is important to be certain of the stability within this range. The size of any object can only be measured to within the diffraction limit, which is 0.3 μm for the current illumination source.

For these calibration experiments the same spheres were used as for the stability experiments, polystyrene microspheres (Sigma-Aldrich Microparticles, 80177, 72938, 95531, 59336, 87896, 88511, 72822 and 80304). All spheres used were length verified using light microscope images, 40x microscope objective (Carl Zeiss, PrimoStar and AxioCam ERc5s). These images were captured from a fixed position calibration slide used for all stability experiments presented here. The analysis of the

Airy Disc patterns produced in this setup from the range of microspheres show the width of the diffraction pattern does not change significantly with size. The parameter of the diffraction pattern which does change with size is ΔI , changing along a linear trend, Figure 2.8. When using the curve to calibrate cells it must first be corrected for the refractive index (RI) of the individual diffracting objects. The calibration is created using spheres with a RI of 1.55 whereas the Gram negative *E. coli* has an RI of 1.395^[33] and the yeast (eukaryotic) cell has an RI of 1.399^[34].

The sources of error in the ADFP have been reduced by averaging the image over a number of acquired frames. Figure 2.13 displays the differences between a single frame capture diffraction pattern for a 30 μm sphere (A) and the same sphere averaged over 225 frames. The noise reduction is shown in, Figure 2.14 as a function of the number of frames averaged. The theoretical noise reduction should reduce by $1/\sqrt{n}$, where n is the number of frames.

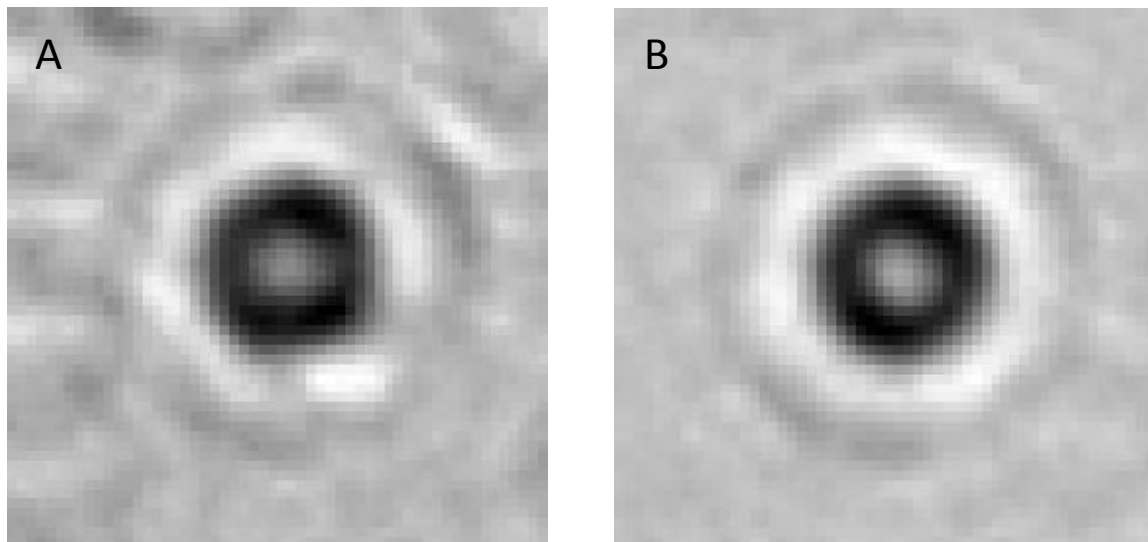


Figure 2.13 A raw diffraction pattern of a thirty micrometre sphere (A) and the same sphere after the images have been averaged 255 times (B).

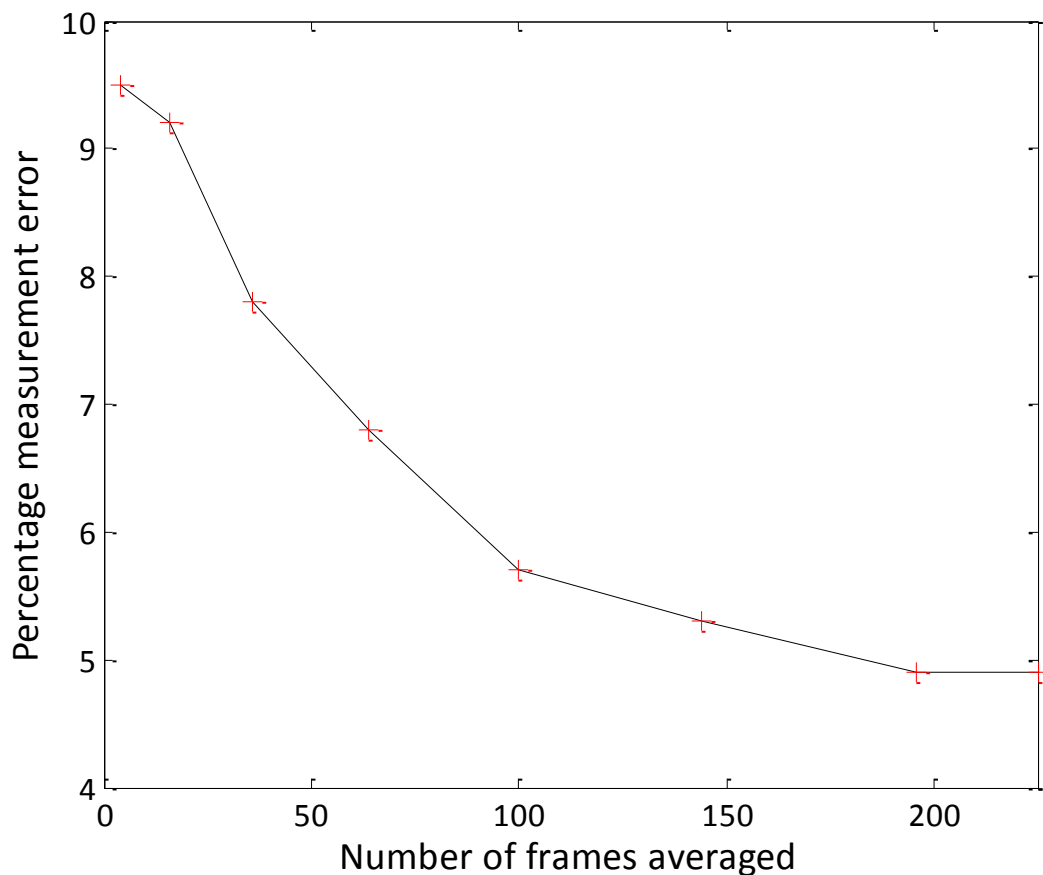


Figure 2.14 The reduction in error between size measurements of 20, 30 μm spheres when frames are averaged over a range of 4 to 225 images.

Figure 2.14 shows that the error in the ADFP measurements reaches 5 % at 196 frames averaged. The maximum error is only marginally larger at 144 frames averaged but with a significant reduction in the image processing and acquisition times. Using the 5 % error target, 196 images can be captured in 120 seconds which allows data points to be collected every 2 minutes during the doubling time of *E. coli* for example. It suggests a lower limit to the accurate determination of a growth phenotype event of about two minutes or one 196-frame collection period. The Lensless microscope, as with all far-field illuminated instruments, has a fundamental limit to the accuracy with which a length dimension can be measured – the diffraction limit. This fundamental limit and the overall error propagation in the ADFP procedure can be compared for the measurement of the diameter of calibration spheres and is summarised in, Figure 2.15.

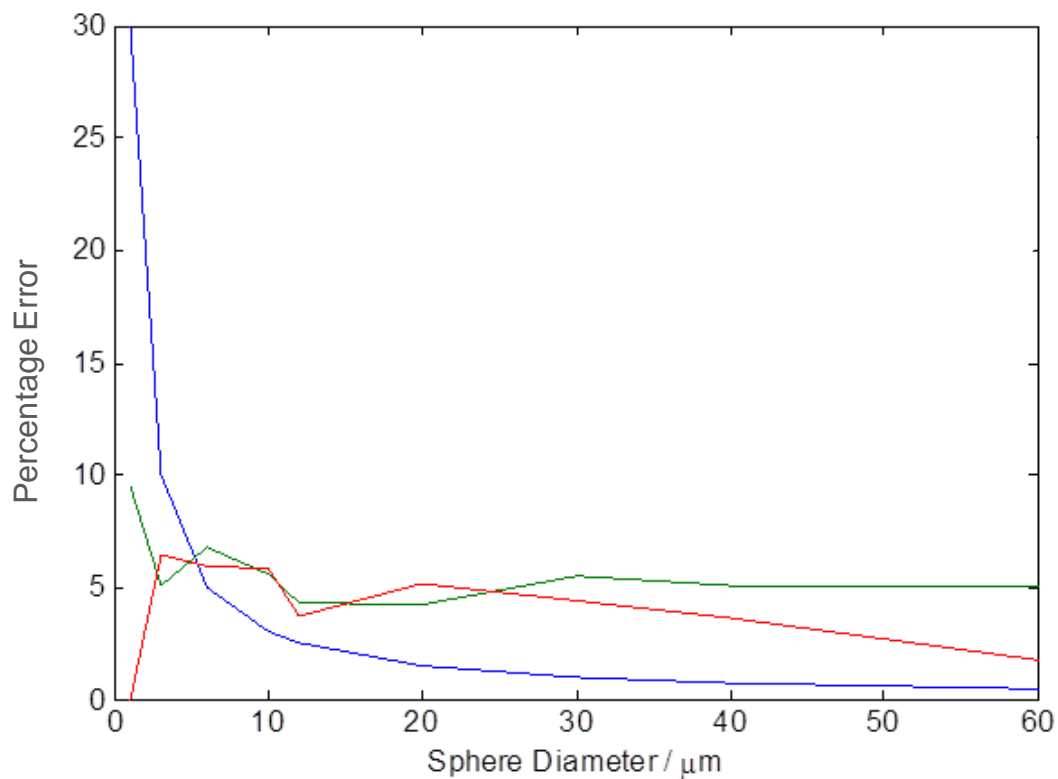


Figure 2.15. The largest error associated with each sphere diameter, blue, the diffraction limit error; red, the error associated with the ADF calculation; and green, the error associated with the light microscope measurements. Sub 6 μm the error is dominated by the diffraction limit of 0.3 μm , above this the error is 5% for measurements calculated by the ADF and from optical measurements.

At smaller sphere diameters the error is dominated by the diffraction limit which for a 1 μm sphere is 30%. The uncertainty in determining the diameter of a 2 μm sphere is also controlled by the diffraction limit which is dependent on the wavelength. The error for the 2 μm sphere for $\lambda = 600 \text{ nm}$ (λ max of the emission spectrum of the lamp) is $\pm 7.5\%$. There are three measurement errors associated with the Lensless microscope. For objects of sizes below 6 μm the error is dominated by the diffraction limit error of 0.3 μm . For objects above 6 μm the error is 5%. This error associated with ADF calculations is attributed to mask calculation error, interaction between close diffracting objects and imaging artefacts. For measurements from the optical microscope we calculate an error of 5%. This error can be attributed to interaction with surface structures and focal plane through the object.

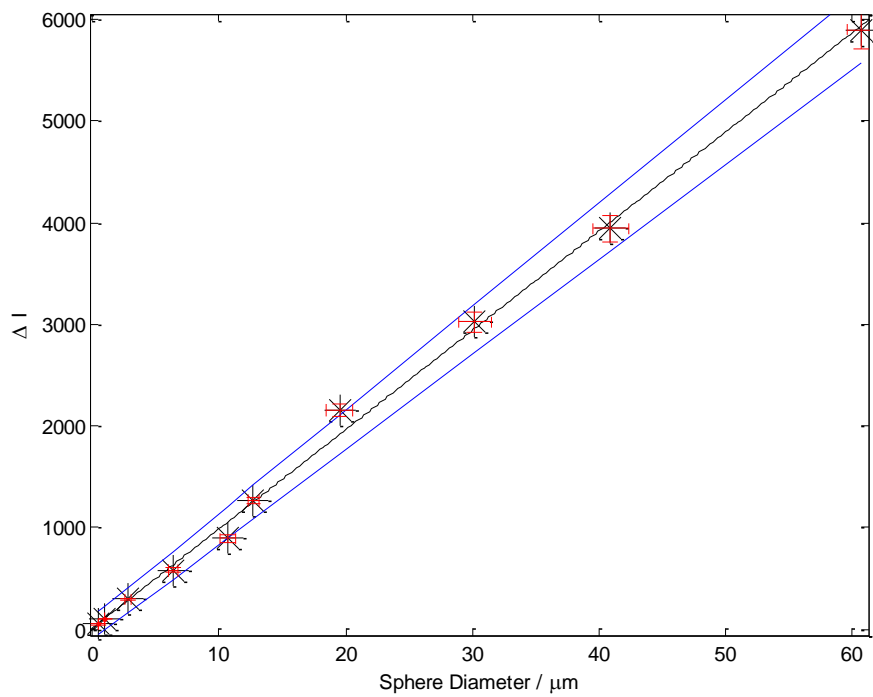


Figure 2.16. Calibration curve for averaging of 225 images for the whole annulus averaged ADF, the line fit errors (blue) and the error bars (red). The error bars show the maximum possible error for each sphere, horizontal bars measured optically and the vertical bars the error output from the ADF algorithm.

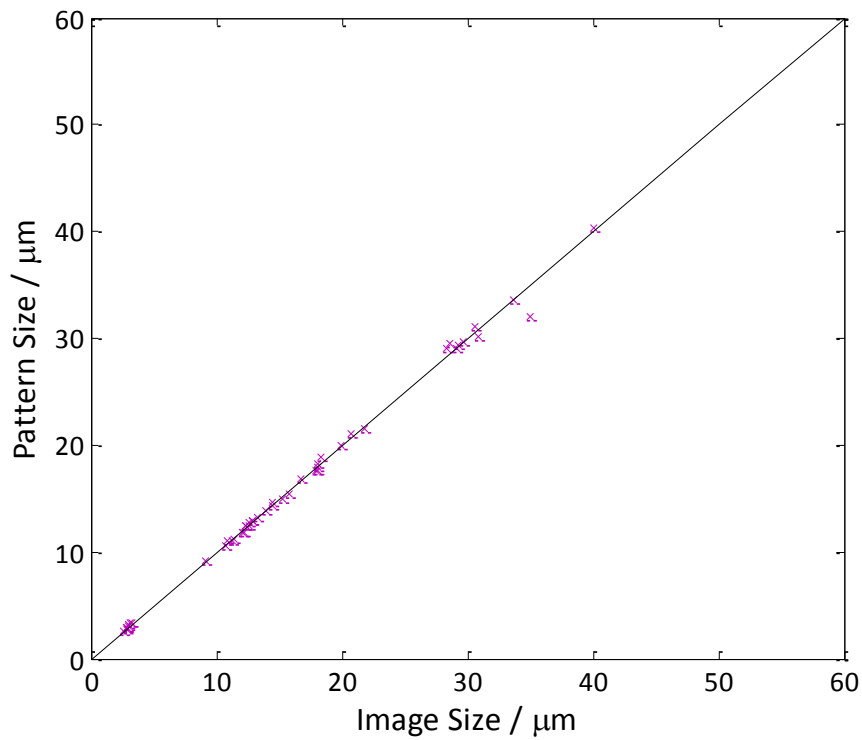


Figure 2.17 The correlation between the optically measured image size and the corresponding ADF calculation using the calibration curve. The slope of the line is 0.992, indicating that this method calculates the correct size of a diffracting object, in the range of 1 – 60 μm, to within 1%. R^2 is 0.997.

The final calibration for the complete Lensless microscope instrument is shown in Figure 2.16 for calibration spheres over the range 1 – 60 μm . The diameter of a sphere was measured by light microscopy with a 40x magnification to produce the sphere size vertical error, the horizontal error coming from the error in the ΔI size calibration, the errors displayed in Figure 2.15. The line of best fit has an error of $R^2 = 0.997$ and an intercept of $-0.1 (+1.0-1.20)$ μm , the perfect measurement line having $R^2 = 1$ and an intercept 0. The 95 % CI fit errors are displayed in blue and the maximum calculated error for each individual size displayed as error bars, horizontally for the error in sphere size within the sample and vertically for the measurement acquired by the ADFP. The calibration is further verified by comparing the ADFP size measurement with the optical measurement of 30 spheres, Figure 2.17. The slope of the fitted line is 0.992 (+0.003-0.004), predicting that there is, on average, a 0.8 % error between the optically measured and ADFP calculated sizes. To ensure that the same spheres were measured by both the optical and Lensless microscope the spheres were bound to a lectin surface (further details in section 2.7.1) to prevent movement within the flow cell. The spheres were first imaged using a AxioCam ERc 5s light microscope and camera, the position marked with a coloured dot. The flow cell was transferred to the Lensless microscope in the same orientation, the coloured dot located and the sphere imaged and measured.

The ADFP method of diffraction pattern analysis is able to extract the dimensions of a symmetrical object with relatively high refractive index ($RI = 1.55$) compared to the surrounding medium ($RI = 1.334$). The dimension information calculated from the diffraction patterns correlates highly with the dimensions measured from optical microscope images, with an R^2 value of 0.997. Above 6 μm the experiment is limited to an error of 5 % but below 6 μm , this is still dominated by the diffraction limit. Biological growth, however, is rarely symmetrical and so for this method to be successful it must now be tested with a particle with aspect ratio. For this purpose the eukaryotic fungus *S. pombe* has been selected.

2.7 *Schizosaccharomyces pombe*

S. pombe, the eukaryotic fission yeast is used in the study of the diffraction of rod shapes. *S. pombe* is a rod-shaped fission yeast widely used as a model organism in the study of the cell cycle and so the growth of a single cell is well characterised^[35]. The *S. pombe* cell has a well defined width which remains fixed during cell growth, which occurs from the two ends of the rod only^[36, 37]. The cell has an average width of 3.9 μm ^[38] and a length of 7 μm at birth extending to 13-14 μm prior to division^[39-41]. It is this fixed aspect ratio control which makes the *S. pombe* length (L_{t0}) and width (W_{t0}) parameters ideal as a proof-of-principle that the analysis algorithm returns the correct value for objects which are not symmetrical. Further *S. pombe* studies can be found in Chapter 3.

2.7.1 Experimental Setup

An exponential phase growth culture of *S. pombe* in YE5S was diluted to OD = 0.01, in the same growth media, and 100 μL of cell suspension was deposited in the flow cell, the lower surface of which was coated in lectin (Sigma-Aldrich, Lectin from Glycine max, L1395, 100 $\mu\text{g}/\text{mL}$). After 2 minutes the excess solution was removed, leaving only the cells that had adhered to the lectin-coated surface. The chamber in the control sample was filled with YE5S broth containing a 3-point calibration of microspheres (sizes 6, 12 and 30 μm) and sealed with the second cover slip.

The flow cell was imaged first using the light microscope and immediately after on the Lensless microscope experiment to allow comparison of optical and Lensless dimensions. Details of the growth conditions and the confirmation of appropriate growth conditions in the flow cell are described in detail in Chapter 3. This set up was then used for subsequent growth experiments in Chapter 3.

2.7.2 Results

The microscope images and diffraction patterns of 18 fission yeast cells were collected and compared to establish the characteristics of single cells and their dimension variability. These findings are displayed in Figure 2.18, the cells were identified as the same cell on both microscopes using the same registration method as described in section 2.6.

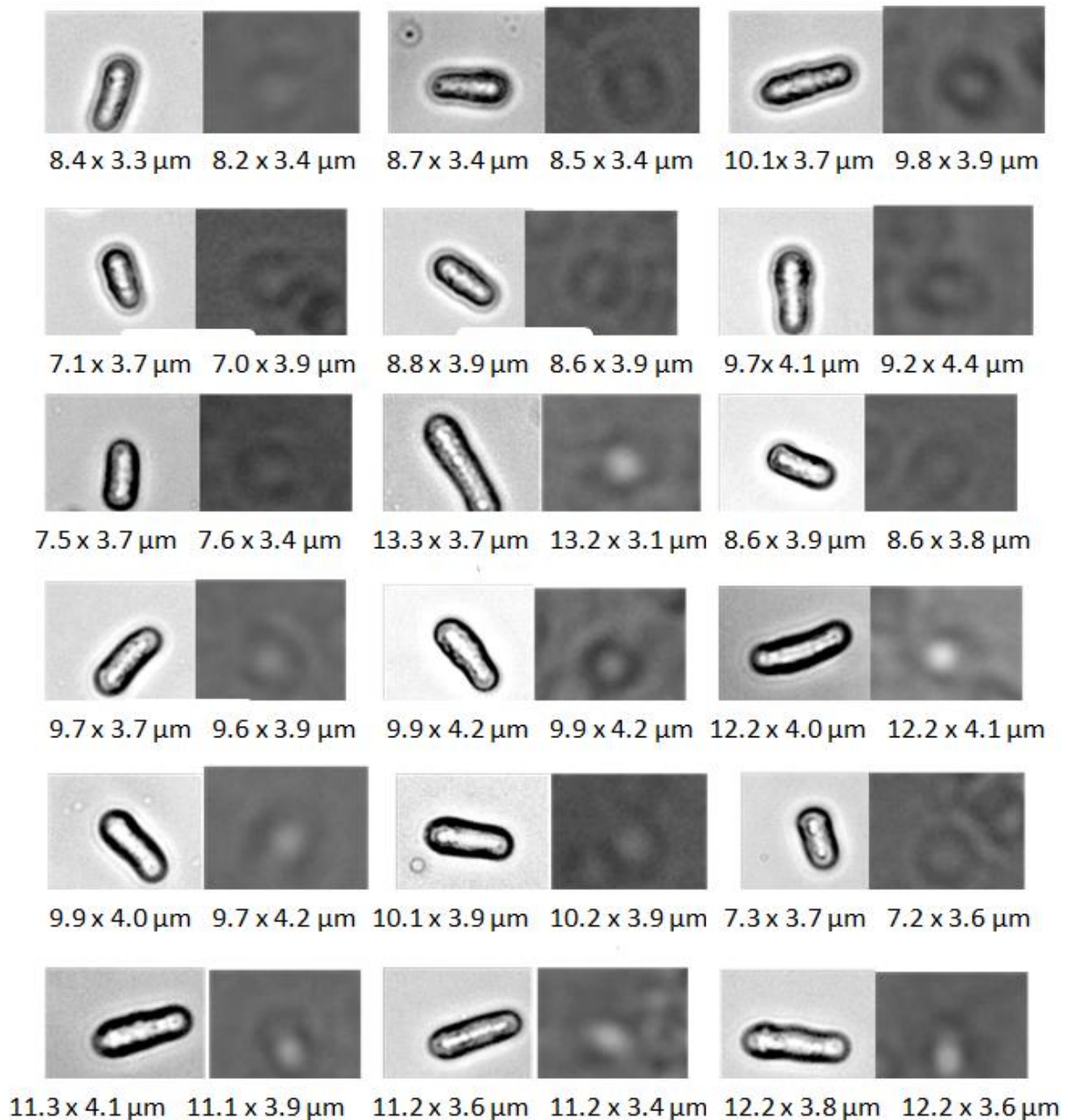


Figure 2.18 A comparison between 18 *S. pombe* microscope images and the corresponding Airy Discs. Images are not as clear as a traditional Airy Disc as these images are heavily influenced by the lectin surface and the depth of the surrounding liquid.

A typical growth curve of *S. pombe* is displayed in Figure 2.19; a total of 11 parameters can be identified and extracted; a histogram of each is displayed in Figure 2.20. It is the subject of this thesis to find, amongst all of the parameters of microbial growth, characteristics of growth which indicate a phenotype. The 11 parameters are potential phenotype classification parameters and a method for assessing their potential has been derived. The 11 parameters extracted are:

- Major and Minor Dimensions at t_0 minutes / μm
- Length of lag period / minutes ;

- Maximum growth rate / $\mu\text{m min}^{-1}$;
- Average growth rate / $\mu\text{m min}^{-1}$;
- Time between lag period and cytokinesis (A_{time}) / minutes;
- Length at cytokinesis (A_{size}) / μm ;
- Estimated birth length (L_B) / μm ;
- Length of the cell cycle (t_{cell}) / minutes;
- Aspect Ratio $t_0(\text{AR}t_0)$;
- Maximum Aspect ratio (AR_{max}).

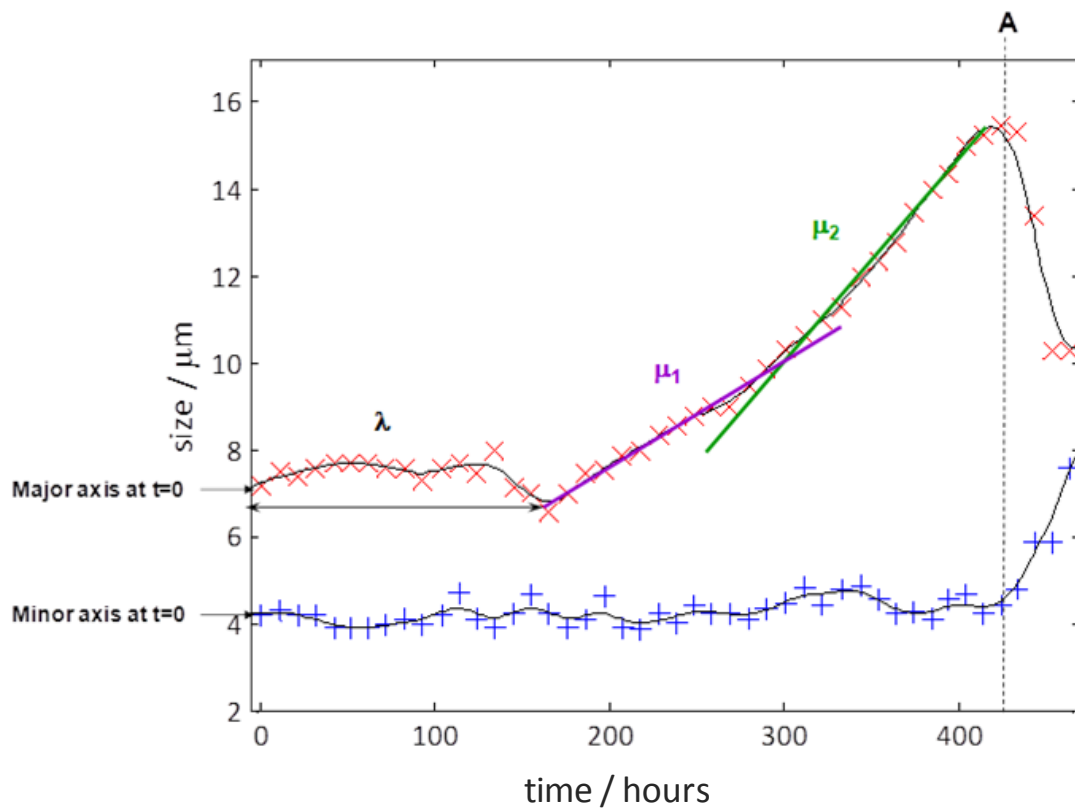


Figure 2.19. A typical *S. pombe* growth curve displaying some of the growth parameters which may be extracted from the data: the length and width at t_0 minutes (L_{t_0}/W_{t_0}); the length of the lag period (λ); the two growth rates μ_1 and μ_2 ; the time in the growth curve that the maximum size is reached (A_{time}) and the maximum size the colony or cell reaches (A_{size}).

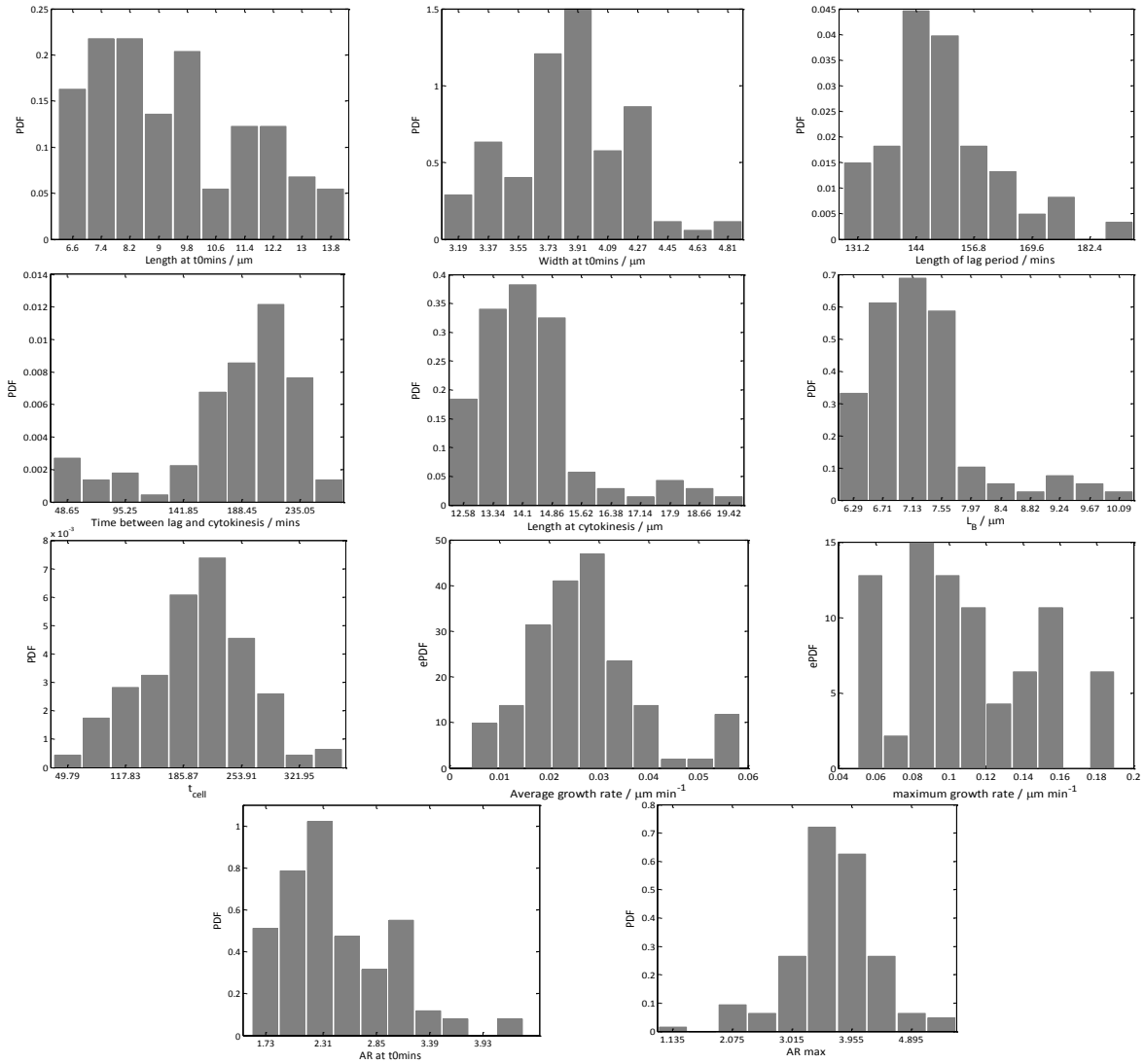


Figure 2.20 The histogram distributions of all 11 parameters extracted and calculated from the growth curve of *S. pombe*. From top left, Length (L_{t_0}); Width (W_{t_0}); Length of lag period (λ); A_{time} ; A_{size} ; L_B ; t_{cell} ; Average growth rate; Maximum growth rate; AR_{t_0} ; AR_{max} .

Analysis of the full parameter set will be performed in Chapter 3. The analysis of the Length and Width at t_0 minutes parameters are now presented as a proof of principle. The ePDFs presented in Figure 2.21 are histograms normalised to an area of 1. Further discussion and explanation of graphical representation methods is in section 2.8.3.

The ePDFs and Boxplots with overlays of Beeswarm plots of length and width of $N = 100$ *S. pombe* cells at t_0 minutes are shown in Figure 2.21, these are also further explored and explained in section 2.8.3.

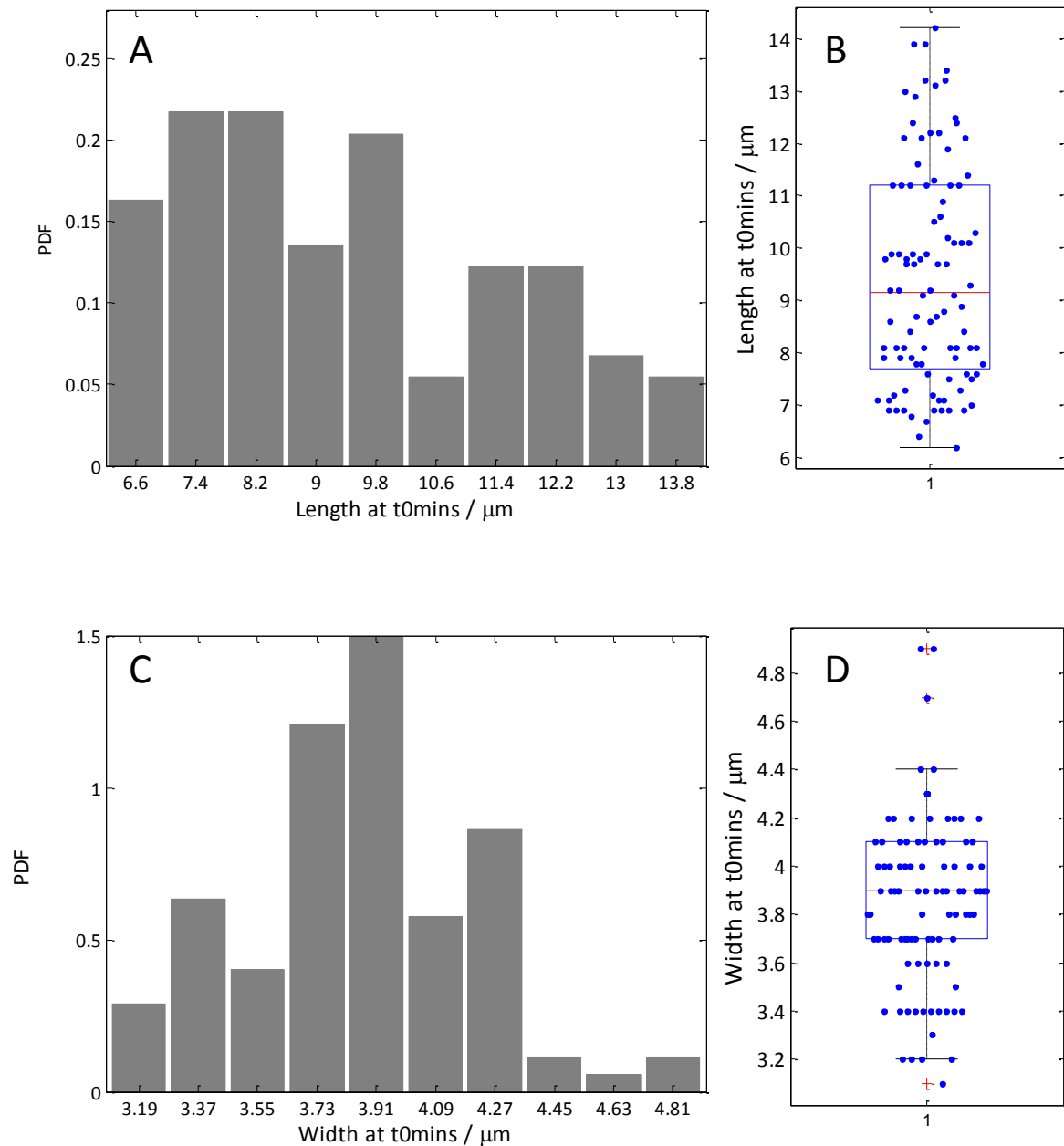


Figure 2.21 The normalised histograms and Box plots for the distributions of A + B major axis at t0mins and C + D minor axis at t0mins for $N=100$ *S. pombe*. The major axis length converges on a median of $9.2 (+0.6 -0.9)$ μm and the minor axis width converges on a median of $3.9 (\pm 0.15)$ μm . The Box plot displays a red line to indicate the median, the box edges indicating the 75th and 25th percentile of the data and the whiskers extending to the range of the data. The whiskers (w) are set at a default length of $\pm 2.7\sigma$ with data outside of this indicated as outliers where σ is the standard deviation of the sample. Outliers are classified as either larger than $q_3 + w(q_3 - q_1)$ or smaller than $q_1 - w(q_3 - q_1)$ where q_1 and q_3 are the lower and upper quartile values respectively

The distributions of both length and width in Figure 2.21, the display of which is discussed further in section 2.8.3, are the first look at two possible phenotype parameters which must be interpreted correctly for phenotype analysis. The distributions do not appear normal. The median of the length distribution is $9.2 (\pm 0.6)$ μm and the median of the width distribution is $3.9 (\pm 0.15)$ μm . The width

distribution Box plot highlights 4 data outliers. The method of analysis of these parameters will now be discussed fully. For discussion on the way in which these values compare with those published in the literature, refer to chapter 3.

2.8 Distribution Analysis – The Classification of a Phenotype

The first distributions of growth phenotype classification parameters have now been measured and a series of tools must be developed to evaluate their potential. Each individual cell is its own phenotype so its location in the distribution is a classifier. However, individuals may be grouped by growth performance such as a stratification to identify a smaller number of growth phenotypes in a population. A phenotype will be determined in one of two ways:

1. As a second distribution or population of outliers at the edge of the main parameter's distribution;
2. The relative position an individual holds in each of the distributions (the phenotype trajectory).

The distributions must be analysed for the strata to identify secondary phenotypes, the two prominent identifiers of phenotype being outliers and bimodal distributions. Data with normal distributions are likely to be a single phenotype with a random spread of properties. The following distributional analysis techniques are methods which may be employed to determine whether the data are normally distributed, or whether the data have a bimodal or skewed distributions and whether the data have significant outliers. All of these distributional characteristics have the potential to highlight groups of phenotypes within the population, and point towards survivors in unfavourable growth conditions. The aim of this thesis is to find phenotype variation within distributions using the parameters of growth. A typical microbial growth curve is displayed in **Error! Reference source not found.**, with the growth parameters which can be extracted from this information.

Each bacterium type analysed in this thesis will have a slightly different set of parameters dependant on the ways in which they grow. As stated in the aims and objectives the analysis of *S. pombe* is the analysis of the growth parameters of single cells whereas the analysis of *E. coli* and *S. aureus* looks at the growth parameters of small colonies.

The parameters of growth, some of which are displayed in **Error! Reference source not found.**, are extracted from the curves collected by the ADFF. These data sets can yield up to 16 separate parameters and so a method has been developed to screen these parameters to determine the ones

which have the strongest possibility of identifying individual growth phenotypes. This method is now referred to as Phenotype Classification Parameter Analysis.

2.8.1 Phenotype Classification Parameter Analysis

A method of parameter analysis is designed to filter the parameters into those which will discriminate between phenotypes uniquely and those which are highly correlated with others. A simple correlation matrix (corrcoef function in Matlab) is used to determine correlation coefficient between each of the parameters in the set. The function produces a correlation matrix based on the matrix of input parameters. The correlation matrix for all of the parameters identified in Figure 2.19 and Figure 2.20 are presented in Table 2.1.

Table 2.1. The process of creating a correlation coefficient matrix on the right from a matrix of parameters, highlighting strong correlations between the parameters in grey to the right of the diagonal. The diagonal line of value 1 comes from the correlation of one parameter with itself, perfect positive correlation.

	Length t0	Width t0	Lag	Atime	Asize	Lb	CCL	Av rate	Max rate	ARt0	ARmax
Length t0	1.000			-0.667						0.913	
Width t0	0.205	1.000									-0.649
Lag	-0.152	-0.027	1.000								
Atime	-0.667	-0.080	-0.023	1.000			0.759			-0.644	
Asize	0.246	0.053	0.155	-0.116	1.000	1.000		0.553			0.718
Lb	0.246	0.053	0.155	-0.116	1.000	1.000		0.553			0.718
CCL	-0.127	0.089	-0.180	0.759	-0.287	-0.287	1.000				
Av rate	-0.380	-0.113	0.301	-0.117	0.553	0.553	-0.594	1.000			
Max rate	-0.090	-0.068	0.063	0.025	0.428	0.428	-0.165	0.341	1.000		
ARt0	0.913	-0.203	-0.130	-0.644	0.216	0.216	-0.177	-0.326	-0.066	1.000	
ARmax	0.055	-0.649	0.134	-0.053	0.718	0.718	-0.299	0.498	0.400	0.317	1.000

The correlation coefficient matrix assigns a correlation coefficient between paired parameters; Length t_0 and Length t_0 are the same parameter and so, as with all positions on the leading diagonal of the matrix, produces a correlation coefficient of exactly 1. A reasonable negative linear correlation is seen between the parameters Length t_0 and A_{time} , the value of coefficient being -0.667 (limiting value -1), whereas the Length t_0 and Width t_0 do not correlate strongly, indicated by a correlation coefficient of 0.205 (limiting value of 0 for no correlation). For the purposes of this analysis we have set the correlation threshold at 0.6. Values of correlation below 0.6 (or above -0.6) are not considered as strong correlations and the parameters are not considered to correlate.

Correlations between parameters can occur because they are related (length and volume for example) although correlation does not always imply causation^[42], accidental or misleading correlations^[43] can occur between parameters. Using the (+-) 0.6 upper correlation threshold, parameters which correlate with other parameters are removed from all subsequent analysis; those parameters that pass the filter will be considered as potential phenotype classification parameters. In the case of Table 2.1 the parameters Length t_0 , Width t_0 , Lag period length (λ), Average growth

rate, L_B and t_{cell} will be taken forward to further analysis in Chapter 3. The parameters which were removed were the aspect ratio measurements, clearly related to the Length and Width parameters and the parameters A_{size} and A_{time} , the former correlated with Length and t_{cell} ; the latter being directly related to L_B . Once the parameters of interest have been identified, their distributions can be displayed and tested to determine outliers, distribution shape and to identify possible phenotype groups. The simplest phenotype would suggest a random variation which would suggest a normal distribution in a parameter derived from a population. Tests for normality on the distribution are clearly then fundamental to the phenotype analysis.

2.8.2 Describing a Distribution as 'Normal'

The standard Normal distribution^[44] is a bell-shaped distribution with a mean (the first moment^[45]), a mode and median of 0 and a standard deviation (the square root of the variance or second moment^[46]) of 1. The distribution is totally symmetric with no bias either side of the mean 50% of the distribution mean and 50% smaller. To standardise data to compare it to a standard normal distribution (SND) or z-statistic the mean (μ) of the data must be subtracted from the distribution and then this new distribution must be divided by the standard deviation (σ), equation (5):

$$z = \frac{x_i - \mu}{\sigma}$$

(5)

Randomly occurring events are normally distributed; therefore cell growth variations, which arise as the result of many controlled small random fluctuations in enzyme concentrations are the simplest definition of a phenotype, are unlikely to be so. Many of the phenotype parameter distributions are not expected to be normally distributed if they are to show phenotypes, and phenotypes will be detectable in parameter distributions that are not highly correlated with other parameters. Phenotypes are expected to appear everywhere in the distributions but those with extraordinary growth properties such as persister cells may be present as in the upper percentiles of the distributions or outliers; in extreme cases the distribution may split becoming bimodal or multimodal. However it is important to test the distributions for normality as a starting point and establish confidence in the initial assignment. In a review published in 2005, Henderson shows that the tests for normality should follow a specific route^[47], graphical representation of Histograms, Boxplots and Q-Q plots and normality testing with either the Anderson-Darling test or the Shapiro-Wilk test for example. The Anderson-Darling test is approved by the Food and Drug Association^[48] for testing the normality of non-parametric distributions.

Nonparametric statistics are those which do not assume that the data have a characteristic or standard distribution which can be well represented by a known equation. Nonparametric models make fewer assumptions, are generally applied to data where little is known about the outcome and are generally considered to be more robust. Nonparametric graphical representations include histograms and kernel density estimators, nonparametric statistical tests include the Anderson-Darling test for normality and the Mann Whitney U test to determine whether two samples are from the same continuous distribution. These tests all use the data median as the parameter by which to compare distributions. The 95 % CI's for all distributions parameters are calculated by bootstrapping them for $N = 1000$ ^[49]. Bootstrapping takes the data available, treats it as a sample of a full population and creates a number of phantom data to better estimate the values asked of it, in this case the 95 % confidence limits^[50].

2.8.3 Graphical Representation

The simplest distribution display is the histogram, Figure 2.22. Histograms are conventionally density estimators^[51] and make no assumptions of parametric or non-parametric distributions. The frequency of an observation is derived by dividing the distribution into a number of bins chosen either by the user or through a number of automated processes. The bin number choice is an important consideration as picking too few bins over-smoothes the data arbitrarily losing information, and too many bins under-smoothes it, making the distribution appear noisy^[52]. There are many rules published for the choice of binwidth, including Sturges's proposal^[53] and the more recent work of Scott^[51]. The bin number here is set to 10 for all data sets unless the width of the bins brought about by this is less than the increment of the unit measured. Meaning that, as there are 10 bins across the range of the data, the bin width for each parameter will be different. Conventionally, the histograms are a plot of frequency against bin but to make a comparison with the probability distribution of the observable, the phenotype parameter as cell cycle time, the histogram is normalised. When normalised to an area of 1, the histogram is referred to as empirical Probability Density Functions (ePDFs) and are mathematically the phenotype parameter probability distributions. Histograms are the simplest graphical method of viewing a distribution there are others that will be useful in thesis, especially in interrogating the distribution characteristics.

A box plot displays the distribution of the data about the median, the mathematical centre of the distribution when the observations are ranked in order from lowest to highest^[54], Figure 2.22. The Box plot displays a red line to indicate the median, the box edges indication the 75th and 25th percentile of the data and the whiskers extending to the range of the data. The whiskers (w) are set at a default length of $\pm 2.7\sigma$ with data outside of this indicated as outliers where σ is the standard deviation of the sample. Outliers are classified as either larger than $q_3 + w(q_3 - q_1)$ or smaller than

$q_1 - w(q_3 - q_1)$ where q_1 and q_3 are the lower and upper quartile values respectively. Adding the data points as a Beeswarm plot to the Boxplot provides a second graphical presentation of the distribution. Outliers in the distributions maybe the first indication of an infrequent phenotype and so with this graphical representation it is possible to see the onset of distribution structure such as deviations from normal. Data with bimodal populations will then appear obviously in the boxplot/beeswarm plot, meaning that analysing the data at the tails of the distribution will provide us with information about a second phenotype distribution. The Q-Q plot is a graphical method of visualising the deviations a data set have from the data from a defined distribution type.

A Quantile-Quantile plot^[55] takes the frequencies of the input distribution and compares it to the frequency of a reference distribution such as normal and then linearised for presentation; taking the quantiles of the input distribution and the theoretical quantiles of a reference distribution and plotting one against the other another produces the Q-Q plot, top right Figure 2.22. The quantiles of a distribution are evenly spaced points taken from the cumulative density function of a data set, quantiles taken over 100 points are termed percentiles, and a quantile taken over 2 points is termed the mean. The comparison of the two distributions should form a straight line, deviations from the line shows the distribution does not fit the reference distribution. The Q-Q is usually plotted for the normal distribution and this is seen in Figure 2.22. The departures from linearity are an excellent graphical representation and may show the onset of bimodality. The Q-Q plot is further used to distinguish graphically between bimodal distributions in Figure 2.23.

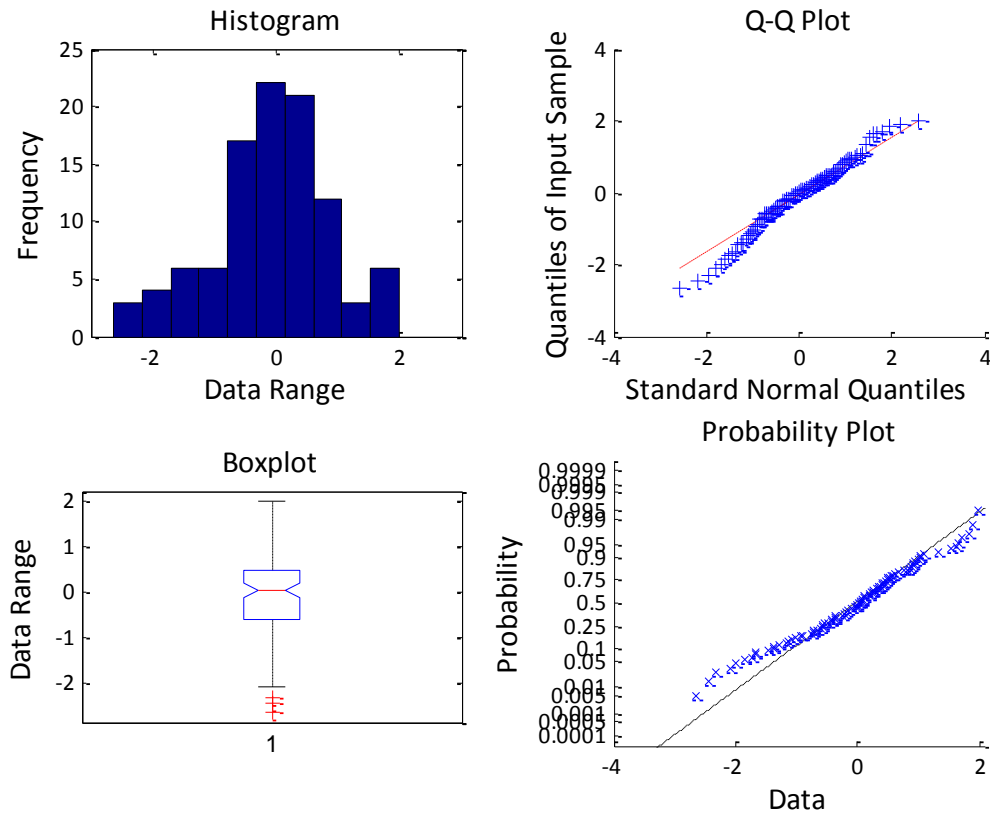


Figure 2.22 Selection of output from the Normality Program on model, randomly generated 'normal' data of $N=100$ samples. The histogram is constructed with 10 bins, the QQ-plot, comparing the quantile values of the input distribution to those of a reference normal distribution, the Boxplot, show the median, 25th and 75th percentiles, range (whiskers) and outliers of the data and the Probability plot, no longer used in our analysis.

A program was written in Matlab to perform a series of normality tests on any distribution. These tests were performed on model and measured data Figure 2.22 and Table 2.2 (See 2.8.5). The program file can be viewed in Appendix 2.

Distributions with clear departures from normality or other reference parametric distributions will then be analysed non-parametrically. However, the graphical representation may be insufficient and other parameter of the distribution may be considered to assess its shape. The distributions can be analysed using normality tests and the parameters of kurtosis and skewness, the 'shape' of the distribution.

2.8.4 Distribution Shape Parameters[56]

Skewness is a measure of the symmetry of the distribution about the sample mean and is the third moment of a distribution^[57]. A negative skewness coefficient means that the distribution is more spread below (to the left of) the mean, a positive coefficient the distribution is more spread to the right of the mean. Any perfectly symmetrical distribution, normal or otherwise, will return a coefficient of 0. The calculation used here for skewness uses equation 8:

$$S = \frac{E(x - \mu)^3}{\sigma^3}$$

(6)

where μ and σ (the sample mean and standard deviation) have been described previously, x is the datum and $E(x - \mu)$ is the expected value of $(x - \mu)$. A distribution highly skewed in either direction is of interest here as the skewed area may be indicative of a phenotype. Distributions are skewed because of a natural limit on one side of the data, for example the pureness of a product is skewed because it cannot be more than 100% pure, with a negative skewness parameter. Distributions with a high positive skewness parameter come from incidences such as maximum length of time of a call received by a call centre in minutes, where the natural limit is 0 minutes. The skewness may extend to the extremes of the distribution and this is captured in the Kurtosis of a distribution, fourth moment^[58] and another parameter which can be used to determine whether a distribution contains a second (or more) phenotype distribution.

Kurtosis described as 'a measure of how outlier-prone a distribution is'^[59] i.e. the 'weight' of the data in the tails of the distribution. A normal distribution has a kurtosis coefficient of 3; a distribution with wider tails (more outlier-prone) has a kurtosis value of more than 3 and is termed platykurtic; a narrower tailed-distribution has a value of less than 3 and is termed leptokurtic^[60]. It is expected that new phenotype populations will be found in distributions which display a wider spread of data, so those with higher kurtosis values. So there are specific tests developed to test the normality of a distribution and these tests can be used to reject the data on the basis of it being normally distributed.

2.8.5 Tests for Normality

The two statistical tests for normality used here are the Anderson-Darling test^[61] and the Shapiro-Wilk test^[62], the two tests recommended for use by Henderson^[63], for non-parametric distribution analysis and recommended by the FDA^[64]. The Anderson-Darling (A-D) test tests whether a sample of data comes from a reference distribution, in one case this is normal distribution. The A-D test measures the distance between the reference (normal) distribution and the empirical cumulative density function (eCDF), normalised to 1 of the input data set^[65]. The test accepts the null hypothesis H_0 that the distribution is normal and derives a P-value, the probability of rejecting the hypothesis by chance alone. The A-D test places more weight on the discrepancies of the data in the tails of the distribution than standard tests for normality^[66], the areas at which may contain interesting growth phenotypes making it comparable to the graphical Q-Q plot. A further test is the S-W test is used; together these two tests are the state-of-the-art tests for Normality

testing. P should be less than 0.05 for hypothesis tests in order for there to be a less than 5 % chance that the null hypothesis would be accepted by chance alone.

Table 2.2 The output moment statistics of the randomly generated model data. All errors are bootstrapped for 1000 samples to derive 95% confidence limits. The h value for the statistical tests determines whether the null hypothesis was accepted or not (H=0 accepts null hypothesis, 1 rejects it) and the p-value is the degree of confidence in the decision.

Parameter	Value
Range	4.625
Mean	-0.075
ErrorMeanL	-0.260
ErrorMeanH	0.122
Median	0.037
ErrorMedianL	-0.189
ErrorMedianH	0.200
Mode	0.002
ErrorModeL	-0.234
ErrorModeH	0.321
StDev	0.979
95th Percentile	1.642
65th Percentile	0.296
Kurtosis	3.082
ErrorKurtosisL	2.675
ErrorKurtosisH	3.321
Skewness	-0.340
ErrorSkewnessL	-0.763
ErrorSkewnessH	0.432
SWh	0.000
SWp	0.209
ADh	0.000
ADp	0.021

The distribution parameters in Table 2.2 are the mean, mode and median with the associated upper and lower 95 % bootstrapped confidence limits; the range and the standard deviation (StDev); the distribution shape parameters, skewness and kurtosis and the 95% bootstrapped confidence limits and the two tests for normality (SWh and ADh) with the calculated P-values (SWp and ADp). The parameters can be used to determine whether a data set is bimodal or not, by applying them to data sets created to be bimodal. It is important to determine between bimodal distributions as a phenotype discriminator. It must be determined at what level of separation between the distribution means we lose the ability to distinguish between them. Four distributions each created from two normal distributions with differences between the means of 8, 4, 2 and 0.5 are displayed

as Q-Q plots in Figure 2.23. A full description of the statistical parameters used in this thesis are in Appendix 3.

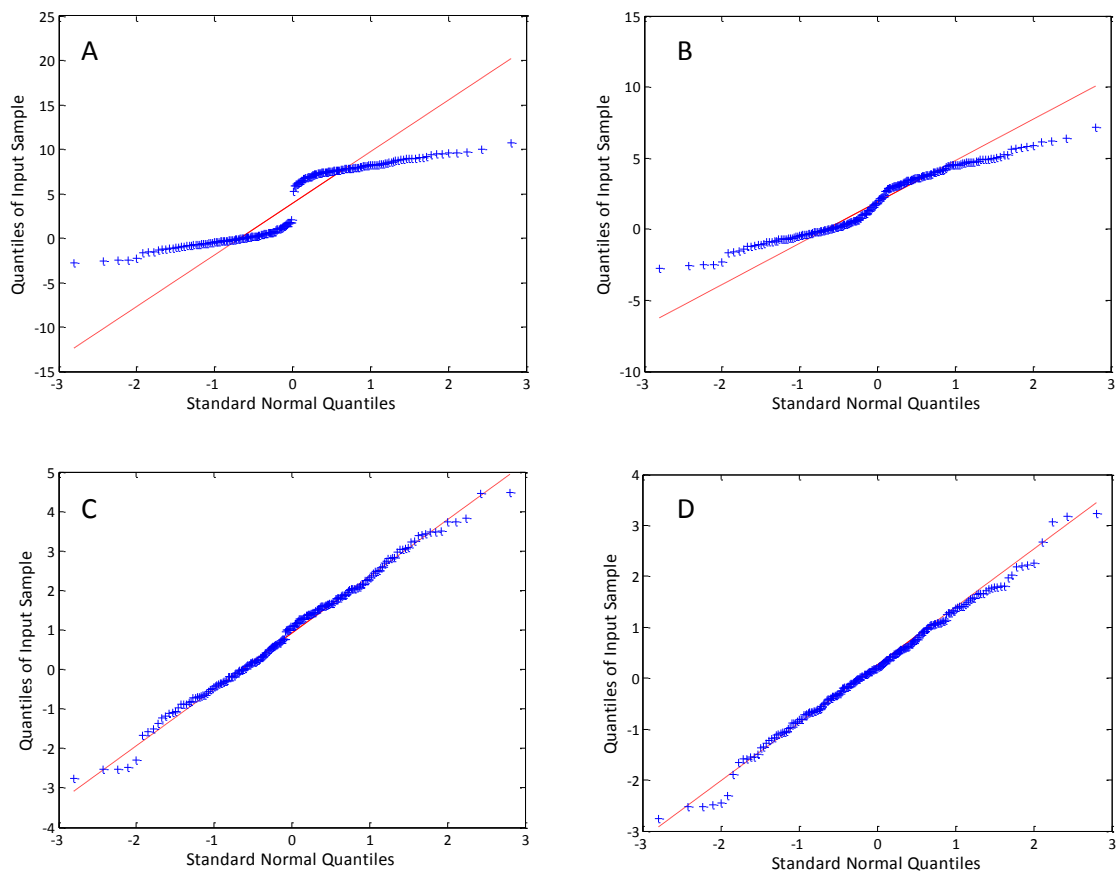


Figure 2.23 The evolution of the QQ plot as the difference between the mean of two bimodal normal distributions decreases from eight (A), to four (B), two (C) and 0.5 (D). These plots show distinctly what our normality analysis shows, that they cannot be distinguished between as two separate continuous distributions when the means are separated by less than 1.

The Q-Q plot provides a simple graphical inspection to determine the normality of data. The Q-Q plot in Figure 2.23 D was compiled of two normal distributions: one centred on a mean of 0 and the other on a mean of 0.5. The SW and AD test both reject that null hypothesis that it is normal but the Q-Q plot is similar to the Q-Q plot in Figure 2.22 for a normal distribution.

2.8.6 Distribution *N*-bias

Bias is an important concept in distributional analysis and can come from a number of sources. There can be observer bias with a user rejecting a cell from an observation selecting only data they expect to ‘fit’ the experiment. Any exclusion criteria may perturb the sample. The Lensless microscope eliminates this in part, in that the user cannot select a “good” diffraction pattern based on any characteristic of a cell. The second source of *N*-bias is the size of the sample and how accurately the sample size properties represent the properties of the parent distributions. The size

of a sample required to perform a statistical hypothesis test between two parameters in different populations is the power of a test^[67]. Only once the size of the effect that is to be tested is known can the power calculation be performed accurately. The experiments presented in this thesis are the necessary prospective studies that would inform a power calculation.

All distributions contain 100 observations in this thesis, each single data point representing 1 % of the distribution. The theory of distribution convergence^[68] states that a sequence of seemingly random sampled events can converge on a behaviour that is essentially unchanging. Assuming that the experimental conditions here do not introduce a bias into the sampling of these cells, the distribution convergence theory can be applied to the data here and tested. In Figure 2.24 the convergence of the median and bootstrapped errors of our width at t_0 distribution as N increases from 10 to 100 is displayed.

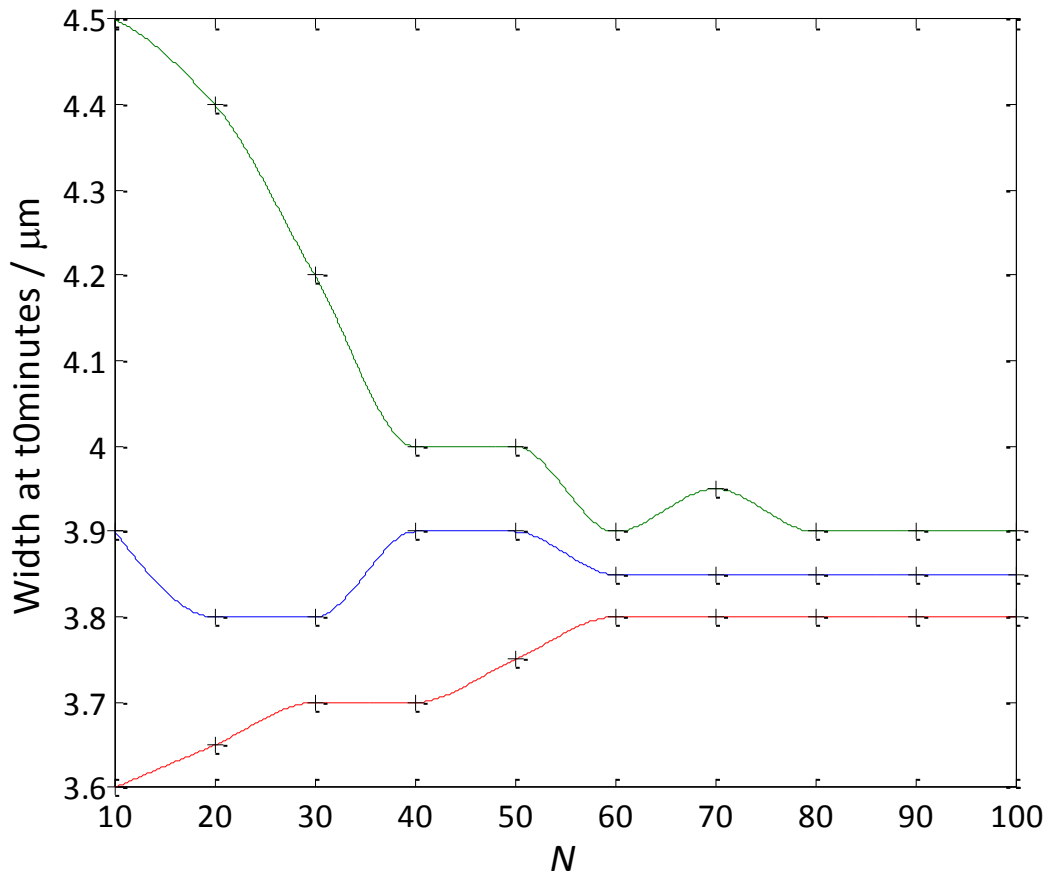


Figure 2.24 The convergence of the median of the distribution of the Width t0 minutes parameter (blue) and the bootstrapped 95% confidence limits (green, upper and red, lower).

The length and width data from the *S. pombe* preliminary tests will be analysed following these parameters and discussed further in Chapter 3.

2.9 Discussion

The Lensless microscope has been used to monitor the growth of *S. pombe* over a time period in excess of 600 minutes. The flow cell has been demonstrated to support microbial growth and the temperature control of the device environment has been shown to be stable over the same time course. The simple algorithm for the extraction of aspect ratio parameters accurately calculates the size of the diffracting objects, $R^2 = 0.997$, so validating the simple ADF analysis technique to extract sufficient information from the Airy Disc patterns to determine the size and aspect ratio of a diffracting object and hence screen for growth phenotype parameters. The method of data collection and measurement is automated reducing the population distribution errors related to the

user; there is no bias over selection of cells which appear to fit the distribution or discrepancies in measurement between cells. There are three measurement errors associated with the Lensless microscope. For objects of size sub 6 μm the error is dominated by the diffraction limit error of 0.3 μm . For objects over this range the error is 5 %. Intensity change errors, This error is attributed to mask calculation error, interaction between close diffracting objects and imaging artefacts, for measurements from the optical microscope an error of 5 % is calculated. The measurement error can be attributed to interaction with surface structures and focal plane through the object.

The growth measurement experiments allow a growth curve to be measured from 100 objects from which 11 parameters may derived. A correlation screening process rejects highly correlated parameter leaving in the case of *S. pombe* 11 potential phenotype parameters of growth. The parameter correlation screening method produces a set of parameters which can be considered the growth phenotype parameters of *S. pombe* but is a general method. The parameter distributions are analysed for normality and assessed for shape forming a set of standard analysis techniques for phenotype screening. Data are plotted as ePDFs and Boxplots (Beeswarm). The distribution shape estimators are Kurtosis and Skewness and will be extracted, along with the mean and standard deviation, median and range. These parameters are bootstrapped to obtain 95 % confidence limits for 1000 re-samples. Finally each distribution is tested for normality using both the A-D and S-W tests. The Q-Q plot is not going to be used as it contains graphical data tested in the A-D test. The parameters of Kurtosis^[59] and Skewness^[69] determine a measure for one aspect of the distribution, based heavily in changes in the tails of the distribution only whereas the tests for normality use several parameters of the distribution to determine whether it is normal^[70]. It can also be observed that the bootstrapped 95 % confidence limit errors for the parameter values often have a large range. It can be concluded that while Kurtosis and Skewness calculations return important information about the shape of the distribution they are not to be relied upon as measurements of distribution normality. The A-D test^[65] is the only approved for use as the normality test of choice by the FDA^[64] and has been shown to be a strong measure of normality for non-parametric distributions^[63].

Cells growing in any environment may exhibit growth characteristics which differ from the genetically identical population, these phenotypes may lead to cancerous growth, film formation or persister cells. These cells will be identifiable from the bulk distributions as outliers; the data will not be normally distributed and may be bimodal. The Q-Q plot appeared to identify distributions which differ from the normal distribution at the fringes of the data, by our definition identifying the potential different phenotype groups. The Q-Q plot, even for the data produced to be normal,

highlights deviation at the edges of the distributions. This method, therefore, provides a misleading visual representation of the data with no quantitative measure of a deviation from normal distribution parameters.

The tests for normality are performed on data sets with a sample size $N=100$. N was chosen as 100 so that each cell in the experiment represents 1 % of the distribution. The experiments here, as discussed previously, are not biased by user choice. The diffraction patterns selected at t_0 minutes are largely indistinguishable from each other and so the whole population is selected regardless of initial appearance. It has been demonstrated that the median of the distributions together with the bootstrapped confidence limits converge after $N = 80$, Figure 2.24. If there was a phenotype identified which appeared to be of interest then perhaps it would be desirable to increase N to be something significantly higher. When deciding what N is high enough, however, it is valuable to think about the prisoner of war John Kerrich and his coin toss experiment, it was only when he reached $N = 10,000$ coin tosses that he reached a 99 % confidence on the probability of returning a tail on the coin toss as 50 %^[71].

Having defined the method by which a set of phenotype parameters is extracted from the parameters of growth and the analysis of the specific organisms of interest has been defined, the thesis will explore phenotype classification of growth phenotypes in the following model organisms; *S. pombe*, *E. coli* and *S. aureus*.

2.10 Conclusions

It has been shown that the diffraction patterns recorded by the Lensless microscope instrument can be analysed and converted to two dimensional size information using a simple algorithm, with no requirement for full holographic reconstruction of the intensity data to a full image. The device has been shown to be stable over time for two elevated temperatures and a known size microsphere.

It has been demonstrated that the calibrated diameters for spheres calculated by the algorithm concur with the measurements for the same spheres obtained using the light microscope, the R^2 of the calibration plot is 0.997, Figure 2.17. The calibration method has been demonstrated for micron sized living objects with an aspect ratio which compared favourably with those determined from the light microscope Figure 2.18. Further to this it has been shown that the length and width parameters measured of the organism *S. pombe* compare to those previously published in the data. The methods of analysing these distributions highlight regions which may contain new phenotypes and methods to remove distributions from our analysis if they will not provide phenotypic information.

It was the aim to apply the data collection, analysis and display methods to analyse the growth parameters of the organism *S. pombe* over a full cell division time course. Phenotypes were extracted from these data and the growth phenotypes from this control sample were compared to those from a sample of cells grown under silver stress conditions. These analyses are in Chapter 3.

2.11 References

1. MartÃ-nez-MartÃ-nez, L., A. Pascual, and G.A. Jacoby, *Quinolone resistance from a transferable plasmid*. The Lancet, 1998. **351**(9105): p. 797-799.
2. Nikolaev, Y.A. and V.K. Plakunov, *Biofilm-"City of microbes" or an Analogue of multicellular organisms*. Microbiology and Molecular Biology Reviews, 2007. **76**(2): p. 125-138.
3. Lewis, K., *Persister Cells*. Annual Review of Microbiology, 2010. **64**: p. 357.
4. Massey, R.C., A. Buckling, and S.J. Peacock, *Phenotypic switching of antibiotic resistance circumvents permanent costs in Staphylococcus aureus*. Current Biology, 2001. **11**(22): p. 1810-1814.
5. Berg, H.C., *How to Track Bacteria*. Review of Scientific Instruments, 1971. **42**(6): p. 868-871.
6. Tseng, D., et al., *Lensfree Microscopy on a Cellphone*. Lab on a Chip, 2010. **10**(14): p. 1.
7. Zhu, H., et al., *Cost-effective and compact wide-field fluorescent imaging on a cell-phone*. Lab on a Chip, 2011. **11**(2): p. 315-322.
8. Ozcan, A. and U. Demirci, *Ultra wide-field lens-free monitoring of cells on-chip*. Lab on a Chip, 2008. **8**(1): p. 98-106.
9. Navarre, W.W. and O. Schneewind, *Surface Proteins of Gram-Positive Bacteria and Mechanisms of Their Targeting to the Cell Wall Envelope*. Microbiology and Molecular Biology Reviews, 1999. **63**(1): p. 174-229.
10. Swoboda, J.G., et al., *Wall teichoic acid function, biosynthesis, and inhibition*. Chembiochem, 2010. **11**(1): p. 35-45.
11. McQuillan, J., *Bacterial-Nanoparticle Interactions*. 2010, University of Exeter. p. 250.
12. McQuillan, J.S., et al., *Silver nanoparticle enhanced silver ion stress response in Escherichia coli K12*. Nanotoxicology, 2012. **6**(8): p. 857-866.
13. Gurkan, U.A., et al., *Miniaturized lensless imaging systems for cell and microorganism visualization in point-of-care testing*. Biotechnology Journal, 2011. **6**(2): p. 138-149.
14. Moon, S., et al., *Integrating microfluidics and lensless imaging for point-of-care testing*. Biosensors and Bioelectronics, 2009. **24**(11): p. 3208-3214.
15. Bishara, W., et al., *Holographic pixel super-resolution in portable lensless on-chip microscopy using a fiber-optic array*. Lab on a Chip, 2011. **11**(7): p. 1276-1279.
16. Seo, S., et al., *Lensfree holographic imaging for on-chip cytometry and diagnostics*. Lab on a Chip, 2009. **9**(6): p. 777-787.
17. Fukui, M., et al., *Journal of Periodontal Research*, 2008. **43**(2): p. 174-8.
18. Tseng, D., et al., *Lensfree microscopy on a cellphone*. Lab on a Chip, 2010. **10**(14): p. 1787-1792.
19. Wang, S., et al., *How to get Airy disc from Airy pattern*. Optics & Laser Technology, 1999. **31**(6): p. 437-441.
20. Katardjiev, I.V., G. Carter, and M.J. Nobes, *The application of the Huygens principle to surface evolution in inhomogeneous, anisotropic and time-dependent systems*. Journal of Physics D: Applied Physics, 1989. **22**(12): p. 1813.
21. Young, T., *The Bakerian Lecture: Experiments and Calculations Relative to Physical Optics*. Philosophical Transactions of the Royal Society of London, 1804. **94**: p. 1-16.
22. Singer, W., M. Totzeck, and H. Gross, eds. *Physical Image Formation, Volume 2*. Handbook of Optical Systems, ed. H. Gross. 2005, WILEY-VCH: Weinheim.
23. Buchwald, J. and S. Feffer, *Ernst Abbe, Carl Zeiss, and the Transformation of Microscopical Optics*, in *Scientific Credibility and Technical Standards in 19th and early 20th century Germany and Britain*. 1996, Springer Netherlands. p. 23-66.
24. de Lange, F., et al., *Cell biology beyond the diffraction limit: near-field scanning optical microscopy*. Journal of cell science, 2001. **114**(23): p. 4153-4160.
25. Volkmann, H., *Ernst Abbe and His Work*. Applied Optics, 1966. **5**(11): p. 1720.

26. Masters, B.R., *Ernst Abbe and the Foundation of Scientific Microscopes*. Optics and Photonics News, 2007. **18**(2): p. 18.
27. Barakat, R., *Rayleigh Wavefront Criterion*. Journal of the Optical Society of America, 1965. **55**(5): p. 572-573.
28. Frohn, J.T., H.F. Knapp, and A. Stemmer, *True optical resolution beyond the Rayleigh limit achieved by standing wave illumination*. Proceedings of the National Academy of Sciences, 2000. **97**(13): p. 7232-7236.
29. Mudanyali, O., et al., *Lensless On-chip Imaging of Cells Provides a New Tool for High-throughput Cell-Biology and Medical Diagnostics*. Journal of Visualised Experiments, 2009. **34**: p. e1650.
30. Ratkowsky, D.A., et al., *Relationship between temperature and growth rate of bacterial cultures*. Journal of bacteriology, 1982. **149**(1): p. 1-5.
31. Lindquist, S. and E.A. Craig, *The Heat-Shock Proteins*. Annual Review of Genetics, 1988. **22**: p. 631-677.
32. Shehata, T.E. and A.G. Marr, *Effect of Temperature on the size of Escherichia coli cells*. Journal of bacteriology, 1975. **124**(2): p. 857-862.
33. Balaev, A.E., K.N. Dvoretzki, and V.A. Doubrovski. *Determination of refractive index of rod-shaped bacteria from spectral extinction measurements*. in *Optical Technologies in Biophysics and Medicine IV*. 2003. Saratov, Russia: International society for optical engineering.
34. Rappaz, B., et al., *Simultaneous cell morphometry and refractive index measurement with dual-wavelength digital holographic microscopy and dye-enhanced dispersion of perfusion medium*. Optics Letters, 2008. **33**(7): p. 744.
35. Fantes, P.A., *Control of Cell Size and Cycle Time in Schizosaccharomyces pombe*. Journal of Cell Science, 1977. **24**: p. 51.
36. Nurse, P., P. Thuriaux, and K. Nasmyth, *Genetic control of the cell division cycle in the fission yeast Schizosaccharomyces pombe*. Molecular and General Genetics MGG, 1976. **146**(2): p. 167-178.
37. Baumgärtner, S. and I.M. ToliÅ†-NÃrrelykke, *Growth Pattern of Single Fission Yeast Cells Is Bilinear and Depends on Temperature and DNA Synthesis*. Biophysical Journal, 2009. **96**(10): p. 4336-4347.
38. Kelly, F.D. and P. Nurse, *Spatial control of Cdc42 activation determines cell width in fission yeast*. Molecular Biology of the Cell, 2011. **22**(20): p. 3801-3811.
39. Mitchison, J.M. and P. Nurse, *Growth in cell length in the fission yeast Schizosaccharomyces pombe*. Journal of cell science, 1985. **75**(1): p. 357-376.
40. Forsburg, S.L. and P. Nurse, *Cell cycle regulation in the yeasts saccharomyces cerevisiae and schizosaccharomyces pombe*. Annual Reviews in Cell Biology, 1991. **7**: p. 227-256.
41. Nurse, P., *Genetic control of cell size at cell division in yeast*. Nature, 1975. **256**(5518): p. 547-551.
42. Aldrich, J., *Correlations Genuine and Spurious in Pearson and Yule*. Statistical Science, 1995. **10**(4): p. 362-376.
43. Haig, B.D., *What is a Spurious Correlation?* Understanding Statistics, 2010. **2**(2): p. 125-132.
44. Gujarati, D.N. and D.C. Porter, *Essentials of econometrics*. 1999.
45. Yun, M.-S., *Decomposing differences in the first moment*. Economics Letters, 2004. **82**(2): p. 275-280.
46. Geary, R.C., *Moments of the ratio of the mean deviation to the standard deviation for normal samples*. Biometrika, 1936. **28**(3/4): p. 295-307.
47. Henderson, A.R., *Testing Experimental Data for Univariate Normality*. Clinica Chimica Acta, 2006. **366**: p. 112.
48. Orchard, T., *Specification Setting: Setting Acceptance Criteria from Statistics of the Data*. BioPharm International, 2006. **19**(11).

49. MatLab. *bootci*. 2013; Available from: <http://www.mathworks.co.uk/help/stats/bootci.html>.
50. Singh, K. and M. Xie, *Bootstrap: A Statistical Method*. 2008.
51. SCOTT, D.W., *On optimal and data-based histograms*. *Biometrika*, 1979. **66**(3): p. 605-610.
52. Wand, M.P., *Data-Based Choice of Histogram Bin Width*. *The American Statistician*, 1997. **51**(1): p. 59-64.
53. Sturges, H.A., *The Choice of a Class Interval*. *Journal of the American Statistical Association*, 1926. **21**(153): p. 65-66.
54. Williamson, D.F., R.A. Parker, and J.S. Kendrick, *The Box Plot: A Simple Visual Method to Interpret Data*. *Annals of Internal Medicine*, 1989. **110**(11): p. 916-921.
55. MatLab. *qqplot*. 2013; Available from: <http://www.mathworks.co.uk/help/stats/qqplot.html>.
56. Royston, P., *Which measures of skewness and kurtosis are best?* *Statistics in Medicine*, 1992. **11**(3): p. 333-343.
57. Scott, R.C. and P.A. Horvath, *On the direction of preference for moments of higher order than the variance*. *The Journal of Finance*, 1980. **35**(4): p. 915-919.
58. Groeneveld, R.A. and G. Meeden, *Measuring skewness and kurtosis*. *The Statistician*, 1984: p. 391-399.
59. MatLab. *Kurtosis*. Documentation Centre [cited 2013 13th December]; Available from: <http://www.mathworks.co.uk/help/stats/kurtosis.html>.
60. Balanda, K.P. and H.L. Macgillivray, *Kurtosis and spread*. *Canadian Journal of Statistics*, 1990. **18**(1): p. 17-30.
61. Anderson, T.W. and D.A. Darling, *Asymptotic Theory of Certain "Goodness of Fit" Criteria Based on Stochastic Processes*. *Annals of Mathematical Statistics*, 1952. **23**(2): p. 193.
62. Shapiro, S.S. and M.B. Wilk, *An analysis of variance test for normality (complete samples)*. *Biometrika*, 1965. **52**(3-4): p. 591.
63. Henderson, A.R., *Testing experimental data for univariate normality*. *Clinica Chimica Acta*, 2006. **366**(1&€"2): p. 112-129.
64. Pena-Rodriguez, M.E., *Statistical Process Control for the FDA-Regulated Industry*, in *Business and Economics*. 2013, ASQ Quality Press.
65. MatLab. *adtest*. Documentation Centre [cited 2013 13th December]; Available from: <http://www.mathworks.co.uk/help/stats/adtest.html>.
66. Sinclair, C.D., B.D. Spurr, and M.I. Ahmad, *Modified anderson darling test*. *Communications in Statistics - Theory and Methods*, 1990. **19**(10): p. 3677-3686.
67. Prajapati, B., M. Dunne, and R. Armstrong, *Sample size estimation and statistical power analyses*. *Optometry Today*, 2010. **16**(07).
68. Muhlenbein, H. and T. Mahnig, *Journal of Computing and Information Theory*, 1999. **1**: p. 19-32.
69. MatLab. *Skewness*. Documentation centre [cited 2013 13th December]; Available from: <http://www.mathworks.co.uk/help/stats/skewness.html>.
70. Joanes, D.N. and C.A. Gill, *Comparing measures of sample skewness and kurtosis*. *Journal of the Royal Statistical Society: Series D (The Statistician)*, 1998. **47**(1): p. 183-189.
71. Mood, A.M., *Introduction to the Theory of Statistics*. 1950.

3 Eukaryotic cell response to sub lethal silver stress – *Schizosaccharomyces pombe*.

3.1 Introduction

The eukaryotic fungus *S. pombe* is studied as a model for the eukaryotic cell cycle, having many features in common with higher eukaryotes^[1]. In 2002 it became the 6th eukaryotic organism to have the full genome sequenced^[2] and contains a total of 13.8 Mb distributed between 3 chromosomes: I (5.7-Mb), II (4.6-Mb) and III (3.5-Mb^[3]) and codes for 4929 genes^[2]. The growth phenotype of single, wild type *S. pombe* cells under control conditions has been the subject of extensive research and so the growth parameters appear to be well known^[4-6] although their potential for classification of growth phenotypes has not been studied.

Additional growth phenotypes will be studied for growth under silver stress which provides a radical change to the growth environment and hence potential phenotypes of *S. pombe*. The toxicity of the silver ion to cells via a number of mechanisms has been well documented^[7-11], and discussed previously (Chapter 2).

The antimicrobial mechanism of silver action which has been observed in prokaryotes is directly applicable to eukaryotic cells, and has also been observed in human cells^[12]. Silver is used in many wound dressing environments to prevent infection from bacteria but there is clearly the potential for the silver to affect adversely the wound healing process itself. In their study of silver stress in eukaryotic cells, Haase *et al.* report that silver nanoparticles induce oxidative stress responses in human macrophages^[13] and silver nanoparticle exposure has been shown to cause morphological cell changes, decreases in mitochondrial function and damage to DNA, proteins and cell membrane components^[14]. The silver ions in silver dressings, therefore, while proving their worth as antibacterial dressings, preventing infection in deep tissue wounds may be detrimental to the healing of the cells which the dressing is meant to be aiding.

This chapter explores the evolving growth phenotype of wild type *S. pombe* and the observable change in growth phenotype which takes place when *S. pombe* is exposed to a known environmental stress, specifically the presence of a sub-lethal concentration of silver ions. The growth phenotypes observed in this chapter are those of a single cell, sufficiently isolated on the surface of the flow cell to avoid the effects of quorum sensing^[15]. The chapter addresses the concept of individual phenotype and by extending these ideas to a set of phenotype parameters they can be used to

predict a cell's ability to survive the silver shock, an individual capacity to survive environmental stress as a phenotype.

Understanding the phenotype as a level of proteins within the cell means that analysis of the cell cycle and determination of the key regulators of growth will lead to predictors of the disruption and resulting phenotype brought about by the silver environmental shift. The concept of the organism having a Minimum Inhibitory Concentration (MIC) means that at some level *S. pombe* is able to cope with the disruptive nature of low concentrations of silver ions. Analysis of the effect of silver on the cell cycle and the specific silver targets can be described as a determination of the MIC for an individual organism on a molecular level. Understanding the *S. pombe* growth cycle and the levels of proteins at each critical check point means that the survival phenotype may be determined. The control of the cell cycle and its vulnerability of silver stress will now be discussed further.

3.1.1 *S. pombe* cell cycle

The cell cycle is a process by which a cell replicates its DNA content, segregates its chromosomes and undergoes cytokinesis to produce two genetically identical daughter cells^[1]. The eukaryotic cell cycle is divided into four distinct sections, the same in *S. pombe* as in humans. The cycle events are S-phase, where DNA synthesis occurs and M-phase, where nuclear division occurs^[16], and are interspersed with two growth phases, G₁ and G₂. The cycle is regulated at many points by checkpoint controls^[17], which keep the events of the cell cycle occurring in an orderly manner^[18]. The cell cycle of *S. pombe* is represented schematically in Figure 3.1, G₂ spanning approximately 75 % of the cell cycle and M, G₁ and S the remaining 25 %.

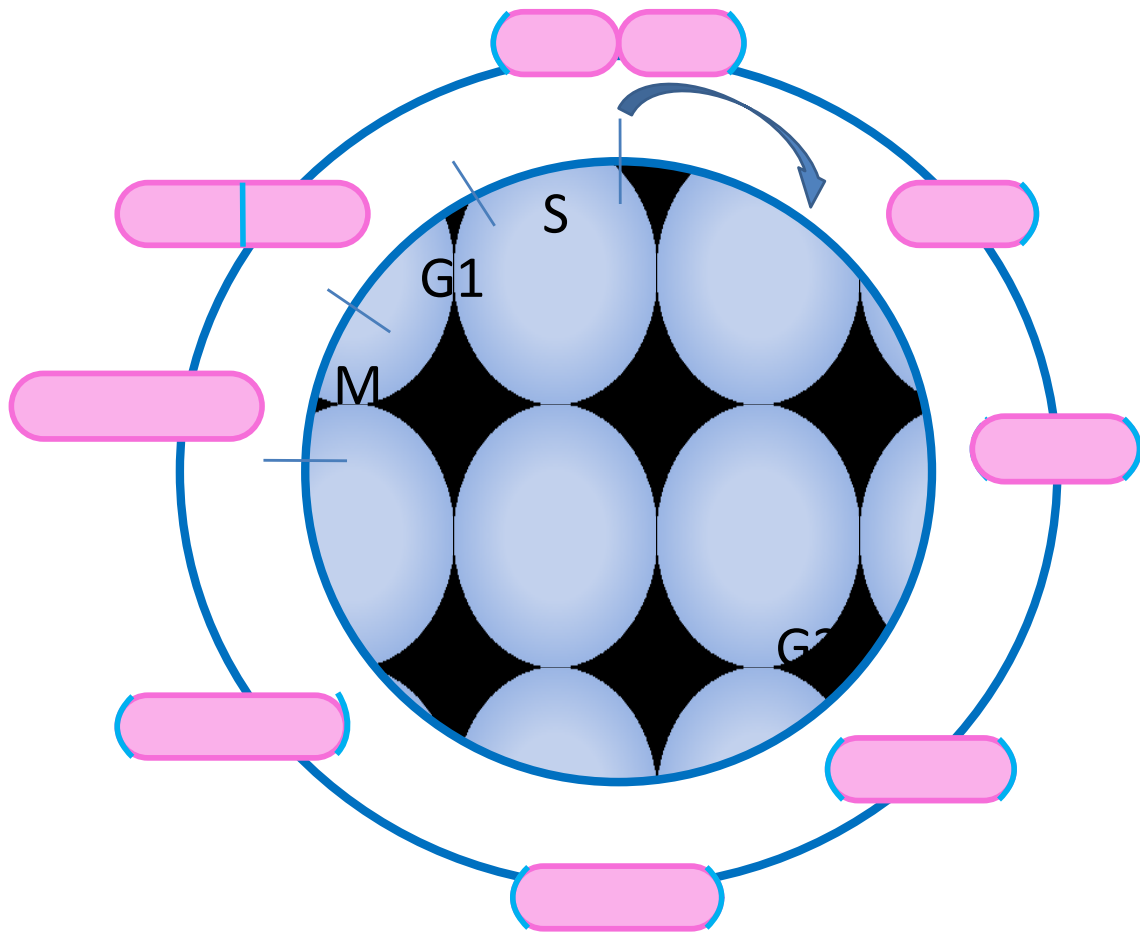


Figure 3.1 Schematic representation of *S. pombe* cell cycle, to scale, divided into the four distinct sections of G₁, S-phase, G₂ and M-phase, the cell spending 75% of the time of the cell cycle in G₂, the remaining 25% divided between the three phases of M, G₁ and S. The arrow depicts the direction of travel through the cell cycle and blue highlights on the pink cells indicate areas of growth. [adapted from Martin & Chang [6]].

It has been predicted that the minimal control machinery of the cell cycle comprises of seven regulatory components Slp1, Cdc2, Cdc13, PP1, APC, Cdc25 and Wee1^[19].

Cdc2 is the control protein in both S and M-phases, and contains three cysteine residues^[20]. Cdc2 controls, in part, the commitment-to-divide checkpoint, called START^[21] in G₁ and triggers mitosis during G₂^[22]. Cdc2 is therefore key to cell cycle progression in the two stages of the cell cycle and conventionally, initiation of cell cycle regulator pathways by Cdc2 is reported to be cell length dependent^[23]. Here, we define the 'reaching of a critical mass' as the accumulation of Cdc2 to beyond a limiting threshold level to trigger cell cycle events. The level of Cdc2 in a cell, therefore, is a strong growth phenotype at the molecular level using the ideas of equation (1), and the correlation of silver stress survival with the level of Cdc2 in a cell on exposure is to be expected.

The localisation of Cdc2 in the nucleus for mitotic initiation is controlled by Cdc13, has 3 cysteine residues in its structure, and it has been postulated^[24] that mitosis will not occur, regardless of the level of Cdc2 in the cell, if the mechanism of cdc13 is disrupted. Cells which have deficiencies in

Cdc13 as part of their phenotype, on silver exposure, may arrest prior to mitosis. Cdc25 and Wee1, are also involved in mitotic induction^[25] and have amino acid sequences containing 12 cysteine residues and 6 respectively^[26]. The control of mitosis is inhibited by the *wee1* gene product^[27] and activated by Cdc25. Wee1 phosphorylates Cdc2, keeping it in an inactive state, while Cdc25 dephosphorylates Cdc2, activating it^[28]. The fact that these four proteins are implicated in mitosis control, and all contain cysteine residues, implies that the initiation of mitosis is a check point which will be heavily influenced by silver. Further, the level of each protein in the cell on silver exposure defines a phenotype which may or may not be able to survive better.

PPI, protein phosphatase 1, has roles in mitosis, the control of polarised growth and endocytosis^[29] and has a protein structure containing 11 cysteine residues^[26]. The implication of PP1 in the control of polarised growth could influence the ability of the cell to undergo NETO, a phenomenon which can be monitored here. Slp1, the protein involved in marking the end of M-phase^[19], has 9 cysteine residues in its secondary protein structure of 587 amino acids^[26] and the major protein complex required by the cell to move through mitosis into anaphase is the Anaphase-promoting Complex, APC/C^[30], containing 15 subunits, each with at least one cysteine residue.

It can be concluded, from this group of 7 proteins that that predominant control of the *S. pombe* cell cycle occurs at the G₂/M-phase intersection and beyond. As these proteins make up the minimum set of proteins required for cell completion of the cycle, deficiencies or surplus levels of these proteins will give rise to either unfavourable or favourable phenotypes in both control and silver stress growth environments.

The sets of genes expressed to produce the proteins required for each cell process may or may not be expressed at every stage of the cell cycle. There have been many attempts to characterise the number of genes which have expression profiles during the cell cycle^[31-33] with estimates ranging from 407 to 1373 genes whose expression oscillate. At the S-phase/G₂ junction expression of genes related to telomere and histone production is at a peak, at mid G₂ the expression of genes involved with Cdc2 (related to mitotic control) and those for ribosomal biogenesis is highest. It is concluded that over 2000 *S. pombe* genes display weak cell cycle oscillations⁴¹.

The vulnerability of the cell to silver via the protein cysteine content points to a direct link between the thiol content of proteins at the molecular level and a μM -level phenotype that can be observed by the Lensless microscope. Similar molecular mechanisms will be possible for all of the growth parameters such as conservation of cell width and how this may be affected by the silver stress. The percentage of proteins containing cysteine in yeast is 85 %, and so the disruption of growth at the

molecular level is also 85 %. The set of proteins and their concentration properties will be interrogated at the μm -level.

The effect of silver environmental stress on the *S. pombe* phenotype has not been reported previously but the phenotype of the wild type cell under control conditions has been well documented^{[4], [34], [35]}. The growth phenotype properties identified thus far are summarised in Table 3.1 and is the reference set by which the growth phenotype parameters determined in this study will be compared.

Table 3.1. The published values for the key wild type *S. pombe* growth parameters when grown at 25°C, Birth length is the length immediately post division, Division length is the length immediately prior to division and Generation time is the length of time between divisions. *N* indicates the number of cells analysed in each case.

Parameter	Mean Value	<i>N</i>	Reference
Birth Length / μm	7.5 \pm (0.5)	24	[4]
	8.2 \pm (0.52)	164	[36]
Division Length / μm	15.8 \pm (1.6)	12	[4]
	13.48 \pm (1.05)	88	[35]
	14.4 \pm (0.85)	164	[36]
Cell Cycle Length / mins	310 \pm (40)	12	[4]
	188.4 \pm (26.4)	88	[35]
	228*	200	[34]
	148 \pm (16)	164	[36]

*No published error

The parameter values represented in Table 3.1 vary significantly within the population (the range of the parameters), particularly those for cell cycle length. The cell cycle length is influenced by a number of factors and a phenotypic growth parameter we can monitor here. Cells which are growing under conditions of starvation, or which become crowded in planktonic cultures may react with changes in their cell cycle. A depletion of nutrients leads to a number of consequences:

- An arrest in the cell cycle in either G_1 or G_2 and the cell entering G_0 , the stationary phase^[1].
- Nitrogen starvation, in particular, causes the cells to divide at shorter lengths than expected, length correlated to length of time a cell is exposed to nitrogen starvation^[37].
- If both mating types are present a diploid organism may form.

The above lists clear changes in the growth phenotype brought about by an environmental shift. The Lensless microscope can monitor a number of growth phenotypes:

- cell length at t_0 minutes;
- cell width at t_0 minutes;

- length of lag period;
- cell length at NETO;
- change of growth rate at NETO;
- time to NETO
- cell length at division
- length of time to division

From the growth curve of the *S. pombe* growth phenotype parameters can be derived for phenotype classification under both growth conditions.

3.1.2 Aims and Objectives

This chapter aims to apply the analysis methods developed in Chapter 2 to study the phenotypic growth of a single eukaryotic cell, *S. pombe*, producing growth curves for $N = 100$ single cells and extracting growth phenotype parameters. The same analysis will be performed under growth stressed conditions with a sub-lethal dose of AgNO_3 of $1 \mu\text{g}/\text{mL}$. Growth parameters will be derived from $N = 100$ viable cells that grow to cytokinesis and the survival rate for silver stress will also be recorded.

The distributions of the growth parameters for wild type and silver-stressed organisms will be analysed using tests of normality and non-parametric distribution comparison methods to assess the structure of the distribution and identify potential growth phenotype populations. The phenotype parameter distributions will be compared with those observed under silver stress conditions to explore the new stressed-induced phenotypes.

3.2 Materials and Methods

The Lensless microscope configuration was used as described in Chapter 2 without alteration.

S. pombe (WT 972 h-) was grown and handled using standard methods^[38, 39]. All experiments were performed in YE5S medium at 25°C (yeast extract with added 250 mg/L histidine, adenine, leucine, uridine and lysine). The experimental set-up is described pictorially in Figure 3.2.

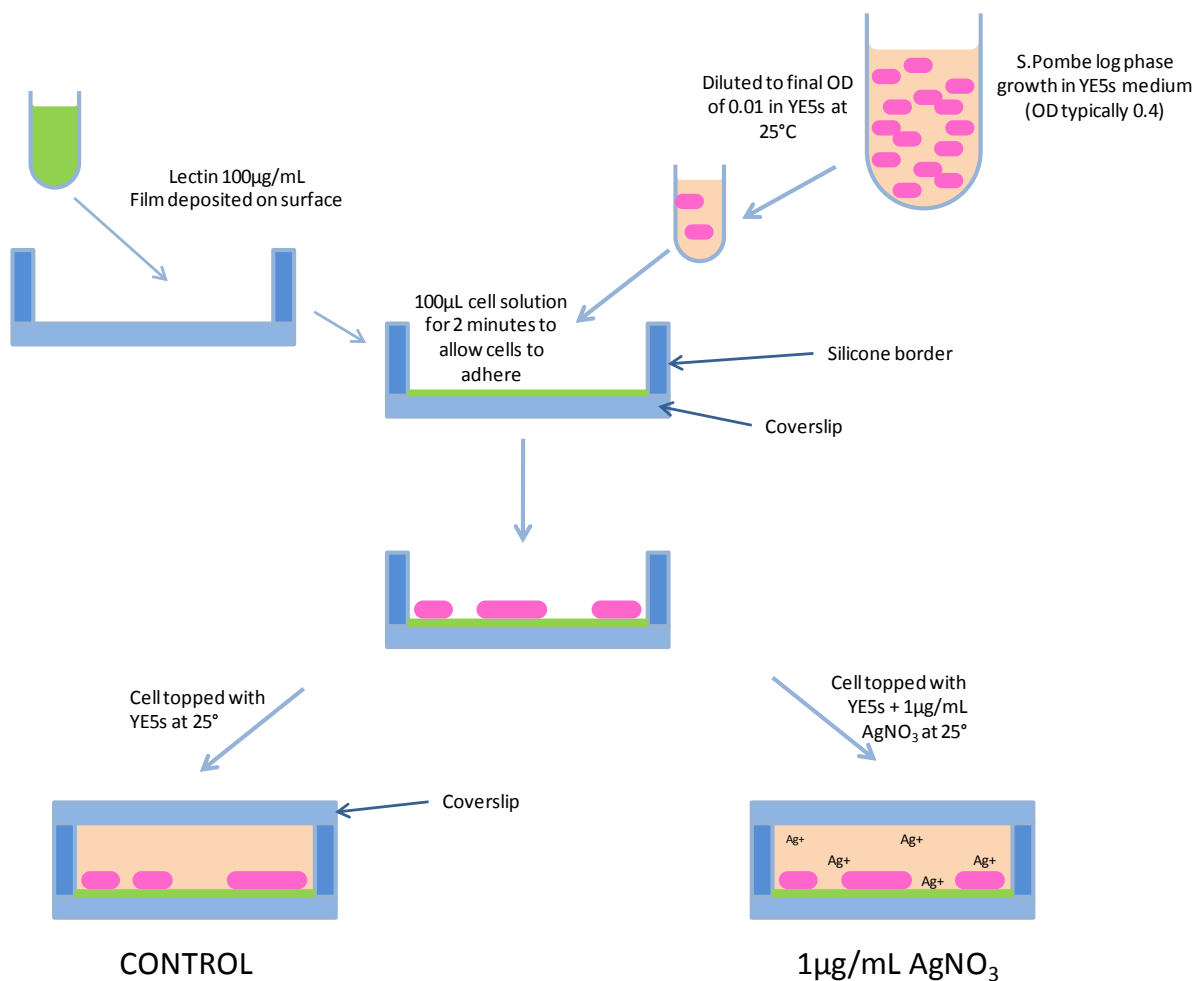


Figure 3.2 The experimental set up for the control and silver stress growth chambers. The set up is identical for both conditions until the final step, the silver stress environment filled with broth containing a concentration of silver nitrate and the control with broth only. The cells in the silver stress environment are not exposed to silver until this point.

A log-phase growth culture of *S. pombe* in YE5S was diluted to OD = 0.01, in the same growth media, and 100 µL of cell suspension was deposited in the flow cell, the lower surface of which was coated in lectin (Sigma-Aldrich, Lectin from Glycine max, L1395, 100 µg/mL). After 2 minutes the excess solution was removed, leaving only the cells that had adhered to the lectin-coated surface. The chamber in the control sample was filled with YE5S broth containing a 3-point calibration of microspheres (sizes 6, 12 and 30 µm) and sealed with the second cover slip.

A series of experiments were performed to measure the MIC for *S. pombe* under planktonic growth condition from which a sub-lethal concentration was derived. YE5S broth with varying AgNO₃ concentrations were inoculated with a exponential-phase growth culture of *S. pombe*. The cultures were incubated at 25°C with a shake of 200 rpm. Cell growth was measured at regular intervals by recording the OD₆₀₀ of the cultures.

The chamber in the silver stress sample was filled with YE5S broth supplemented with the same 3 control spheres and the sub-lethal concentration of AgNO₃. The Lensless microscope was placed in an optically dark, temperature controlled chamber. The temperature of this chamber was maintained at 25°C (±1), this remained stable over the time course of the experiment. The temperature of the growth cultures was maintained at 25°C. The control growth experiment was repeated 12 times, with each repeat containing between 6 and 12 cells. The silver growth experiment was repeated 14 times with each repeat containing between 4 and 9 viable cells.

3.3 Results

To collect the growth data presented here the growth experiment was performed 10 times under control conditions and 14 times under silver stress conditions. The Lensless microscope monitored growth, during the experiments exposing cells to silver, remained stable for over 2000 minutes, the constant, consistent measurement of the minor axis verifying this. The cells were grown in the flow cell, without the use of flow. This means that the media within the cell is not constantly oxygenated. *S. pombe* is known to not grow well under anaerobic conditions but the collusion of our growth data with that of data obtained from cells grown in aerobic planktonic conditions confirms that either the cells are not affected by the dwindling supply of oxygen or that, within the time course, oxygen does not become limited.

The preliminary silver stress growth experiments were conducted in planktonic conditions[40], Figure 3.3, using YE5S as the growth medium supplemented with a range of silver nitrate concentrations.

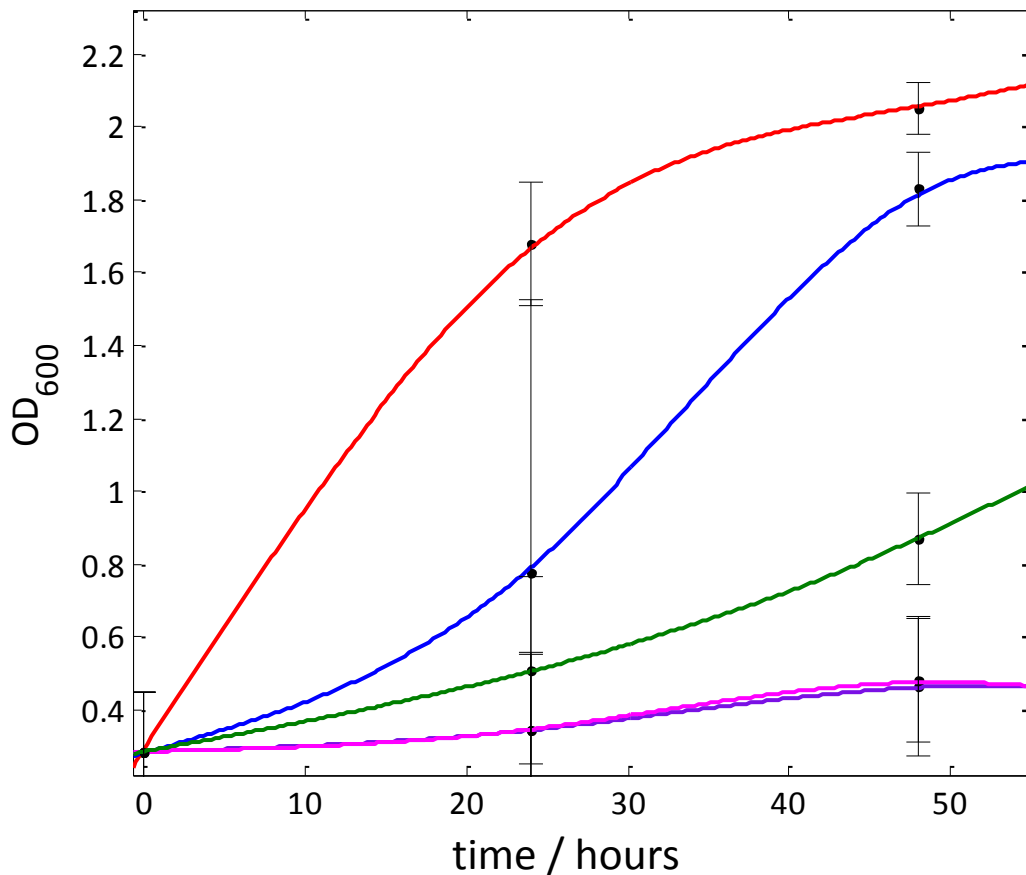


Figure 3.3. The planktonic growth curve, measured in optical density, for *S.pombe* when grown in YE5S broth (red), YE5S with 0.5 µg/mL AgNO₃ (blue), 1µg/mL AgNO₃ (green), 2 µg/mL AgNO₃ (purple) and 4 µg/mL AgNO₃ (pink). Error bars are ± standard deviation. Each data set is the average of 3 biological repeats.

These experiments were all performed using the same initial cell inoculum in the same YE5S medium at the same temperature, 25°C. The minimum inhibitory concentration (MIC) of silver, the lowest concentration of antimicrobial which will inhibit visible growth after overnight incubation^[41], is 2 µg/mL. We have selected 1 µg/mL as the sub-lethal silver concentration in which to observe the growth phenotype shift in silver stress conditions for *S. pombe*

The cell viability on transfer from the planktonic culture to the flow cell in the control experiments was > 98 %, assessed for $N = 100$, viability defined here as a cell which increases along at least one dimension during the experimental time course. A typical silver stress experiment resulted in the transfer of 12 cells into the flow cell to a total of 156 cells deposited throughout the course of the stress response analysis. 100 viable cells grew to cytokinesis and, allowing for a 2 % attrition rate on transfer to the surface (derived from the control) the 1 µg/mL AgNO₃ sub-lethal concentration causes 35 % of cells to die/prevents them from growing to cytokinesis within the time scale of the experiment, of 1000 minutes.

3.3.1 Growth Curves

The typical recorded growth curves for a single *S. pombe* cell, on a lectin surface, in YE5S broth at 25°C with and without silver stress are displayed, Figure 3.4. The growth along the major and the minor axis displayed, from which the growth parameters are derived, chapter 2 and below.

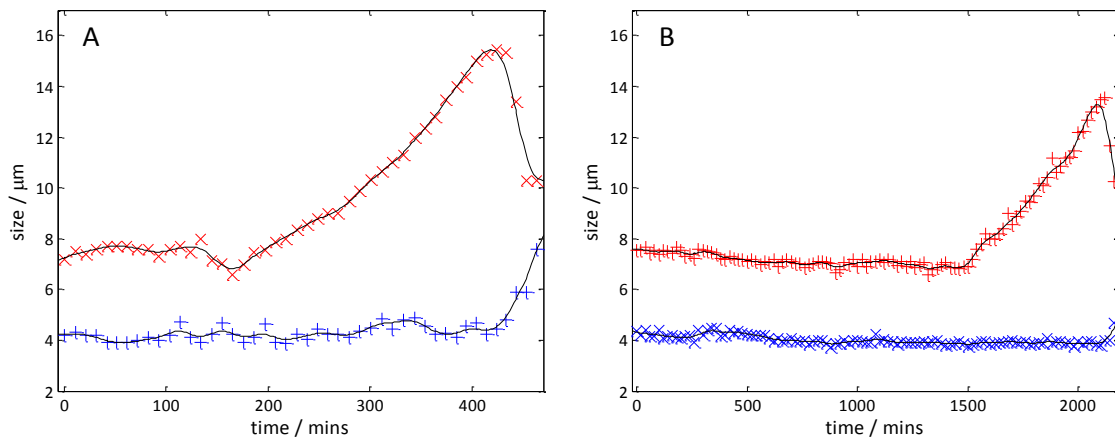


Figure 3.4 Typical growth curves, recorded by the Lensless microscope, for *S. pombe* under control conditions (A) and silver stress conditions (B), showing both the extension along the major axis (red) and the minor axis (blue). The time course for a single cell division under silver stress is over 4 times longer than the time course for the cell grown under control conditions.

The growth curve may be characterised by a number of parameters shown in Figure 3.5 which are the length at t_0 (L_{t_0}), the width at t_0 (W_{t_0}), the lag time (λ), the initial growth rate (μ_1), the post-inflection point growth rate (μ_2), the time to cytokinesis (A_{time}) and length at cytokinesis (A_{length}). The rate parameters were determined as the maximum of the numerical differentiated Pchip fit of the growth, NETO identified as a step change in this plot. A was determined as the numerical maximum of the major axis growth curve and the end of the lag period was identified when the maximum length was larger than $2 \times \sigma$ of the noise.

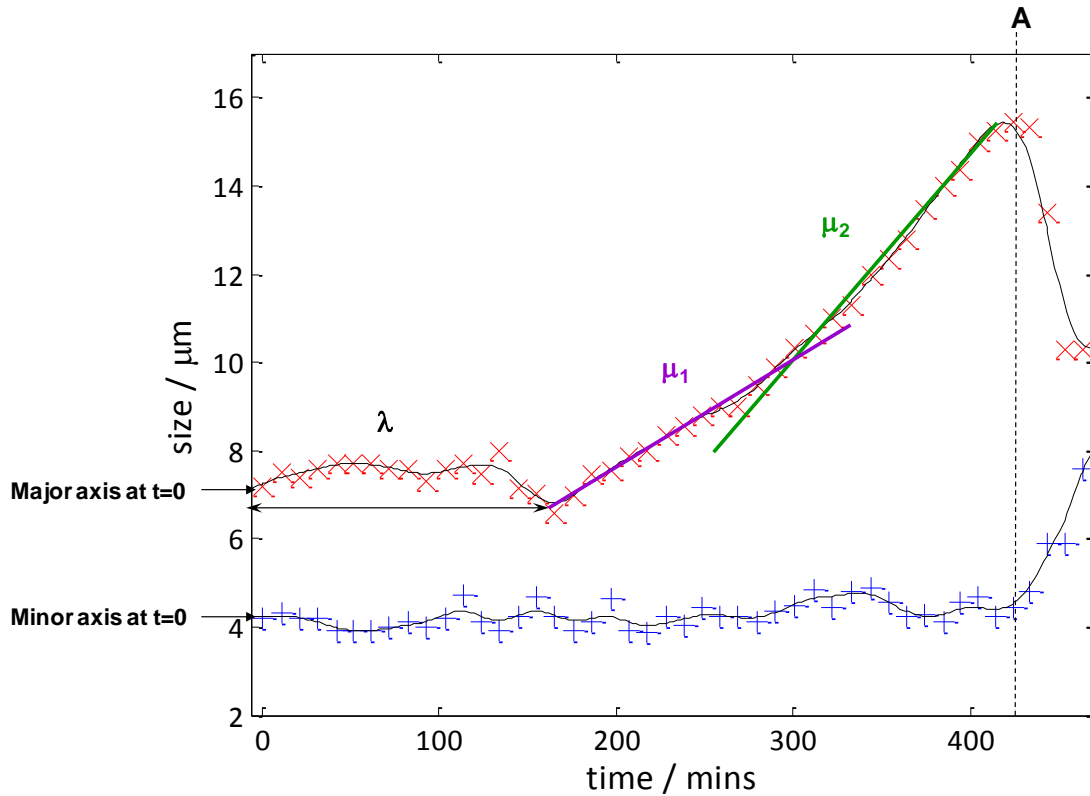


Figure 3.5. The growth parameters extracted from all cell growth observations: cell length at t_0 minutes (L_{t0}), cell width at t_0 minutes (W_{t0}), length of lag period (λ), growth rates μ_1 and μ_2 , the size at A (A_{length}), and the time that A is reached (A_{time}). Other parameters, such as t_{cell} , L_B and average growth rates are calculated from these data sets.

NETO and the parameters associated with it (μ_1 , μ_2 , size at RCP, time elapsed at RCP the μ_2/μ_1 ratio) are not observed in the growth curves recorded from the silver stressed *S. pombe* cells and so are analysed separately from the following silver stress data.

The choice of $N = 100$ *S. pombe* is based on a reasonable collection time and the number of cells reported in the literature for each of the cell parameters, so as to maintain consistent accuracy. Cells were analysed in each growth condition and a full set of parameters extracted. $N = 100$ here compares to or exceeds the number of cells measured in other publications^{[4],[35]}, the length and width parameters defined in Chapter 2 consistent with those in the literature and the bootstrapped median of these parameters shown to converge before $N = 100$.

3.3.2 Phenotype Classification Parameter Screening

The correlation matrix screening process, detailed in Chapter 2, identified 11 parameters that fall below the 0.6 correlation threshold and the correlation matrix for the wild type and silver stressed growth parameter analyses are presented in Table 3.2 and Table 3.3 respectively.

Table 3.2 The correlation coefficient table for the control *S. pombe* sample. Strong correlations are highlighted in grey to the right of the table.

	Length t0	Width t0	Lag	Atime	Asize	Lb	CCL	Av rate	Max rate	ARt0	ARmax
Length t0	1.000			-0.667						0.913	
Width t0	0.205	1.000									-0.649
Lag	-0.152	-0.027	1.000								
Atime	-0.667	-0.080	-0.023	1.000			0.759			-0.644	
Asize	0.246	0.053	0.155	-0.116	1.000	1.000		0.553			0.718
Lb	0.246	0.053	0.155	-0.116	1.000	1.000		0.553			0.718
CCL	-0.127	0.089	-0.180	0.759	-0.287	-0.287	1.000				
Av rate	-0.380	-0.113	0.301	-0.117	0.553	0.553	-0.594	1.000			
Max rate	-0.090	-0.068	0.063	0.025	0.428	0.428	-0.165	0.341	1.000		
ARt0	0.913	-0.203	-0.130	-0.644	0.216	0.216	-0.177	-0.326	-0.066	1.000	
ARmax	0.055	-0.649	0.134	-0.053	0.718	0.718	-0.299	0.498	0.400	0.317	1.000

Table 3.3 The correlation coefficient table for the sample of *S. pombe* cells which have been grown in silver stress conditions. The strong correlations are highlighted in grey on the right hand side of the table.

	Length t0	Width t0	Lag	Atime	Asize	Lb	CCL	Av rate	Max rate	ARt0	ARmax
Length t0	1.000							-0.665		0.882	
width t0	-0.181	1.000									-0.758
Lag	-0.470	-0.081	1.000								
Atime	-0.514	0.142	0.172	1.000			0.678				
Asize	0.401	0.089	-0.462	-0.391	1.000	1.000					
Lb	0.401	0.089	-0.462	-0.391	1.000	1.000					
CCL	0.182	-0.054	-0.029	0.678	-0.437	-0.437	1.000	-0.733			
Av rate	-0.665	0.208	0.183	-0.091	0.299	0.299	-0.733	1.000	0.634	-0.624	
Max rate	-0.354	-0.096	0.152	-0.085	0.276	0.276	-0.432	0.634	1.000		
ARt0	0.882	-0.575	-0.365	-0.464	0.307	0.307	0.168	-0.624	-0.239	1.000	0.690
ARmax	0.371	-0.758	-0.196	-0.334	0.522	0.522	-0.214	0.008	0.266	0.690	1.000

The correlation analysis for both growth conditions give different results for the phenotype parameter sets, there are 6 common which will be taken forwards for phenotype screening :

- Length at t_0 mins / μm
- Width at t_0 mins / μm
- Length of lag period / minutes
- Average growth rate / $\mu\text{m min}^{-1}$
- Birth length (L_B)/ μm
- t_{cell} / minutes

For the comparison of two data sets we have developed the ePDF mirror plot, which is displayed with the other graphical comparison methods in Figure 3.6.

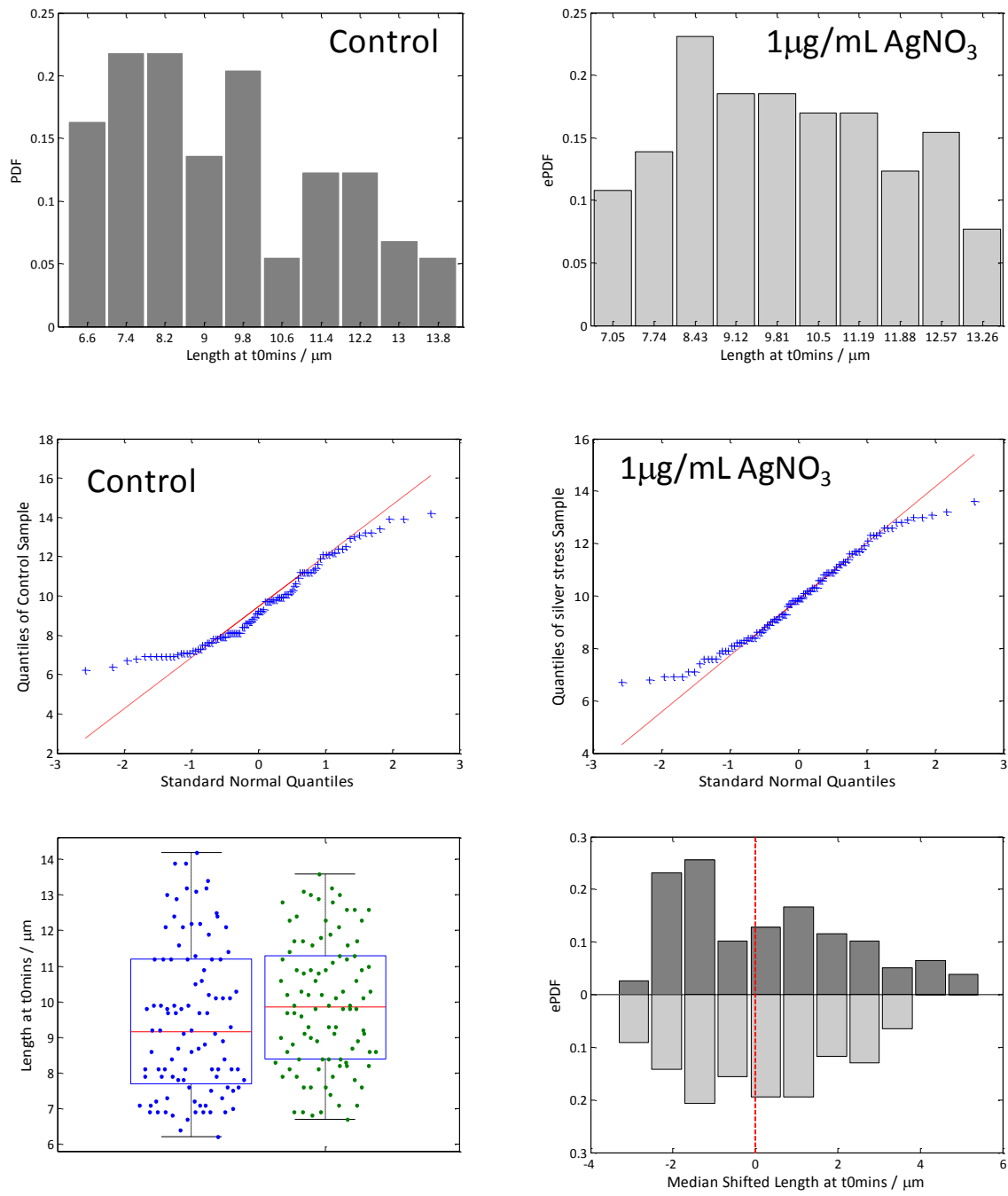


Figure 3.6. The graphical representations of the length at t_0 mins distributions for both the control sample (left) and the silver stressed sample (right). The distributions are displayed as fixed bin number histograms, Q-Q plots, Box plots with the individual data points spread below (bottom left) and a histogram 'mirror plot' of the median shifted distributions (bottom right). We conclude from this that the distributions are best compared and represented by the mirror plot.

The mirror plot is a histogram for each data set, the control data above the x-axis and the silver stressed data below the x-axis. The control distribution histogram bins were set automatically to 10 and the same bin width was chosen for the silver stress. The graphical comparison of the distributions such as range, skewness and kurtosis is best performed on the median-shifted distributions which are aligned on the mirror plots indicated by the dotted vertical line. For

comparison the data is displayed as both the raw data and the median shifted mirror plot in each case.

The distributions of the length of the cell populations at t_0 in both growth conditions is presented in Figure 3.7, the parameters of these distributions are summarised in Table 3.4.

Table 3.4 The measured distribution parameters of the length at t_0 mins parameter for three classes of cells the control (dark grey), all cells arriving on the surface in the silver experiment and the viable cells in the silver experiment (both silver columns). Values in brackets are the 95% confidence limits, bootstrapped for $N = 1000$.

Parameter	Control	All on surface	Viable cells
Skewness	0.49(+0.33-0.29)	0.36(+0.26-0.24)	0.12 (± 0.28)
Kurtosis	2.16 (+0.7-0.4)	2.11(+0.42-0.20)	2.01 (+0.32 -0.3)
St. Dev	2.1 (+0.23 -0.21)	2.26(+0.22-0.18)	1.81 (± 0.18)
Range / μm	8.0 (-0.2)	8.4 (-0.3)	6.9 (-0.1)
Mean / μm	8.9 (± 0.3)	9.6 (± 0.2)	9.9 (± 0.3)
Median / μm	9.2 (± 0.6)	9.3 (± 0.6)	9.9 (± 0.6)

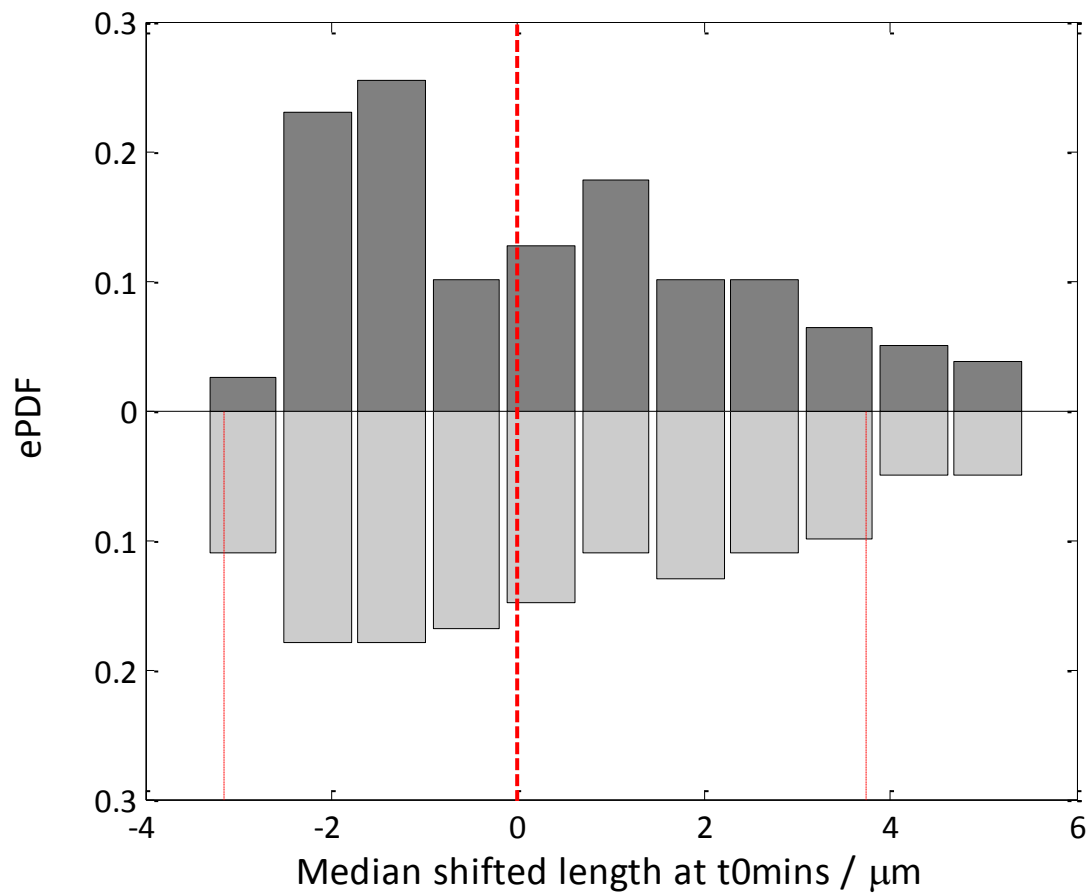
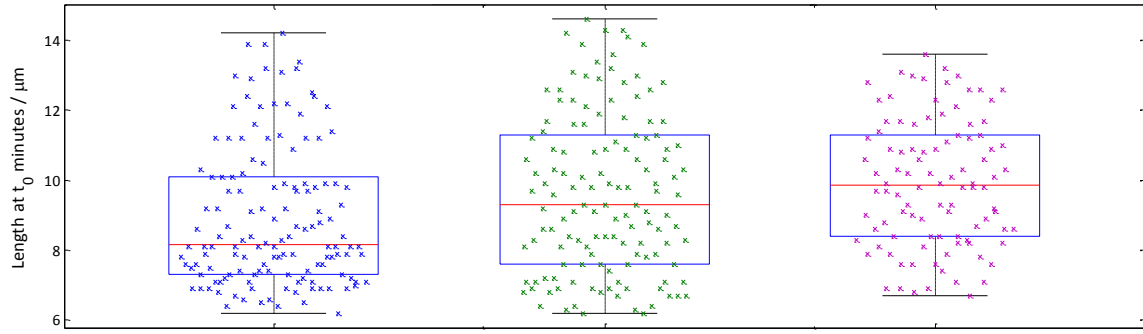


Figure 3.7. Top: The Box plot and Beeswarm plots of the raw data for Length at t_0 minutes, the control sample in blue, the silver surface arrivers in green and the silver surface survivors in purple. Bottom: The mirror plot of the median shifted distributions of the lengths at t_0 mins for both the control (top) and silver stressed (bottom) samples. The wider dashed line represents the median of the data and the thinner dashed lines represent the range of the distribution of the viable cells, those at t_0 mins which grew to cytokinesis.

Both the S-W test and the A-D test show that all three distributions are not normally distributed, with the control and the silver t_0 distributions returning P-values for both tests of <0.001 and the

viable cell under silver conditions distribution returning P-values <0.04. Other tests for normality, Skewness of 0 and a Kurtosis value of 3, indicate that the viable cell distribution under silver stress has a closer to normal distribution. The distribution of lengths at t_0 under control and silver stress growth conditions are from the same distribution (Mann-Whitney U) but with a P-value of 0.4, the probability of accepting the null hypothesis by chance alone being 60 %. The three distributions have the same median within the bootstrapped 95 % confidence limit error. The range of the distributions is however different. The range of the control growth conditions is 8 μm compared with those reaching cytokinesis under silver growth conditions of 6.9 μm . Cells of extreme dimension either short or long are compromised in the silver-stress survival process. .

The distribution of widths at t_0 minutes is shown in Figure 3.8 and the accompanying parameters summarised in n Table 3.5.

Table 3.5 The measured distributions parameters of the width at t_0 mins parameter for three classes of cells the control (dark grey), all cells arriving on the surface in the silver experiment and the viable cells in the silver experiment (both silver columns). Values in brackets are the 95 % confidence limits, bootstrapped for $N=1000$.

Parameter	Control	All on surface	Viable cells
Skewness	0.19(+0.48 -0.53)	0.26(+0.51-.39)	0.15 (+0.53-0.4)
Kurtosis	3.38 (+1.1 -0.8)	3.23 (+1.49 -1)	3.1 (+1.1 -0.67)
St. Dev	0.35(+0.06-0.04)	0.37 (+0.5 -0.6)	0.39(+0.07-0.05)
Range/ μm	1.8 (-0.15)	2 (-0.15)	2 (-0.15)
Mean/ μm	4.1 (+0.15-0.2)	3.8 (\pm 0.15)	3.8 (\pm 0.15)
Median/ μm	3.9 (\pm 0.15)	3.8 (\pm 0.15)	3.9 (\pm 0.15)

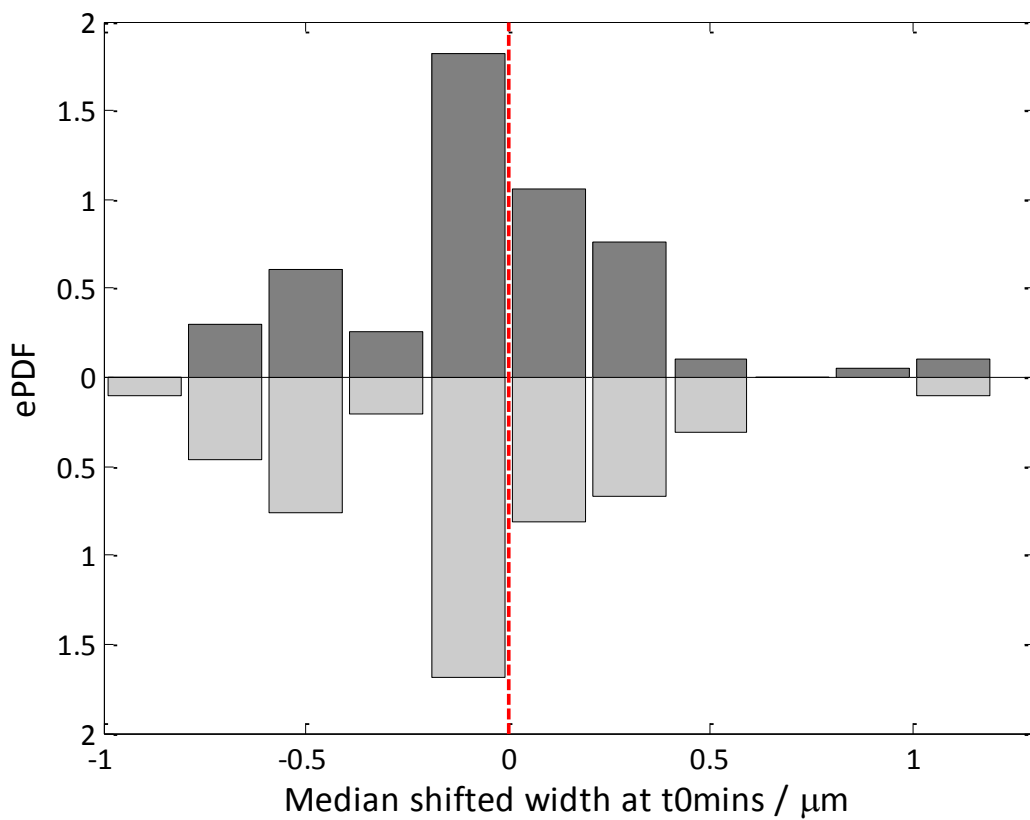
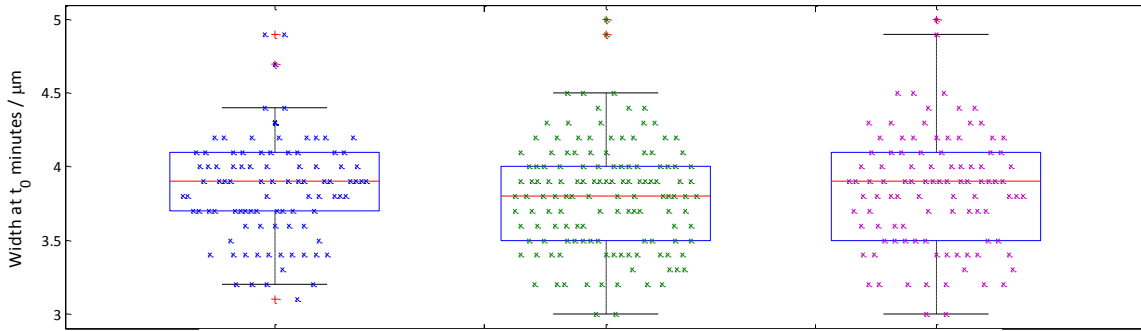


Figure 3.8 Top: The Box plot and Beeswarm plots of the raw data for Width at t_0 minutes, the control sample in blue, the silver surface arrivers in green and the silver surface survivors in purple. Bottom: The mirror plot of the median shifted distributions of the widths at t_0 mins for both the control (top) and silver stressed (bottom) samples. The dashed line represents the median of the data. The addition of the cells which fail to grow in the silver environment does not significantly change the distributions.

The S-W and the A-D test for both the control and all cells at t_0 under silver stress reject the null hypothesis that the width distributions are normal at the 95 % confidence level with P-values <0.01. The distribution of the viable cells at t_0 in the silver sample is normal, in both the S-W and A-D test, the probability of accepting the null hypothesis by chance is 88 %. The normal values for kurtosis and skewness (3 and 0 respectively) are within the bootstrapped errors for all three distributions. The

median and the range of the distributions are the same, the error for the median limited by the diffraction limit error.

The lag period, the length of time between deposition of the cell into a new environment and the onset of elongation along the major axis, in the control sample and the silver stress sample are displayed in Figure 3.9, with the distribution parameters in Table 3.6.

Table 3.6 The measured distributions parameters of the lag period parameter for two classes of cells the control (dark grey) and the viable cells in the silver experiment (silver column). Values in brackets are the 95 % confidence limits, bootstrapped for $N = 1000$. The length of the lag period is over 10 times longer when the *S. pombe* cell is under silver stress.

Parameter	Control	Silver
Skewness	0.92 (-0.4+0.54)	0.09 (-0.45 +0.4)
Kurtosis	4.00 (-1.2+1.9)	2.82 (-0.5 +0.9)
St. Dev	12.8 (-1.7 +2.7)	97.8(-10.2+13.8)
Range/ μm	64 (-1)	516 (-7)
Median/ μm	149 (+3 -2)	1521 (+35 -28)
Mean/ μm	150 (+3 -1)	1518 (± 20)

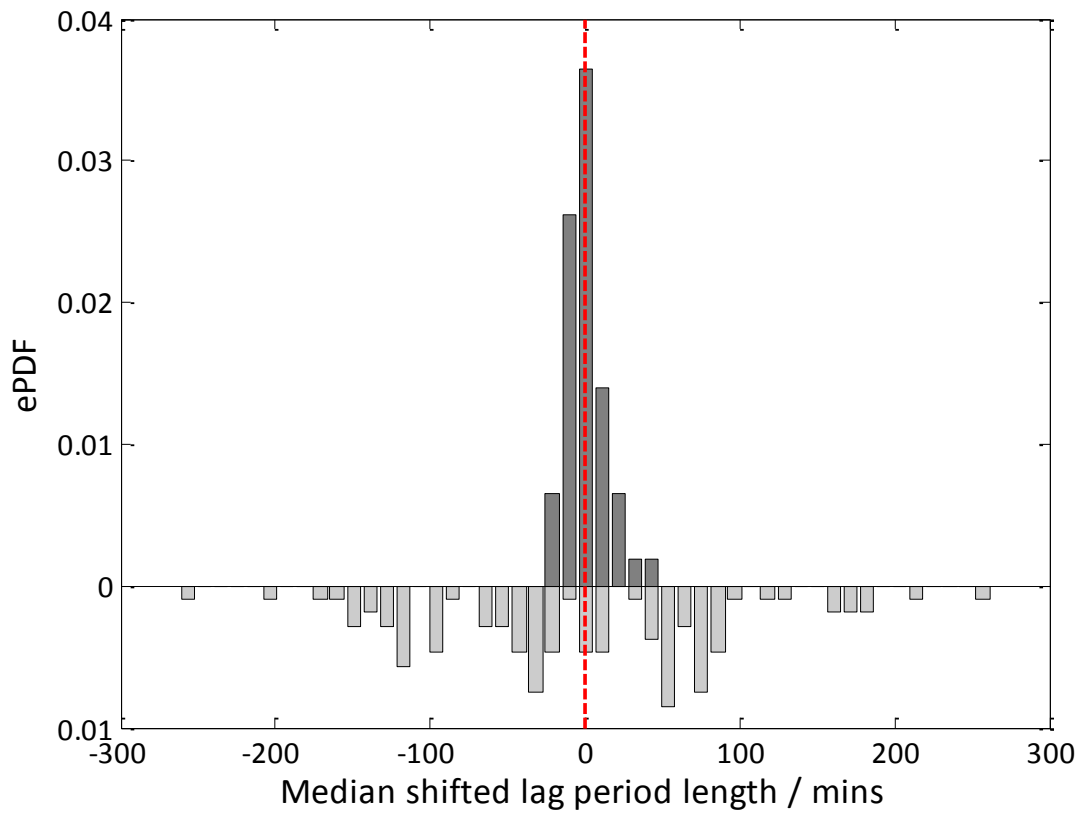
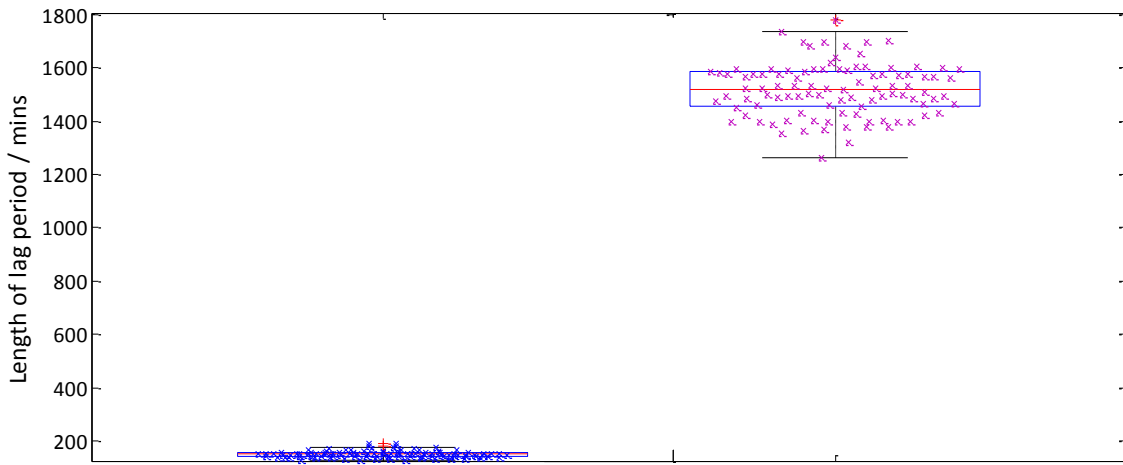


Figure 3.9 Top: The Box plot and Beeswarm plots of the raw data for length of lag period, the control sample in blue and the silver surface survivors in purple. Bottom: The mirror plot of the median-shifted distributions of the lag period lengths for both the control (top) and silver stressed (bottom) samples. The dashed line represents the median of the data sets.

The lag period has a median of 1521 (+35 -28) minutes under silver stress, 10 times the length of the lag period under control conditions and a range of 516 (-7) minutes, 8 times the range under control conditions. Under control conditions both normality tests return a P-value <0.001, confirming that this distribution is not normal. The lag phase is normally distributed at the 95 % confidence limit but with P of 0.6. Both the skewness and the kurtosis values confirm this relative proximity to normal, the values for normal within the bootstrapped error. The distributions are not from the same distribution with the Mann-Whitney U test rejecting the null hypothesis with a P-value <0.001.

The birth length, L_B defined as half the cell length at cytokinesis (A_{size}). It is then adjusted for the correction factor for two cells dividing, based on the increase in length which occurs at septation when two cells transition from joined with straight ends to separate with hemispherical ends^[35]. L_B is the predicted size of a cell at birth based on the fact that a cell doubles in size during 1 cell cycle^[34, 35] and the length it reached at division. Figure 3.10 is the distribution of L_B for both the control and silver stress samples and Table 3.7 the distributional parameters.

Table 3.7 The measured distributions parameters of the birth length (L_B) parameter for two classes of cells the control (dark grey) and the viable cells in the silver experiment (silver). Values in brackets are the 95 % confidence limits, bootstrapped for $N = 1000$. The cells divide shorter under silver stress conditions.

Parameter	Control	Silver
Skewness	1.5 (-0.43 +0.62)	-0.32(-0.43 +0.3)
Kurtosis	5.78(-1.71+3.14)	2.53(-0.53+1.24)
St. Dev	0.8 (-0.15 +0.21)	0.51(-0.05+0.09)
Range	4.2 (-0.5)	2.5 (-0.2)
Median	7.1 (+0.2 -0.1)	6.6 (+0.1 -0.2)
Mean	7.6 (\pm 0.2)	6.5 (\pm 0.1)

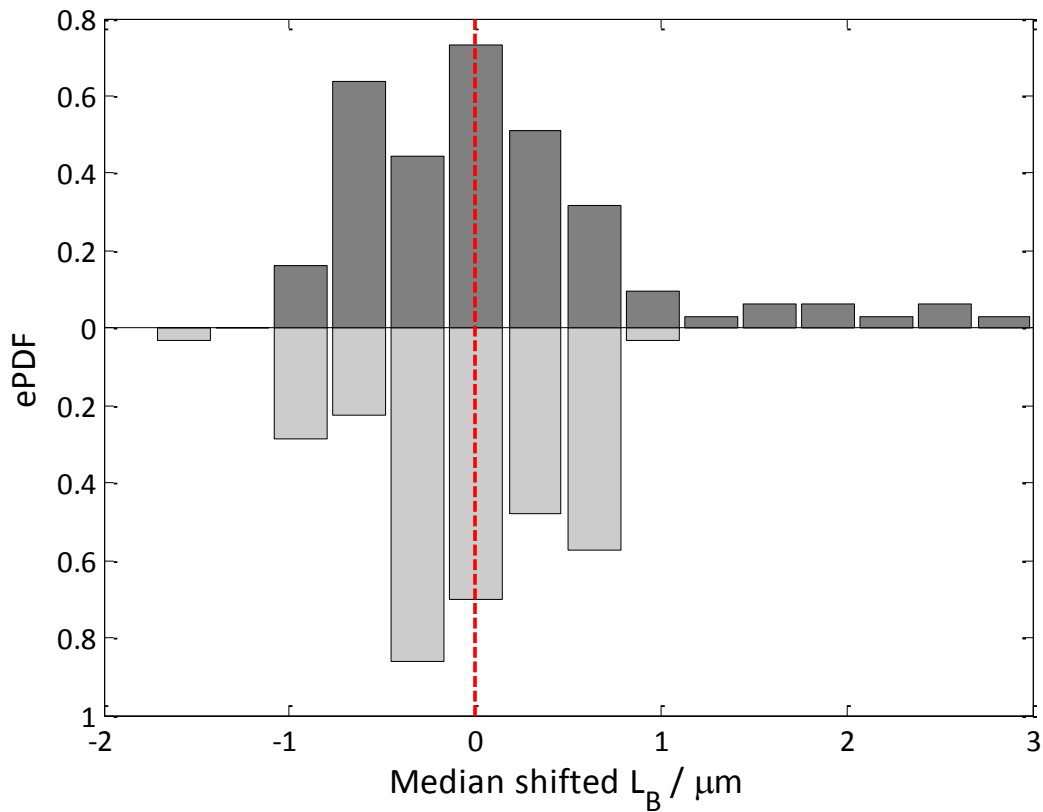
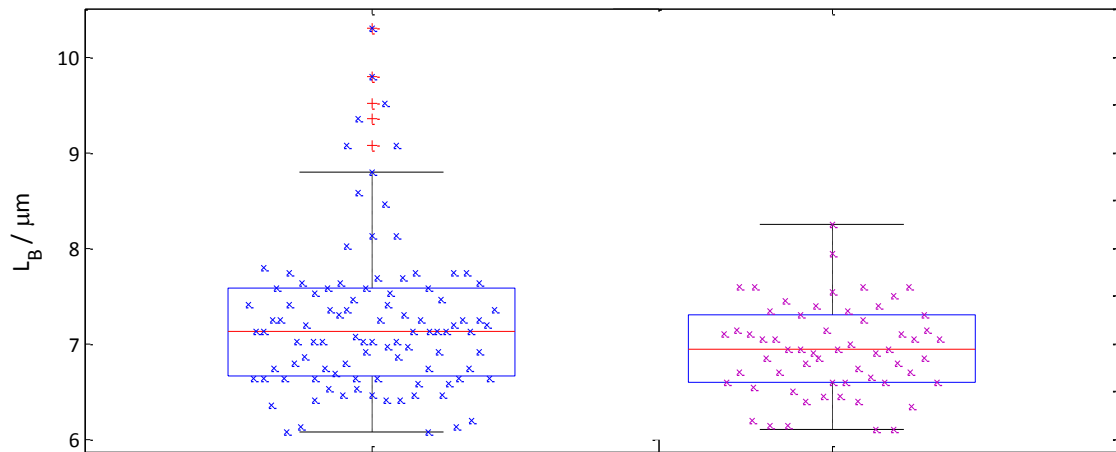


Figure 3.10 Top: The Box plot and Beeswarm plots of the raw data for L_B , the control sample in blue and the silver surface survivors in purple. Bottom: The mirror plot of the median shifted distributions of the calculated L_B for both the control (top) and silver stressed (bottom) samples. The dashed line represents the median of the data sets.

The tests reject the null hypothesis of normality for both distributions with P-values all <0.01 . The distributions are not part of the same continuous distribution according to the Mann-Whitney U test with a P-value <0.01 . The control distribution is skewed towards longer birth length (Skewness coefficient 1.5), reflected in the large kurtosis value of 5.78 (normal = 3). The silver stress

distribution is skewed towards the shorter lengths at birth, but this is less significant than the skewness of the control sample (kurtosis 2.53).

The length of the cell cycle is the growth time between cytokinesis and lag, corrected for the ratio between L_B and length at t_0 mins, and is calculated using equation (2) derived here:

$$(t_A - \lambda) = \frac{L_B}{l} t_{cell}$$

(2)

where t_A is the time of cytokinesis in minutes, λ the length of the lag period in minutes, L_B our predicted length at birth in μm , the length of the cell measured at t_0 and t_{cell} the cell cycle length in minutes. Figure 3.11 and Table 3.8 are the distribution and analysis of the calculated cell cycle length for both the control and the silver stress data sets.

Table 3.8 The measured distributions of the cell cycle length (t_{cell}) parameter for two classes of cells the control (dark grey) and the viable cells in the silver experiment (silver). The cell cycle time increases by over 4 times when the cells grow under silver stress.

Parameter	Control	Silver
Skewness	-0.28(-.32+0.38)	0.60(-0.73+0.98)
Kurtosis	2.94(-0.53+0.86)	4.80(-2.36+3.87)
St. Dev	66.8(-8.1 +10.1)	195(-26.4+49.3)
Range / mins	324 (-19)	1214 (-24)
Median / mins	207 (+8 -13)	881 (+29 -75)
Mean / mins	200 (+12 -10)	900 (+40 -38)

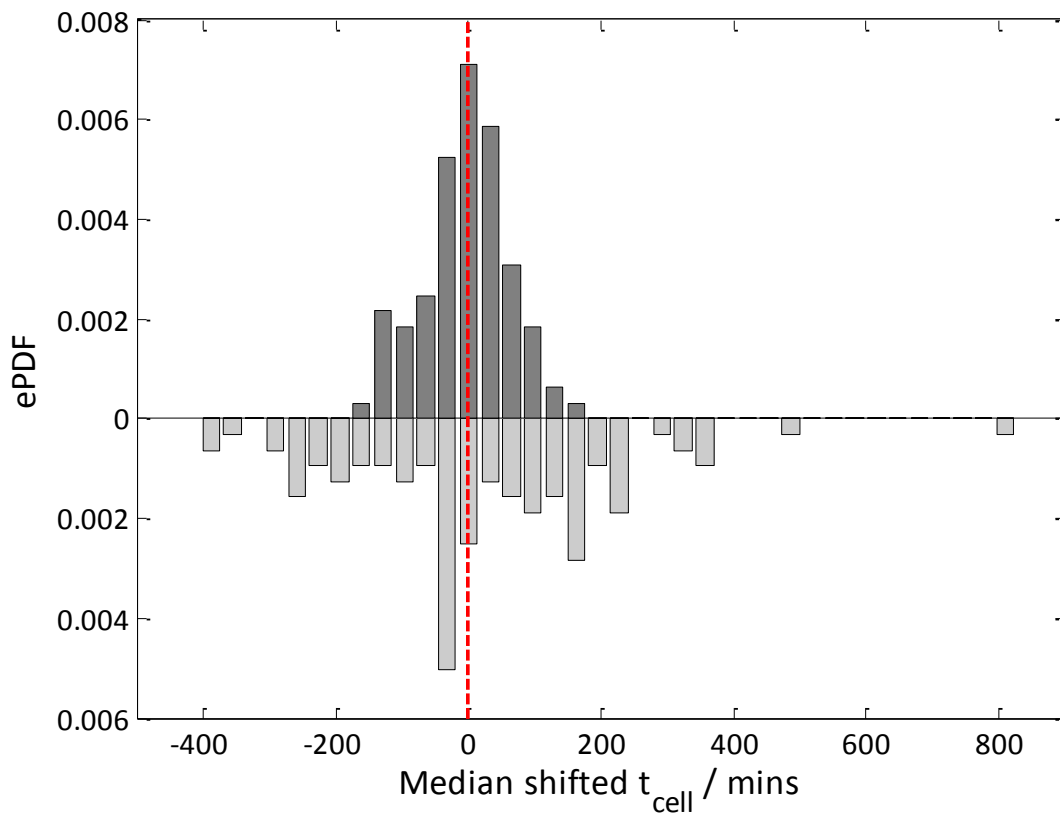
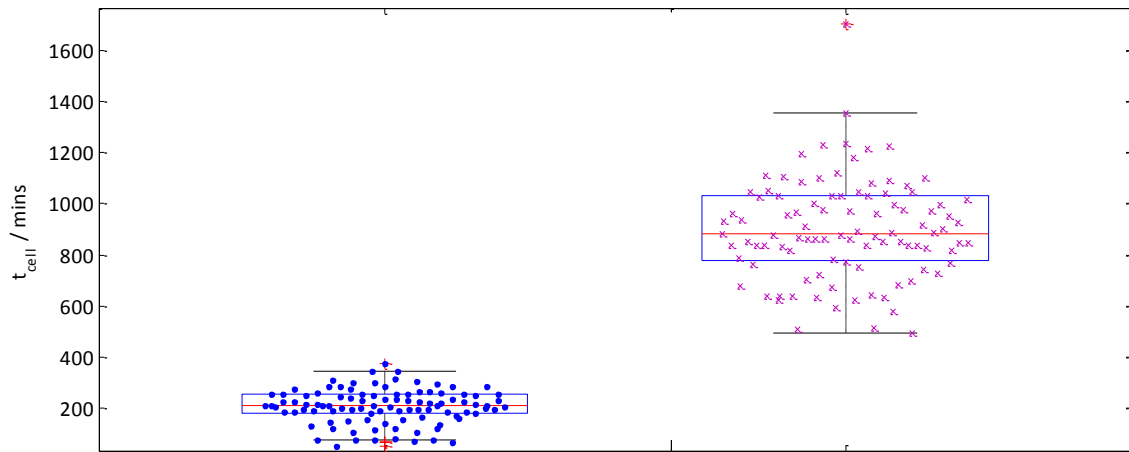


Figure 3.11 Top: The Box plot and Beeswarm plots of the raw data for t_{cell} , the control sample in blue and the silver surface survivors in purple. Bottom: The mirror plot of the median shifted distributions of the Cell Cycle Length (t_{cell}) for both the control and silver stressed samples. The dashed line represents the median of both the data. The cell cycle length has a much larger range when the cells grow under silver stress.

Neither of the t_{cell} distributions in normal or stressed growth conditions are normally distributed when tested with the S-W and A-D tests, the control sample P-values <0.1 and the silver stress

sample P-values <0.001. The two distributions are not from the same continuous distribution, when tested with the Mann-Whitney U test, with a P-value <0.001. Both distributions contain the normal values for kurtosis and skewness in the bootstrapped range of values for these parameters. The median cell cycle time is length of the cell cycle is 4 times larger when the cell is under silver stress. This is the only distribution in which the silver stress sample becomes less normal, very outlier prone and more skewed. The length of the cell cycle increases over 4 fold to 881 (+29 -75) minutes under silver stress, with the range of the distribution increasing 3.7 times.

The average rate of growth is calculated over all the points between the end of the lag phase (λ) the time to cytokinesis, this excluding μ_1 and μ_2 as the rate changing point of NETO is not observed under silver stress. The distributions of average growth rate and corresponding parameters are displayed in Figure 3.12 and Table 3.9 respectively.

Table 3.9 The measured distributions of the average growth rate parameter for two classes of cells the control (dark grey) and the viable cells in the silver experiment (silver). The average growth rate decreases by over 5 times under silver stress.

Parameter	Control	Silver
Skewness	0.8 (-0.3 +0.6)	0.82 (-0.3 +0.52)
Kurtosis	4 (-0.8 +1.2)	3.4 (-0.9 +2)
St. Dev	0.01(0.001+0.004)	0.003 (-0.001)
Range / $\mu\text{m min}^{-1}$	0.05 (-0.001)	0.013 (-0.002)
Median / $\mu\text{m min}^{-1}$	0.027(\pm 0.003)	0.005 (\pm 0.001)
Mean / $\mu\text{m min}^{-1}$	0.027 (\pm 0.002)	0.005 (\pm 0.001)

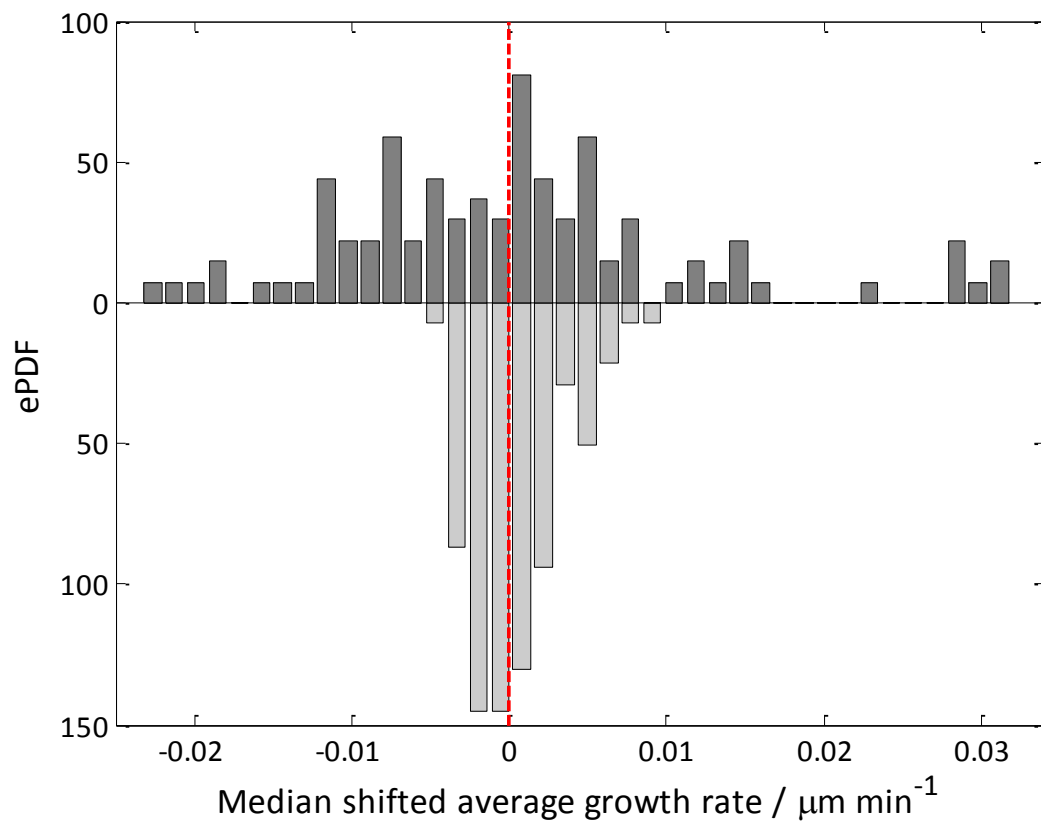
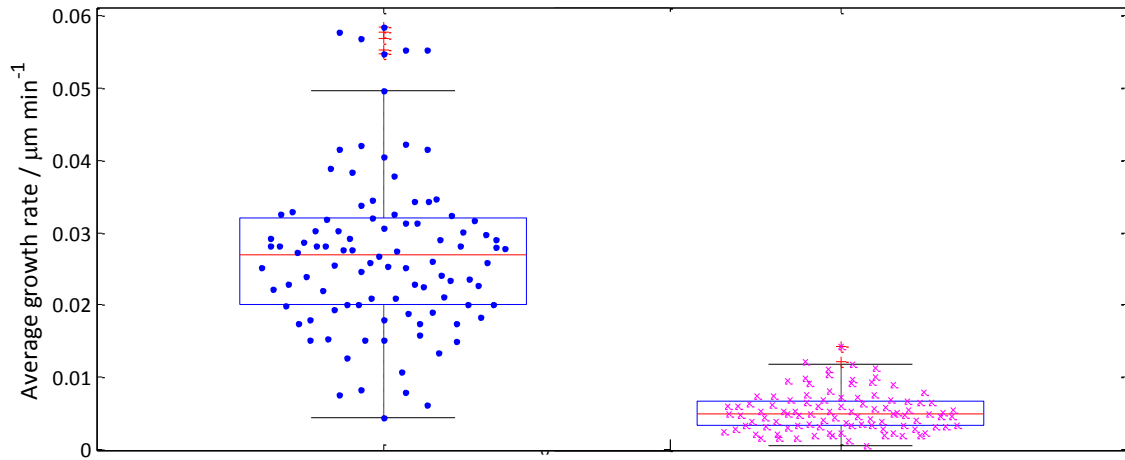


Figure 3.12 Top: The Box plot and Beeswarm plots of the raw data for average growth rate, the control sample in blue and the silver surface survivors in purple. Bottom: The mirror plot of the median shifted distributions of the average growth rates for both the control (top) and silver stressed samples (bottom). The dashed line represents the median of the distributions. The cells under silver stress have a much smaller range than those under normal conditions as the average growth rate is 5 times slower.

The median growth rate of the control sample was $0.027 (\pm 0.003) \mu\text{m min}^{-1}$, the median growth rate for the sample under silver stress was over 5 times slower than the control at $0.005 (\pm 0.001) \mu\text{m min}^{-1}$. It is to be noted that this is the only distribution in which the silver stress phenotype has a narrower range than the control sample. The silver stress distribution is normal according to both the S-W and A-D tests for normality but the null hypothesis accepted with the change of it being normal happening by chance being 75 %. The control distribution is not normal according to both tests for normality, with P-values < 0.01 . There are other rate parameters associated growing *S. pombe*, specifically the RCP indicating NETO. These are discussed next.

3.3.3 New End Take Off and Sub Population Correlations

NETO was only observed in the control growth and not in the silver growth conditions. The measurement of the time to NETO is determined by locating the RCP in the growth curve and determining the change in growth rate, typically 31 %^[36]. The prevalence of NETO in the cell population was 62 %; the 62nd percentile of our data is $9.9 \mu\text{m}$. The rate of growth before and after the RCP and the ratio of the two growth rates are displayed in Figure 3.13 and Table 3.10.

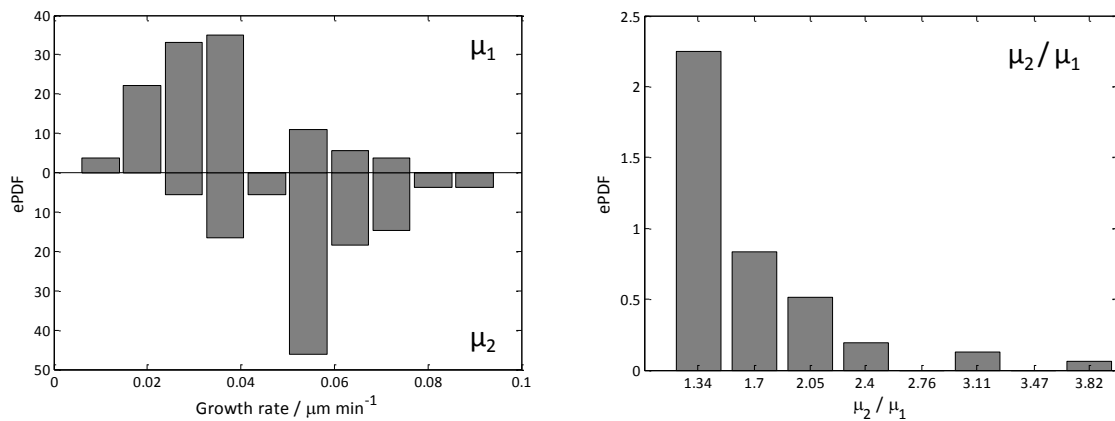


Figure 3.13 The mirror plot of the median shifted distributions of the widths at t_0 mins for both the control and silver stressed samples. The dashed line represents the median of the data. The addition of the cells which fail to grow in the silver environment does not significantly change the distributions.

Table 3.10 The measured distributions of the growth rate parameters for the cells which undergo NETO, μ_1 , the rate of growth before NETO and μ_2 , the rate of growth after NETO.

Parameter	μ_1	μ_2
Skewness	0.55 (+0.6-0.5)	0.63 (\pm 0.6)
Kurtosis	3.3 (+1.3 -0.8)	3.3 (+1.6 -0.9)
St. Dev	0.01 (\pm 0.003)	0.01 (\pm 0.003)
Range / $\mu\text{m min}^{-1}$	0.06 (-0.001)	0.06 (-0.001)
Median / $\mu\text{m min}^{-1}$	0.03 (+0.01)	0.05 (+0.003)
Mean / $\mu\text{m min}^{-1}$	0.035 (\pm 0.004)	0.05 (\pm 0.003)

The modal rate increase between μ_2 and μ_1 is 1.34, but the distribution is highly skewed (skewness coefficient 2.19). None of the three distributions is normally distributed according to the tests of normality, with P-values all <0.01 . The distributions of μ_1 and μ_2 are not from the same distribution with a P-value <0.01 .

The distribution of cell length at t_0 of the control sample is shown in Figure 3.14 and compared with subset of cells lengths at t_0 that go on to show NETO. Table 3.11 summarise the distributional analysis parameters. For clarity, Figure 3.16 is not a mirror plot; the distribution above and below the x-axis is the total sample distribution with below the axis the subset of the distribution showing NETO. The bin number is set as 11.

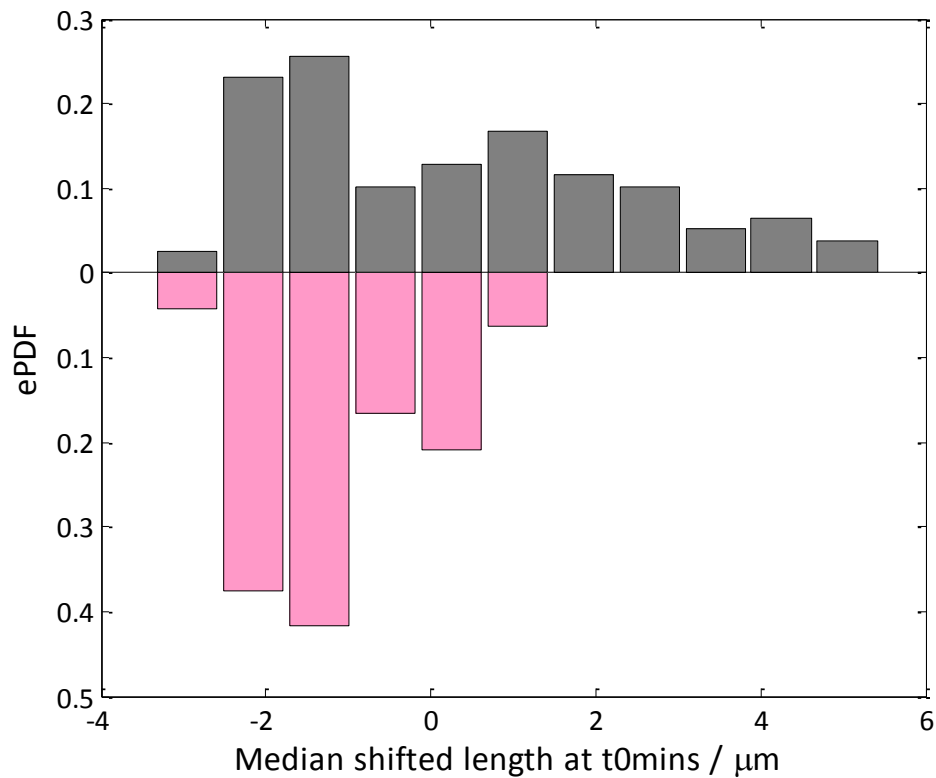


Figure 3.14 A comparison mirror plot of the length at t_0 of all the cells on the surface in the control sample (top) and those cells which later went on to display NETO (bottom).

Table 3.11. The parameters of the distributions of length at t_0 mins for the whole control sample (dark grey) and the distribution just of the cells which contain a RCP during the growth period (pink).

Parameter	Control	Showing NETO
Skewness	0.49 (+0.33-0.29)	0.32 (-0.34 +0.37)
Kurtosis	2.16 (+0.7-0.4)	2.07(-0.41 +0.65)
St. Dev	2.1 (+0.23 -0.21)	0.99 (-0.11 +0.14)
Range / μm	8 (-0.2)	3.6 (-0.2)
Median / μm	8.9 (± 0.3)	7.9 (-0.3 +0.2)
Mean / μm	9.2 (± 0.6)	8.0 (-0.3 +0.2)

The range of lengths of cells which display NETO is half the size of the range of lengths of all the cells deposited on the flow cells surface, 8 μm reduced to 3.6 μm . The NETO sub-population lengths have a lower median, 7.9 (-0.3 +0.2) μm compared to 8.9 (± 0.3) μm , significantly different with a

P-value = 0.01. The cells which arrive on the surface at a length of less than 9.8 μm have not undergone NETO previously and so display it during the monitored growth curve.

The distribution of L_B for all cells in the control sample is compared to sub-population of L_B which underwent NETO shown in Figure 3.15, with the distribution parameters in Table 3.12.

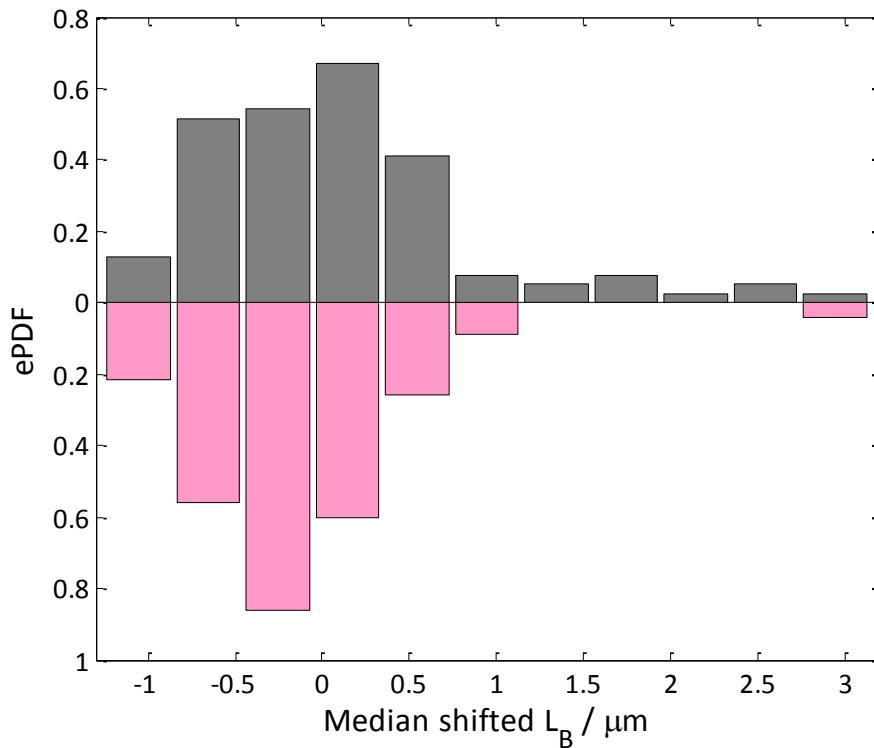


Figure 3.15 A comparison mirror plot of the calculated L_B of all the cells on the surface in the control sample (top) and those cells which later went on to display NETO (bottom).

Table 3.12 The parameters of the distributions of the calculated L_B for the whole control sample (dark grey) and the distribution just of the cells which contain a RCP during the growth period (pink).

Parameter	Control	Showing NETO
Skewness	1.5 (-0.43 +0.62)	1.94 (-1.8 +1.26)
Kurtosis	5.78 (-1.71+3.14)	10.7 (-7.5 +9.4)
St. Dev	0.8 (-0.15 +0.21)	0.6 (-0.16 +0.36)
Range / μm	4.2 (-0.5)	3.8 (-1.7)
Median / μm	7.1 (+0.2 -0.1)	7.0 (-0.1 +0.2)
Mean / μm	7.6 (\pm 0.2)	7.0 (-0.1 +0.2)

Neither L_B distribution is normal, with the P-values from both the S-W and the A-D test returning P-values <0.01. Both distributions are skewed towards the longer lengths at birth and have large values of kurtosis, not one of these parameters straddle the values of a normal distribution within the errors. Due to one outlier in the L_B showing NETO distributions the two data sets have comparable ranges, medians and means.

3.4 Discussion

The Lensless microscope and associated image processing algorithm accurately monitored the growth of 100 *S. pombe* cells in a control sample under normal growth conditions and a further 100 cells that survived to cytokinesis under silver-stressed growth conditions; in a total, 24 experiments were performed. Before cells even begin to grow they display a phenotype, transition to the flow cell surface results in 98 % viability. Then under silver stress conditions there are 35 % of cells which do not grow, perhaps not having reached a threshold of a protein required for survival.

It has been demonstrated that the distributions of growth parameters are significantly different after environmental condition shift by $AgNO_3$. The phenotype parameter screen reduced the number of growth parameters uncommon to both growth media from 11 to 6. A summary of the growth parameters calculated here are compared with the literature values in Table 3.13.

Table 3.13 A summary of some published growth parameters compared with the parameters calculated here and the parameters observed when *S. pombe* is grown under silver stress conditions.

Parameter	Literature Mean Value	Average	Mean and 95% CI for Control growth	Mean and 95% CI for Silver stress growth
Birth Length / μm	7.5 \pm (0.5)	7.9	7.1 (+0.2 -0.1)	6.6 (+0.1 -0.2)
	8.2 \pm (0.52)			
Division Length / μm	15.8 \pm (1.6)	14.6	14.2 (+0.4 -0.2)	13.2 (+0.2 -0.4)
	13.48 \pm (1.05)			
Cell cycle time / mins	14.4 \pm (0.85)	218	207 (+8 -13)	881 (+29 -75)
	310 \pm (40)			
Width / μm	188.4 \pm (26.4)	3.9	3.9 (\pm 0.15)	3.8 (\pm 0.15)
	228*			
	148 \pm (16)			

The growth parameters were screened and reduced from a possible 11 to the 6 phenotype parameters presented above:

1. Length at t_0 / μm ;
2. Width at t_0 / μm ;
3. Lag Period / mins
4. Birth Length(L_b) / μm ;
5. Growth rate / $\mu\text{m min}^{-1}$;
6. NETO

The parameters calculated here are more representative of the population as using the Lensless microscope no user collection or measurement bias is introduced. The number of cells analysed in the published data sets varies from 12 to 200^[4,19,22,46] with an average of 98, further supporting the N choice of 100 cells in these preliminary screening experiments. Cell growth phenotype parameters are not expected to be normally distributed unless the simplest phenotype associated with single random fluctuations in the concentrations is observed. Normal distributions come from random fluctuations no biased outcome favouring growth or a set of parameter such as length or capacity to resist the silver stress. Cell growth events are not random and each cell deposited on the flow cell in these experiments has a unique combination of proteins and is at a different phase of the growth cycle, the fact that the growth parameters do not give rise to normal distributions is to be expected and explains the 98 % survival during environment transfer.

The effect that silver has on the proteins within the cell has been discussed briefly here and at length in Chapter 1. It has been highlighted that the vulnerability of a cell to silver is linked to the reactivity of the silver ion to the amino acid cysteine, specifically the sulphur containing thiol group. The specific proteins which control the *S. pombe* cell cycle have been described above and we now link these proteins to the action silver might have on them to describe the change in phenotype induced by silver stress. Each of the 11 growth phenotype parameter distributions will now be considered in turn.

Cell Length and Width at t_0

Cell length and width at t_0 of the wild type control sample have been discussed in chapter 2, have been used to verify this Lensless microscope pattern analysis technique^[39] and are further discussed here.

The width does not change with silver stress and this is expected due to the high level of control that exists in the *S. pombe* width parameter^[42]. The width of the cell is already determined by the time

the cells are exposed to silver and it appears that once set the structure will not change. However as the cells begin to grow the structural integrity may be lost. The width over time may be something to further to analyse. If this indeed were the case then it would account for the shorter division length at division for cells grown in the presence of silver, if division is governed by a threshold protein concentration related to volume as opposed to cell length. The volume of a cell as a phenotype is described in equation (1). The higher the cell volume the higher the number of proteins in a cell and possibly the better able the cell is to overcome environmental stress.

The length of cells deposited on the surface in the silver stress experiment is the same distribution as the length of the cells at t_0 in the control sample, as expected as cells are taken from log phase of growth in a planktonic culture prepared in the same way with the same clone of cells in the same nutrient conditions each time. The cells which survive are from the centre of the length distribution, the upper quartile (top 25 %) and the lowest decile (10 %) of the distribution are not viable under the silver stress, the extremes of the sample die/enter G_0 , a stable dormant state^[37].

Cells which are close to passing the START check point, either because they have just divided or are just about to divide, do not pass this checkpoint in the presence of silver. The protein, Cdc2, which is implicated in the initiation of mitosis and the control of entry to both S and M phase, contains three cysteine residues^[20], and therefore 3 points of vulnerability to silver. As Cdc2 controls the cell progression around the cycle at G_1 and at G_2 , it controls the growth of cell lengths at the two extremes of the distributions. The cells which have not entered S-phase will not be able to without Cdc2 and cells which have finished the growth phase of G_2 and reached their final linear length will not be able to enter M-phase without Cdc2. It suggests that cells which have an immediate requirement for Cdc2 on exposure to silver ions will not survive, as the protein is silver-labile. The mechanism is at its most vulnerable when the cells are at the extremes of length, the MIC is much lower for cells at this point than at any other stage of the cell cycle, indicating a G_0 phenotype.

It is not possible using this measurement technique, however, to determine whether the cells which have not grown are not viable or dormant. Although not yet documented in *S. pombe* it is possible that a proportion of the cells which show no growth characteristics beyond initial characterisation, are not dead but in a state much like that of the bacterial persister cell.

Lag Period

The median lag period observed here is 150 minutes for the control sample with a skew towards the longer lag times. A skewed phenotype can be associated with a differential ability to adapt to new surroundings. Based on previous statements it can be hypothesised that a time of 2.5 hours is taken

for the cell to adjust to very similar environments as previously, on transfer from exponential phase growth in YE5S to YE5S in the flow cell. The cells are taken from the exponential phase of growth and this, coupled with microscope images (Chapter **Error! Reference source not found.**), verify that the cells are of good structural integrity although osmotic stress cannot be ruled out. The lag period in *S. pombe* is rarely studied, there are no published studies. Studies on the induction on genes in brewing yeasts in the lag and early exponential phases of the cell cycle showed that during this time the gene for an enzyme implicated in nucleotide biosynthesis *Ade17p* is up-regulated and subsequently deregulated before the end of the lag period^[43]. One gene in *S. pombe* which is involved in nucleotide biosynthesis belongs to the *thi* family for the biosynthesis of thiamine^[44], is the *thi4* and it codes for 9 cysteine residues - 9 points of vulnerability within the protein. Additionally proteins with more than one cysteine residue, can be structurally modified by silver ions by bonding one thiol residue to another to create additional disulphide bridges^[10]. It has been empirically measured to be approximately two hours in planktonic growth.

The lag period has a median of 150 minutes in the control and under silver stress conditions has a median length of 1518 minutes, over 10 times longer. Drawing on what is known from the bacterial lag phase, it is thought to be the period of time, before the exponential growth phase, in which the bacterium is adjusting to the new environmental conditions^[45], repairing oxidative damage and developing intracellular macromolecular stores^[46]. Analysis performed on bacterial cells during the lag period has shown that these cells are metabolically active. Lag time length in bacteria is said to be influenced by a number of factors, increasing in length with reduced inoculum size, poor physiological cell state and a vast gulf between the nutrient conditions of the new and existing cell growth environments^[47].

We can assume that the silver stress phenotype requires 10 times longer than the control phenotype to adjust to the conditions in which it finds itself, not only is the cell acclimatising to a change in nutrient conditions but also the detrimental effects the nutrient change has. The silver stress does not just affect the cell at the start of the growth curve but continues to throughout cell extension. The distribution of lag period indicates directly there is a range of phenotypes associated with the ability to adjust to the change of the environment from the broth culture to the surface.

It can be proposed that the cells with the shortest lag times have a set of proteins or enzymes that is best suited to rapid preparation of growth under the new conditions. Broadly, this may attributed to the lower quartile of the distribution. If the short lag period indicated an ability to grow faster, then the cells in the lower percentile of the lag period would appear in the upper percentile of the distribution of growth rates. This relatedness is a cell phenotype, by analysing the data this way, and

comparing it to the same analysis in the silver stressed distributions we can demonstrate if and when silver disrupts *S. pombe* growth.

L_B

The length at cytokinesis is another parameter distribution which is shifted under silver stress. L_B is half the length at cytokinesis, corrected using the 1.11 correction factor for two dividing cells^[48] and tells us the predicted length at birth. The average (mean in the literature) length at birth is expected to be between 7 and 8 μm ^[4] and found to be true in both the silver stress and control samples. The control sample distribution of L_B is skewed towards the long lengths (Skewness 1.5) and the silver stress distribution is skewed towards the short lengths (-0.32). As opposed to hypothesising that the cells which skew the control conditions were in the upper quartile of the distribution at birth it is thought that these cells divide long. This identifies a group of cells with a phenotype susceptible to significantly long growth prior to division. One possible explanation for the long division length distribution was thought to be that the cells arrived on the surface at a length close to cytokinesis and so grown past a 'normal' length. It has been reported by others^[35] that these cells which grow far past the median length expected take more than one cell cycle to adjust and return to a dividing length within the range expected because the cell cycle of *S. pombe* can only be shortened by $1/4$ ^[35].

Both the tables of correlation coefficients and subpopulation analyses show that while some cells which are in the top 5th percentile for length on arrival at the surface are "long dividers" there is not a strong correlation between length at t_0 minutes and length at cytokinesis. Miyata *et al.* showed in 1978^[49] that the average length at plate formation was tightly controlled between 12 and 15 μm , with a mean length at formation of 13.4 μm . The distribution had outliers defined as small as 10.5 μm and as large as 16.5 μm , verifying that there are outliers in the distribution. The range of the distribution of the L_B parameter of the control sample is 4.2 μm , the range of the distribution under silver stress is 2.5 μm . The environmental shift reducing the range of predicted birth lengths by 40%. The unknown mechanism by which the cells extend past the average maximum length range is inhibited by the silver ion. The effect that silver has on the cell cycle as a whole is an accumulation of the disruption of all the cell processes, and the ability of the cell to overcome that is reflected in the time the cell takes to complete a full round of division.

Cell Cycle

In this chapter we have defined the cell cycle using equation (2). This is based on the assumption that the length of time between the commencement of linear extension in the flow cell and the time of cell division is a fraction of the time the cell spends in the cell cycle. To calculate total cell cycle

length, the time period ($t_A - \lambda$) can be adjusted for the ratio between birth length and length at 0 minutes. This equation can be rearranged to give us equation (3) for t_{cell} :

$$t_{cell} = \frac{(t_A - \lambda)}{l/L_B} \quad (3)$$

The published cell cycle length in wild type *S. pombe* at 25°C is approximately 3.1 (± 0.44) hours^[5, 6], calculated for 88 cells. The length of t_{cell} , conventionally calculated using time-lapse optical images[4]^[35], [34]. The cell cycle here has a median length determined by equation 2 is 207 (+8 -13) minutes, 3.4 (+0.1 -0.2) hours, for $N = 100$ cells. Taking into account the error on both of these measurements it can be concluded that these cell cycle time measurements are the same, confirming for the first time the cell cycle length is related to the birth length. The relationship between birth length and cell cycle length can be described as the length as a proxy for concentration as discussed above. For example, the longer the birth length, the higher the levels of proteins within the cell and the shorter the resulting time to complete the cell cycle and vice versa. The range of the t_{cell} distribution is interesting, it is thought that the length of G₂ in *S. pombe* is non-variable in length, when the cell cycle needs to adjust to cells which have grown past the normal length range it can only be shortened by ¼, often taking 2 or 3 cycles to reach normal cell lengths at division^[35]. These results show that this previous observation is not the case.

It has been reported that the cell cycle control can be reduced to the action of 7 proteins or protein complexes, Slp1, Cdc2, Cdc13, PP1, APC/C, and Cdc25 along with Wee1^[19]. As discussed previously each of these proteins or complexes contain one or more cysteine residue. This means that the cell cycle is vulnerable from silver attack at every stage, at the S-phase check point with Cdc2, during polarised growth and anaphase with PP1 and the APC/C complex respectively and numerous initiators and controllers of mitosis. The role of PP1 in the cell cycle and controlling cell polarity is of increased interest when we report that of the $N = 100$ cells analysed under silver stress conditions none of them displayed the rate changing point of NETO.

Cells subjected to silver stress do not display a RCP in the linear extension phase of growth, Figure 3.4. The Lensless microscope method coupled with the image processing algorithm developed here only records the overall changes in length and does not record the features that are present on the image such as septation. It is not possible therefore to distinguish between single end growth and slow growth at one end. There are two considerations:

1. The cell polarity mechanism is damaged by the silver ion, the new end does not take off

2. The new end commences growth but the rates of growth are not determined by the Lensless microscope.

The cell polarity, as discussed previously, is controlled by a number of proteins^[6], the damage of any of which will cause the polarity changes to be lost, , to occur much later or to distort the shape of the cell beyond the rod shape. We have shown previously that the PP1 sequence contains cysteine residues, and the recruitment of PP1 to the cell tip is important for the regulation of polarised growth^[29]. Another protein involved in NETO Tea1p, of which knockout mutants grow but in a monopolar fashion, contains 7 cysteine residues in its amino acid sequence^[26]. Either of these processes could therefore be disrupted by the ongoing presence of silver ions in the environment.

It is, however, more likely that the cell does undergo NETO, the new end does start growing, but the change in rate is so small that it is within the detection noise and so not detectable by diffraction pattern analysis. This could have been verified by staining mid-G₂ cells with calcofluor, using a method such as the one described by Calonge *et al.* in 2000^[50]. This stain stains the septal material and cells walls, as the cell divides the two new ends are left with dark scar tissue, which remains at the tip of the cell until this end starts to grow. Cells which have never grown from this new end will all have one dark tip^[5].

Average Growth Rates

The rate of cell growth is related, in part, to the cell cycle with the median rate of growth decreasing by over 5 times from 0.027 (± 0.003) $\mu\text{m min}^{-1}$ to 0.005 (± 0.001) $\mu\text{m min}^{-1}$ under silver stress. This reduction in growth rate is to be expected as each of the 7 key cell cycle control proteins are silver labile and so are likely to be affected at some level by a silver containing growth environment. It is to be noted that this is the only distribution in which the silver stress phenotype has a narrower range than the control sample. This could be due to device measurement limitations, the Lensless microscope set-up, due to the diffraction limit, does not have the capability to measure the more discrete changes in rate which may occur when the cells are growing so slowly. The more interesting cell phenotype growth rates are those of NETO.

NETO

The NETO parameters distributions are well determined for the control sample and show a median time to NETO of 78 (+10 -7) minutes and a modal ratio of fast to slow growth rates of 1.35. The average percentage of cell growth rate increase has been published as 30 % but the skewed phenotype of ratios has not been observed before. There is an upper length to the cells length at t0 which shows NETO of 9.8 μm , at the upper limit of the published values of length range 9 –10.4 μm

published for NETO^[5, 6], observed in a distribution of 44 cells. In wild type cells, the NETO event is thought to be controlled by the cell cycle and the septation events, figure whatever, typically within 35 % of the start of the cell cycle and a cell size of above 9 μm ^[51].

S. pombe Growth Phenotypes under normal and Aq-stressed growth conditions

In conclusion there are a potential six growth phenotype parameters for *S. pombe* derived from both the silver and normal growth conditions. Analysis of these parameter distributions indicates a number of growth phenotype classifications:

- G_0 phenotype;
- Long length at division (L_B);
- Modal quartile of lengths at t_0 survive silver stress;
- A ratio of NETO rates larger than 1.35;
- NETO not apparent in silver stress distribution;
- Lag period length skewed towards longer recovery times;
- Long length at t_0 leads to long length at division

3.5 Conclusion

This chapter aimed to determine whether there are growth parameters within the control growth sample which indicate that there may be phenotypes within the data. All parameters showed distributions that were non-normal but not bimodal; phenotype is therefore only defined as the relative position in a distribution. In terms of the length at t_0 there is a survival phenotype based on position in the distribution. It appears that cells in the lower 10 % and upper 25 % of the length distribution do not grow, position of the cell in the distribution indicating viable entry into the subsequent growth cycles.

The distribution for L_B is skewed towards long length at birth. The length at birth is reported to be conserved to be between 6 and 8 μm with no known mechanism published to explain a reason for cells growing significantly longer than the median of the distribution. This conclusion therefore alerts us to the fact that the “long dividing” phenotype is not an advantageous phenotype and those cells which display it are less able to respond to a hostile environment. The range of phenotypes under silver stress is greater compared to the median of the control however compared to its own median the range is narrower. Relatively, silver stress slows down every cell process, distributions are more spread, perhaps, because an accumulation of proteins which would ordinarily take 1 minute takes 10 minutes in silver stress.

Further, phenotypes identified in this chapter are growth related changes which may, in planktonic growth, be masked by the bulk changes of the population. Some of these phenotypes have a low prevalence, the long L_B phenotype occurring in 9 % of the population. The Lensless microscope can be used as a screening method to identify the individuals with different phenotypes which can then be selected for molecular level investigation.

Silver stress significantly changes the growth phenotype of *S. pombe*. The length of the lag period, the time the cell takes to adjust to new environmental conditions, is increased by over 10-fold, the rate of growth reduced over 5 times and the cell cycle time, t_{cell} , increased by over 4 times. More subtly cells, with short or long cell cycles, in the upper and lower quartiles or tails of the data are more likely to be effected by the change in environmental conditions at the introduction of silver nitrate, reflected in the length at t_0 distribution compared with the length at t_0 of the cells which survive.

Generally, the distributions produced from cells under silver stress tend to approximate to a normal distribution are less prone to outliers and less skewed. Outliers are therefore more generally different phenotypes compared with the averages to the normal wildtype expression set, the hostile silver environment is a filter for phenotype. These outliers, while they may appear favourable, are not present in the distributions of the surviving cells under silver stress, implying that these either require more energy than absolutely necessary for cell survival (L_B) or that they are, in the expression of a different gene set, more vulnerable to the effects silver has on cysteine residues in proteins.

The significant change in the cell cycle length implies that the silver stress environment is not something that the cell manages to overcome during the lag period. The cell does not build up an immunity or resistance to the silver and it continues to cause disruption to the essential proteins of *S. pombe* growth and division.

3.6 References

1. Forsburg, S.L. and P. Nurse, *Cell cycle regulation in the yeasts Saccharomyces cerevisiae and Schizosaccharomyces pombe* Annual Review of Cell Biology, 1991. **7**: p. 227.
2. Wood, V., et al., *The genome sequence of Schizosaccharomyces pombe*. Nature, 2002. **415**(6874): p. 871-880.
3. Smith, C.L., et al., *An electrophoretic karyotype for Schizosaccharomyces pombe by pulsed field gel electrophoresis*. Nucleic Acids Research, 1987. **15**(11): p. 4481-4489.
4. Baurngartner, S. and I.M. Tolic-Norrelykke, *Growth Pattern of Single Fission Yeast Cells Is Bilinear and Depends on Temperature and DNA Synthesis*. Biophysical Journal, 2009. **96**: p. 4336.
5. Mitchison, J.M. and P. Nurse, *Growth in the Cell Length in the Fission Yeast Schizosaccharomyces Pombe*. Journal of Cell Science, 1985. **75**: p. 357.
6. Martin, S.G. and F. Chang, *New End Take Off: Regulating Cell Polarity during the Fission*. Cell Cycle, 2005. **4**(8): p. 4046-4049.
7. Gupta, A., M. Maynes, and S. Silver, Applied and Environmental Microbiology, 1998. **64**: p. 5042-5045.
8. van Montfort, R.L.M., et al., Nature, 2003. **423**: p. 773-777.
9. Wouters, M.A., S.W. Fan, and N.L. Haworth, . Antioxidants & Redox Signalling, 2010. **12**: p. 53.
10. Davis, R.L. and S.F. Etris, Catalysis Today, 1997. **36**: p. 107.
11. Leung, B.O., et al., *Silver(I) Complex Formation with Cysteine, Penicillamine, and Glutathione*. Inorganic Chemistry, 2013. **52**(8): p. 4593-4602.
12. AshaRani, P.V., et al., *Cytotoxicity and Genotoxicity of Silver Nanoparticle in Human Cells*. American Chemical Society Nano, 2009. **3**(2): p. 279.
13. Haase, A., et al., *Toxicity of silver nanoparticles in human macrophages: uptake, intracellular distribution and cellular responses*. Journal of Physics: Conference Series, 2011. **304**(1): p. 012030.
14. Liu, P., et al., *Toxicity of nano- and micro-sized silver particles in human hepatocyte cell line L02*. Journal of Physics: Conference Series, 2011. **304**(1): p. 012036.
15. Hogan, D.A., *Talking to Themselves: Autoregulation and Quorum Sensing in Fungi*. Eukaryotic Cell, 2006. **5**(4): p. 613-619.
16. Nurse, P., P. Thuriuax, and K. Nasmyth, *Genetic control of the Cell Division Cycle of the Fission Yeast Schizosaccharomyces pombe*. Molecular Genetics and Genomics, 1976. **146**: p. 167.
17. Rhind, N. and P. Russell, *The Schizosaccharomyces pombe S-Phase Checkpoint Differentiates Between Different Types of DNA Damage*. Genetics, 1998. **149**(4): p. 1729-1737.
18. Rowley, R., S. Subramani, and P.G. Young, *Checkpoint controls in Schizosaccharomyces pombe: rad1*. The EMBO Journal, 1992. **11**: p. 1335.
19. Anbumathi, P., S. Bhartiya, and K.V. Venkatesh, *Quantitative Analysis of a Dynamic Cell Cycle Regulatory Model of Schizosaccharomyces pombe*. Current Synthetic and Systems Biology, 2013. **1**(1): p. 1-7.
20. Hindley, J. and G.A. Phear, *Sequence of the cell division gene CDC2 from Schizosaccharomyces pombe; patterns of splicing and homology to protein kinases Gene*, 1984. **31**: p. 129-134.
21. Aves, S.J., et al., *Cloning, sequencing and transcriptional control of the Schizosaccharomyces pombe cdc10 'start' gene*. The EMBO Journal, 1985. **4**: p. 457.
22. Turnbull, E.L., I.V. Martin, and P.A. Fantes, *Activity of Cdc2 and its interaction with the cyclin Cdc13 depend on the molecular chaperone Cdc37 in Schizosaccharomyces pombe*. Journal of Cell Science, 2006. **119**(2): p. 292-302.
23. Carlson, C.R., et al., *Regulation of the start of DNA replication in Schizosaccharomyces pombe*. Journal of Cell Science, 1999. **112**(6): p. 939-946.

24. Chandra, A., et al., *Cdc13 both positively and negatively regulates telomere replication*. *Genes & development*, 2001. **15**(4): p. 404-414.
25. Kovelman, R. and P. Russell, *Stockpiling of Cdc25 during a DNA replication checkpoint arrest in Schizosaccharomyces pombe*. *Molecular and Cell Biology*, 1996. **16**(1): p. 86-93.
26. Stanford_University. *Saccharomyces Genome Database:SLP1/YOR154W Protein Information*. 2013 [cited 2013 8th December]; Available from: <http://www.yeastgenome.org/cgi-bin/protein/proteinPage.pl?dbid=S000005680>.
27. Singer, R.A. and G.C. Johnston, *Indirect suppression of the wee1 mutant phenotype in Schizosaccharomyces pombe*. *Experimental Cell Research*, 1985. **158**(2): p. 533.
28. Perry, J. and S. Kornbluth, *Cdc25 and Wee1: analogous opposites?* *Cell Division*, 2007. **2**(1): p. 12.
29. Alvarez-TabarÃ©s, I., et al., *Schizosaccharomyces pombe protein phosphatase 1 in mitosis, endocytosis and a partnership with Wsh3/Tea4 to control polarised growth*. *Journal of Cell Science*, 2007. **120**(20): p. 3589-3601.
30. Acquaviva, C. and J. Pines, *The anaphase-promoting complex/cyclosome: APC/C*. *Journal of Cell Science*, 2006. **119**(12): p. 2401-2404.
31. Oliva, A., et al., *The Cell Cycle Regulated Genes of Schizosaccharomyces pombe*. *PLoS Biol*, 2005. **3**(7): p. e225.
32. Peng, X., et al., *Identification of Cell Cycle-regulated Genes in Fission Yeast*. *Molecular Biology of the Cell*, 2005. **16**(3): p. 1026-1042.
33. Rustici, G., et al., *Periodic gene expression program of the fission yeast cell cycle*. *Nat Genet*, 2004. **36**(8): p. 809-817.
34. Nurse, P., *Genetic control of cell size at cell division in yeast*. *Nature*, 1975. **256**: p. 548.
35. Fantes, P.A., *Control of Cell Size and Cycle Time in Schizosaccharomyces pombe*. *Journal of Cell Science*, 1977. **24**: p. 51.
36. Sveiczer, A., B. Novak, and J.M. Mitchison, *The size control of fission yeast revisited*. *Journal of Cell Science*, 1996. **109**: p. 2947.
37. Su, S.S.Y., et al., *A nitrogen starvation-induced dormant G0 state in fission yeast: the establishment from uncommitted G1 state and its delay for return to proliferation*. *Journal of Cell Science*, 1996. **109**: p. 1347.
38. Moreno, S., A. Klar, and P. Nurse, *Molecular Genetics Analysis of Fission Yeast Schizosaccharomyces pombe*. *Methods in Enzymology*, 1991. **194**: p. 795.
39. Penwill, L.A., et al., *Growth Phenotype Screening of Schizosaccharomyces pombe using a Lensless microscope*. *Biosensors and Bioelectronics*, 2014. **54**: p. 345.
40. Castagnetti, S., *Preliminary Planktonic S.pombe Growth in the presense of Silver Nitrate*, L.A. Penwill, Editor. 2013.
41. Andrews, J.M., *Determination of minimum inhibitory concentrations*. *Journal of Antimicrobial Chemotherapy*, 2001. **48**(suppl 1): p. 5-16.
42. Kelly, F. and P. Nurse, *Spatial control of Cdc42 activation determines cell width in fission yeast*. *The American Society for Cell Biology*, 2011. **22**(20): p. 3801.
43. Brejning, J., N. Arneborg, and L. Jespersen, *Identification of genes and proteins induced during the lag and early exponential phase of lager brewing yeasts*. *Journal of applied microbiology*, 2005. **98**(2): p. 261-271.
44. Zurlinden, A. and M.E. Schweingruber, *Cloning, nucleotide sequence, and regulation of Schizosaccharomyces pombe th14, a thiamine biosynthetic gene*. *Journal of Bacteriology*, 1994. **176**(21): p. 6631-6635.
45. Rolfe, M.D., et al., *Lag Phase Is a Distinct Growth Phase That Prepares Bacteria for Exponential Growth and Involves Transient Metal Accumulation*. *Journal of Bacteriology*. **194**(3): p. 686-701.

46. Rolfe, M.D., et al., *Lag Phase Is a Distinct Growth Phase That Prepares Bacteria for Exponential Growth and Involves Transient Metal Accumulation*. Journal of bacteriology, 2012. **194**(3): p. 686-701.
47. Swinnen, I.A.M., et al., *Predictive modelling of the microbial lag phase: a review*. International Journal of Food Microbiology, 2004. **94**(2): p. 137-159.
48. Mitchison, J.M. and P.M. Walker, *RNA synthesis during the cell life cycle of a fission yeast Schizosaccharomyces pombe*. Experimental Cell Research, 1959. **16**: p. 49.
49. Miyata, H., M. Miyata, and M. Ito, *The Cell Cycle in the Fission Yeast, Schizosaccharomyces pombe*. I. Relationship between Cell Size and Cycle Time. Cell Structure and Function, 1978. **3**(1): p. 39-46.
50. Calonge, T.M., et al., *Schizosaccharomyces pombe Rho2p GTPase Regulates Cell Wall β -Glucan Biosynthesis through the Protein Kinase Pck2p*. Molecular Biology of the Cell, 2000. **11**(12): p. 4393-4401.
51. Forsburg, S.L., *Comparison of Schizosaccharomyces pombe expression systems*. Nucleic Acids Research, 1993. **21**(12): p. 2955-2956.

4 *Escherichia coli* Colony Growth Phenotypes under Optimal and sub lethal silver stress conditions.

4.1 Introduction

This chapter focuses on the growth phenotypes of the model Gram negative prokaryote *Escherichia coli* to silver stress. The growth dynamics of single cells are only a small part of the growth phenotype which is now dominated by colony growth. The transcriptome-level response of *E. coli* to silver stress had been studied previously^[1, 2] and now the growth phenotypes which arise from control and silver stress growth environments are compared.

E. coli is a rod-shaped, Gram negative bacterium which divides by binary fission to form two genetically identical daughter cells. The cell grows longitudinally from each pole, with very little change in the cell width^[3]. However, there is some evidence to suggest that in periods of rapid growth the cell becomes thinner, but returning to its original thickness upon division^[4]. The cells are typically 2 μm in length^[5] and between 0.5 and 1 μm in width^{[6],[7]}, with an average cell volume^[8] of 0.6-0.7 μm^3 .

The strain of *E. coli* used here is a derivative of *E. coli* K-12, and is referred to as MG1655. The genome was sequenced in 1997 and reported to contain 4,639,221 base pairs, with 4288 protein-coding genes, 38 % of which have no known function^[9]. The genome was updated in 2006, reporting discrepancies of < 1 bases in 13,000 in the initial sequencing and a genome size of 4,639,675 base pairs^[10] contained in one circular chromosome. Stress responses in *E. coli* have been well characterised and the response of the cell to osmotic stress^[11], oxidative stress^[12] and heat shock^[13] are all well documented. Each of these stress responses demonstrates an up-regulation of a different subset of genes, conferring a phenotype in order to survive in the environment in which they find themselves; “The life of a bacterial cell is feast or famine. To survive the bacterium must rapidly adapt to changing environmental conditions”^[14]. It is these environment-driven phenotype changes that will be studied in this chapter.

The identification of the 7 key cell cycle control proteins in *S. pombe* led to the identification of stages of cell cycle arrest and the prediction of growth phenotypes associated with the vulnerable phases of the eukaryotic cell cycle when exposed to silver stress. Knowledge of the proteins and

processes involved in the control of the cell cycle will lead to understanding of the changes in phenotype the bacteria may exhibit. Of the proteins encoded by the *E. coli* genome, 85% contain cysteine and therefore 85% of the proteins will be susceptible to disruption on exposure to silver. The phenotype parameters measured here are the reflection, on the growth level of the cell's proteins at the molecular level, and how these levels influence subsequent growth.

4.2 *E. coli* Cell Cycle

The bacterial cell cycle is conventionally divided into three stages; the B-period, the time between birth and chromosome replication initiation, the C-period, the time it takes to replicate the chromosome, and the D-period, the time between chromosome replication completion and cell division^[14], Figure 4.1. The cells divide at a maximum reported growth rate approximately every 20 minutes.

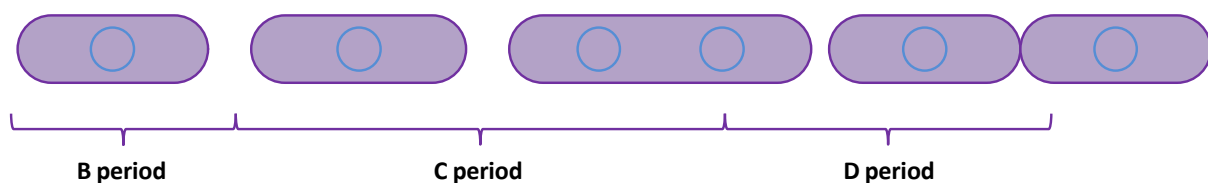


Figure 4.1 A simplified representation of the *E. coli* cell cycle from birth at the start of the B period, through the initiation of chromosome replication at the beginning of the C period to the termination of the DNA replication and the initiation of cell division at the junction between C and D periods. The cells are depicted as purple rod shapes, the singular chromosome as a blue ring. [Figure adapted from reference ^[14]].

The start of the cell cycle and so the start of metabolic cell control of division occurs at the initiation of chromosome replication^[15]. The initiation of chromosome replication occurs when DnaA binds to the origin of replication, OriC, the highly conserved segment of DNA that is able to promote *E. coli* specific initiation of replication^[16, 17]. The binding of DnaA causes the DNA at the site of replication^[17] to unwind, so beginning the binding of the replication machinery^[14] and the start of chromosome replication is dependent upon DnaA concentration. The fact that replication is controlled by DnaA is reinforced by studies showing increased concentrations of DnaA leads to over-initiation^[18] and studies blocking DnaA synthesis inhibiting chromosome replication^[19]. The *diaA* gene encodes for a the 196 amino acid long DnaA protein, which contains 4 cysteine residues^[20] and synthesis of which is initiated by the decrease in concentration of nucleotides^[15]. Therefore, initiation of chromosomal replication is coupled to the nutrient conditions surrounding the bacteria^[14]. It has also been shown that this major cell cycle control point is controlled by a cell mass and cell growth rate. The accumulation of DnaA is growth rate dependent; levels sufficient to initiate replication are achieved at the 'initiation mass'^{[22],[23]}.

DNA replication in *E. coli* begins at the single origin (OriC) and proceeds bi-directionally around the circular chromosome^[17]. The process of chromosome elongation is heavily reliant on the presence of nucleotides, the pool needing to be constantly replenished^[14]. The synthesis of nucleotides is, in part, controlled by ribonucleotide reductase, R1^[15]. The radical-based reaction involving synthesis involves five cysteine residues, two redox-active, two at the carboxyl end of the protein and one initiator of the reaction^[24]. The rate of chromosome replication, therefore, is reliant on the rate of nucleotide synthesis, controlled by the presence of ribonucleotide reductase R1. The completion of the round of DNA replication is the point at which the cell is committed to division^[25]. As stated previously, at optimum conditions the generation time of “fast-growing” *E. coli* cells is approximately 20 minutes, but the time taken for chromosome duplication in these same conditions can be up to 40 minutes^[26].

Fast growing cells are defined as such by the fact that their mass doubling time is less than the length of time taken to proceed through the C and D period of the cell cycle^[14]. The current explanation for the apparent paradox is rapidly growing bacterial cells appear to begin a round of DNA replication before the first replication is complete^[27]. Cooper and Helmstetter^[28] show that, using the concept of multi-fork replication, each new, partially replicated chromosome initiates another round of replication before the old one has completed during rapid cell growth, Figure 4.2.

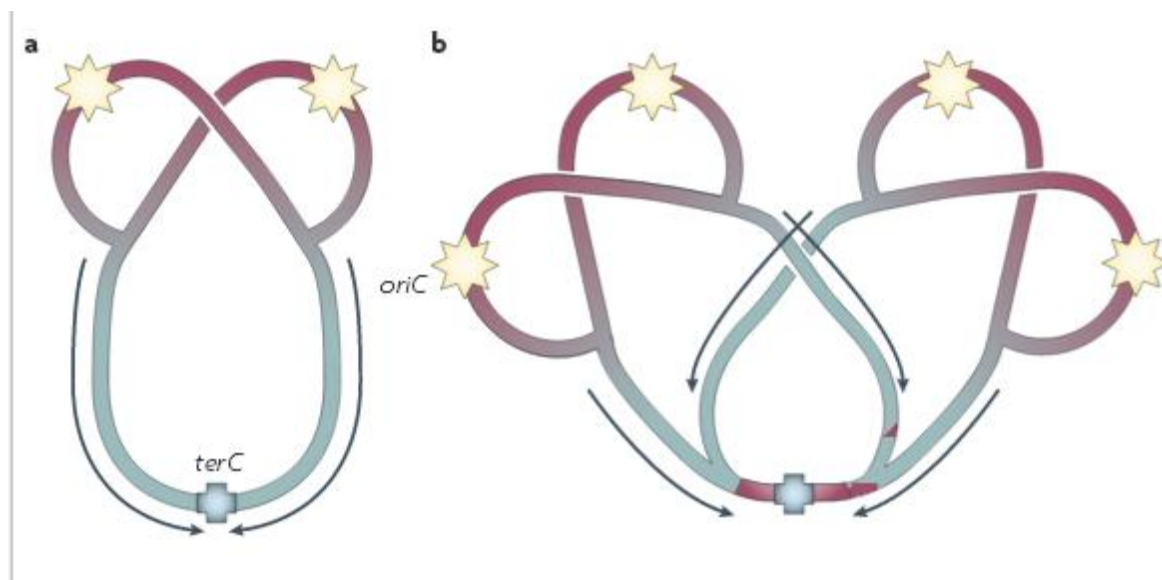


Figure 4.2 Chromosome replication in *E. coli*. a. displays the typical chromosome replication of a cell which has a mass doubling time of longer than the length of time that cell takes to complete C and D phase and b. displays the multi-fork replication of the chromosome which occurs in fast growing *E. coli* cells [Reproduced with permission^[14]].

Under conditions where the C period is longer than the cell mass doubling time, the cells may have numerous copies of the chromosome close to the OriC origin but only one copy of the chromosome near the terminus of replication^[29]. The initiation of replication relies on a threshold level of DnaA,

and the level of DnaA is controlled by the nutrient conditions of the environment and the cell growth rate, the multifork replication model appears feasible^[30]. The bidirectional replication of the chromosome is halted by three separate termination regions. The region *terC1* has the ability to stop the anticlockwise replication fork from proceeding further than a position of 180° from *oriC*, the clockwise replication is terminated by the regions *terC2* and *terC3*^[31]. Segregation of the chromosomes following replication termination acts as a checkpoint for the cell, in conditions of nutrient stress the high levels of small nucleotide complexes cause replication to terminate immediately prior to segregation^[32]. Following successful chromosome segregation the cell can proceed into division.

Cell division is controlled by the group of *fts* genes. Specifically the FtsZ protein forms a plate, indicating the division plane, and recruits other proteins, including FtsA forming a complex which ultimately forms the septum^[33]. For division to occur there is a ratio of FtsZ and FtsA which must be recognised. Dai & Lutkenhaus show that cells with high levels of FtsZ are division inhibited, a situation which can be overcome by increasing levels of FtsA and vice versa^[34]. The protein FtsA is 420 amino acids long, 9 of which are cysteine residues, the FtsZ protein consists of 383 amino acids but not one cysteine residue^[20].

The *E. coli* cell cycle has been shown to be heavily nutrient reliant, the initiation of chromosome replication inhibited strongly in conditions of nutrient stress. The bacterial growth observed in this chapter is that of small colonies. This growth is therefore influenced by the growth of neighbouring cells, reminiscent of the growth in biofilms, discussed previously. Single cells have their own individual phenotypes, a colony of cells has the potential to take the favourable elements of each member, producing a stronger phenotype as a community. The combination of organisms working synergistically, creating an environment more favourable to their survival, forming an extended phenotype.

4.3 *E. coli* colonies as a multicellular organism

Whilst bacteria in the laboratory are grown under controlled conditions and so have the variables of temperature and osmolality tightly controlled, there are other variables which cannot be experimentally controlled; pH and nutrient availability, for example, within the microenvironment variations, dominating growth. Bacteria have adapted phospho-relay systems to allow them to sense and respond to environmental factors, up or down regulating genes accordingly^[35]. Environmental factors can include proteins expressed by bacteria in close proximity and as discussed previously studies have shown that bacteria growing in a biofilm, a community of bacteria on a solid surface encased in an exo-polysaccharide matrix, have an increased resistance to antimicrobial agents,

specifically these are dangerous in infection scenarios^[36]. The study of susceptibility to metal toxicity has shown that biofilms are between 2 and 64 times less susceptible to metal toxicity than the equivalent cells in planktonic growth^[37, 38]. The bacteria within a biofilm are vulnerable to influence by other bacteria in the same matrix. One form of bacterial communication relevant to the biofilm/colony state is called quorum sensing and enables the control of gene expression in a bacterial colony in response to the changing cell density^[39]. Quorum sensing is used to explain how biofilms form, to distinguish between like cells and intruders, and to initiate whole colony death^[40].

The chapter aims to determine the phenotypic growth changes within a colony derived from a single cell grown under control conditions and silver stress conditions. I also aim to determine the phenotypic shift between growth in the control environment and growth in the silver stress environment. The reaction of silver with cysteine-containing proteins has been discussed in chapter 1, and the effect on the eukaryotic cell cycle demonstrated in chapter 3. The effect of silver ions on the *E. coli* transcriptome has been previously analysed^[1, 2] and is discussed below.

4.4 Response to Silver Stress

The response of prokaryotic cells to silver stress is of particular interest to the medical industry, with silver ions present in wound dressings^[46] and as a surface coating for implanted medical instruments^[47, 48]. Silver is used in medical devices in an attempt to prevent microbial attachment which can lead to the promotion of infection at the site of insertion^[49] and as an antimicrobial agent in circumstances where infections have become antibiotic resistant^[46]. Silver ions are known to possess a broad spectrum of antimicrobial properties, and have been conventionally reported to have no detrimental effects on normal mammalian cells^[50], although the findings in chapter 3 appear to contradict this. Silver ions are shown to slow bacterial growth and inhibit subsequent cell divisions, increase membrane permeability and *E. coli* cells under silver stress appear to undergo morphological changes^[51].

The phenotypic changes which occur in a planktonic *E. coli* suspension when exposed to silver stress have been observed on a molecular level^[1, 2]. These studies show that post treatment with silver ions there is a down-regulation of genes related to transcription and translation, indicating a slowing of protein synthesis. The genes which are up-regulated in these studies include the ones implicated in sulphur metabolism, protein unfolding and iron-sulphur cluster assembly^[2]; in total 497 genes are differentially regulated within 10 minutes.

4.5 Aims and Objectives.

This chapter aims to explore the growth phenotype of single cells and small colonies of the model Gram negative organism *Escherichia coli* K-12 MG1655 under controlled growth conditions and silver

stress conditions. The growth parameters will be extracted and the phenotypes characterised arising from both the normal growth conditions and as a result of growth in the presence of silver ions. These parameters will be identified using the distribution analysis techniques discussed in Chapter 2. Colonies displaying different growth phenotypes under the influence of silver stress will be sequenced and genotypically compared to a control sample and the known genomic sequence of *Escherichia coli* K-12 MG1655. The comparison process determining whether favourable changes in growth are genotypic or phenotypic.

4.6 Materials and Experimental Methods

The Lensless microscope detailed in Chapter 2 was used without further modification to the optics and image collection protocol. The flow cell surface, previously a lectin surface, was replaced with a layer of Matrigel (BD-Biosciences) in the experiments for *E. coli* growth. Materials are detailed below.

4.6.1 Growth Media

All materials were purchased from Sigma unless otherwise stated and used without further purification. *Escherichia coli* K12 MG1655 (CGSC #7740) was purchased from the Coli Genetic Stock Centre (CGSC, Yale University, USA), and the stock maintained at -80°C, and on Luria Agar at 37°C.

E. coli was cultured in Luria Broth (LB) (pH 7.5, 5 g/L yeast extract, 10 g/L Tryptone, 10 g/L NaCl, the agar equivalent modified with the addition of 1.5% (w/v) agar). The cultures were shaken at 200 rpm, at 37°C and under aerobic conditions. Cultures were grown to the exponential growth phase, Optical Density at 600 nm (OD_{600}) 0.3/0.4 and diluted 1/1000 in fresh LB broth at 37°C to form the stock cell solution.

To determine the MIC of $AgNO_3$ for *E. coli* the stock cell solution was used to inoculate LB dosed with different concentrations of $AgNO_3$. The cultures were shaken at 200 rpm at 37°C and under aerobic conditions. The OD_{600} was measured at regular intervals to determine the growth of *E. coli* in each culture.

The bottom of the flow cell was lined with BD Matrigel™ (Basement Membrane Matrix, Growth Factor Reduced (GFR), Phenol Red-free, 10 mL LDEV-Free 356231) under aseptic conditions, Figure 4.3. The Matrigel solution stored in aliquots of 100 µL and thawed when required on ice. Then, 90 µL of Matrigel was added to the flow cells, forming a layer on the bottom. The layer was dried at 37°C for 5 minutes and washed 5 times with fresh LB broth, 15 minutes for each wash.

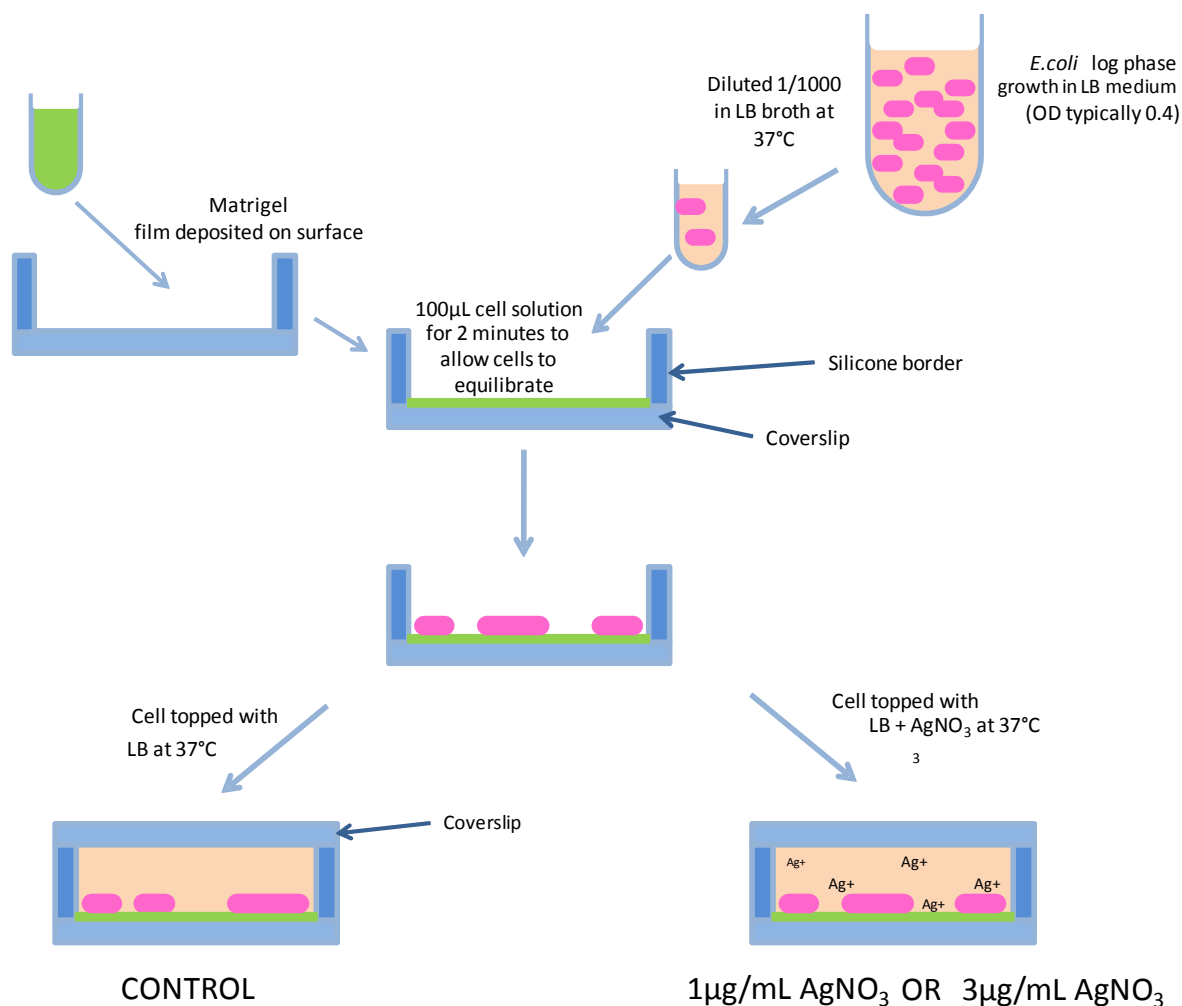


Figure 4.3 The basic flow cell set up for the experiments with *E. coli* cells.

Matrigel is the basement membrane from mouse sarcoma, consisting of approximately 60% laminin, 30% collagen IV, and 8% entactin, the entactin acting as a cross-linker between the laminin and collagen IV. The Matrigel is a liquid when thawed on ice, rapidly gelling at temperatures above 22°C[52]. When solidified the Matrigel has a refractive index of 1.3406 to 1.3407 at 20 °C.

20 µL of stock *E. coli* solution were added to the washed Matrigel and left to equilibrate for 2 minutes; 20 µL of a solution of three sizes of microspheres diluted in LB broth to a concentration equating to approximately 3 spheres of each dilution were then added to the flow cell. The flow cell was then topped up with fresh LB, ~150 µL, sealed with the lid cover slip. The process was the same for the silver stress experiments but the cell was topped up with LB containing the relevant concentration of silver nitrate prior to sealing with the cover slip.

The remaining stock solution was used to measure the colony forming units (CFUs) in the sample. Ringers solutions was prepared by dissolving 6.5 g NaCl, 0.42 g KCl, 0.25 g CaCl₂ and 1 mole of

sodium bicarbonate in one litre of distilled water. The sample was serially diluted 10-fold in Ringers solution, and then 50 μ L of each dilution spread onto LB plates in triplicate. The colonies were counted after an overnight incubation at 37°C to calculate CFU / mL, and the result used to derive the number of cells in the 20 μ L added to the flow cell.

Colonies exhibiting new growth phenotypes were tested for genotypic changes by selecting those colonies and culturing them in LB. These cells were then re-exposed to the stress environment in which they arose and the survival rates and production of new growth phenotypes recorded. The growth phenotypes were also tested for genomic changes using sequencing technology.

4.6.2 Illumina DNA Genome Sequencing

A series of experiments was performed to sequence the genome of different phenotypes using the Illumina platform. After 3 hours of monitored growth the colonies of interest were removed into Eppendorf tubes containing a small volume of LB with a spreading loop, the Lensless microscope setup enables the user to identify the colony of interest on the computer screen, using this visual to guide the spreading loop. The colonies were selected according to growth phenotype observed and in order to harvest a sufficient level of DNA, each sample for sequencing was the culmination of between 5 and 10 individual colonies displaying the same phenotype.

The *E. coli* DNA was isolated using the GenElute™ Bacterial Genomic DNA Kit (Sigma Aldrich NA2110) according to the manufacturer's protocol, the quality checked on a 0.8% agarose gel and the quantity of dsDNA was determined using the Qubit® dsDNA BR Assay Kit (Life Technologies, Q32850). The DNA was fragmented by 15 min sonication (Bioruptor, Diagenode) on medium power cycling for 25s on and 25s off, in an ice bath. Sequencing libraries were prepared using Solid Phase Reversible Immobilization cartridges with TruSeq indexed adapters and 300-600 bp size selection. Libraries were amplified by 15 cycles of PCR, the primers removed using AmpureXP beads, and quantified on a Bioanalyser DNA 7500 chip (Agilent). DNA was denatured and diluted to 6.5 pM, clustered on a cBOT (Illumina) and 100 PE sequencing undertaken on HiSeq2000 (Illumina).

4.7 Results

From a series of 10 growth experiments the survival rate on the transfer to the Matrigel surface estimated from colony density and deposited volume is greater than 95 % in all experiments under control conditions with no flow. A typical growth curve under control conditions along both the major and minor axis is displayed in Figure 4.4. The growth along the major and minor axis from the calibration suggests that growth starts from a single cell (within the diffraction limit error) to form a colony.

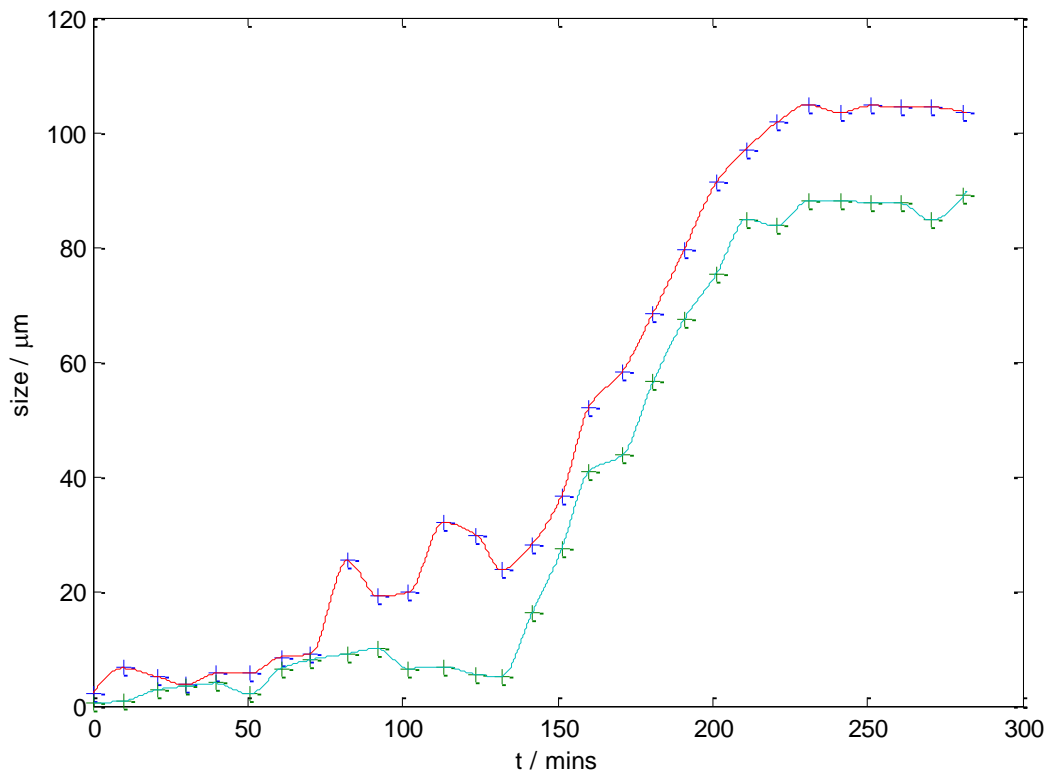


Figure 4.4. A typical growth curve for *E. coli* K-12 MG1655 on a Matrigel surface, surrounded by LB, in the flow cell fabricated here and monitored by the Lensless microscope device. Growth along both the major (red) and minor (green) axis are presented here.

The curve in Figure 4.6 shows the conventional growth curve trend, the lag period of a single cell, the growth of the single cell into a colony and the dynamics associated with colony expansion, and finally the slowing of the colony extension indicating the environment is nutrient limited.

Silver stress challenges were performed at 1 $\mu\text{g}/\text{mL}$ and 3 $\mu\text{g}/\text{mL}$ with the MIC on the Matrigel surface verified to be the same level as the level established in planktonic growth, Figure 4.5, as 8 $\mu\text{g}/\text{mL}$.

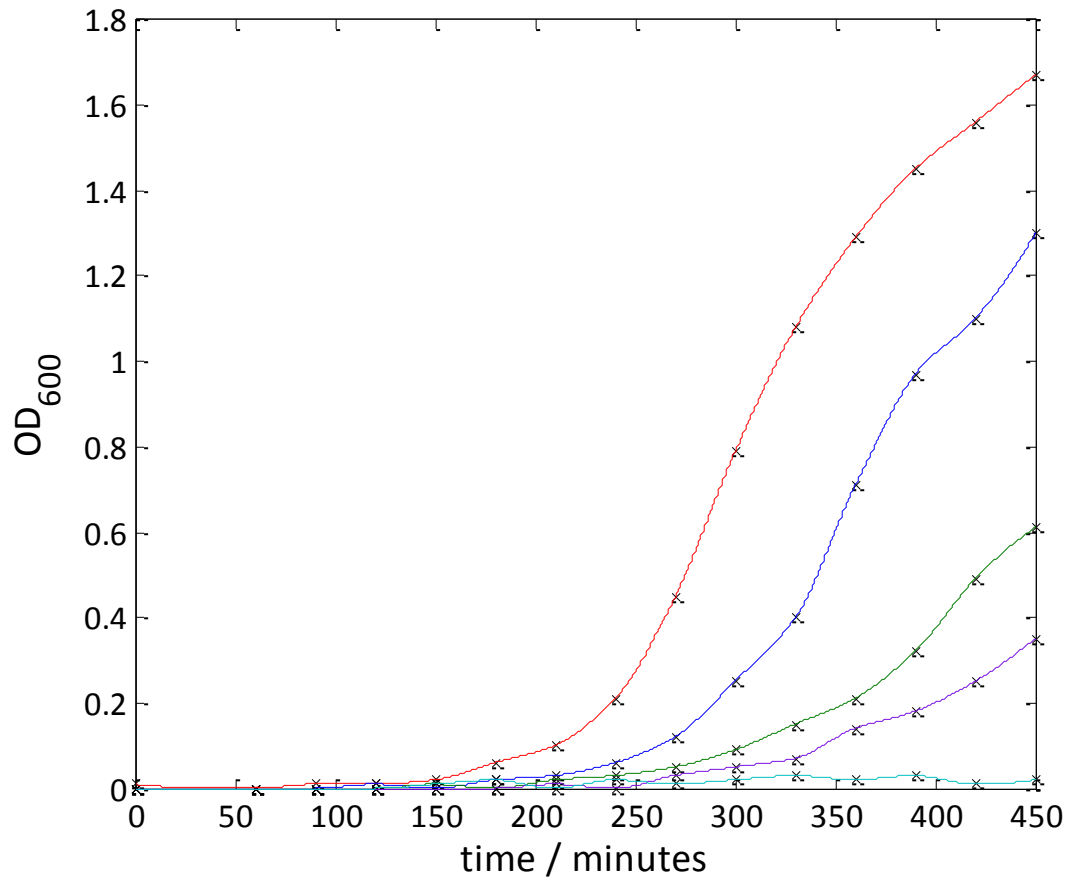


Figure 4.5 The determination of the MIC of silver ions on planktonic *E. coli* growth displaying growth curves under varying levels of silver stress, red, the control; blue 1 µg/mL; green 2 µg/mL; purple 4 µg/mL and turquoise 8 µg/mL.

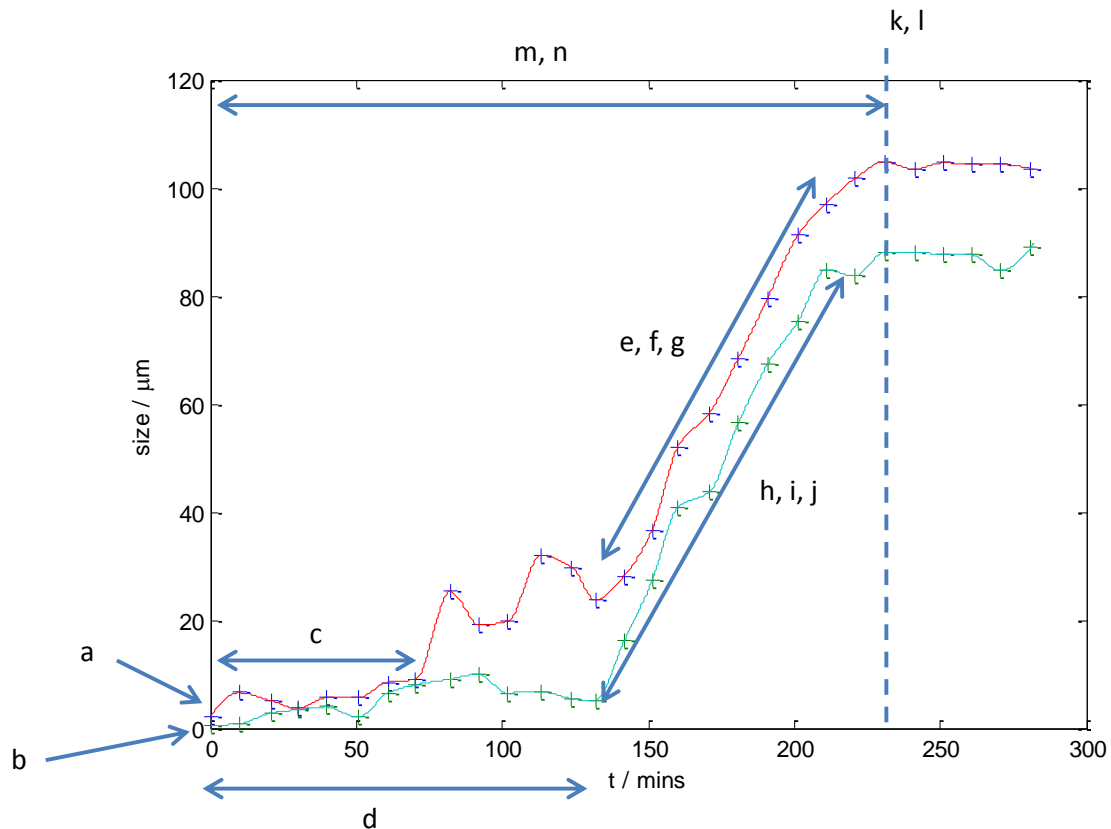


Figure 4.6 A typical *E. coli* growth curve indicating the growth parameters which can be extracted; Major (a) and Minor (b) Dimensions at t_0 minutes / μm ; Major (c) and Minor (d) lag period / minutes; Major (e) and Minor (h) maximum growth rate / $\mu\text{m min}^{-1}$; Major (f) and Minor (i) time to maximum growth rate / mins; Major (g) and Minor (j) average growth rate / $\mu\text{m min}^{-1}$; Major (k) and Minor (l) maximum size reached / μm ; Major (m) and Minor (n) time to maximum size / mins; Aspect Ratio t_0 ; and Maximum Aspect ratio.

The parameters of growth were extracted from the growth curves, Figure 4.6. The full list of parameters is as follows below (all parameters having an equivalent parameter for both the major and minor axis apart from the aspect ratio parameters):

- Major (a) and Minor (b) Dimensions at t_0 minutes / μm
- Major (c) and Minor (d) lag period / minutes ;
- Major (e) and Minor (h) maximum growth rate / $\mu\text{m min}^{-1}$;
- Major (f) and Minor (i) time to maximum growth rate / mins;
- Major (g) and Minor (j) average growth rate / $\mu\text{m min}^{-1}$;
- Major (k) and Minor (l) maximum size reached / μm ;
- Major (m) and Minor (n) time to maximum size / mins;
- Aspect Ratio t_0 ;
- Maximum Aspect ratio

The parameters analysed using the correlation matrix method in detailed in Chapter 2, the full correlation in all three growth conditions are in Table 4.1 (control), Table 4.2 (1 µg/mL) and Table 4.3 (3 µg/mL).

Table 4.1 The table of correlation coefficients for the control sample of *E.coli*, N=100. Above the diagonal of the table highlights the parameters with a correlation coefficient greater than 0.6.

	length	width	Lagmajor	Lagminor	Rmajor	Rminor	RmajorT	RminorT	MaxRmajor	MaxRminor	Amajor	Aminor	AmajorT	AminorT	ART0	Armax
length	1	0.834499	0.702402	0.70536	0.708537											
width	0.834499	1			0.604315											
Lagmajor	0.702402	0.599512	1	0.99568	0.727159											
Lagminor	0.70536	0.597916	0.99568	1	0.734738											
Rmajor	0.708537	0.604315	0.727159	0.734738	1											
Rminor	-0.33646	-0.43264	-0.33363	-0.33088	-0.19105	1			0.80227131	0.83207085	0.776823	0.819652				
RmajorT	0.086879	0.329506	-0.04845	-0.04469	-0.02347	-0.23296	1	0.752535								
RminorT	-0.06259	0.105326	-0.1232	-0.14314	-0.17668	-0.1901	0.752535	1								
MaxRmajor	-0.18142	-0.33885	0.028743	0.039137	-0.00589	0.802271	-0.25695	-0.15638	1	0.95883802	0.931455	0.914534				
MaxRminor	-0.17703	-0.34769	0.022036	0.020886	0.002622	0.832071	-0.254	-0.14241	0.95883802	1	0.890989	0.945691				
Amajor	-0.18863	-0.38015	-0.00327	0.001149	-0.05778	0.776823	-0.21134	-0.10121	0.93145519	0.8909892	1	0.963191				
Aminor	-0.2185	-0.40962	-0.02527	-0.02503	-0.05438	0.819652	-0.20853	-0.10384	0.91453363	0.94569094	0.963191	1				
AmajorT	-0.34697	-0.32378	-0.36221	-0.38321	-0.40206	-0.06883	0.173314	0.238446	-0.2078216	-0.196032	0.10387	0.075388	1	0.976611		
AminorT	-0.32601	-0.31691	-0.34735	-0.34868	-0.37131	-0.07853	0.187578	0.195598	-0.1903776	-0.2060437	0.118636	0.078089	0.976611	1		
ART0	-0.08989	-0.44729	0.026836	0.039335	0.152434	0.203372	-0.2851	-0.22355	0.26875306	0.28359564	0.348358	0.366482	0.122117	0.158235	1	
Armax	0.179583	0.228036	0.227919	0.21785	0.148573	-0.11876	-0.06642	-0.08752	-0.0747013	-0.0438478	-0.09775	-0.08202	-0.06035	-0.07782	-0.05662	1

Table 4.2 The table of correlation coefficients for *E. coli* k-12 MG1655 when grown in the presence of a low level, 1 µg/mL, of AgNO₃, N=100

	length	width	Lagmajor	Rmajor	RmajorT	AvRmajor	Amajor	AmajorT	ARt0
length	1								0.659602
width	0.489964	1							
Lagmajor	0.124721	0.260184	1		-0.6021				
Rmajor	-0.17364	-0.1711	-0.52789	1					
RmajorT	-0.01159	-0.07336	-0.6021	0.283467	1				
AvRmajor	-0.07543	-0.03736	-0.07919	0.446778	-0.27725	1	0.882236		
Amajor	0.216859	0.065867	-0.06177	0.337443	-0.06485	0.882236	1		
AmajorT	0.406427	0.118312	-0.00485	-0.28606	0.559832	-0.4706	-0.01384	1	
ARt0	0.659602	-0.30777	-0.11753	0.021454	0.097498	-0.08149	0.127213	0.312858	1

Table 4.3 The table of correlation coefficients for *E. coli* k-12 MG1655 when grown in the presence of a higher level, 3 µg/mL, of AgNO₃, N=100

	length	width	Lagmajor	Rmajor	RmajorT	AvRmajor	Amajor	AmajorT	ARt0
length	1								
width	0.500725	1							-0.64406
Lagmajor	-0.3556	-0.37348	1						
Rmajor	0.077101	0.045228	-0.23515	1	-0.80838	0.939277	0.929392		
RmajorT	-0.01372	0.032549	-0.06348	-0.80838	1	-0.79661	-0.79105	0.624469	
AvRmajor	0.094522	0.110203	-0.27754	0.939277	-0.79661	1	0.995786	-0.79243	
Amajor	0.089192	0.106455	-0.24806	0.929392	-0.79105	0.995786	1	-0.76664	
AmajorT	-0.01269	-0.0029	0.312973	-0.8158	0.624469	-0.79243	-0.76664	1	
ARt0	-0.25449	-0.64406	0.146107	-0.05299	0.079184	-0.08229	-0.07766	-0.00098	1

It is observed from Table 4.1 that the data for one parameter along the major axis correlate with the corresponding data along the major axis. For example, Length at t0 minutes is highly correlated with Width at t0 minutes (0.8), length of lag period along the major axis is highly correlated to length of lag period along the minor axis (0.99) and the maximum size along the major axis is highly correlated to the maximum size along the minor axis. The observation of the high correlation between major and minor axis has meant that all subsequent analyses of growth phenotypes are performed using just the parameters collected along the major axis. From the phenotype parameter classification analysis, the following parameters have been identified as potential growth phenotype parameters:

- Length at t0 minutes / µm
- Width at t0 minutes / µm
- Length of lag period / minutes
- Maximum growth rate / µm minute⁻¹
- Maximum length reached / µm

At the lower level of silver stress (1 $\mu\text{g/mL}$ AgNO_3) the calculated survival rate is in the range 60 - 63%, falling to 44 – 47 % for the higher silver concentration (3 $\mu\text{g/mL}$ AgNO_3).

Data is displayed using Box-plots with Beeswarm plots underneath them, as detailed in chapter 2 and mirror plots, as detailed in Chapter 3. The MIC of *E. coli* is higher than that of *S. pombe* and so the effect of two concentrations of AgNO_3 on the growth parameters was tested here.

The length distributions of viable cells and colonies for the control sample and both the silver stress conditions are shown in Figure 4.7, with the distribution parameters in Table 4.4.

Table 4.4 The parameters of the three length distributions of viable cells.

Parameter	Control	1 $\mu\text{g/mL}$	3 $\mu\text{g/mL}$
Skewness	1.56 (+0.54-0.62)	1.45 (+0.52-0.56)	0.72 (\pm 0.4)
Kurtosis	6.54 (+2.69-1.87)	5.0 (+3.00 -2.29)	3.2 (+1.1 -0.86)
St. Dev	1.8 (+0.55 -0.34)	1.0 (+0.36 -0.27)	1.0 (+0.21 -0.17)
Range / μm	9.4	4.2	4.2
Mean / μm	3.3 (+0.39 -0.33)	3.0 (+0.30 -0.24)	3.7 (+0.3 -0.3)
Median / μm	2.9 (+0.5 -0.2)	2.9 (+0.2 -0.1)	3.6 (\pm 0.4)

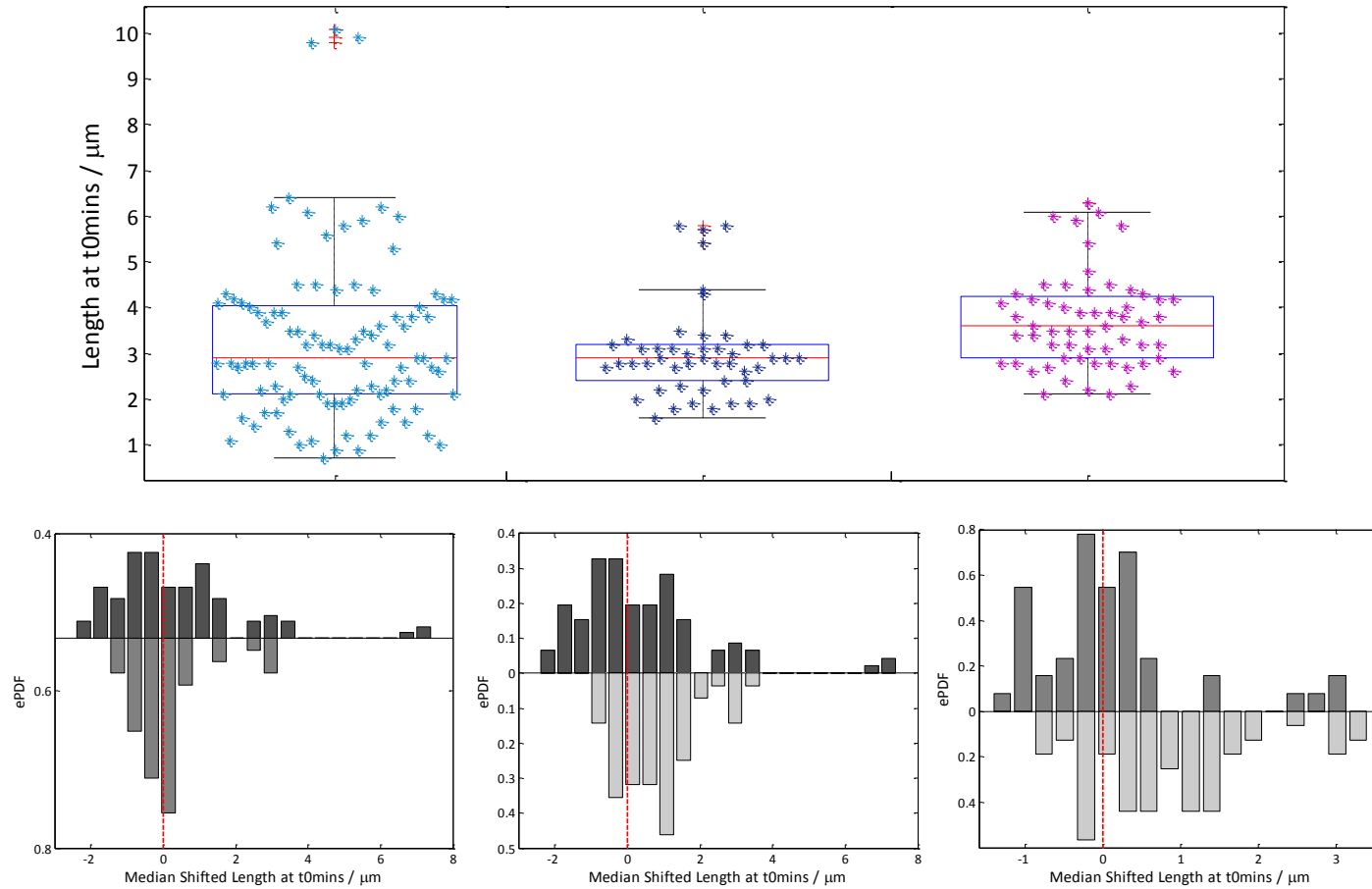


Figure 4.7 Comparison of viable cells lengths at t_{0mins} distributions for the control, low and high Ag stressed medium. The Box plot (A) showing the control sample, light blue, the low silver stress sample, navy blue and the high silver stress sample, purple. The median shifted mirror histograms, from left to right, comparing the control (top) and the low level silver stress conditions (B), the control (top) and the high level silver stress conditions (B) and the low level (top) and high level silver stress conditions (C), dotted red line indicating the median of the data sets, $N=100$

The length at t_0 has a median of $2.9 (+0.5 -0.2) \mu\text{m}$ under control conditions and remains unchanged in the viable colony length for minutes under a low level of silver stress. When the silver concentration is increased to $3 \mu\text{g/mL}$ the length median increases to $3.6 (\pm 0.4)$, and is no longer part of the same continuous distribution (Mann-whitney U P-value <0.01). The length distributions are all skewed towards the long lengths, the degree of skewness reducing as silver concentration increases, and all prone to outliers, the kurtosis value also reducing as the silver concentration increases. None of the distributions are normal, with the A-D and S-W tests both returning P-values <0.01 . The ranges of both the viable colony length data sets under silver stress are the same and under half the range of the distribution of viable colony lengths under control conditions. The narrowing in the range of the data sets under silver stress coming from both the upper and lower percentiles of the control distribution.

Width at t_0 distribution parameters are compared in Table 4.5 and Figure 4.8. The range of viable colony widths is the same for both no silver stress and high silver stress, the range reducing by over 25% for colonies arising from exposure to low silver stress. All three distributions are skewed towards the longer widths, the values of Skewness the same within the error. The Kurtosis of the distributions of cells in the control and high silver stress sample is slightly higher than the values for a normal distribution and the kurtosis of the low silver stress distribution is slightly lower. However within the bootstrapped errors these values are the same. The colonies surviving after exposure to a low level of silver stress are wider than those surviving from the control environment and the high level of silver stress, with a median of $2.1 \mu\text{m}$ compared with $1.1 \mu\text{m}$ and $1.5 \mu\text{m}$ respectively.

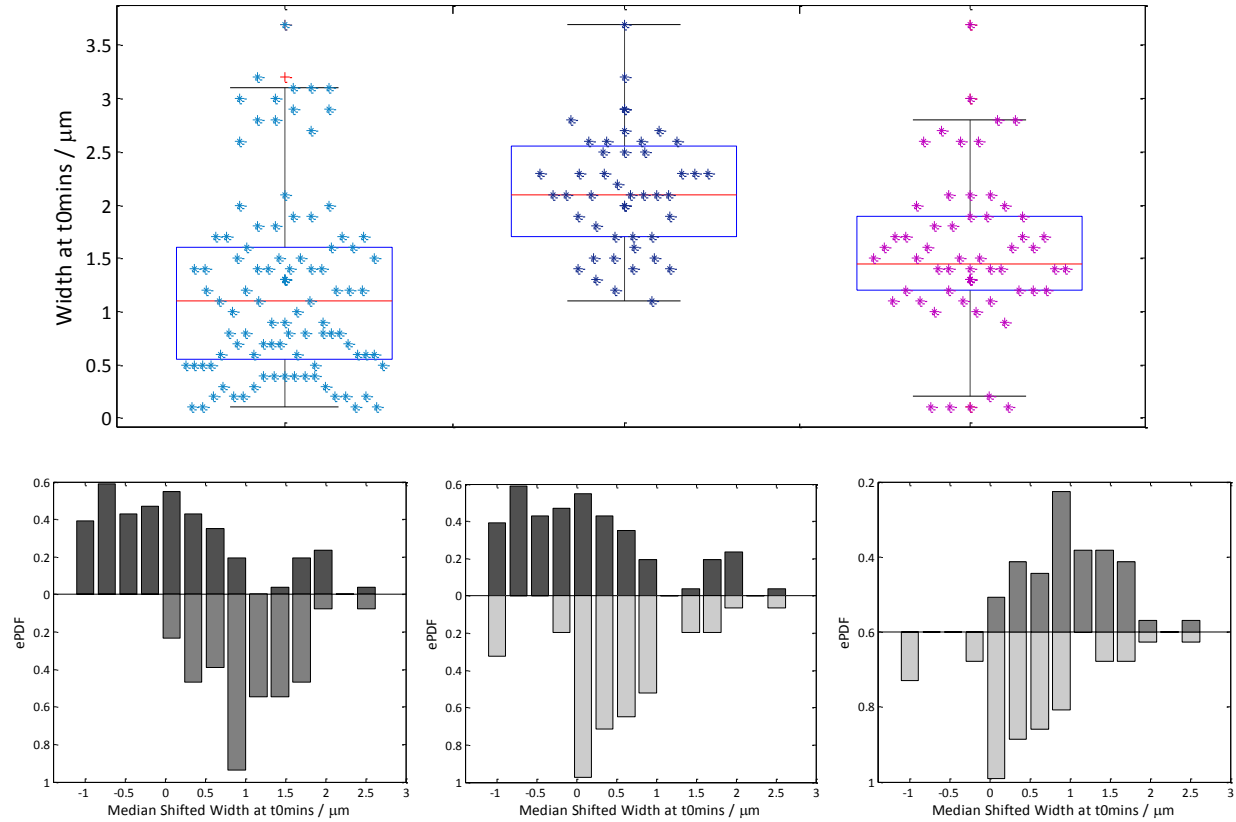


Figure 4.8 Comparison of cell width distributions of the viable cells at t0mins. The Box plots (A) show the control sample, (extreme left, light blue), the low silver stress sample, (centre navy blue) and the high silver stress sample,(extreme right purple). The median-shifted mirror histograms, from left to right, comparing the control (top) and the low level silver stress conditions (B), the control (top) and the high level silver stress conditions (C) and the low level (top) and high level silver stress conditions (D), dotted red line indicating the median of the data sets.

Table 4.5 The parameters of the three distributions of widths at t0mins of viable cells.

Parameter	Control	1 $\mu\text{g}/\text{mL}$	3 $\mu\text{g}/\text{mL}$
Skewness	0.92(+0.35-0.28)	0.28 (0.73-0.51)	0.32 (+1.0-0.51)
Kurtosis	3.15(+1.4-0.79)	2.94 (+1.90-0.86)	3.97 (+2.62-0.99)
St. Dev	0.86 (+0.13-0.11)	0.55(+0.14-0.09)	0.71 (+0.19 -0.14)
Range / μm	3.6	2.6	3.6
Mean / μm	1.22 (+0.17-0.16)	2.14 (\pm 0.16)	1.55 (+0.19-0.17)
Median / μm	1.1 (+0.2 -0.3)	2.1 (+0.2 -0.18)	1.45 (+0.2 -0.1)

The length of the lag period is shifted by silver stress conditions and the distributions are displayed graphically in Figure 4.9, with the parameters compared in Table 4.6.

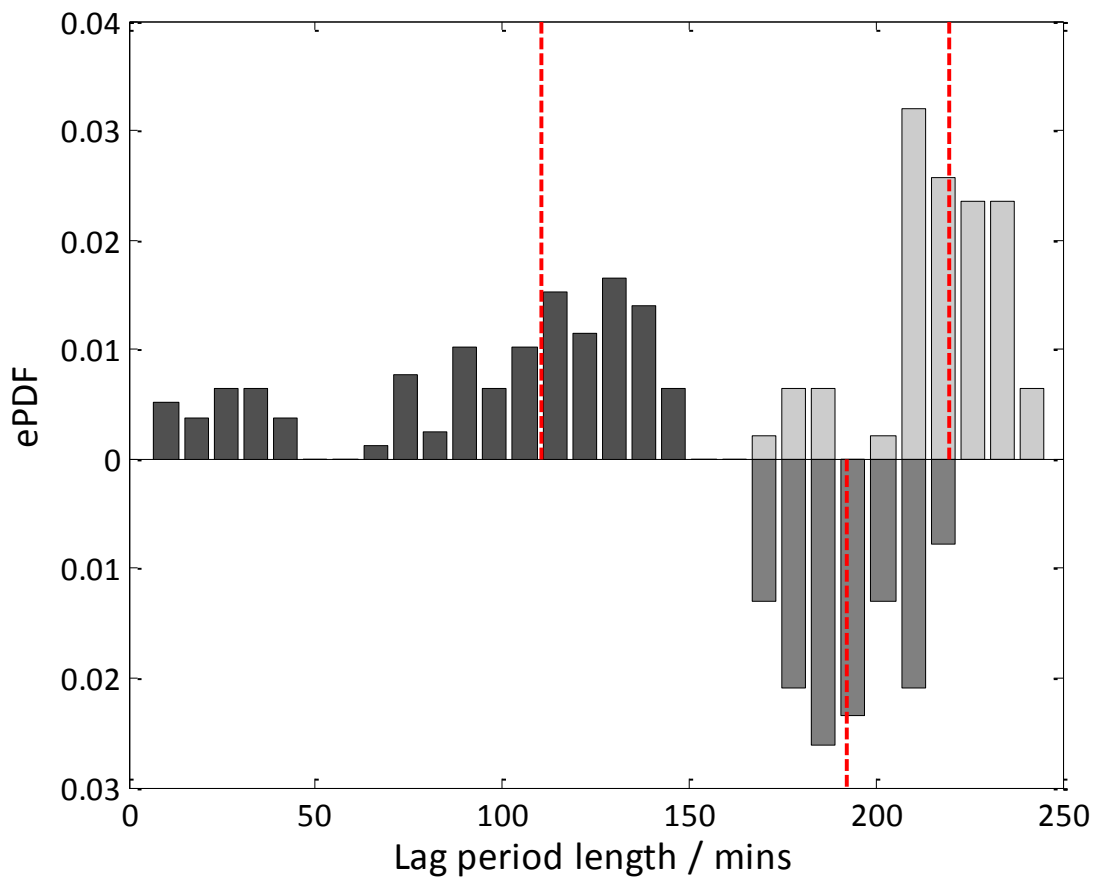


Figure 4.9 Distribution of lag periods of the three *E. coli* populations: the control sample (dark grey), low level of silver stress, 1 µg/mL (mid grey) and higher level of silver stress, 3 µg/mL (light grey). The medians of each sample are indicated by dashed red lines.

Table 4.6. The parameters of the three distributions of lengths of lag period in all of viable colonies.

Parameter	Control	1 µg/mL	3 µg/mL
Skewness	-0.9 (±0.3)	0.3 (±0.4)	-1 (±0.4)
Kurtosis	2.5 (+1 -0.8)	2 (+0.7 -0.4)	4 (+1.7 -1.3)
St. Dev	40.2 (+5 -5)	13.8 (+2.2 -1.7)	17.3 (+4.3 -3.3)
Range / mins	135 (-1)	48 (-1)	80 (-1)
Mean / mins	96.7 (+7.4 -7.6)	192.6 (+4.1-3.7)	218.5 (+4 -4.5)
Median / mins	111 (+5 -3)	192 (+5 -6)	220 (+4 -6)

In general, the median lag period in minutes for each of the colony distributions increases with the concentration of silver ions to which the *E. coli* cells are exposed, increasing from 111 minutes, to

192 minutes under low silver stress and 220 minutes under higher silver stress. The parameters in Table 4.6 show that the distributions of colony lag period are skewed towards the short time lengths in both the high silver stress distribution and in the control sample distributions. The separation in the distributions of both of these data sets indicate that they are bimodal, separating each data set into two and testing them with the Mann-Whitney U test indicates that the data sets for the control lag period and the high silver concentration lag period are bimodal. Under control conditions, 20% of the colonies have a short lag period, defined as short by being less than 50mins. The other 80% have a lag period of above 60mins. The short lag time distributions have a median of 28 (+5 -8) minutes and the long lag distribution have a median of 115 (+5 -7) minutes. Similarly the distribution of lag periods of colonies grown under high levels of silver stress have a bimodal distribution, 12% with a short lag period with a median of 182 (+3-2) minutes and the remaining 88% of the data having a median of 223 (\pm 2) minutes.

The tests for normality show that none of the distributions are normal, with both the SW and AD tests returning P-values<0.001. Comparisons of the distributions using the Mann-Whitney U test show that the distributions come from separate continuous distributions, all comparisons with P-values<0.01.

The effect that silver stress has on the maximum growth rate of the colony along the major axis is shown in Figure 4.10 and in Table 4.7.

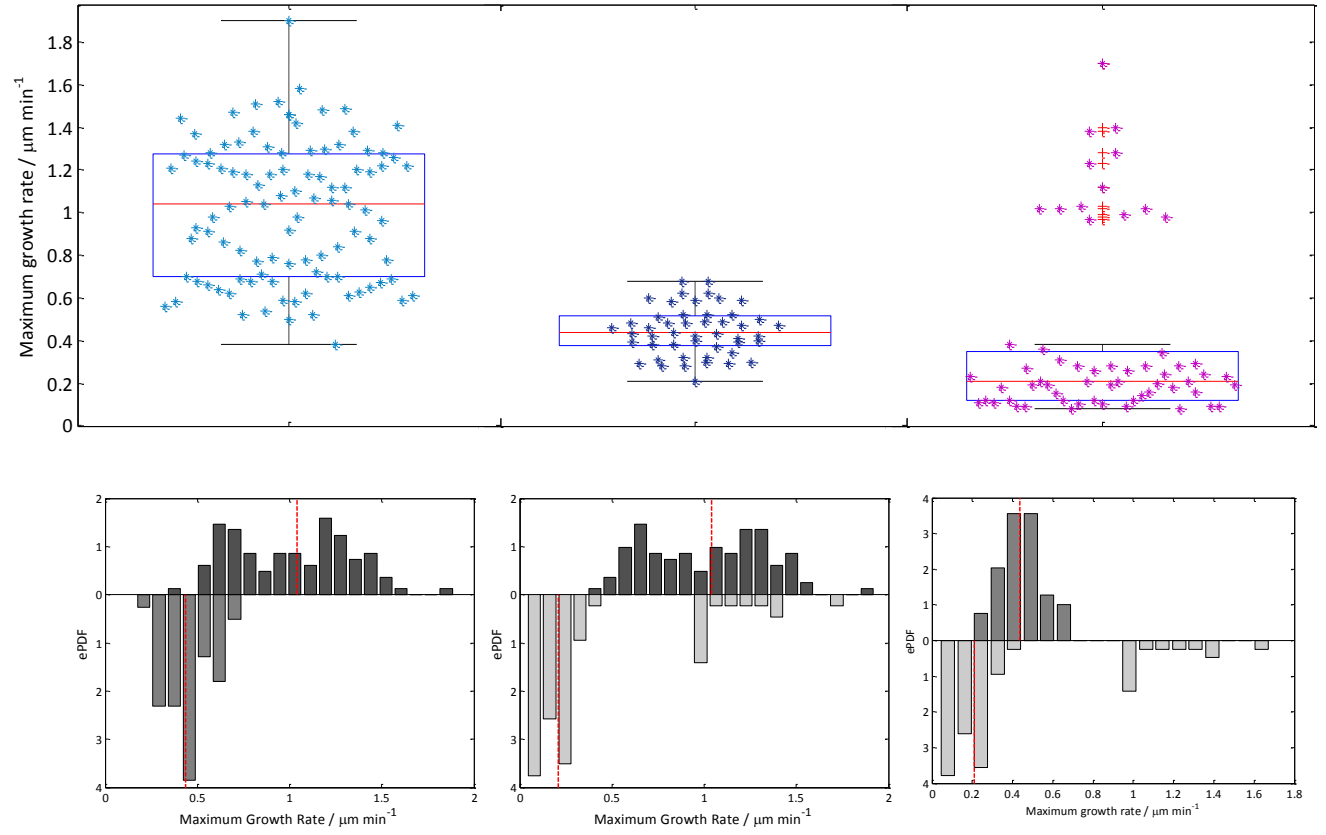


Figure 4.10 Comparison of the maximum growth rate of *E. coli* grown under three silver concentrations. The Box plot (A) showing the control sample, light blue, the low silver stress sample, navy blue and the high silver stress sample, purple. The median shifted mirror histograms, from left to right, comparing the control (top) and the low level silver stress conditions (B), the control (top) and the high level silver stress conditions (C) and the low level (top) and high level silver stress conditions (D), dotted red line indicating the median of the data sets

Table 4.7 The parameters of the three distributions of the maximum growth rates of the viable colonies.

Parameter	Control	1 $\mu\text{g/mL}$	3 $\mu\text{g/mL}$
Skewness	0.1 (+0.5 -0.3)	0.17 (+0.43 -0.44)	1.5 (+0.82-0.65)
Kurtosis	2.1 (+1.1 -0.43)	2.4 (+0.8 -0.52)	3.9 (+4.1 -1.6)
St. Dev	0.3 (+0.04 -0.03)	0.11 (+0.02 -0.17)	0.42 (+0.1 -0.09)
Range / $\mu\text{m min}^{-1}$	1.5	0.47	1.62
Mean / $\mu\text{m min}^{-1}$	1.0 (+0.07 -0.06)	0.44 (\pm 0.03)	0.4 (+0.12 -0.10)
Median/ $\mu\text{m min}^{-1}$	1.0 (+0.13 -0.16)	0.44 (0.05 -0.04)	0.21 (+0.05 -0.03)

The median growth rate decreases as the silver ion concentration of the growth conditions increases. The distribution under a silver concentration of 3 $\mu\text{g/mL}$ is significantly skewed towards the faster growth rates (Skewness 1.5 and Kurtosis 3.9), reflected in the population of outliers in Figure 4.10 A. The SW and AD tests reject the null hypothesis that the distributions are normal, returning P-values of <0.01 for all three distributions. Further to this test, the Mann-Whitney U comparisons of the distributions show that the three medians all come from separate continuous distributions.

Further analysis of the distributions indicates that the distribution of growth rates of colonies grown at the higher level of silver stress is bimodal. The larger distribution, consisting of 87% of the population, has a median of 0.19 (+0.02 -0.03) $\mu\text{m min}^{-1}$ and the secondary distribution, consisting of the remaining 13% of the data set, has a median of 1.05 (+0.08 -0.01) $\mu\text{m min}^{-1}$.

The maximum length reached for each of the groups of cells is displayed in Figure 4.11 and further analysed in Table 4.7.

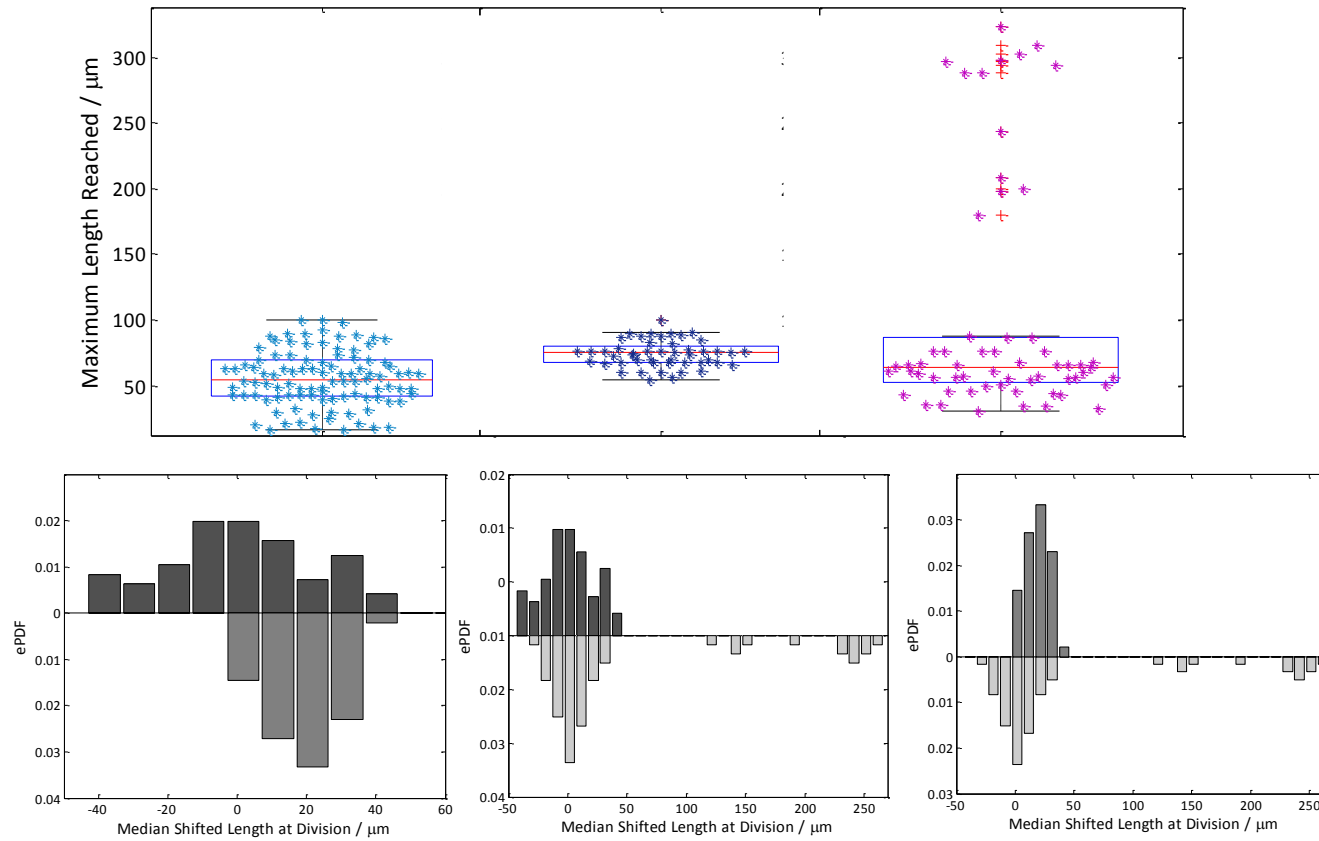


Figure 4.11 Comparison of the maximum lengths reached for control, low and high stress environments. The Box plot (A) shows the control sample, light blue, the low silver stress sample, navy blue and the high silver stress sample, purple. The median shifted mirror histograms, from left to right, comparing the control (top) and the low level silver stress conditions (B), the control (top) and the high level silver stress conditions (C) and the low level (top) and high level silver stress conditions (D), dotted red line indicating the median of the data sets.

Table 4.8 The normality-testing parameters of the three distributions of maximum lengths of viable colonies.

Parameter	Control	1 µg/mL	3 µg/mL
Skewness	0.09 (+0.29 -0.27)	0.25 (+0.57 -0.39)	1.5 (+0.88-0.65)
Kurtosis	2.40 (+0.51 -0.35)	2.61 (+1.3 -0.57)	3.72 (+3.9 -1.6)
St. Dev	21.0 (+2.4 -2.3)	10.2 (+2.3 -1.5)	89.4 (+17.0 -19.5)
Range / µm	84	45.4	293.23
Mean / µm	55.6 (+4.4 -4.1)	74.3 (+3.0 -2.4)	102.6 (+24 -21)
Median / µm	54.5 (+5.2 -6.0)	74.9 (+1.7 -5.05)	63.9 (+3.8 -7.2)

The distributions arising from the lower two levels of silver stress have Skewness parameters which are comparable to the normal value, within error and are both slightly leptokurtic. All three distributions are not normal, returning values for the S-W and A-D tests of <0.01. The median lengths of colonies increases between the control and the low level of silver stress from 54.5 µm to 74.9 µm. The data appear to be following a trend with increasing silver concentration, more positively skewed, shorter range and larger colony length. The distribution of colony lengths arising from the 3 µg/mL silver stress environment do not follow this trend as the distribution is bimodal. The primary distribution, consisting of 87% of the population, has a median maximum length of 58.7 (+4.3 -3.8) µm and the secondary distribution has a median maximum length of 237 (+12.3 -8.9) µm.

The typical growth curves for an *E. coli* cell under control conditions and the two populations of cells produced by a silver concentration of 3 µg/mL are displayed in Figure 4.12. The silver concentration of 3 µg/mL induced two populations of cells, separated the medians of three growth parameters:

- Lag period
- Final length
- Growth rate

The two phenotypes produced under high silver stress are named ‘super-bugs’ and ‘sub-bugs’, the ‘super-bugs’ colonies belonging to the distributions of faster growth rate, larger final size and shorter lag period and the ‘sub-bugs’ are the colonies belonging to the distributions of slower growth rate, smaller final size and longer lag period.

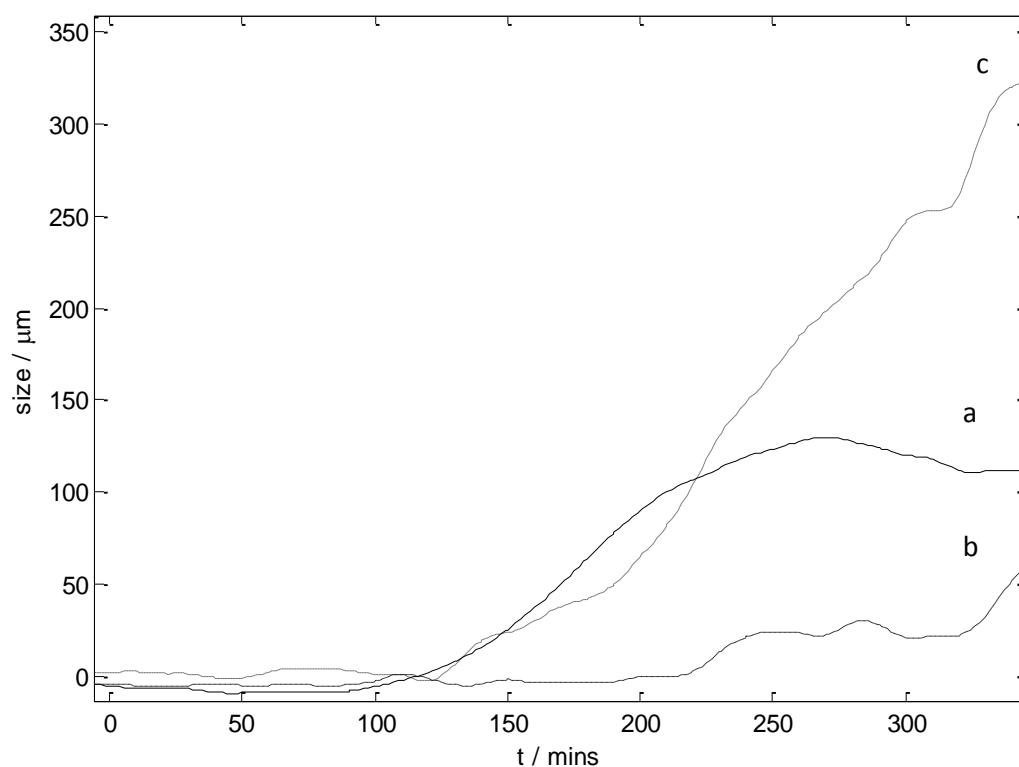


Figure 4.12. The typical growth curve for the growth along the maximum axis for the control *E.coli* sample (a) and the two populations observed during growth under a silver concentration of 3 $\mu\text{g}/\text{mL}$: the sub-bug population (b) and the 'super-bug' population (c).

Colonies were selected as being in one group or the other based on satisfying the three phenotype parameters of each group. Sub-bugs have a lag period longer than 200 minutes, a length after 400 minutes of less than 80 μm and a maximum growth rate of less than $0.4 \mu\text{m min}^{-1}$. Super-bug colonies have a lag period shorter than 190 minutes, a length after 400 minutes longer than 100 μm and a maximum growth rate above $0.9 \mu\text{m min}^{-1}$. The colonies were analysed and removed from the surface for genome analysis as detailed in 4.6.2 and compared to the NIS GenBank reference sample using the Illumina Sequencing Technology, the control, the sub- and the super-bug.

Table 4.9 The nature of each SNP detected from the comparative Illumina sequencing; *pseudogene.

Reference	SNP			Type	Position (bp)	Gene	Gene Function
	No Silver	"Sub-Bug"	"Super-Bug"				
T	A	A	A	Non-silent	1129576	<i>flgA</i>	Assembly protein for flagellar basal-body periplasmic P ring
G	T	T	T	Non-silent	1139601	<i>flgL</i>	Flagellar hook-filament junction protein
A	G	G	G	Non-silent	1169059	<i>ycfS</i>	L2CD-transpeptidase linking Lpp to murein
A	G	G	G	Silent	1189203	<i>phoP</i>	DNA-binding response regulator in two-component regulatory system with PhoQ
G	C	C	C	Non-silent	1232827	<i>nhaB</i>	Sodium:proton antiporter
T	G	G	G	Non-silent	1304760	<i>oppF</i>	Oligopeptide transporter subunit
A	G	G	G	Non-silent	1335418	<i>acnA</i>	Aconitate hydratase 1
C	T	T	T	Non-silent	1351453	<i>sapD</i>	Antimicrobial peptide transport ABC system ATP-binding protein
T	C	C	C	Non-silent	1356883	<i>puuP</i>	Putrescine importer
A	T	T, G	T		1395266	non-coding	
A	G	G	G		1395269	non-coding	
A	T	T	T	Non-silent	1641703	<i>ydfU</i>	Qin prophage 3B predicted protein
T	C	C	C	Non-silent	1650355	<i>intQ</i>	Qin prophage; predicted defective protein
G	A	A	A	Non-silent	1975381	<i>flhC</i>	DNA-binding transcriptional dual regulator with FlhD
C	A	A	A	Non-silent	2038457	<i>yedY</i>	Membrane-anchored 2C periplasmic TMAO 2C DMSO reductase
C	A	A	A		2041546	<i>serU</i>	Endodeoxyribonuclease RUS (Holliday junction resolvase)
A	T	T	T		2796921	non-coding	
T	G	G	G	Silent	283759	<i>yagF</i>	CP4-6 prophage 3B predicted dehydratase
G	A	A	A	Non-silent	2865477	<i>rpoS</i>	RNA polymerase sigma factor
T	G	G	G	Non-silent	3386063	<i>aaeB</i>	p-hydroxybenzoic acid efflux system component
T	C	C	C	Non-silent	3398523	<i>mreB</i>	Cell wall structural complex MreBCD actin-like component MreB
T	G	G	G	Non-silent	3563505	<i>glgP</i>	Glycogen phosphorylase
C	A	A	A		3705970	non-coding	
C	A	A	A	Non-silent	3764026	<i>rhsA</i>	RhsA element core protein RshA
C	A	A	A	Non-silent	3801973	<i>waaB</i>	UDP-D-galactose: glucosyl lipopolysaccharide-6-D-galactosyltransferase
C, T	C, G, T	C, G, T	C, G, T	Indel	3813952	<i>Rph*</i>	Defective ribonuclease
C	T	T	T		3957957	non-coding	
C	A	A	A	Non-silent	3986426	<i>hemX</i>	Predicted uroporphyrinogen III methyltransferase
T	C	C	C		4221661	<i>iclR</i>	Pyruvate DNA binding transcriptional repressor
T	G	G	G		4508261	non-coding	
G	T, A	T	T	Indel/Non-silent	519233	<i>ybbA</i>	Predicted transporter subunit: ATP-binding component of ABC superfamily
A	G	G	G	Silent	547694	<i>ylbE*</i>	Function unknown
G	A	G	G	Silent	565468	<i>ybcC</i>	DLP12 prophage; predicted exonuclease
T	C	C	C	Silent	578054	<i>borD</i>	DLP12 prophage predicted lipoprotein
T	C	C	C		578350	non-coding	
T	C	C	C		578357	non-coding	
G	A	A	A	Silent	578494	<i>ybcV</i>	DLP12 prophage predicted protein
A	G	G	G	Silent	578608	<i>ybcV</i>	DLP12 prophage predicted protein
A	G	G	G	Silent	578725	<i>ybcV</i>	DLP12 prophage predicted protein

4.8 Discussion

The Lensless microscope and ADF algorithm successfully monitors the growth of single and small groups of *E. coli* cells over time. Matrigel replaced agar as the growth surface as it ensures the refractive index contrast between the cell and the background is sufficient to record the diffraction patterns accurately for objects as small as the single *E. coli* cell, $2\ \mu\text{m} \times 0.5\ \mu\text{m}$ (restricted by the diffraction limit of $0.3\ \mu\text{m}$). Matrigel has a refractive index of $1.34\ \text{RIU}^{[52]}$, lower than that of the *E. coli* cell, reportedly $1.40\ \text{RIU}^{[53]}$. Preliminary investigations showed that the growth under these conditions, on a solid Matrigel surface, surrounded by LB was comparable to *E. coli* growth on solid agar. The Matrigel medium is designed as a support matrix for growth without influencing the growth in anyway. It is predicted that this does not induce a phenotypic stress response as the cells are surrounded in LB, much like planktonic growth conditions.

The Matrigel surface in this experimental set up and the Lensless microscope instrument can monitor the growth of single cells within the diffraction limit of $0.3\ \mu\text{m}$. A cell with a width of $0.5\ \mu\text{m}$ will have a diffraction-limited error of $\pm 30\%$ when illuminated with white light centred at $667\ \text{nm}$ and so this study has been about the analysis of the phenotypic growth properties of colonies of cells and the ability of the colonies to act as a multicellular organism, responding to extra cellular signals and the growth environment, a particular consideration in the healthcare setting.

The growth phenotypes arising from growth under control conditions, without induction of phenotypes with silver stress, are discussed first.

4.8.1 Growth Phenotypes under normal growth conditions

Of the possible growth parameters extracted from the *E. coli* growth curve 6 parameters were analysed and now discussed in further detail.

Length and Width at t_0

The length and width (major and minor axis) of a single *E. coli* cell is 2 μm by 0.5-1 μm , a single *E. coli* cell prior to division will have a length of 4 μm , approximately double. There is a fundamental limit in the determination of the length of dimensions of each measurement and this is the diffraction limit determined by the wavelength of the radiation. A single cell length measurement of 1 μm has an error of +/- 0.15 μm , for it to be a single cell it must have a width parameter no larger than 1.15 μm .

The length distribution under control conditions contains 56 colonies which have both lengths and widths within the one cell range reported here and 44 colonies with either the length, width or both dimensions longer than a single cell. From these statistics it can be observed that 56 % of the analysis results from colonies derived from a single cell whereas 44 % derive from two cells, verified by the fact that the length and widths at t_0 minutes under controlled conditions are skewed towards the longer dimension measurements

Cells deposited on the flowcell surface had undergone repeated pipetting to generate turbulence and separate the cells into singles for deposition on the flow cell surface. However, the Matrigel surface is not a smooth surface and *E. coli* cells are motile and so in the initial settling/association stage of the setup it is likely that the cells will settle in micro-valleys in the Matrigel surface morphology. Consequently the cells which are sheltered by the Matrigel may have an altered phenotype, in this control environment governed by the nutrients available to the cell, the cells no longer surrounded by nutrients.

Lag period length

The length of the lag period appears to be split into two populations, indication two phenotypes; those which have a lag period with a median of 28 minutes, the Lag₁ phenotype and those with a median of 115 minutes, the Lag₂ phenotype, Figure 4.9. The length of the lag period in many bacteria is reported to decrease with inoculum size^[54], however, these cells are found in all experiments and occur in 20 % of the cells and each experiment contains a similar size inoculum, between 60 and 70 cells in 20 μL .

Cells which have passed a certain checkpoint within the cell cycle in the exponential growth phase in planktonic growth exhibit little, or none, of a lag period and are able to divide almost at the time expected prior to the cell transfer. Lag period is defined as the lull in growth, after transfer to a new environment, where the cells are adjusting before starting exponential growth^[55] and it appears that these cells, for whatever reason, do not require this time to adjust. It is possible that the cells which are the product of fewer divisions are very quick to divide, the lag period length is affected by the

number of division cycles in which the cell has taken part^[56]. The study in which the age of the cell was related to the subsequent length of lag period, however, was performed on cells from a stationary population, a population which has been shown to carry a higher degree of heterogeneity already^[57], and does not collaborate with the experimental conditions created here.

A study of the first three division times of cells post transfer to a new environment showed that the time to initial division was over three times that of the times to subsequent divisions^[58]. The time between divisions then rapidly stabilised. It can be proposed that the 20 % of cells observed to have a significantly shorter lag period are those cells which have arrived on the cell surface having terminated DNA replication, at the end of the C-phase of the cell cycle, and committed to division, they will be the youngest cells in the population.

The colonies which exhibit a short lag period, Lag_1 , are not in the upper or lower quartiles of the lag period distribution, 40 % of the growth curves exhibiting short lag periods coming from the single cell length and 60 % coming from 2-cell colony length and width parameters. They do not grow faster or slower than the other 80 % of the population, get larger, or stay smaller. They are neither the larger colonies at t_0 nor the smaller ones. It does not appear that in a control environment that these cells have any phenotypical survival benefits over the 80 % which appear to have a lag period in-line with the length of adjustment on a new surface published in the literature^[59].

Average Growth rate

The growth rate under control conditions appears to contain a complex number of growth rates, with a possible bimodal distribution, indicating phenotypes GR_1 and GR_2 although not one which can be easily determined. The position in the growth rate distribution is not correlated to the position in the length distribution, the fastest growing colonies arise from both single and multicellular dimensions at t_0 . The position in the growth rate distribution also not affected by position in the lag period distribution, the Lag_1 distribution having positions in the lower, modal and upper quartiles of the growth rate.

Maximum colony length

The maximum colony rate has a small range and is not skewed significantly towards longer or shorter lengths. It appears that regardless of previous growth rate, initial colony length or lag period cells reach similar colony length prior to slowing in growth. This indicates that the maximum colony size is a parameter related purely to nutrient availability. It also highlights that previous discussion points about the position in Matrigel perhaps limiting nutrients to some cells is not valid.

4.8.2 Silver-Stress *E. coli* Growth Phenotypes,

The survival phenotypes under the two levels of silver stress are; 63 % survive in the low silver stress conditions and 47 % under the higher levels of silver stress.

Length and Width at t_0

The lengths and width distribution of the viable colonies at t_0 remain mostly unchanged between the control and silver samples, with none of the distributions being normally distributed. The longest dimension colonies from the control sample not present in either of the silver stress samples. Comparison of the t_0 distributions from the control sample and the survivors from the low and high silver stress conditions show that the range of lengths at t_0 is significantly shorter under silver stress with no cell viable under with stress condition with a t_0 length of greater than 6.2 μm . The arrival on the surface as a double cell or becoming a double-cell colony as a result of initial motility on the surface would be advantageous to survival with two cells mounting an effective stress response. The distribution of single and double-cell initial colonies is shown in Table 4.10.

Table 4.10 A comparison of colony size types of the viable colonies in all three experimental conditions, the control, and the silver concentrations of 1 $\mu\text{g}/\text{mL}$ and 3 $\mu\text{g}/\text{mL}$.

Colony size	Control	1 $\mu\text{g}/\text{mL}$	3 $\mu\text{g}/\text{mL}$
One cell	56%	4%	28%
Larger than one	44%	96%	72%

Under control conditions over 50 % of the growth curves measured were those produced by a single cell and not a double cell initial colony but under low levels of silver stress the viable cells fall significantly to only 4 %.

The three silver Phenotypes

There are three main silver stress phenotypes identified in this chapter, the viable cells which grow in low levels of silver stress (S_1) and the two viable phenotypes arising from high silver stress ('Super-bugs' and 'sub-bugs'). Each of these phenotypes is the combination of significant differences from the control in three growth parameters, the length of the lag period, the final length of the colony and the maximum colony growth rate.

The formation of the two phenotypes in the presence of a starting concentration 3 µg/mL of silver nitrate occurred both when *E. coli* was grown on a solid agar surface with the toxin below it and when grown on a Matrigel surface with the toxin surrounding it. The Matrigel / LB set up was also beneficial in maintaining a moist environment for cell growth and easily transferable to experimental circumstances which would involve the use of flow (see Chapter 7).

Preliminary experiments and the literature indicate that the closer the colonies are to neighbouring colonies the smaller the overall colony size, the size limited by the accumulation of metabolic inhibitors within the medium^[60]. Given the kill rate, the surface is sparsely occupied so inter-colony communication and nutritional stress will not be a limit for these cells. The rate of growth, under silver stress is reduced for both concentrations which is a systems-level response propagated at the molecular level perhaps at the cell cycle. The cell cycle is regulated by a number of proteins; the initiation of chromosome replication for example is controlled by DnaA, replication commencing when a threshold level of the molecule is achieved. The secondary structure of DnaA protein contains 4 cysteine residues and attack from the silver ion on these proteins would mean that that accumulation of the protein to the threshold level would be delayed triggering the slower growth rate. Once this hurdle has been cleared the rate of chromosome elongation relies, in part, on the ribonucleotide reductase R1, a protein shown to have 5 cysteine residues in the active site alone. Further to this the division of cells requires the cooperation of the two proteins FstA and FstZ, levels of one protein without the other shown to inhibit cell division. While the protein sequence of FstZ contains no cysteine residues, the FstA sequence does, this possibly leading to a high level of FstZ compared to FstA, inhibiting septum formation.

4.8.3 Super-bug and Sub-bug Growth Phenotypes

The maximum growth rate of the bacteria in the three growth groups (control, 3 µg/mL sub-bug and 3 µg/mL super-bug) is compared to the time this maximum growth rate is achieved, in Figure 4.14.

The high silver stress colonies are clustered predominantly top left in this 2D space indicating a long delay to start growing with a slow growth rate, accounting for 87 % of the distribution, these are the sub-bug population. It is clear to see that at a high level of silver stress a second phenotype is induced, indicated by the small cluster of cells in purple, 13 % of the population which reach a faster growth rate at a much shorter time. These cells also have the property of a shorter lag period and are displayed in Figure 4.15 when compared to the maximum growth rate. The genetic analysis confirms this as a genotype so the superbug phenotype is a phenotypical resistance to the higher silver stress.

The low silver stress phenotype, forms one cluster, indication a single growth phenotype under this concentration of silver. The bimodal lag period phenotype, Lag_1 and Lag_2 , splits the control distribution, giving it the curved shape appearance, and indicating that the top 20 % of the lag period distribution (Lag_1) have a wide range of maximum growth rates.

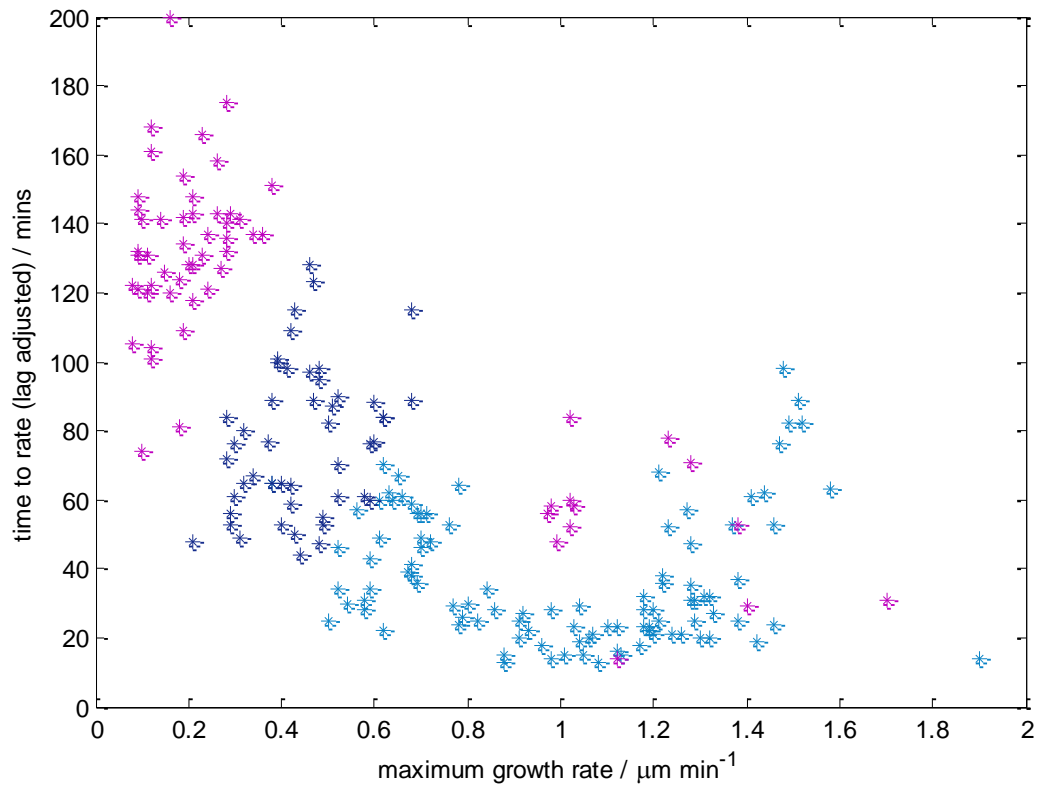


Figure 4.14. A comparison between the correlation between the maximum growth rate of an *E. coli* colony and the time this maximum rate is reached for the control *E. coli* sample (N = 100, light blue), the low silver stress sample (1 $\mu\text{g/mL}$, N = 48, navy blue) and the high silver stress sample (3 $\mu\text{g/mL}$, N = 60, purple).

It is clear to see that at a high level of silver stress a second phenotype is induced, indicated by the small cluster of cells in purple which reach a faster growth rate at a much shorter time. These cells also have the property of a shorter lag period and are displayed in Figure 4.15 when compared to the maximum growth rate.

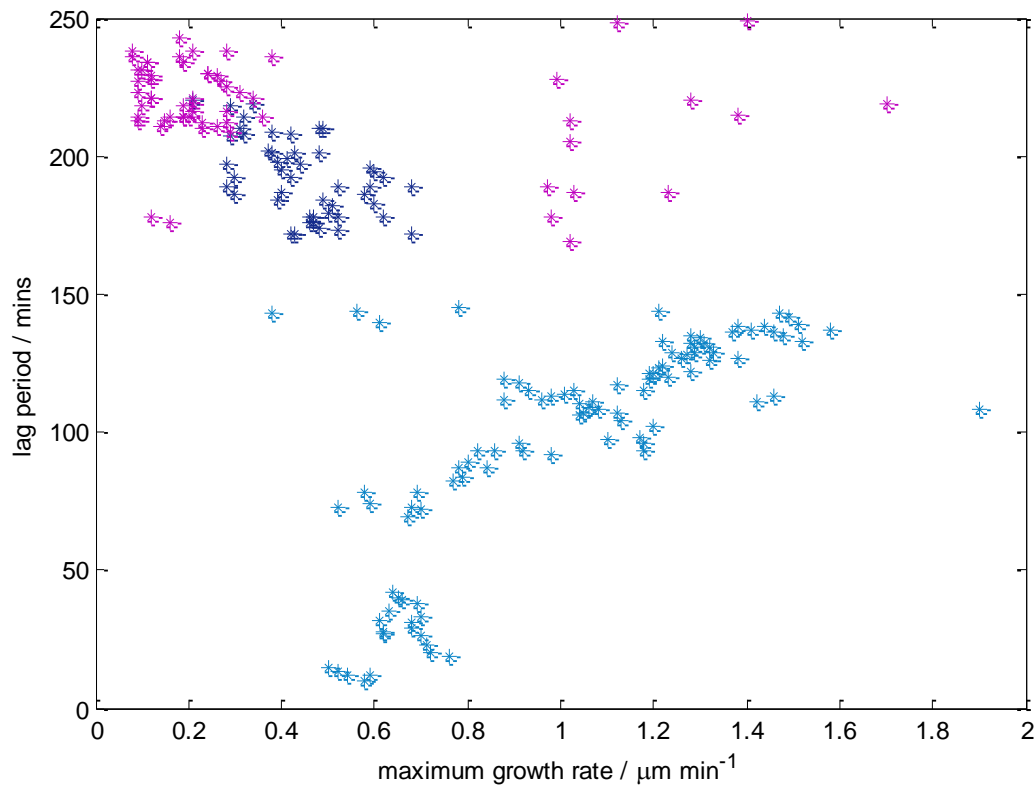


Figure 4.15 A comparison between the correlation between the maximum growth rate of an *E.coli* colony and the lag period length for the control *E.coli* sample (N = 100, light blue), the low silver stress sample (1 $\mu\text{g/mL}$, N = 48, navy blue) and the high silver stress sample (3 $\mu\text{g/mL}$, N = 60, purple).

These cells have been termed super-bugs and the other *E. coli* population within this distribution sub-bugs and are discussed in the following section, the difference in growth curve between these two phenotypes was presented in Figure 4.12.

Super-bug colonies have the following distinguishing characteristics:

- a lag period shorter than 190 minutes,
- a length after 400 minutes longer than 100 μm
- maximum growth rate above 0.9 $\mu\text{m min}^{-1}$
- time to maximum rate less than 80 minutes.

Sub-bug colonies have the following distinguishing characteristics:

- a lag period longer than 200 minutes,
- a length after 400 minutes of less than 80 μm
- maximum growth rate of less than 0.4 $\mu\text{m min}^{-1}$
- time to maximum rate more than 80 minutes.

The resistance to silver is striking these phenotypes and an obvious explanation would be some genetically conferred resistance. The genetic sequence for each sub population was tested and the three genomes, within error, are shown to be the same, indicating that the cells confer no genotypic variation which could confer the measured resistance to silver ions. The polymorphisms between the different isolates, which are summarised in Table 4.10. However, as these changes occurred in the bacteria exposed to no silver in addition to the observed sub- and super-bug phenotypic variants this may reflect random mutation during the cultivation of bacterial stocks (revival from cryo-storage and routine culture for experiments).

The growth phenotype analysis produced six parameters from which a number of phenotypes could be identified. The phenotypes identified in the control and silver stress growth and their prevalence in distribution are summarised in Table 4.11.

Table 4.11 The main growth phenotypes identified from both control and silver stressed *E. coli* growth. All of the phenotypes, except the short lag phenotype, consist of differences in more than one phenotype parameter.

Phenotype	Prevalence
Survivors under low silver stress	63%
Survivors under high silver stress	47%
Short lag under control conditions	20%
Long lag under control conditions	80%
'super-bugs' under high silver stress viable colonies	6%
'sub-bugs' under high silver stress viable colonies	41%

4.9 Conclusion

The growth phenotype screening process developed for single cells in *S. pombe* has been extended successfully to colony growth monitoring for *E. coli*. The screen identified six parameters to classify the growth phenotypes. There is significant heterogeneity in *E. coli* cells taken from the exponential growth phase which is separated following the transition to a biofilm surface growth phenotype. The resulting colonies, whether starting from single or double cells, show significantly different lag periods. Previous studies have reported that cells taken from a culture in this phase of growth show uniformity in their growth parameters^[57]. The colony forming unit (CFU) density is implicated in producing a bimodal distribution of doubling times, a population below 100 CFU mL⁻¹ displayed a bimodal distribution of doubling times^[61]. The results of this study support evidence for the heterogeneity observed in the biofilm colonies monitored by the Lensless microscope. The growth appears not to be nutrient limited in the flow cell and in the *in vivo* growth environment as *E. coli* are facultative anaerobes^[61]. We have demonstrated that the transfer from planktonic growth also produced heterogeneity in the response of the cells under normal growth conditions, inducing a complex growth rate distribution.

It has been demonstrated that under silver stress conditions cell populations have an increased length of lag period and a slower growth rate, and these can be coupled to the effect that silver has on the major proteins of cell cycle regulation. Further to this it can be demonstrated that growth in the presence of a silver concentration of 3 µg/mL results in the production of two separate growth phenotypes, super-bugs and sub-bugs, separated by length of lag period, growth rate and maximum size reached. These sub-populations show growth phenotypes for silver resistance.

The promotion of the favourable super-bug phenotype has implications in the use of silver ions in the medical industry. Lethal concentration of silver may prevail proximal to the silver dressing but as the silver concentration falls distal to the dressing there is a concentration gradient and the potential to select for resistance. This, in turn, may promote the formation of Gram-negative superbugs which could thrive in environments containing silver, free from competition with other, non-resistant microorganisms. Further, the eukaryote response to silver suggests the wound healing may also be compromised.

Escherichia coli has been used as a model organism to investigate the effect of silver stress on the prokaryotic Gram negative cell cycle and I have identified a phenotype arising from this stress. In chapter 5 the focus changes to look at the effect of silver stress in the cell cycle of the model organism for the Gram positive bacteria, *Staphylococcus aureus*.

4.10 References

1. McQuillan, J.S., et al., *Silver nanoparticle enhanced silver ion stress response in Escherichia coli K12*. *Nanotoxicology*, 2012. **6**(8): p. 857-866.
2. McQuillan, J., *Bacterial-Nanoparticle Interactions*. 2010.
3. Begg, K.J. and W.D. Donachie, *Cell Shape and Division in Escherichia coli: Experiments with shape and division mutants*. *Journal of Bacteriology*, 1985. **163**(2): p. 615.
4. Trueba, F.J. and C.L. Woldringh, *Changes in Cell Diameter During the Division Cycle of Escherichia coli*. *Journal of Bacteriology*, 1980. **142**(3): p. 869.
5. Madigan, M., et al., *Brock Biology of Microorganisms*. 13th ed. 2012, San Francisco: Pearson Education Inc.
6. Brock, T.D., D.W. Smith, and M.T. Madigan, *Biology of Microorganisms*. 1984, USA: Prentice-Hall International.
7. Nester, E.W., et al., *Microbiology*. 2nd ed. 1978, USA: Holt, Rinehart and Winston.
8. Kubitscheck, H.E., *Cell Volume increase in Escherichia coli after shifts to richer media*. *Journal of Bacteriology*, 1990. **172**(1): p. 94.
9. Blattner, F.R., et al., *The Complete Genome Sequence of Escherichia coli K-12*. *Science*, 1997. **277**(5331): p. 1453-1462.
10. Hayashi, K., et al., *Highly accurate genome sequences of Escherichia coli K-12 strains MG1655 and W3110*. *Mol Syst Biol*, 2006. **2**.
11. Record Jr, M.T., et al., *Responses of *E. coli* to osmotic stress: large changes in amounts of cytoplasmic solutes and water*. *Trends in biochemical sciences*, 1998. **23**(4): p. 143-148.
12. Farr, S.B. and T. Kogoma, *Oxidative stress responses in Escherichia coli and Salmonella typhimurium*. *Microbiological Reviews*, 1991. **55**(4): p. 561-585.
13. Hightower, L.E., *Heat shock, stress proteins, chaperones, and proteotoxicity*. *Cell*, 1991. **66**(2): p. 191-197.
14. Wang, J.D. and P.A. Levin, *Metabolism, cell growth and the bacterial cell cycle*. *Nat Rev Micro*, 2009. **7**(11): p. 822-827.
15. Zyskind, J.W. and D.W. Smith, *DNA replication, the bacterial cell cycle, and cell growth*. *Cell*, 1992. **69**(1): p. 5-8.
16. Meijer, M., et al., *Nucleotide sequence of the origin of replication of the Escherichia coli K-12 chromosome*. *Proceedings of the National Academy of Sciences*, 1979. **76**(2): p. 580-584.
17. Fuller, R.S., B.E. Funnell, and A. Kornberg, *The dnaA protein complex with the E. coli chromosomal replication origin (oriC) and other DNA sites*. *Cell*, 1984. **38**(3): p. 889-900.
18. Xu, Y.-C. and H. Bremer, *Chromosome replication in Escherichia coli induced by oversupply of DnaA*. *Molecular and General Genetics MGG*, 1988. **211**(1): p. 138-142.
19. Schaus, N., et al., *Isolation and characterization of amber mutations in gene dnaA of escherichia coli K-12*. *Journal of Bacteriology*, 1981. **145**(2): p. 904-913.
20. EcoCyc. *Escherichia coli K-12 substr. MG1655*. 2013; Available from: <http://ecocyc.org/ECOLI/NEW-IMAGE?type=ENZYME&object=YRAO-MONOMER>.
21. Chiamello, A.E. and J.W. Zyskind, *Coupling of DNA replication to growth rate in Escherichia coli: a possible role for guanosine tetraphosphate*. *Journal of Bacteriology*, 1990. **172**(4): p. 2013-2019.
22. Donachie, W., *Relationship between cell size and time of initiation of DNA replication*. 1968.
23. Donachie, W.D., *The Cell Cycle of Escherichia coli*. *Annual Review of Microbiology*, 1993. **47**: p. 199.
24. Uhlin, U. and H. Eklund, *Structure of the Ribonucleotide reductase protein R1*. *Nature*, 1994. **370**: p. 533.
25. Rogers, H.J., *Bacterial Growth and the Cell Envelope*. *Bacteriological Reviews*, 1970. **34**(2): p. 194.
26. Schlegel, H.G., *General Microbiology*. 6th ed. 1986, Cambridge: Cambridge University Press.

27. Cooper, S. and C.E. Helmstetter, *Chromosome replication and the division cycle of Escherichia coli* Br. Journal of Molecular Biology, 1968. **31**(3): p. 519-540.
28. Cooper, S. and C.E. Helmstetter, *Chromosome replication and the division cycle of Escherichia coli* Br. Journal of Molecular Biology, 1968. **31**(3): p. 519-540.
29. Nielsen, H.J., et al., *Dynamics of Escherichia coli Chromosome Segregation during Multifork Replication*. Journal of Bacteriology, 2007. **189**(23): p. 8660-8666.
30. Fossum, S., E. Crooke, and K. Skarstad, *Organization of sister origins and replisomes during multifork DNA replication in Escherichia coli*. The EMBO journal, 2007. **26**(21): p. 4514-4522.
31. Hidaka, M., M. Akiyama, and T. Horiuchi, *A consensus sequence of three DNA replication terminus sites on the E. coli chromosome is highly homologous to the terR sites of the R6K plasmid*. Cell, 1988. **55**(3): p. 467-475.
32. Ferullo, D.J. and S.T. Lovett, *The stringent response and cell cycle arrest in Escherichia coli*. PLoS genetics, 2008. **4**(12): p. e1000300.
33. Ma, X., D.W. Ehrhardt, and W. Margolin, *Colocalization of cell division proteins FtsZ and FtsA to cytoskeletal structures in living Escherichia coli cells by using green fluorescent protein*. Proceedings of the National Academy of Sciences, 1996. **93**(23): p. 12998-13003.
34. Dai, K. and J. Lutkenhaus, *The proper ratio of FtsZ to FtsA is required for cell division to occur in Escherichia coli*. Journal of Bacteriology, 1992. **174**(19): p. 6145-6151.
35. Whitehead, N.A., et al., *Quorum-sensing in Gram-negative bacteria*. FEMS Microbiology Reviews, 2001. **25**(4): p. 365-404.
36. Mah, T.-F.C. and G.A. O'Toole, *Mechanisms of biofilm resistance to antimicrobial agents*. Trends in microbiology, 2001. **9**(1): p. 34-39.
37. Harrison, J.J., et al., *Biofilm susceptibility to metal toxicity*. Environmental Microbiology, 2004. **6**(12): p. 1220-1227.
38. Harrison, J.J., H. Ceri, and R.J. Turner, *Multimetal resistance and tolerance in microbial biofilms*. Nature Reviews Microbiology, 2007. **5**(12): p. 928-938.
39. Miller, M.B. and B.L. Bassler, *Quorum Sensing in Bacteria*. Annual Review of Microbiology, 2001. **55**(165): p. 165.
40. Williams, P., *Quorum sensing*. International Journal of Medical Microbiology, 2006. **296**(2-3): p. 57-59.
41. Antunes, L.C.M., et al., *Quorum sensing in bacterial virulence*. Microbiology, 2010. **156**: p. 2271.
42. Hughes, D.T. and V. Sperandio, *Inter-kingdom signalling: communication between bacteria and their hosts*. Nature Reviews Microbiology, 2008. **6**(2): p. 111-120.
43. Surette, M.G. and B.L. Bassler, *Quorum sensing in Escherichia coli and Salmonella typhimurium*. Proceedings of the National Academy of Sciences, 1998. **95**(12): p. 7046.
44. Surette, M.G., M.B. Miller, and B.L. Bassler, *Quorum sensing in Escherichia coli, Salmonella typhimurium, and Vibrio harveyi: a new family of genes responsible for autoinducer production*. Proceedings of the National Academy of Sciences, 1999. **96**(4): p. 1639.
45. Walters, M. and V. Sperandio, *Quorum sensing in Escherichia coli and Salmonella*. International Journal of Medical Microbiology, 2006. **296**(2-3): p. 125-131.
46. Silver, S., L.T. Phung, and G. Silver, *Silver as biocides in burn and wound dressings and bacterial resistance to silver compounds*. Journal of Industrial Microbiology and Biotechnology, 2006. **33**(7): p. 627-634.
47. Furno, F., et al., *Silver nanoparticles and polymeric medical devices: a new approach to prevention of infection?* Journal of Antimicrobial Chemotherapy, 2004. **54**(6): p. 1019-1024.
48. Schierholz, J., et al., *Efficacy of silver-coated medical devices*. Journal of Hospital Infection, 1998. **40**(4): p. 257-262.

49. Monteiro, D.R., et al., *The growing importance of materials that prevent microbial adhesion: antimicrobial effect of medical devices containing silver*. International Journal of Antimicrobial Agents, 2009. **34**(2): p. 103-110.
50. Berger, T.J., et al., *Electrically Generated Silver Ions: Quantitative Effects on Bacterial and Mammalian Cells*. Antimicrobial Agents and Chemotherapy, 1976. **9**(2): p. 357.
51. Soo-Hwan, K., et al., *Antibacterial Activity of Silver-nanoparticles Against Staphylococcus aureus and Escherichia coli*. Korean Journal of Microbiological Biotechnology, 2011. **39**(1): p. 77.
52. BD_Biosciences. *BD Matrigel Matrix: Frequently Asked Questions*. 2011 [cited 15th December 2013]; Available from: http://www.bdbiosciences.com/documents/BD_CellCulture_Matrigel_FAQ.pdf.
53. Balaev, A.E., K.N. Dvoretzki, and V.A. Doubrovski. *Determination of refractive index of rod-shaped bacteria from spectral extinction measurements*. in *Optical Technologies in Biophysics and Medicine IV*. 2003. Saratov, Russia: International society for optical engineering.
54. Augustin, J.-C., et al., *Significance of Inoculum Size in the Lag Time of Listeria monocytogenes*. Applied and Environmental Microbiology, 2000. **66**(4): p. 1706-1710.
55. Rolfe, M.D., et al., *Lag Phase Is a Distinct Growth Phase That Prepares Bacteria for Exponential Growth and Involves Transient Metal Accumulation*. Journal of Bacteriology, 2012. **194**(3): p. 686-701.
56. Pin, C. and J. Baranyi, *Single-Cell and Population Lag Times as a Function of Cell Age*. Applied and Environmental Microbiology, 2008. **74**(8): p. 2534.
57. Roostalu, J., et al., *Cell division in Escherichia coli cultures monitored at single cell resolution*. BMC Microbiology, 2008. **8**(68): p. 1.
58. MÃ©tris, A., et al., *Modelling the variability of lag times and the first generation times of single cells of E. coli*. International Journal of Food Microbiology, 2005. **100**(1-3): p. 13-19.
59. Borneman, D.L., S.C. Ingham, and C. Ane, *Mathematical Approaches to Estimating Lag-Phase Duration and Growth Rate for Predicting Growth of Salmonella serovars, Escherichia coli O157:H7, and Staphylococcus aureus in Raw Beef, Bratwurst, and Poultry*. Journal of Food Protection, 2009. **72**(6): p. 1190.
60. Hochberg, M.S. and J. Folkman, *Mechanism of size limitation of Bacterial Colonies*. The Journal of Infectious Diseases, 1972. **126**(6): p. 629.
61. Irwin, P.L., et al., *Evidence for a bimodal distribution of Escherichia coli doubling times below a threshold initial cell concentration*. BMC Microbiology, 2010. **10**(207): p. 1.

5 Growth Phenotypes in Colonies of *Staphylococcus aureus* under normal and silver stressed Growth Conditions

5.1 Introduction

E. coli is a Gram negative bacterium which has a thin cell wall, sandwiched between two cell membranes; by contrast the Gram positive bacterium *S. aureus* has a thicker cell wall outside of one cell membrane. This organism is of interest for two main reasons, initially it provides a basic structural first level comparison to the results we have collected in Chapter 4, the comparison of the effect of silver stress on Gram positive and Gram negative organisms. Secondly *S. aureus* is strongly implicated in the causation of HAIs, during a three year study in the hospitals of the United States 64 % of all HAIs were caused by Gram positive organisms, with 16 % attributed to *S. aureus*^[1]. The high incidence of infection caused by this bacterium is attributed to *S. aureus*' presence in the 'normal' skin flora^[2], the fact that it colonises areas in close proximity to possible wound sites. In particular, the patient nasal carriage of staphylococcus plays a key part in the pathogenesis of infection^[3], with up to 20% of the population being long term *S. aureus* carriers^[4].

The *S. aureus* reference genome consists of one circular chromosome, containing 2872 genes, encoding 2767 proteins^[5] and an appearance phenotype typically classified by the golden yellow coccid appearance. The cells are 0.5 - 1.5 μm in diameter^[6], spherical in shape and divide by binary fission. The label Gram-positive means the cells have a cell wall, approximately 0.25 μm thick^[7] consisting of a higher level of peptidoglycan than the Gram-negative cell wall, and teichoic acid residues, both factors implicated in virulence^[8], and the ability of the bacteria to cause septic shock when colonised in a host^[9]. So if a silver covered implant were to cause a growth phenotype such as the one detected in *E. coli*, it could be a real problem with subsequent systemic infections. *S. aureus* also confers virulence via its genome, containing a large number of such genes which are transposable elements subject to lateral gene transfer^[10]. It is this readiness to transfer and accept DNA from others which is responsible for the continuously evolving genotype.

S. aureus is implicated in the incidence of hospital acquired infections, notably MRSA strains in ~50 % in affected hospitals. Therefore the use of a new antimicrobial agent is required to address the rise in infections which are no longer susceptible to attack by the conventional methods. Silver ions have

been shown to affect *S. aureus* cells morphologically, causing the cell membrane to detach from the cell wall and shrink slightly^[11]. Studies on the level of viable *S. aureus* cells present at the site of a wound, with and without the treatment plan containing silver, show significantly lower levels of infection in the presence of silver^[12]. This chapter looks at the effect that silver has on the growth phenotypes of *S. aureus*, below the growth and structure of *S. aureus* is discussed, highlighting the proteins related to cell growth which may be susceptible to attack by silver ions.

5.1.1 *S. aureus* Growth Phenotype and Structure.

S. aureus cells divide by binary fission along one of three planes x, y and z, and have been observed by phase-contrast microscopy to divide along the planes in sequence with sister cells remaining attached to each other after division^[13]. These are grape-like 'clumps' of cells which fail to separate fully after division. The daughter cells are attached to one other at any point along the septal disk which separated them to begin with but they do have the ability to shift with respect to each other while still remaining attached^[13]. In the early stages of colony formation, three morphological forms are observed, linear, square and 'crooked', arising from the direction of the initial two cell divisions^[14]. The staphylococcal mode of division means that colonies of *S. aureus* will very rapidly become three dimensional, the colony shape being an interesting phenotype to study.

The cell wall of the Gram-positive organism is credited, partially, with the protection of the bacteria from antimicrobial attack^[15]. The cell wall makes up approximately 20% of the total dry weight^[16] of the staphylococcus cell and there are two main components of the cell wall; teichoic acid^[17], approximately 40%, and peptidoglycan^[18], approximately 50%. There are two main classes of teichoic acid, wall teichoic acid (WTA) and the lipoteichoic acid (LTA). LTA links the cell membrane to the cell wall and the WTA attaches to the wall peptidoglycan, extending beyond the cell^[19]. The teichoic acid in *S. aureus* consists of repetitive polyol phosphate subunits such as ribitol phosphate (Rbo-P) or glycerol phosphate (Gro-P)^[20] and has been implicated with cell protection against environmental stress and also bacterial ability to colonise the host. Cells with mutations in the *S. aureus* modifications of WTA demonstrate higher susceptibility to neutrophil attack^[8] and the antibiotic vancomycin^[21]. Further studies into the role of WTA have shown that it is essential in the colonisation of the bacteria within the anterior nares^[22], an important consideration which it has been shown that approximately 40% of the population are *S. aureus* carriers^[23] and in turn this has been implicated in the spread of HAIs^[3]. Whilst the biosynthetic pathway for WTA remains largely unknown^[24] it has been demonstrated that mutations in the *tarJ'* gene, which codes for the enzyme TarJ' responsible for the rate limiting step in ribitol formation, effects levels of teichoic acid in the cell wall^[25]. As mentioned previously the other component in high proportion in the Staphylococcal cell wall is peptidoglycan. Peptidoglycan features in both the Gram positive and Gram negative cell

wall and so the effect that the environmental stress of silver has on it will be evident in both bacteria studied, not inducing a new comparable phenotype. *S. aureus* cell walls are also associated with other extra cellular proteins; these cells are implicated in the cells ability to bind extracellular protein complexes, similar to the growth conditions of the Matrigel in the flow cell used in this thesis as a growth chamber. Extracellular proteins are often associated with bacterial virulence, the small colony protection which the proteins provide creating an extended phenotype environment.

Virulence genes have been identified in *S. aureus* which enhance their level of pathogenicity. Virulence factors are typically exoproteins, proteins expressed outside the cells, which aid cell adherence and host attack^[26]. The virulence of *S. aureus* is controlled by the *agr* locus which controls a two component signalling pathway^[27]. There are 4 types of *agr* which classify the *S. aureus* into 4 groups^[28]. Other pathways of virulence include the *sar* and *sae* and, while none of these are directly related to a measureable growth phenotype, the effect silver has on the expression of these genes may become a consideration if classifying the bacteria using the 'Phenotype Fingerprinting' idea introduced in Chapter 3. The fact that the extracellular proteins are excreted means that changes in levels of the expression of these proteins will be detectable. *S. aureus* resistance against antibiotics is one of the reasons why silver ions are now so widely used in hospital equipment. The rapid formation of antibiotic resistant strains recently has led to the knowledge that MRSA is a prevalent hospital acquired infection.

5.1.2 Antibiotic Resistance and the Effect of Silver

S. aureus strains are resistant to penicillin due to the acquired gene *mecA* which encodes a penicillin-resistant peptidoglycan transpeptidase^[29], there now emerging *S. aureus* strains which have a higher resistance to methicillin and other antibiotics due to genes which are thought to code for a thicker cell wall^[30]. All currently isolated strains of vancomycin resistant *S. aureus* have acquired resistance due to mutation and consequent thickening of cell wall due to accumulation of additional peptidoglycan^[31]. The emergence of these strains made it apparent that the bacteria will acquire resistance to new antibiotics in time and following this there is no reason why *S. aureus*, over time, can acquire resistance to silver ions as well.

Silver dressings have been shown to have both antimicrobial and barrier effects against strains of MRSA^[32]. Silver has been shown to lyse *S. aureus* cells at high concentration and cause the cell membrane to separate from the cell wall at low concentration^[33] and has obvious benefits as it is a broad spectrum antimicrobial substance. when first developed had no bacteria which displayed resistance to it^[34]. A review published in 2005 reported the increase in the incidence of silver resistant microorganisms^[35], reporting that that the silver resistance is most likely to be found in

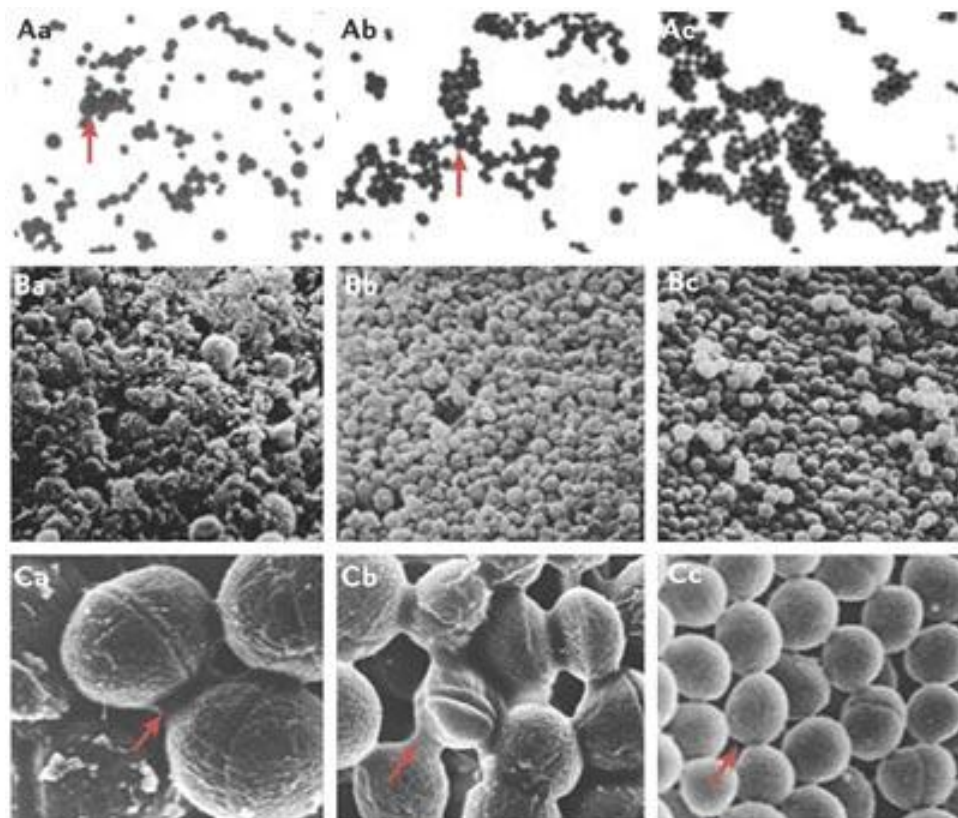
environments associated with the greatest levels of silver use. A silver resistance gene in *S. aureus* has been identified, *silE*^[36] and isolated from infections in both humans and pets, although with no known function.

It has been shown, in Chapter 4 however, that a population of cells in an *E. coli* sample display a phenotypic advantage in the presence of silver stress, it is an advantage such as this which is of interest in this study.

It has been discussed in Chapter 1 the incidence of phenotypic antibiotic resistance which is displayed in *S. aureus* in the form of Small Colony Variants (SCVs). The frequency of detection of these and their specific characteristics are outlined next.

5.1.3 Small Colony Variants

Some of the morphological changes observed in SCV cells manifest as cells growing large and an increased production of intercellular substances^[37], Figure 5.1.



Copyright © 2006 Nature Publishing Group
Nature Reviews | Microbiology

Figure 5.1 Gram stains (A) and scanning electron micrographs at low resolution (B) and high resolution (C) of *S. aureus* SCVs (a,b) and the wild type *S. aureus* strain (c) are shown. There are two SCV phenotypes: 'fried egg' SCVs (a) and pin-point-colony SCVs (b). Arrows indicate large cells in Aa and Ab, in Ca and Cb arrows point to the increase in excreted protein that is present in SCVs compared with wild-type *S. aureus*. Original magnification of image is $\times 6,700$ (B) and $\times 35,000$ (C) [Reproduced with permission from reference^[38]]

The SCV is a phenotype which can easily be identified by the Lensless microscope due to these very obvious changes in growth phenotypes. The phenotype indicated in Figure 5.1 Aa and Ab are a large cell phenotype and the increase in extracellular proteins between wild type and SCVs are displayed in Ca and Cb. The up-regulation of extracellular proteins implying a higher metabolic rate meaning that the cell has a slower relative growth rate. The SCV of *S. aureus* behaves much the way that a conventional bacterial biofilm might^[39], having increased resistance to silver and antibiotics. These phenotypic changes alone do not make SCVs of any particular interest. They are the subject of such study because the specific set of phenotypic characteristics are linked to an ability to persist within a mammalian host and the fact that they are less susceptible to antibiotics than the bulk of the population^[38]. It is this link between growth phenotype and pathogenic properties which make the extraction of these cells from a population of many cells the aim of this chapter.

5.1.4 Aims and Objectives

This chapter aims to extract the growth parameters from the growth curves of the Gram positive bacterium *S. aureus*. It is the aim to monitor the response of *S. aureus* to silver stress and to determine, from distributional analysis, the phenotype variations within both the control population and the silver stress population. Eight parameters will be screened from the growth curves of *S. aureus*, and, as in previous chapters, the phenotype parameters extracted.

This chapter will analyse the growth of a Gram positive organism which divides in three dimensions, previously the microorganisms analysed grew along one dimension, dividing along this dimension at the end of the cell cycle. The difference in growth and response to silver between Gram positive and Gram negative will be explored.

5.2 Materials and Methods

The Lensless microscope was operated as in Chapter 2 with no further modifications. All growth experiments were performed at 37°C.

S. aureus was cultured in Luria Broth (LB), pH 7.5, 5 g/L yeast extract, 10 g/L Tryptone, 10 g/L NaCl, the agar equivalent modified with the addition of 1.5% (w/v) agar. The cultures were shaken at 200 rpm, at 37°C and under aerobic conditions. Cultures were grown to the exponential growth phase, OD 0.3/0.4 and diluted 1/1000 times in fresh LB broth at 37°C to form the stock cell solution.

The bottom of the flow cell was lined with BD Matrigel™ (Basement Membrane Matrix, Growth Factor Reduced (GFR), Phenol Red-free, 10 ml *LDEV-Free 356231) under aseptic conditions. The Matrigel solution stored in aliquots of 100 µL and thawed when required on ice. 90 µL of Matrigel

was added to the flow cells, forming a layer on the bottom. The layer was dried at 37°C for 5 minutes and washed 5 times with fresh LB broth, 15 minutes each wash.

Of a stock *S. aureus* solution, 20 µL was added to the washed Matrigel and left to equilibrate for 2 minutes; 20 µL of a solution of three sizes of microspheres diluted in LB broth to a concentration equating to approximately 3 spheres of each dilution was then added to the cell. The cell was then topped up with fresh LB, ~150 µL, sealed with the lid coverslip. The process was the same for the silver stress experiments but the cell was topped up with LB containing the relevant concentration of silver nitrate prior to sealing with the coverslip.

The remaining stock solution was used measure the colony forming units (CFUs) in the sample. The sample was diluted into a 10-fold serial dilution in Ringers solution, and then 50 µL of each dilution spread onto subsequent LB plates in triplicate. The plates were counted after an overnight incubation at 37°C to calculate CFU / mL, and adjusted to calculate the number of cells in the 20 µL added to the flow cell.

5.3 Results

From a series of 14 growth experiments the survival rate on the transfer to the Matrigel surface estimated from colony density and deposited volume is greater than 97% in all experiments under control conditions with no flow. The MIC of *S. aureus* within this experimental set up was calculated as 4 µg/mL, Figure 5.2.

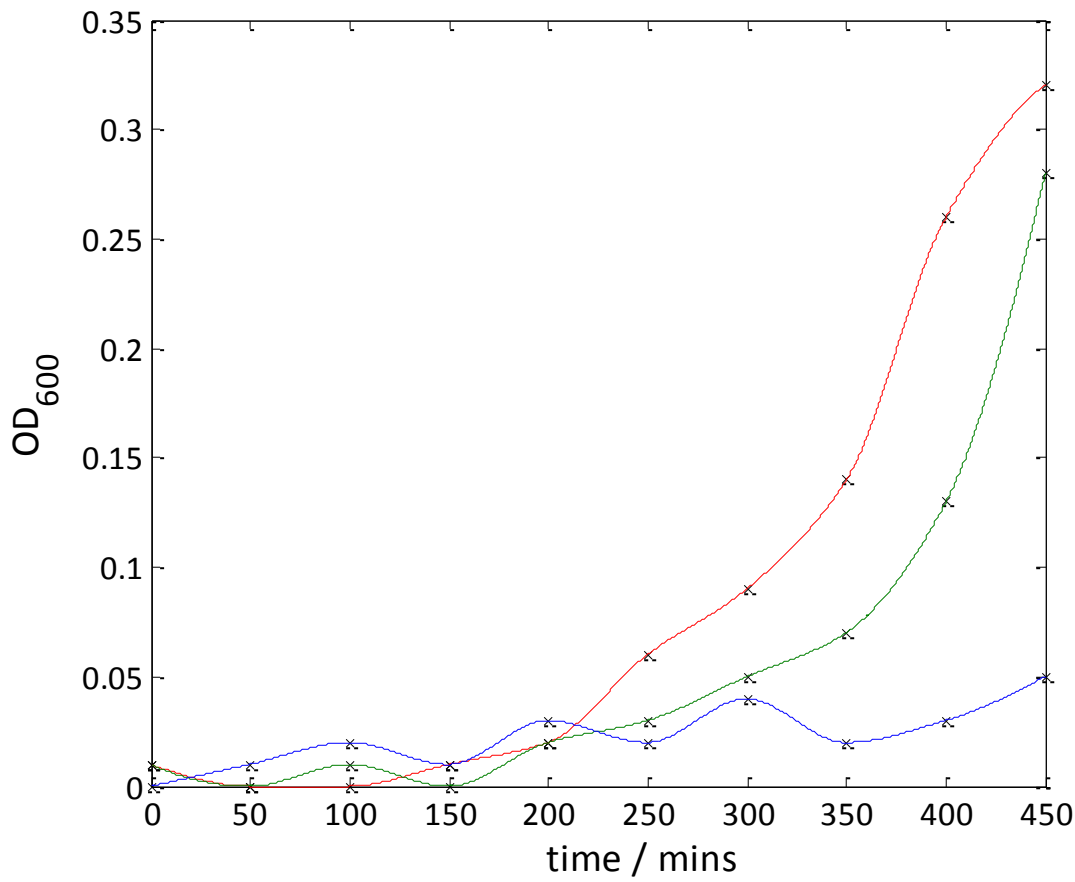


Figure 5.2 The determination of the MIC of silver ions on planktonic *S. aureus* growth displaying growth curves under varying levels of silver stress, red, the control; green, 1 µg/mL; and blue 4 µg/mL.

Silver stress challenges were performed at 1 µg/mL and 2 µg/mL, the cell survival rate at 1 µg/mL was 62% and at 2 µg/mL there was a 33% survival rate. The parameters of growth were extracted from the growth curves as for *E. coli*, chapter 4. The full list of parameters is as follows below (all parameters having an equivalent parameter for both the major and minor axis apart from the aspect ratio parameters):

- Major and Minor Dimensions at t_0 minutes / µm
- Major lag period / minutes ;
- Major maximum growth rate / µm min⁻¹;
- Major time to maximum growth rate / mins;
- Major average growth rate / µm min⁻¹;
- Major maximum size reached / µm;
- Major time to maximum size / mins;

The parameters detailed were subjected to the correlation screening with the resulting matrices: Table 5.1, the control population parameters; Table 5.2 those from a low level of silver stress, 1 µg/mL; and Table 5.3 a higher level of silver stress 2 µg/mL.

Table 5.1 The correlation coefficient table for the control *S. aureus* sample. Strong correlations are highlighted in grey to the right of the table.

	length	width	lag	average rate	max rate	maxrate time	asize	atime
length	1.000	0.606						
width	0.606	1.000						
lag	0.277	0.396	1.000					
averagerate	-0.199	-0.198	-0.152	1.000	0.983		0.743	
maxrate	-0.199	-0.175	-0.129	0.983	1.000		0.736	
maxrate time	0.069	-0.027	0.283	-0.038	-0.077	1.000		
asize	0.016	-0.083	0.083	0.743	0.736	0.000	1.000	
atime	0.341	0.172	0.079	-0.463	-0.456	0.080	0.068	1.000

Table 5.2 The correlation coefficient table for the growth of *S. aureus* under silver stress conditions of 1 µg/mL. Strong correlations are highlighted in grey to the right of the table.

	length	width	lag	average rate	max rate	maxrate time	asize	atime
length	1.000	0.928	-0.690					
width	0.928	1.000	-0.662					
lag	-0.690	-0.662	1.000					
averagerate	-0.100	-0.140	-0.010	1.000		0.872	0.714	
maxrate	0.201	0.232	-0.064	0.041	1.000			
maxrate time	-0.061	-0.077	-0.100	0.872	0.065	1.000	0.867	
asize	-0.027	0.001	-0.269	0.714	-0.020	0.867	1.000	
atime	0.005	0.082	-0.268	-0.450	-0.107	-0.408	0.030	1.000

Table 5.3 The correlation coefficient table for *S. aureus* under silver stress conditions of 2 µg/mL. Strong correlations are highlighted in grey to the right of the table.

	length	width	lag	average rate	max rate	maxrate time	asize	atime
length	1.000	0.776						
width	0.776	1.000						
lag	-0.096	-0.048	1.000					
averagerate	0.034	0.116	0.137	1.000				
maxrate	-0.109	-0.066	0.351	0.443	1.000		0.948	
maxrate time	-0.169	-0.073	-0.263	0.055	-0.026	1.000		
asize	0.016	0.059	0.406	0.513	0.948	-0.056	1.000	
atime	0.213	0.288	0.102	0.136	-0.308	-0.064	-0.012	1.000

From the phenotype parameter classification analysis, the following parameters have been identified as potential growth phenotype parameters:

- Length at t_0 minutes / μm
- Width at t_0 minutes / μm
- Length of lag period / minutes
- Maximum growth rate / $\mu\text{m minute}^{-1}$

The ePDF mirror plots compare the two silver concentrations B and C with the control and then with one another D. In each case, $N = 100$ viable cells surviving the transition to the surface and the initial toxic shock are screened. The length at t_0 distributions for all experimental Figure 5.3, the parameters of these distributions are in Table 5.4.

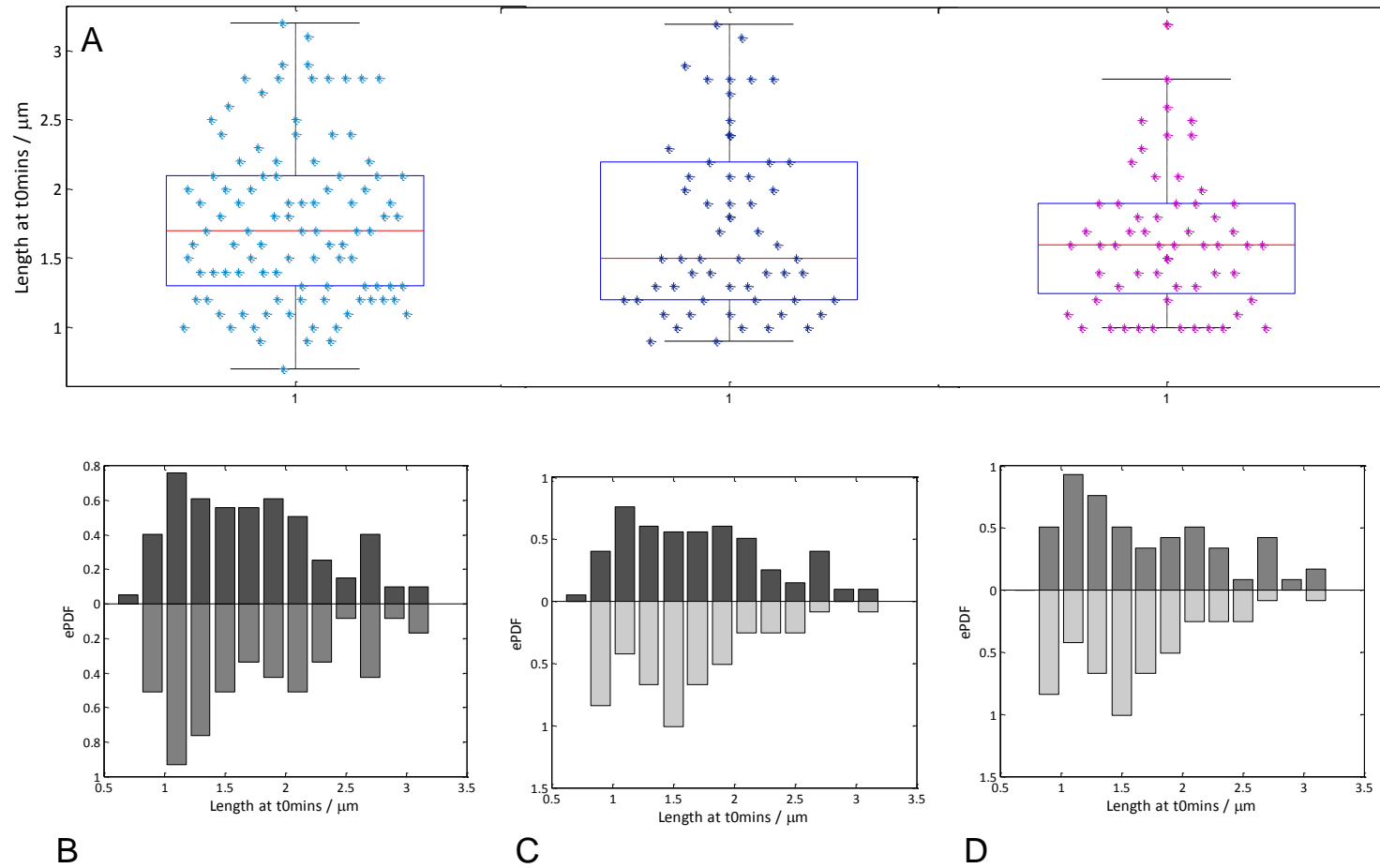


Figure 5.3 Comparison of viable cells lengths at t_0 mins, $N = 100$. The Box plot (A) showing the control sample, light blue, the low silver stress sample, navy blue and the high silver stress sample, purple. The median shifted mirror histograms, from left to right, comparing the control (top) and the low level silver stress conditions (B), the control (top) and the high level silver stress conditions (C), dotted red line indicating the median of the data sets.

Table 5.4 The distribution parameters for the length at t_0 of *S. aureus* grown at all three silver concentrations, the control, 1 $\mu\text{g/mL}$ and 3 $\mu\text{g/mL}$.

Parameter	Control	1 $\mu\text{g/mL}$	2 $\mu\text{g/mL}$
Skewness	0.48(+0.34-0.29)	0.62(+0.44-0.39)	0.8(+0.67-0.42)
Kurtosis	2.4 (+0.65-0.42)	2.3(+0.98-0.51)	3.42(+2.9-0.99)
St. Dev	0.59(+0.08-0.05)	0.63(+0.10-0.08)	0.5(+0.14-0.08)
Range / μm	2.5 (-0.1)	2.3 (-0.1)	2.2 (-0.1)
Mean / μm	1.82(+0.13-0.1)	1.74(+0.16-0.15)	1.6 (+0.14-0.11)
Median / μm	1.7(\pm 0.2)	1.3 (+0.3-0.2)	1.6 (+0.1-0.15)

The distributions for cell length become more skewed towards the longer lengths the as the silver ion concentration increases. Within the error, all three distributions have a similar kurtosis value, with the distributions; the number of outliers in the silver stressed distributions is appears larger than in the control. The three distributions have comparable ranges and the same median length within the error. The A-D and S-W tests show that these distributions are not normal with P-values all <0.01 . The distributions from the control and low silver stress are from the same continuous distribution according to the Mann-Whitney U test, P-value <0.2 . The distribution of viable lengths under higher silver stress is not from the same distribution as the other two distributions but with a P-value of 0.43.

The distribution of colony widths at t_0 for three experimental growth conditions is displayed in Figure 5.4 and Table 5.5. The width parameter was not rejected, regardless of the high correlation it has with the length parameter as a combination of both length and width provides information about shape which may indicate a range of phenotypes.

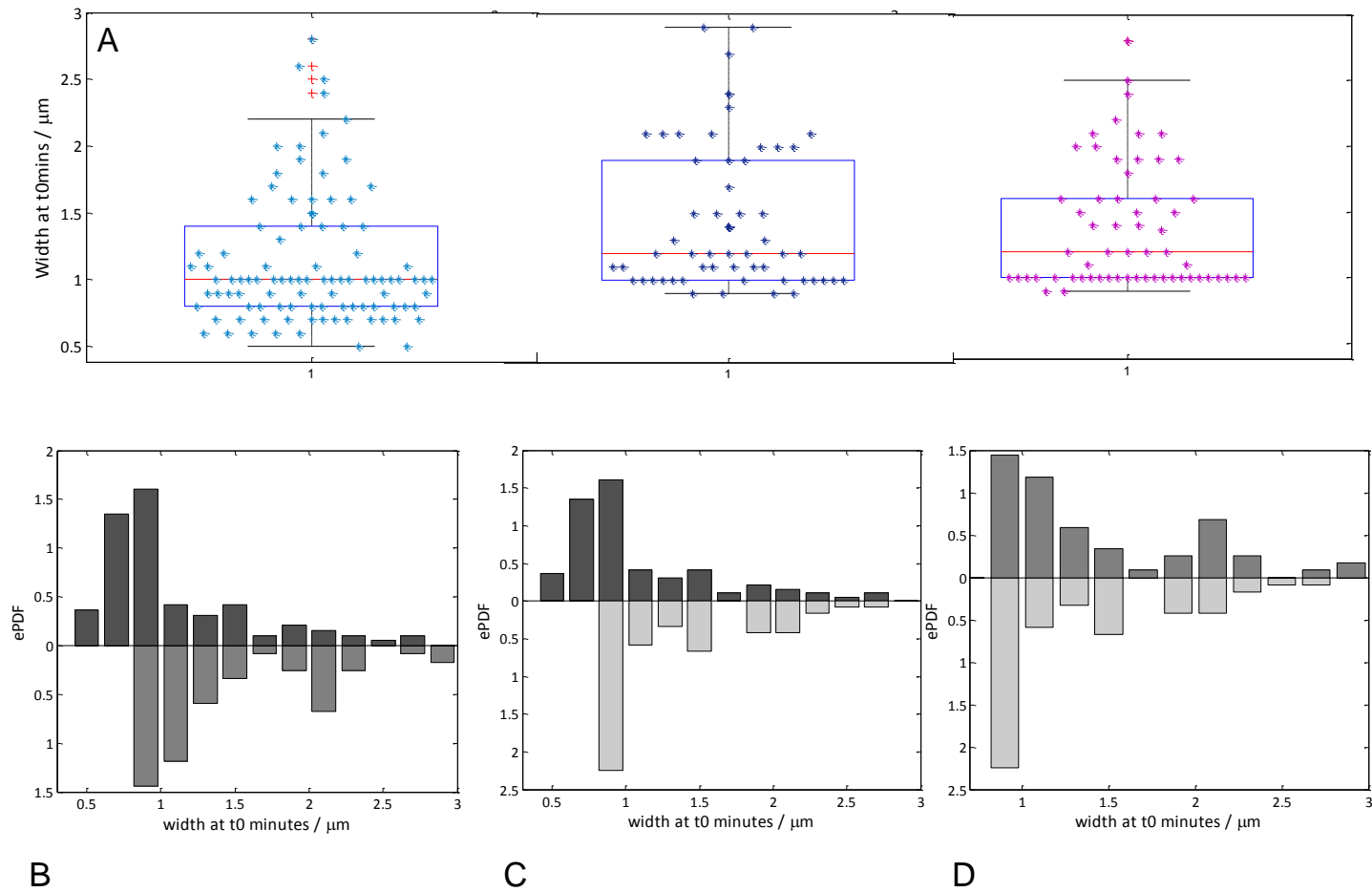


Figure 5.4 Comparison of viable cells width at t_{0mins} . The Box plot (A) showing the control sample, light blue, the low silver stress sample, navy blue and the high silver stress sample, purple. The median shifted mirror histograms, from left to right, comparing the control (top) and the low level silver stress conditions (B), the control (top) and the high level silver stress conditions (C) and the low level (top) and high level silver stress conditions (D), dotted red line indicating the median of the data sets.

Table 5.5 The distribution parameters for the width at t_0 of *S. aureus* grown at all three silver concentrations, the control, 1 $\mu\text{g/mL}$ and 3 $\mu\text{g/mL}$.

Parameter	Control	1 $\mu\text{g/mL}$	2 $\mu\text{g/mL}$
Skewness	1.38(+0.53-0.39)	1.0(+0.6-0.47)	1.1(+0.7-0.4)
Kurtosis	4.5 (+2.4 -1.4)	3.10(+1.98-1.0)	3.2(+2.8-1.0)
St. Dev	0.49(+0.11-0.08)	0.54(+0.12-0.08)	0.47(+0.12-0.07)
Range / μm	2.3 (-0.1)	2 (-0.1)	1.9 (-0.1)
Mean / μm	1.1 (+0.1-0.09)	1.45(+0.14-0.12)	1.38(+0.12-0.11)
Median / μm	1 (-0.05)	1.2(+0.2-0.1)	1.2(-0.35+0.2)

The kurtosis for the control distribution is significantly larger than the theoretical value of 3 for a normal distribution and the Skewness is significantly different from the theoretical value of 0, within the 95 % confidence limits. The Skewness and Kurtosis for the silver distributions tend toward the theoretical values for a normal distribution. All three distributions fail the A-D and S-W tests for normality. Unlike the distributions for length, all three of these distributions come from the same continuous distribution when tested with the Mann Whitney U test accepting the null hypothesis with P-values <0.1 . Within the error the silver stress distributions have the same range, with the control distribution being marginally wider. The three distributions have the same median.

The length of the lag period in minutes increases as the concentration of silver ions in the growth environment increases. The data are presented in Figure 5.5 and Table 5.6.

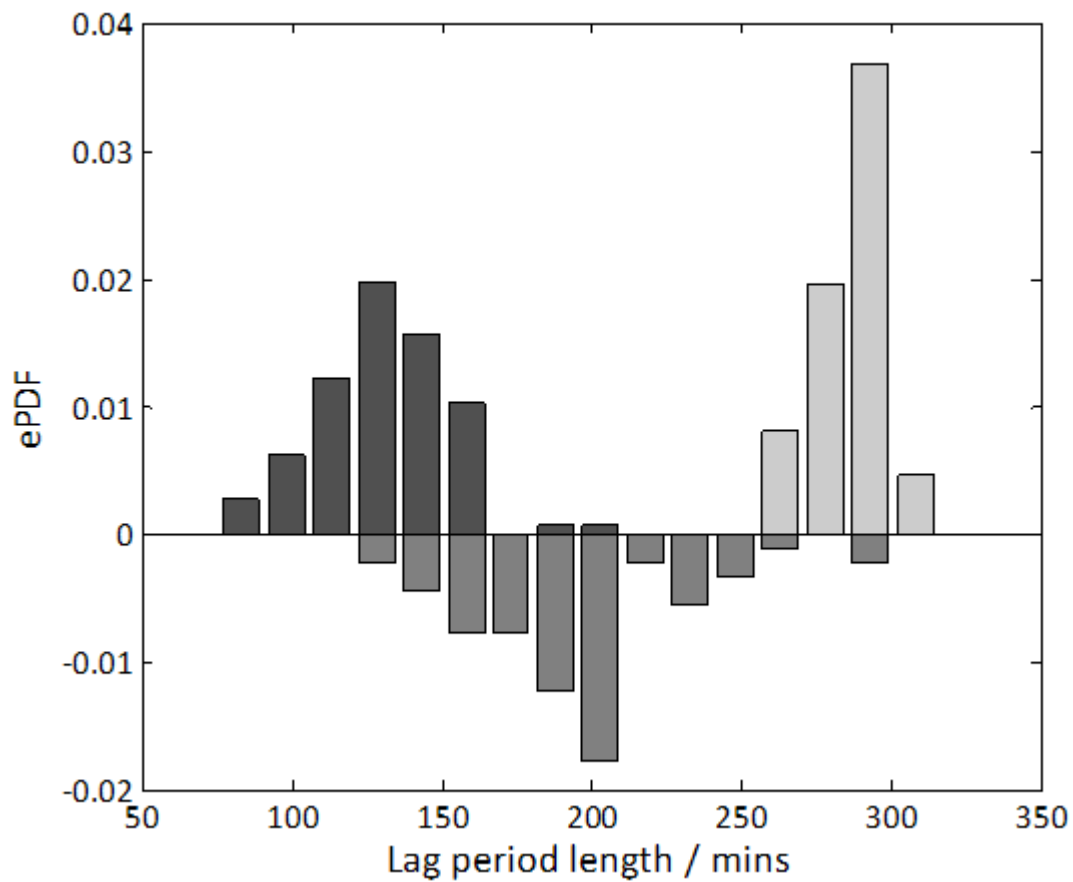


Figure 5.5 Distribution of lag periods of the three *S. aureus* populations: the control sample (dark grey), low level of silver stress, 1 µg/mL (mid grey) and higher level of silver stress, 2 µg/mL (light grey).

Table 5.6 The distribution parameters for the length of the lag period of *S. aureus* grown at all three silver concentrations, the control, 1 µg/mL and 3 µg/mL.

Parameter	Control	1 µg/mL	2 µg/mL
Skewness	0.24(+0.7-0.5)	0.62(+0.59-0.60)	-0.13(±0.70)
Kurtosis	3.6 (+1.6-1.2)	3.7 (+2.3-1.1)	3.4(+1.6-1)
St. Dev	21.7 (+4.4-2.8)	35.7(+8.2-6.4)	11.6(+2.5-1.8)
Range / mins	119 (-8)	176 (-12)	63 (-4)
Mean / mins	131 (+3.9-4.3)	194(+9.2-8.2)	286.6(+3.0-2.7)
Median / mins	131(+3-7)	194.5(+8.5-10.5)	289(+3-2.5)

The low level of silver stress has the largest range, spanning 176 minutes compared to 119 minutes under control conditions and 63 when exposed to a higher level of silver stress. All the distributions

are slightly skewed, the two lower levels of silver stress skewed towards the longer times and the highest level of silver stress skews the distribution towards the shorter times. The distribution of lag times of bacteria grown under 2 µg/mL passes the hypothesis test for normality and are surprisingly for this thesis, normal after testing with both the A-D and the S-W test accepting the null hypothesis with a P-value <0.1. Neither of the other distributions are normal, with all P-values <0.3. The Mann-Whitney U test confirms what the medians show that the distributions are not from the same continuous distribution.

The data for the average colony growth rate under three levels of silver stress are displayed in Table 5.7 and Figure 5.6.

Table 5.7 The distribution parameters for average colony growth rate of *S. aureus* grown at all three silver concentrations, the control, 1 µg/mL and 3 µg/mL..

Parameter	Control	1 µg/mL	2 µg/mL
Skewness	1.5(+0.9-0.7)	2.0 (+1.3-1.2)	0.71(+0.62-0.38)
Kurtosis	6.9(+7.7-3.9)	9.7(+9.0-5.6)	2.9(+2.0-0.7)
St. Dev	0.2(+0.07-0.03)	0.09(+0.05-0.02)	0.04(±0.007)
Range /µm min ⁻¹	1.2	0.51	0.16
Mean /µm min ⁻¹	0.33(+0.04-0.03)	0.14(+0.03-0.02)	0.10(±0.01)
Median /µm min ⁻¹	0.31(±0.04)	0.13(+0.04-0.02)	0.09(+0.01-0.02)

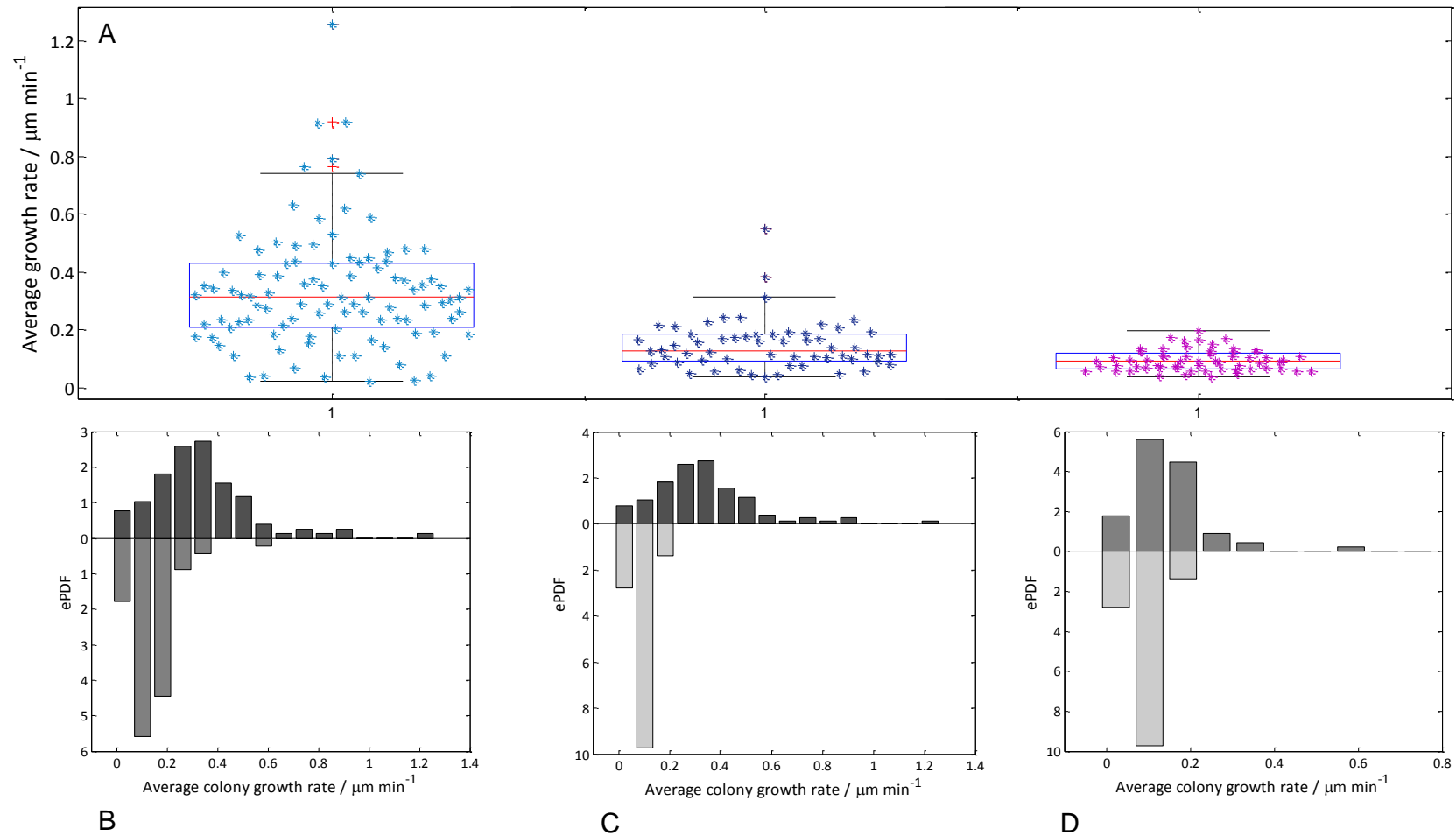


Figure 5.6 Comparison of average growth rate, $N = 100$. The Box plot (A) showing the control sample, light blue, the low silver stress sample, navy blue and the high silver stress sample, purple. The median shifted mirror histograms, from left to right, comparing the control (top) and the low level silver stress conditions (B), the control (top) and the high level silver stress conditions (B) and the low level (top) and high level silver stress conditions (C), dotted red line indicating the median of the data sets.

The average growth rate reduces as the silver ion concentration increases, with the rate of growth under 2 µg/mL over three times slower than the median growth rate of the control sample. The range of the data also reduces with increasing silver ion concentration. The distribution of growth rates at 1 µg/mL has the highest kurtosis parameter, but as with the other two distributions the error of the kurtosis value straddles the value for normal. Each of the distributions are skewed towards the longer growth rates. None of the distributions are normal, P-values <0.1, and the distributions are not from the same continuous distribution (P-values <0.3).

5.4 Discussion

The growth of single and small groups of *S. aureus* cells over time was successfully monitored by the Lensless microscope and ADF algorithm. Preliminary investigations showed that the growth under these conditions, on a solid Matrigel surface, surrounded by LB was comparable to *S. aureus* growth on solid agar.

Growth was successful and 100 viable cells were imaged, for each growth condition. The survival rate of cells under the low level of silver stress was 63 %, the survival rate of cells under high silver stress was 33 %. The parameter screen was performed and produced a correlation matrix which showed that all parameters derived from the growth curve could be usefully included in the characterisation of growth phenotypes. The correlation between length and width in the control growth conditions is high and would have been rejected but it becomes decoupled from the length under conditions of silver stress: a first indication of different growth phenotype.

The Lensless microscope instrument can monitor the growth of single cells within the diffraction limit of 0.3 µm. A cell with a width of 0.5 µm will have a diffraction-limited error of ± 30 % when illuminated with white light centred at 667 nm and so this study, the same as Chapter 4, has been about the analysis of the phenotypic growth properties of colonies of cells, the percentage of single and more than one cell colonies at t0 minutes for each experimental condition is displayed in Table 5.8.

Table 5.8 A comparison of colony size types of the viable colonies grown at all three silver concentrations, the control, 1 µg/mL and 3 µg/mL.

Colony size	Control	1 µg/mL	2 µg/mL
One cell	46%	33%	27%
Larger than one	54%	67%	73%

The growth parameters were screened and reduced from a possible 8 to the 4 phenotype parameters presented below:

7. Length at t_0 / μm ;
8. Width at t_0 / μm ;
9. Lag Period / mins
10. Growth rate / $\mu\text{m min}^{-1}$;

The identification of growth phenotypes in the distributions of the screened parameters is now discussed. Length and width at t_0

Cells with shorter widths in the lower 20 % of the width distribution for growth under normal conditions in the control appear not to be present in the silver stress distributions at either concentration. The silver lower width cut-off is 0.9 μm compared with 0.5 μm in the control set. The shorter cell colonies appear to be less well able to withstand the silver stress, a length phenotype, L1. Conversely, the larger cell colonies perhaps reflecting a capacity to mount an effective stress response.

Colonies of *S. aureus* excrete extra cellular proteins which are implicated in host pathogenicity and protein matrix binding^[37]. A larger colony may then have a greater capacity to produce the protective proteins in larger concentration and so mount an effective stress response, the larger colony benefiting from an extended phenotype.

S. aureus colonies, unlike the colonies of *E. coli*, show a high correlation between width and length at t_0 which could indicate an unbiased growth direction possibly associated with continuing association either on the surface or in planktonic growth. It has been reported that the colonies of *S. aureus* appear circular after 4 divisions^[14] suggesting a symmetric growth phenotype. This symmetry is broken however with the silver stress; the length and width parameters become significantly uncoupled indicating an asymmetric colony.

Length of Lag period

The analysis of lag period in *E. coli* identified two phenotypes under control growth conditions and two distinct phenotypes under high levels of silver stress. The distribution of lag period for *S. aureus* does show a very small long lag phenotype accounting for 4 % of the population potentially a bimodal distribution. These colonies have a significantly longer lag period, with a median of 189 minutes compared to the majority of the colonies which have a median lag time of the distribution of 119 minutes. This apparent dormant behaviour is consistent with SCVs. SCVs are defined as

having a slow growth rate and remaining dormant for longer than other cells in the distribution. The small subset of cells could be identified as SCVs morphologies or slower growth rates.

The ranks of the four colonies in the lag phase distribution are 96-100 which may be compared with their position in the length at t_0 distribution 10th, 27th, 49th and 68th percentiles, and width at t_0 of 12th, 23rd, 59th and 62nd, demonstrating no correlation between the colony size at t_0 and the resulting position in the lag period distribution. The colonies are, however, all in the lower 15 % of the average growth rate distribution, they are among the slowest growing of all the *S. aureus* cells screened under control conditions. It is, therefore, reasonable to suggest that the 4 colonies in the upper extreme of the lag period distribution are SCVs indicating prevalence of 4 % under normal growth conditions.

The second possible lag phenotype is a more complex one. The lag period of *S. aureus* under low silver stress appears to contain more than one distribution:

- Approximately 10 % of the cells have a lag period comparable with the mode of the population of cells grown under control conditions;
- Approximately 30 % of the population have a lag period comparable to that of the secondary distribution of the cells grown under control conditions;
- Approximately 10 % of the cells have a lag period comparable with the median of the higher silver stressed population.

As with the control sample, the 10 % of the distribution which have a comparatively slow lag period could be identified as SCVs, however these cells are not lowly ranked in the rate distribution, and do not fit the classification of SCVs suggested above. The cells with a short lag period, in the lower 10 % of the distribution could be classified as colonies much like the 'super bugs' identified in the *E. coli* growth distributions. However, of the 10 cells in this distribution, 5 of them have growth rates which were among the skewed region of the growth rates and 5 did not. It is possible that this identifies 5 % of the distribution which have a 'super-bug' phenotype but this would require further classifications.

Growth Rate

The average growth rate reduces as the silver ion concentration increases, with the rate of growth for the highest silver stress concentration over three times slower than the median growth rate of the control sample. On average 85 % of the proteins within the genome are vulnerable to silver based on their cysteine residue content^[40] and so a silver dose-dependent decreases in the growth

rate is expected and consistent with the results. The range of the parameter distribution reduces significantly with increasing silver dose; the distributions of cells grown under control conditions and low silver stress conditions having fast growing outliers defined the Boxplot. The outliers of the control growth rate distribution account for 6 % of the population in the upper limit and are similarly in the upper 20 % of the length at t_0 distribution. On division, *S. aureus* cells remain closely associated^[13] and can be considered as one individual with an extended phenotype⁵⁴. If the ability to withstand the silver stress depends on threshold levels of particular proteins within an organism and the attainment of a particular cell volume (as discussed in Chapter 3) then the larger *S. aureus* colony will have reached or attained these protective or critical concentrations more rapidly and therefore grow faster; the colony growing synergistically. Similarly, for low silver stress, the top 2 % of cells with the fastest growth rate are also in the top 5 % of the length at t_0 distribution. These two classifications corroborate that the size phenotype confers protection to the environment. Larger colonies do not however dominate the viable cells in the high silver stress growth. The formation of SCVs in populations of *S. aureus* has been well documented^[41-43] and SCVs characterised phenotypically by a slow growth rate and have an atypical cell morphology^[44]. There is a reasonable case for SCVs to also have long lag phases on transition to surface growth. The prevalence of the possible SCV colonies is small, to better quantify this phenotype the screening should be repeated for a larger starting N .

The Lensless microscope collected only a 2D diffraction pattern which does however contain the information for the 3D image re-construction. The ADF calibration technique does not, however, produce the 3D image preferring the multi-wavelength illumination to not hinder growth. As a result the dimension derived from the colonies are 2D reflecting a projection of the dimensions of what is known to be a 3D colony growth pattern in *S. aureus*^[14]. In addition, the rates of growth and, less likely, lag may not represent the growth dynamics of the colonies, which would need to be characterised potentially along all three axes. Disruption of the 3D growth by silver could then show directional dependence.

Nevertheless, there are some interesting phenotypes extracted from the 4 parameters that survived the screening process. This investigation has identified 5 possible growth phenotypes:

1. Longer survivors under silver stress conditions;
2. The complex distribution containing 2 or more phenotypes for lag period under low levels of silver stress;
3. The long lag period outliers in the control growth data;
4. The fast growth rate outliers correlated to length in the low silver stress conditions;

5. The fast growth rate outliers correlated to length in the control growth data;

The prevalence of the lag phase SCV candidate is low at 4 % which suggests a much larger study would be required. The multi-dimensional classification however suggests the potential for automated classifications based on an algorithm looking simultaneously position or rank in a number of distributions to provide a phenotype classification.

5.5 Conclusion

The running theme of the thesis is the growth phenotype derived from a common genotype that is triggered in response to the environment. This chapter aimed to determine whether there are growth parameters within the control and silver stress growth samples which indicate that there may be phenotypes within the data. The length and widths of colonies at t_0 minutes show that the lower percentiles of the distributions, in both silver stressed growth environments, are not viable. The smallest colonies have not got the required volume of proteins to overcome silver stress. The MIC of silver for *S. aureus* is lower than that for *E. coli* but not *S. pombe*. The lower MIC coupled with the fact that silver does not induce favourable stress phenotypes in *S. aureus*, as it does in *E. coli*, suggests that being Gram positive is not advantageous in a silver shifted growth environment.

The response to the environment and the time it takes to respond is the lag period. Some cells do not survive the transition and others have longer or short delays before growth starts. This is a systems-level response and in *S. aureus*, *S. pombe* and *E. coli* this seems to have provided a number of candidate phenotypes. The range of lag period under low levels of silver stress is high, indication that the range of phenotypes of lag periods is high under low silver stress. The range of the lag period distribution is three times wider than the range of lag periods under higher silver stress, the distribution of cells grown under high levels of silver stress having a median of 289 (+3 -2.5) minutes, the same length as the extreme outliers on the low silver stress growth distribution. Relatively, silver stress slows down every cell process; distributions are more spread, perhaps, because an accumulation of proteins which would ordinarily take 1 minute takes 10 minutes in silver stress.

Silver stress significantly changes the growth phenotype of *S. aureus*. The length of the lag period, the time the cell takes to adjust to new environmental conditions, is increased by over 2-fold, the rate of growth reduced over 3 times and the viable cells have to have passed a threshold size to survive under silver stress.

The growth phenotypes of observed under control growth conditions of this Gram positive bacteria can be compared to those observed under control conditions for Gram negative bacteria, in-order to build up an initial look at the discrimination between cells based on their growth phenotypes. In

Chapter 6 the distributions collected and analysed here and in Chapter 4 will be compared to the data obtained from unknown cells from dirty environments to assess the validity of this technique as a microbial discrimination technique.

5.6 References

1. Edmond, M.B., et al., *Nosocomial Bloodstream Infections in United States Hospitals: A Three-Year Analysis*. Clinical Infectious Diseases, 1999. **29**(2): p. 239-244.
2. Evans, C.A., et al., *Bacterial Flora of the Normal Human Skin*. The Journal of Investigative Dermatology, 1950. **15**(4): p. 305-324.
3. von Eiff, C., et al., *Nasal Carriage as a Source of Staphylococcus aureus Bacteremia*. New England Journal of Medicine, 2001. **344**(1): p. 11-16.
4. Kluytmans, J., A. van Belkum, and H. Verbrugh, *Nasal carriage of Staphylococcus aureus: epidemiology, underlying mechanisms, and associated risks*. Clinical Microbiology Reviews, 1997. **10**(3): p. 505-20.
5. NCBI. *Genome*. 2013 [cited 2013 14th December]; Available from: http://www.ncbi.nlm.nih.gov/genome/154?project_id=57795.
6. Harris, L.G., S.J. Foster, and R.G. Richards, *AN INTRODUCTION TO STAPHYLOCOCCUS AUREUS, AND TECHNIQUES FOR IDENTIFYING AND QUANTIFYING S. AUREUS ADHESINS IN RELATION TO ADHESION TO BIOMATERIALS: REVIEW*. European Cells and Materials, 2002. **4**: p. 39-60.
7. Touhami, A., M.H. Jericho, and T.J. Beveridge, *Atomic Force Microscopy of Cell Growth and Division in Staphylococcus aureus*. Journal of Bacteriology, 2004. **186**(11): p. 3286-3295.
8. Collins, L.V., et al., *Staphylococcus aureus strains lacking D-alanine modifications of teichoic acids are highly susceptible to human neutrophil killing and are virulence attenuated in mice*. Journal of Infectious Diseases, 2002. **186**(2): p. 214-219.
9. De Kimpe, S.J., et al., *The cell wall components peptidoglycan and lipoteichoic acid from Staphylococcus aureus act in synergy to cause shock and multiple organ failure*. Proceedings of the National Academy of Sciences, 1995. **92**(22): p. 10359-10363.
10. Thomas, J.C., et al., *Draft Genome Sequences of Staphylococcus aureus Sequence Type 34 (ST34) and ST42 Hybrids*. Journal of Bacteriology, 2012. **194**(10): p. 2740-2741.
11. Feng, Q., et al., *A mechanistic study of the antibacterial effect of silver ions on Escherichia coli and Staphylococcus aureus*. Journal of biomedical materials research, 2000. **52**(4): p. 662-668.
12. Gauger, A., et al., *Silver-coated textiles reduce Staphylococcus aureus colonization in patients with atopic eczema*. Dermatology, 2003. **207**(1): p. 15-21.
13. Tzagoloff, H. and R. Novick, *Geometry of cell division in Staphylococcus aureus*. Journal of Bacteriology, 1977. **129**(1): p. 343-350.
14. Amako, K. and A. Umeda, *Mode of cell separation and arrangement of Staphylococcus*. Microbiology and immunology, 1979. **23**(5): p. 329.
15. Suzuki, T., et al., *Wall teichoic acid protects Staphylococcus aureus from inhibition by Congo red and other dyes*. Journal of Antimicrobial Chemotherapy, 2012. **67**(9): p. 2143-2151.
16. Schwandner, R., et al., *Peptidoglycan-and lipoteichoic acid-induced cell activation is mediated by toll-like receptor 2*. Journal of Biological Chemistry, 1999. **274**(25): p. 17406-17409.
17. Waldvogel, F.A., *Staphylococcus aureus*. Principles and Practice of Infectious Disease, ed. Mandell GL, Douglas RG, and B. JE. 1990, London: Churchill Livingstone.
18. Knox, W.E. and K.H. Schleifer, *Genus IV –Staphylococcus Rosenbach 1884*. Bergey's Manual of Systemic Bacteriology, ed. Sneath PHA, Mair NS, and S. ME. 1986, Baltimore.
19. Swoboda, J.G., et al., *Wall Teichoic Acid Function, Biosynthesis, and Inhibition*. ChemBioChem, 2010. **11**(1): p. 35-45.
20. Xia, G., T. Kohler, and A. Peschel, *The wall teichoic acid and lipoteichoic acid polymers of Staphylococcus aureus*. International Journal of Medical Microbiology, 2010. **300**(2-3): p. 148-154.

21. Peschel, A., et al., *The d-Alanine Residues of Staphylococcus aureus Teichoic Acids Alter the Susceptibility to Vancomycin and the Activity of Autolytic Enzymes*. Antimicrobial agents and chemotherapy, 2000. **44**(10): p. 2845-2847.
22. Aly, R., et al., *Role of teichoic acid in the binding of Staphylococcus aureus to nasal epithelial cells*. Journal of Infectious Diseases, 1980. **141**(4): p. 463-465.
23. Weidenmaier, C., et al., *Role of teichoic acids in Staphylococcus aureus nasal colonization, a major risk factor in nosocomial infections*. Nat Med, 2004. **10**(3): p. 243-245.
24. Meredith, T.C., J.G. Swoboda, and S. Walker, *Late-stage polyribitol phosphate wall teichoic acid biosynthesis in Staphylococcus aureus*. Journal of Bacteriology, 2008. **190**(8): p. 3046-3056.
25. Pereira, M.P., et al., *Duplication of teichoic acid biosynthetic genes in Staphylococcus aureus leads to functionally redundant poly (ribitol phosphate) polymerases*. Journal of Bacteriology, 2008. **190**(16): p. 5642-5649.
26. Cross, A.S., *What is a virulence factor?* Critical Care, 2008. **12**(6): p. 196.
27. Recsei, P., et al., *Regulation of exoprotein gene expression in Staphylococcus aureus by agr*. Molecular and General Genetics MGG, 1986. **202**(1): p. 58-61.
28. Jarraud, S., et al., *Relationships between Staphylococcus aureus Genetic Background, Virulence Factors, agr Groups (Alleles), and Human Disease*. Infection and Immunity, 2002. **70**(2): p. 631-641.
29. Livermore, D.M., *Antibiotic resistance in staphylococci*. International Journal of Antimicrobial Agents, 2000. **16**: p. 3-10.
30. Hiramatsu, K., *Vancomycin resistance in staphylococci*. Drug resistance updates, 1998. **1**(2): p. 135-150.
31. Hiramatsu, K., *Vancomycin-resistant Staphylococcus aureus: a new model of antibiotic resistance*. The Lancet Infectious Diseases, 2001. **1**(3): p. 147-155.
32. Edwards-Jones, V., *Antimicrobial and barrier effects of silver against methicillin-resistant Staphylococcus aureus*. Journal of Wound Care, 2006. **15**(7): p. 285-290.
33. Jung, W.K., et al., *Antibacterial Activity and Mechanism of Action of the Silver Ion in Staphylococcus aureus and Escherichia coli*. Applied and Environmental Microbiology, 2008. **74**(7): p. 2171-2178.
34. Lansdown, A.B.G., *Silver 1: its antibacterial properties and mechanism of action*. Journal of Wound Care, 2002. **11**(4): p. 125-130.
35. Percival, S.L., P.G. Bowler, and D. Russell, *Bacterial resistance to silver in wound care*. Journal of Hospital Infection, 2005. **60**(1): p. 1-7.
36. Loh, J.V., et al., *Silver resistance in MRSA isolated from wound and nasal sources in humans and animals*. International wound journal, 2009. **6**(1): p. 32-38.
37. von Eiff, C., *Staphylococcus aureus small colony variants: a challenge to microbiologists and clinicians*. International Journal of Antimicrobial Agents, 2008. **31**(6): p. 507-510.
38. Vesga, O., et al., *Staphylococcus aureus small colony variants are induced by the endothelial cell intracellular milieu*. Journal of Infectious Diseases, 1996. **173**(3): p. 739-742.
39. Massey, R.C., A. Buckling, and S.J. Peacock, *Phenotypic switching of antibiotic resistance circumvents permanent costs in Staphylococcus aureus*. Current Biology, 2001. **11**(22): p. 1810-1814.
40. Miseta, A. and P. Csutora, *Relationship Between the Occurrence of Cysteine in Proteins and the Complexity of Organisms*. Molecular Biology and Evolution, 2000. **17**(8): p. 1232-1239.
41. Proctor, R.A., et al., *Persistent and Relapsing Infections Associated with Small-Colony Variants of Staphylococcus aureus*. Clinical Infectious Diseases, 1995. **20**(1): p. 95-102.
42. Kahl, B., et al., *Persistent infection with small colony variant strains of Staphylococcus aureus in patients with cystic fibrosis*. Journal of Infectious Diseases, 1998. **177**(4): p. 1023-1029.
43. Sendi, P., et al., *Staphylococcus aureus small colony variants in prosthetic joint infection*. Clinical Infectious Diseases, 2006. **43**(8): p. 961-967.

44. Proctor, R.A., et al., *Small colony variants: a pathogenic form of bacteria that facilitates persistent and recurrent infections*. Nat Rev Micro, 2006. **4**(4): p. 295-305.

6 Conclusions and Future Work

The aim of the investigations in this thesis was to assess the performance of the Lensless microscope technology for the rapid identification of growth phenotypes with potential for rapid identification of organism at point of care. The first objective was to develop the Lensless microscope technology to measure accurately growth of organisms monitoring larger numbers of cells or colonies simultaneously in the large field of view. The instrument supports and monitors microorganism growth at an elevated temperature and is temperature stable over 600 minutes, the elevated temperature having no detrimental effects on the image collection. An image processing algorithm was invented to extract 2-dimensions from the Airy Disc diffraction pattern at the accuracy of the diffraction limit below 6 microns and with 5 % accuracy up to 600 microns. The algorithm was successful and the length and the width of spherical and rod shaped organisms we measured to within 5% and an $R^2=0.997$ with optically validated images.

A method for deriving, and screening, a set of growth phenotype classification parameters has been developed which were then used for the subsequent classification of phenotypes whether from within an extended parameter distribution or the evolution into a bimodal distribution. The methods of determining phenotypes have been applied to analyse the growth parameters of three model organisms;

- a. Single cellular behaviour of eukaryote *S. pombe*;
- b. Phenotypes of single cells and small colonies of the Gram-negative prokaryote *E. coli*;
- c. Phenotypes of single cells and small colonies of the Gram-positive prokaryote *S. aureus*.

In total, 19 different growth phenotypes were identified for all three organisms under normal and silver stressed growth condition. The characteristics of a phenotype have been developed in this thesis and the most promising definition is: a phenotype is the response of a genotype to its environment. The growth parameters that reflect this directly are the survival rate for organism moving from planktonic to surface growth with and without silver. There is a lag time or period of adjustment to the new environment which again appears point strongly to the phenotype identification. The most striking phenotype identified from lag time alone produced the most promising results of the thesis.

The growth parameters lag time and growth rate identified phenotypes of *E. coli* under silver stress growth conditions. The 64 % of cells that survive the transition to the silver stressed growth medium, 54 % for two distinct sub populations classified by their lag period, growth rate and large final colony size. These two phenotypes were termed 'super-bug' and 'sub-bug' both of which have a phenotypic resistance to the growth on silver. Several colonies were screened using the Lensless microscope and sent for genetic sequencing using the Illumina platform in-house. The genomes match the reference genome within comparison error confirming the phenotype resistance. Similar phenotypic resistance is seen in the sub-bug population but with a slower growth rate. These findings have implications in the medical industry in the use of silver in wound care. The data imply that at some sub-lethal level of silver, distal to the silver-impregnated wound site results in the promotion of these 'super-bugs' can occur. Silver is included in wound dressings to act as a broad spectrum antimicrobial, so aiding wound healing. Wound healing is also affected by the effect silver has on the growth of the eukaryotic cell, if the growth of *S. pombe* is an indicator of eukaryotic growth. The growth phenotypes identified in the eukaryotic *S. pombe* display several interesting properties most importantly a significant elongation of the cell cycle which is related to wound repair. The median of the cell cycle is over 4 times longer than the median of the cell cycle in the phenotype grown without silver nitrate. The cells also display a significantly longer lag period, a slower growth rate and a shorter division length. Cells above the 85th percentile, on exposure to silver, are unlikely to subsequently grow and divide.

The analysis of *S. aureus* growth phenotypes shows that there are outliers in the lag period distribution, under normal growth conditions which may be the first indicator of a distribution of small colony variants. *S. aureus* has implications in HAIs, the use of antibiotics too high, causing the introduction of silver as an antimicrobial agent. This thesis has demonstrated that, while silver appears to have only a detrimental effect on *S. aureus* growth, the effect on the phenotype of *E. coli* is pronounced. However these results should be verified using the alternative silver delivery by nanoparticle as the nanoparticle will induce higher local silver ion concentration.

S. aureus cells gain resistance readily from other bacteria by lateral gene transfer. Lateral gene transfer between clonal populations will likely not give rise to resistant genotypes as there is no introduction of new resistant genetic material. The analysis of mixed colonies is a first look at the ability of the device to perform in a point of care environment. The analysis here can be combined with the growth parameters determined in the previous chapters for a first look at grouping organisms based on their individual growth phenotypes. Future expansion of this data can take one of a few routes.

The Lensless microscope has been demonstrated as a successful screening instrument for growth phenotypes and can be used to identify and potentially classify phenotypes and for further analysis. *E. coli* shows a bimodal wild type lag period phenotype and a bimodal silver stress growth phenotype, both observed by the Lensless microscope. The cells can be removed from the surface and analysed for proteomics and metabolomics using Atmospheric pressure matrix-assisted laser desorption/ionization (AP MALDI TOF) as we have verified that the cells from these distributions do not vary in genome composition. Persister cells have been known for some time in *E. coli* but their study is hampered by identification techniques. The Lensless microscope can identify these colonies rapidly and then progress further experiments.

Extending the method of simple distributional analysis may be achieved by considering the evolution of the phenotype in time and how it might change position or rank in a distribution. A method of classification of growth phenotypes can therefore be considered a trajectory, indeed the trajectory itself may be considered the phenotype. For example, the position a cell occupies in the length distribution over time defines its constantly changing phenotype and is surely related to the complement of proteins within a cell, as was discussed in chapter 1 that a cell in a clonal population may have a larger concentration of one protein than another cell. This population heterogeneity, the effect that specific protein levels have on growth, is what the Lensless microscope can rapidly determine.

Another trajectory analysis would look at whether the position an organism occupies in the distribution of one parameter is a predictor of where it would be in a subsequent distribution. An initial look at how this might separate interesting phenotypes is displayed in Figure 6.1 for *E. coli* cells grown in control conditions. Here the lines take the position of each colony (percentile) in the distribution between the parameter distributions, colour coded for starting colony size.

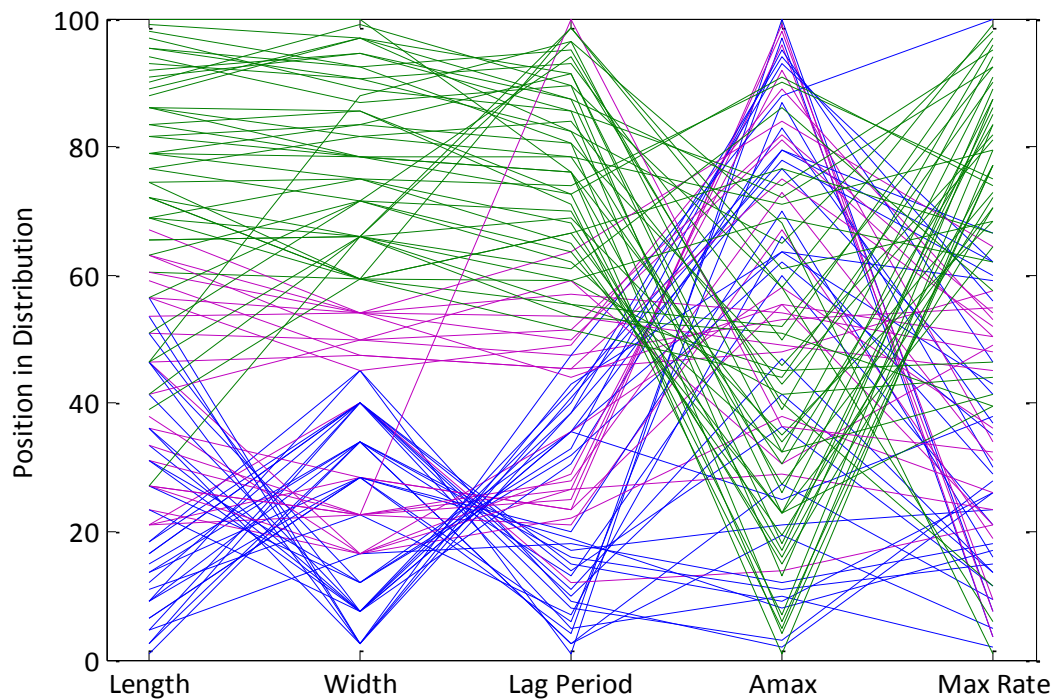


Figure 6.1 The evolution of individual cell phenotypes through various distributions colour coded for a combination of their lengths and widths at t_0 , blue cells are single cells, purple cells are calculated to be two cells and green cells are those which are likely to be small colonies.

The trajectory analysis in Figure 6.1, while demonstrating general trends, does not show groups of cells with comparable phenotype or help demonstrate whether a long length at t_0 has implications on the positioning in subsequent distributions. To develop this method further would require development or evaluation of analysis techniques such as cluster analysis (kmeans). Another analysis could take the trajectories through the parameters distributions and analyse them to determine emerging phenotypes. The Lensless microscope has many advantages as a device to monitor bacterial growth over the phase-contrast microscope found traditionally in the laboratory. The Lensless microscope can monitor the growth of 100s of cells simultaneously over a time course, recording and analysing the growth parameters of all the cells in the population. The device has a flow cell which closely mimics the growth conditions of planktonic growth and surface growth and is thermostatically regulated for favourable growth conditions. The Lensless microscope is able to track a single cell as it moves, having a depth of focus of at least 4000 times that of the phase contrast microscope and a field of view of two orders of magnitude larger. The Lensless microscope images the whole sample at one time, meaning that if there is only one cell in the sample it will be easily detected and monitored, and the internal calibration allowing for initial user assembly error. This method can be used, without modification, to investigate the effect of various antimicrobials on cell populations, the effects of stress types on the cell population and the emergence of persister cells in

different environmental conditions. The Lensless microscope has the potential to replace the light microscope within the laboratory to provide basic aspect ratio data about the cells imaged, as this device requires no calibration or focusing, and has its own measurement algorithm, results will be more rapid.

To conclude, this thesis has identified 19 growth phenotypes in three different microorganisms, *S. pombe*, *E. coli* and *S. aureus*, Table 6.1.

Table 6.1 A table of all the growth phenotypes identified in this thesis.

Organism	Phenotype	Prevalence
<i>S. pombe</i>	G ₀ phenotype;	35%
	Long length at division (L _B);	12%
	Modal quartile of lengths at t ₀ survive silver stress;	65%
	A ratio of NETO rates larger than 1.35;	8%
	Long length at t ₀ leads to long length at division	9%
	Lag period length skewed towards longer recovery times;	10%
	NETO not apparent in silver stress distribution;	100%
<i>E. coli</i>	Survivors under low silver stress	67%
	Survivors under high silver stress	43%
	Short lag under control conditions	20%
	Long lag under control conditions	80%
	'super-bugs' under high silver stress viable colonies	6%
	'sub-bugs' under high silver stress viable colonies	41%
<i>S. aureus</i>	Long lag period under control conditions	4%
	Survivors under low silver stress	63%
	Survivors under high silver stress	33%

	Threshold width of survival under silver stress	80%
	Fast growth rate outliers correlated to length	4%

The field of phenotype identification is significantly behind that of genotype taxonomy and the identification of species and yet the phenotype and extended phenotype are potential response identifiers for the development of resistant strains of bacteria. This thesis has identified that the silver stress has detrimental consequences for eukaryotic cells as well as prokaryotic cells. The device has the potential to explore the effects of silver on other eukaryotic cell growth, namely human cells, to determine whether the response of *S. pombe* to the presence of silver in the growth environment has implications to wound healing. This thesis has highlighted that there is only limited understanding of the response to a mixed cell sample to a stress, an environment which could be simulated and monitored using the Lensless microscope.

Appendix 1

A list of components required for the
Lensless Microscope.

Optical Breadboard (Thorlabs B6090AE)

Ø1" Pillar Post Extension, L = 12" (Thorlabs, RS12)

Ø1" Ceramic Pedestal Pillar Post, Length = 1/2" (Thorlabs, RS05PC)

Post Mounting Clamp for Ø1" Post (Thorlabs, C1001)

4 x 25 mm Construction Rail, L = 18" (Thorlabs, XE25L18)

2 x 25 mm Construction Rail, L = 12" (Thorlabs, XE25L12)

2 x 25 mm Construction Rail, L = 9" (Thorlabs, XE25L09)

4 x Quick Corner Cube for 25 mm Rails (Thorlabs, XE25W3)

1/4"-20 Low-Profile Channel Screws (100 Screws/Box) (Thorlabs, SH25LP38)

2 x Black posterboard (Thorlabs, TB5)

Newport 900PH-100 100 Micron Aperture Pinhole (Lightglass Optics)

White mounted high power LED (Thorlabs, MWWHL3^c)

Exo Terra Ceramic Heat Emitter 100W (Blue Lizard Reptiles)

Microclimate Prime 1 thermostat (Blue Lizard Reptiles)

Komodo Mountable Ceramic Lamp Fixture (Blue Lizard Reptiles)

Appendix 2

The ADFP algorithm

The 'normality.m' program

Program Name: ADFF

```
display('running find aspect ratio eighth bowtie black and white. . .');
pause on
workspace;

%Load data into matlab separately first
%Chose section and input in as below (?:?,?:?)
SUB= %insert file name here;

subplot(2,4,1);
imshow(SUB,[min(SUB(:)) max(SUB(:))]);
drawnow;
caption = sprintf('Airy Disc');
title(caption);
axis square;

%create mask
%(cx,cy)=centre coordinates of the circle
%(ix,iy)=size of the whole mask
%r=radius
cx=280;
cy=280;
r=150;
ix=560;
iy=560;
[x,y]=meshgrid(-(cx-1):(ix-cx),-(cy-1):(iy-cy));
c_mask=(x.^2+y.^2)<=r^2);

%create a mask for the central region in the same way as above
%r is the only element to change and note < changes to >.
r=50;
[x,y]=meshgrid(-(cx-1):(ix-cx),-(cy-1):(iy-cy));
c_mask1=(x.^2+y.^2)>=r^2);

%create anulus mask
AnulusFull=c_mask.*c_mask1;

AnulusFull=AnulusFull.*SUB;

subplot(2,4,2)
imshow(AnulusFull,[min(AnulusFull(:)) max(AnulusFull(:))]);
drawnow;
caption = sprintf('Mask');
title(caption);
axis square;

%
%%%%%%%%%%%%%%%%%%%%%%%%%%%%%%%%%%%%%%%%%%%%%%%%%%%%%%%%%%%%%%%%%%%%%%%%%%
%ZERO Choose section to analyse
x=[0 280 280]; %3 values for x
y=[280 0 280]; %3 values for y

%Turn into a mask
ThetaMask0 = poly2mask(x, y, 560, 560); %560=size of whole mask

%Choose section to analyse
x=[0 560 280]; %3 values for x
```

```

y=[0 0 280]; %3 values for y

%Turn into a mask
ThetaMask0a = poly2mask(x, y, 560, 560); %560=size of whole mask

%Multiply mask by mask by anulus matrix
Anulus0=(ThetaMask0.*ThetaMask0a).*AnulusFull;

%Choose section to analyse
x=[560 280 280]; %3 values for x
y=[280 560 280]; %3 values for y

%Turn into a mask
ThetaMask57 = poly2mask(x, y, 560, 560); %560=size of whole mask

%Choose section to analyse
x=[560 0 280]; %3 values for x
y=[560 560 280]; %3 values for y

%Turn into a mask
ThetaMask57a = poly2mask(x, y, 560, 560); %560=size of whole mask

%Multiply mask by mask by anulus matrix
Anulus57=(ThetaMask57.*ThetaMask57a).*AnulusFull;

Anulus0=Anulus0+Anulus57;

%Average the mask
ANULUS0=sum(Anulus0);
ANULUS0=sum(ANULUS0/(nnz(Anulus0)));

subplot(2,4,3)
imshow(Anulus0,[min(Anulus0(:)) max(Anulus0(:))]);
drawnow;
caption = sprintf('0 degrees');
title(caption);
axis square;
%
%
%Choose section to analyse
x=[0 260 280]; %3 values for x
y=[300 0 280]; %3 values for y

%Turn into a mask
ThetaMask1 = poly2mask(x, y, 560, 560); %560=size of whole mask

%Choose section to analyse
x=[0 540 280]; %3 values for x
y=[20 0 280]; %3 values for y

%Turn into a mask
ThetaMask1a = poly2mask(x, y, 560, 560); %560=size of whole mask

%Multiply mask by mask by anulus matrix
Anulus1=(ThetaMask1.*ThetaMask1a).*AnulusFull;

%Choose section to analyse

```

```

x=[560 300 280]; %3 values for x
y=[260 560 280]; %3 values for y

%Turn into a mask
ThetaMask58 = poly2mask(x, y, 560, 560); %560=size of whole mask

%Choose section to analyse
x=[560 20 280]; %3 values for x
y=[540 560 280]; %3 values for y

%Turn into a mask
ThetaMask58a = poly2mask(x, y, 560, 560); %560=size of whole mask

%Multiply mask by mask by anulus matrix
Anulus58=(ThetaMask58.*ThetaMask58a).*AnulusFull;

Anulus1=Anulus1+Anulus58;

%Average the mask
ANULUS1=sum(Anulus1);
ANULUS1=sum(ANULUS1/(nnz(Anulus1)));
%
%%%%%%%%%%%%%%%%%%%%%%%%%%%%%%%%%%%%%%%%%%%%%%%%%%%%%%%%%%%%%%%%%%%%%%%%%%
%Choose section to analyse
x=[0 240 280]; %3 values for x
y=[320 0 280]; %3 values for y

%Turn into a mask
ThetaMask2 = poly2mask(x, y, 560, 560); %560=size of whole mask

%Choose section to analyse
x=[0 520 280]; %3 values for x
y=[40 0 280]; %3 values for y

%Turn into a mask
ThetaMask2a = poly2mask(x, y, 560, 560); %560=size of whole mask

%Multiply mask by mask by anulus matrix
Anulus2=(ThetaMask2.*ThetaMask2a).*AnulusFull;

%Choose section to analyse
x=[560 320 280]; %3 values for x
y=[240 560 280]; %3 values for y

%Turn into a mask
ThetaMask59 = poly2mask(x, y, 560, 560); %560=size of whole mask

%Choose section to analyse
x=[560 40 280]; %3 values for x
y=[520 560 280]; %3 values for y

%Turn into a mask
ThetaMask59a = poly2mask(x, y, 560, 560); %560=size of whole mask

%Multiply mask by mask by anulus matrix
Anulus59=(ThetaMask59.*ThetaMask59a).*AnulusFull;

Anulus2=Anulus2+Anulus59;

```

```

%Average the mask
ANULUS2=sum(Anulus2);
ANULUS2=sum(ANULUS2/(nnz(Anulus2)));

%
%%%%%%%%%%%%%%%%%%%%%%%%%%%%%%%%%%%%%%%%%%%%%%%%%%%%%%%%%%%%%%%%%%%%%%%%%%%%%%
%Choose section to analyse
x=[0 230 280]; %3 values for x
y=[330 0 280]; %3 values for y

%Turn into a mask
ThetaMask3 = poly2mask(x, y, 560, 560); %560=size of whole mask

%Choose section to analyse
x=[0 500 280]; %3 values for x
y=[60 0 280]; %3 values for y

%Turn into a mask
ThetaMask3a = poly2mask(x, y, 560, 560); %560=size of whole mask

%Multiply mask by mask by anulus matrix
Anulus3=(ThetaMask3.*ThetaMask3a).*AnulusFull;

%Choose section to analyse
x=[560 340 280]; %3 values for x
y=[220 560 280]; %3 values for y

%Turn into a mask
ThetaMask60 = poly2mask(x, y, 560, 560); %560=size of whole mask

%Choose section to analyse
x=[560 60 280]; %3 values for x
y=[500 560 280]; %3 values for y

%Turn into a mask
ThetaMask60a = poly2mask(x, y, 560, 560); %560=size of whole mask

%Multiply mask by mask by anulus matrix
Anulus60=(ThetaMask60.*ThetaMask60a).*AnulusFull;

Anulus3=Anulus3+Anulus60;

%Average the mask
ANULUS3=sum(Anulus3);
ANULUS3=sum(ANULUS3/(nnz(Anulus3)));

%
%%%%%%%%%%%%%%%%%%%%%%%%%%%%%%%%%%%%%%%%%%%%%%%%%%%%%%%%%%%%%%%%%%%%%%%%%%%%%%
%Choose section to analyse
x=[0 210 280]; %3 values for x
y=[340 0 280]; %3 values for y

%Turn into a mask
ThetaMask4 = poly2mask(x, y, 560, 560); %560=size of whole mask

%Choose section to analyse
x=[0 480 280]; %3 values for x
y=[80 0 280]; %3 values for y

```

```

%Turn into a mask
ThetaMask4a = poly2mask(x, y, 560, 560); %560=size of whole mask

%Multiply mask by mask by anulus matrix
Anulus4=(ThetaMask4.*ThetaMask4a).*AnulusFull;

%Choose section to analyse
x=[560 360 280]; %3 values for x
y=[200 560 280]; %3 values for y

%Turn into a mask
ThetaMask61 = poly2mask(x, y, 560, 560); %560=size of whole mask

%Choose section to analyse
x=[560 80 280]; %3 values for x
y=[480 560 280]; %3 values for y

%Turn into a mask
ThetaMask61a = poly2mask(x, y, 560, 560); %560=size of whole mask

%Multiply mask by mask by anulus matrix
Anulus61=(ThetaMask61.*ThetaMask61a).*AnulusFull;

Anulus4=Anulus4+Anulus61;

%Average the mask
ANULUS4=sum(Anulus4);
ANULUS4=sum(ANULUS4/(nnz(Anulus4)));

%


---


%
%Choose section to analyse
x=[0 190 280]; %3 values for x
y=[360 0 280]; %3 values for y

%Turn into a mask
ThetaMask5 = poly2mask(x, y, 560, 560); %560=size of whole mask

%Choose section to analyse
x=[0 460 280]; %3 values for x
y=[100 0 280]; %3 values for y

%Turn into a mask
ThetaMask5a = poly2mask(x, y, 560, 560); %560=size of whole mask

%Multiply mask by mask by anulus matrix
Anulus5=(ThetaMask5.*ThetaMask5a).*AnulusFull;

%Choose section to analyse
x=[560 380 280]; %3 values for x
y=[180 560 280]; %3 values for y

%Turn into a mask
ThetaMask62 = poly2mask(x, y, 560, 560); %560=size of whole mask

%Choose section to analyse
x=[560 100 280]; %3 values for x

```

```

y=[460 560 280]; %3 values for y

%Turn into a mask
ThetaMask62a= poly2mask(x, y, 560, 560); %560=size of whole mask

%Multiply mask by mask by anulus matrix
Anulus62=(ThetaMask62.*ThetaMask62a).*AnulusFull;

Anulus5=Anulus5+Anulus62;

%Average the mask
ANULUS5=sum(Anulus5);
ANULUS5=sum(ANULUS5/(nnz(Anulus5)));
%
%
%Choose section to analyse
x=[0 170 280]; %3 values for x
y=[380 0 280]; %3 values for y

%Turn into a mask
ThetaMask6 = poly2mask(x, y, 560, 560); %560=size of whole mask

%Choose section to analyse
x=[0 440 280]; %3 values for x
y=[120 0 280]; %3 values for y

%Turn into a mask
ThetaMask6a = poly2mask(x, y, 560, 560); %560=size of whole mask

%Multiply mask by mask by anulus matrix
Anulus6=(ThetaMask6.*ThetaMask6a).*AnulusFull;

%Choose section to analyse
x=[560 400 280]; %3 values for x
y=[160 560 280]; %3 values for y

%Turn into a mask
ThetaMask63 = poly2mask(x, y, 560, 560); %560=size of whole mask

% Choose section to analyse
x=[560 120 280]; %3 values for x
y=[440 560 280]; %3 values for y

%Turn into a mask
ThetaMask63a = poly2mask(x, y, 560, 560); %560=size of whole mask

%Multiply mask by mask by anulus matrix
Anulus63=(ThetaMask63.*ThetaMask63a).*AnulusFull;

Anulus6=Anulus6+Anulus63;

%Average the mask
ANULUS6=sum(Anulus6);
ANULUS6=sum(ANULUS6/(nnz(Anulus6)));
%
%
%Choose section to analyse
x=[0 150 280]; %3 values for x

```

```

y=[400 0 280]; %3 values for y

%Turn into a mask
ThetaMask7 = poly2mask(x, y, 560, 560); %560=size of whole mask

%Choose section to analyse
x=[0 420 280]; %3 values for x
y=[140 0 280]; %3 values for y

%Turn into a mask
ThetaMask7a = poly2mask(x, y, 560, 560); %560=size of whole mask

%Multiply mask by mask by anulus matrix
Anulus7=(ThetaMask7.*ThetaMask7a).*AnulusFull;

%Choose section to analyse
x=[560 420 280]; %3 values for x
y=[140 560 280]; %3 values for y

%Turn into a mask
ThetaMask64 = poly2mask(x, y, 560, 560); %560=size of whole mask

%Choose section to analyse
x=[560 140 280]; %3 values for x
y=[420 560 280]; %3 values for y

%Turn into a mask
ThetaMask64a = poly2mask(x, y, 560, 560); %560=size of whole mask

%Multiply mask by mask by anulus matrix
Anulus64=(ThetaMask64.*ThetaMask64a).*AnulusFull;

Anulus7=Anulus7+Anulus64;

%Average the mask
ANULUS7=sum(Anulus7);
ANULUS7=sum(ANULUS7/(nnz(Anulus7)));
%
%
%
%
%Choose section to analyse
x=[0 130 280]; %3 values for x
y=[420 0 280]; %3 values for y

%Turn into a mask
ThetaMask8 = poly2mask(x, y, 560, 560); %560=size of whole mask

%Choose section to analyse
x=[0 400 280]; %3 values for x
y=[160 0 280]; %3 values for y

%Turn into a mask
ThetaMask8a = poly2mask(x, y, 560, 560); %560=size of whole mask

%Multiply mask by mask by anulus matrix
Anulus8=(ThetaMask8.*ThetaMask8a).*AnulusFull;

% Choose section to analyse
x=[560 440 280]; %3 values for x

```

```

y=[120 560 280]; %3 values for y

%Turn into a mask
ThetaMask65 = poly2mask(x, y, 560, 560); %560=size of whole mask

%Choose section to analyse
x=[560 160 280]; %3 values for x
y=[400 560 280]; %3 values for y

%Turn into a mask
ThetaMask65a = poly2mask(x, y, 560, 560); %560=size of whole mask

%Multiply mask by mask by anulus matrix
Anulus65=(ThetaMask65.*ThetaMask65a).*AnulusFull;

Anulus8=Anulus8+Anulus65;

%Average the mask
ANULUS8=sum(Anulus8);
ANULUS8=sum(ANULUS8/(nnz(Anulus8)));
%
%%%%%%%%%%%%%%%%%%%%%%%%%%%%%%%%%%%%%%%%%%%%%%%%%%%%%%%%%%%%%%%%%%%%%%%%%%%%%%
%Choose section to analyse
x=[0 110 280]; %3 values for x
y=[440 0 280]; %3 values for y

%Turn into a mask
ThetaMask9 = poly2mask(x, y, 560, 560); %560=size of whole mask

%Choose section to analyse
x=[0 380 280]; %3 values for x
y=[180 0 280]; %3 values for y

%Turn into a mask
ThetaMask9a = poly2mask(x, y, 560, 560); %560=size of whole mask

%Multiply mask by mask by anulus matrix
Anulus9=(ThetaMask9.*ThetaMask9a).*AnulusFull;

%Choose section to analyse
x=[560 460 280]; %3 values for x
y=[100 560 280]; %3 values for y

%Turn into a mask
ThetaMask66 = poly2mask(x, y, 560, 560); %560=size of whole mask

%Choose section to analyse
x=[560 180 280]; %3 values for x
y=[380 560 280]; %3 values for y

%Turn into a mask
ThetaMask66a = poly2mask(x, y, 560, 560); %560=size of whole mask

%Multiply mask by mask by anulus matrix
Anulus66=(ThetaMask66.*ThetaMask66a).*AnulusFull;

Anulus9=Anulus9+Anulus66;

```

```

%Average the mask
ANULUS9=sum(Anulus9);
ANULUS9=sum(ANULUS9/(nnz(Anulus9)));
%
%
%Choose section to analyse
x=[0 90 280]; %3 values for x
y=[460 0 280]; %3 values for y

%Turn into a mask
ThetaMask10 = poly2mask(x, y, 560, 560); %560=size of whole mask

%Choose section to analyse
x=[0 360 280]; %3 values for x
y=[200 0 280]; %3 values for y

%Turn into a mask
ThetaMask10a = poly2mask(x, y, 560, 560); %560=size of whole mask

%Multiply mask by mask by anulus matrix
Anulus10=(ThetaMask10.*ThetaMask10a).*AnulusFull;

%Choose section to analyse
x=[560 480 280]; %3 values for x
y=[80 560 280]; %3 values for y

%Turn into a mask
ThetaMask67 = poly2mask(x, y, 560, 560); %560=size of whole mask

%Choose section to analyse
x=[560 200 280]; %3 values for x
y=[360 560 280]; %3 values for y

%Turn into a mask
ThetaMask67a = poly2mask(x, y, 560, 560); %560=size of whole mask

%Multiply mask by mask by anulus matrix
Anulus67=(ThetaMask67.*ThetaMask67a).*AnulusFull;

Anulus10=Anulus10+Anulus67;

%Average the mask
ANULUS10=sum(Anulus10);
ANULUS10=sum(ANULUS10/(nnz(Anulus10)));

subplot(2,4,4)
imshow(Anulus10,[min(Anulus10(:)) max(Anulus10(:))]);
drawnow;
caption = sprintf('32 degrees');
title(caption);
axis square;
%
%
%Choose section to analyse
x=[0 70 280]; %3 values for x
y=[480 0 280]; %3 values for y

%Turn into a mask
ThetaMask11 = poly2mask(x, y, 560, 560); %560=size of whole mask

```

```

%Choose section to analyse
x=[0 340 280]; %3 values for x
y=[220 0 280]; %3 values for y

%Turn into a mask
ThetaMask11a = poly2mask(x, y, 560, 560); %560=size of whole mask

%Multiply mask by mask by anulus matrix
Anulus11=(ThetaMask11.*ThetaMask11a).*AnulusFull;

%Choose section to analyse
x=[560 500 280]; %3 values for x
y=[60 560 280]; %3 values for y

%Turn into a mask
ThetaMask68 = poly2mask(x, y, 560, 560); %560=size of whole mask

% Choose section to analyse
x=[560 220 280]; %3 values for x
y=[340 560 280]; %3 values for y

%Turn into a mask
ThetaMask68a= poly2mask(x, y, 560, 560); %560=size of whole mask

%Multiply mask by mask by anulus matrix
Anulus68=(ThetaMask68.*ThetaMask68a).*AnulusFull;

Anulus11=Anulus11+Anulus68;

%Average the mask
ANULUS11=sum(Anulus11);
ANULUS11=sum(ANULUS11/(nnz(Anulus11)));
% _____ %

%Choose section to analyse
x=[0 50 280]; %3 values for x
y=[500 0 280]; %3 values for y

%Turn into a mask
ThetaMask12 = poly2mask(x, y, 560, 560); %560=size of whole mask

%Choose section to analyse
x=[0 320 280]; %3 values for x
y=[240 0 280]; %3 values for y

%Turn into a mask
ThetaMask12a = poly2mask(x, y, 560, 560); %560=size of whole mask

%Multiply mask by mask by anulus matrix
Anulus12=(ThetaMask12.*ThetaMask12a).*AnulusFull;

%Choose section to analyse
x=[560 520 280]; %3 values for x
y=[40 560 280]; %3 values for y

%Turn into a mask
ThetaMask69 = poly2mask(x, y, 560, 560); %560=size of whole mask

```

```

%Choose section to analyse
x=[560 240 280]; %3 values for x
y=[320 560 280]; %3 values for y

%Turn into a mask
ThetaMask69a = poly2mask(x, y, 560, 560); %560=size of whole mask

%Multiply mask by mask by anulus matrix
Anulus69=(ThetaMask69.*ThetaMask69a).*AnulusFull;

Anulus12=Anulus12+Anulus69;

%Average the mask
ANULUS12=sum(Anulus12);
ANULUS12=sum(ANULUS12/(nnz(Anulus12)));
%
%
%Choose section to analyse
x=[0 30 280]; %3 values for x
y=[520 0 280]; %3 values for y

%Turn into a mask
ThetaMask13 = poly2mask(x, y, 560, 560); %560=size of whole mask

%Choose section to analyse
x=[0 300 280]; %3 values for x
y=[260 0 280]; %3 values for y

%Turn into a mask
ThetaMask13a = poly2mask(x, y, 560, 560); %560=size of whole mask

%Multiply mask by mask by anulus matrix
Anulus13=(ThetaMask13.*ThetaMask13a).*AnulusFull;

%Choose section to analyse
x=[560 540 280]; %3 values for x
y=[20 560 280]; %3 values for y

%Turn into a mask
ThetaMask70 = poly2mask(x, y, 560, 560); %560=size of whole mask

%Choose section to analyse
x=[560 260 280]; %3 values for x
y=[300 560 280]; %3 values for y

%Turn into a mask
ThetaMask70a = poly2mask(x, y, 560, 560); %560=size of whole mask

%Multiply mask by mask by anulus matrix
Anulus70=(ThetaMask70.*ThetaMask70a).*AnulusFull;

Anulus13=Anulus13+Anulus70;

%Average the mask
ANULUS13=sum(Anulus13);
ANULUS13=sum(ANULUS13/(nnz(Anulus13)));

```

```

%
%
%Choose section to analyse
x=[0 10 280]; %3 values for x
y=[540 0 280]; %3 values for y

%Turn into a mask
ThetaMask14 = poly2mask(x, y, 560, 560); %560=size of whole mask

%Choose section to analyse
x=[0 280 280]; %3 values for x
y=[280 0 280]; %3 values for y

%Turn into a mask
ThetaMask14a = poly2mask(x, y, 560, 560); %560=size of whole mask

%Multiply mask by mask by anulus matrix
Anulus14=(ThetaMask14.*ThetaMask14a).*AnulusFull;

%Choose section to analyse
x=[560 560 280]; %3 values for x
y=[0 560 280]; %3 values for y

%Turn into a mask
ThetaMask71 = poly2mask(x, y, 560, 560); %560=size of whole mask

%Choose section to analyse
x=[560 280 280]; %3 values for x
y=[280 560 280]; %3 values for y

%Turn into a mask
ThetaMask71a = poly2mask(x, y, 560, 560); %560=size of whole mask

%Multiply mask by mask by anulus matrix
Anulus71=(ThetaMask71.*ThetaMask71a).*AnulusFull;

Anulus14=Anulus14+Anulus71;

%Average the mask
ANULUS14=sum(Anulus14);
ANULUS14=sum(ANULUS14/(nnz(Anulus14)));
%
%
%Choose section to analyse
x=[10 0 280]; %3 values for x
y=[560 10 280]; %3 values for y

%Turn into a mask
ThetaMask15 = poly2mask(x, y, 560, 560); %560=size of whole mask

%Choose section to analyse
x=[0 260 280]; %3 values for x
y=[300 0 280]; %3 values for y

%Turn into a mask
ThetaMask15a = poly2mask(x, y, 560, 560); %560=size of whole mask

```

```

%Multiply mask by mask by anulus matrix
Anulus15=(ThetaMask15.*ThetaMask15a).*AnulusFull;

%Choose section to analyse
x=[540 560 280]; %3 values for x
y=[0 540 280]; %3 values for y

%Turn into a mask
ThetaMask72 = poly2mask(x, y, 560, 560); %560=size of whole mask

%Choose section to analyse
x=[560 300 280]; %3 values for x
y=[260 560 280]; %3 values for y

%Turn into a mask
ThetaMask72a = poly2mask(x, y, 560, 560); %560=size of whole mask

%Multiply mask by mask by anulus matrix
Anulus72=(ThetaMask72.*ThetaMask72a).*AnulusFull;

Anulus15=Anulus15+Anulus72;

%Average the mask
ANULUS15=sum(Anulus15);
ANULUS15=sum(ANULUS15/(nnz(Anulus15)));
%

```

```

%Choose section to analyse
x=[30 0 280]; %3 values for x
y=[560 30 280]; %3 values for y

%Turn into a mask
ThetaMask16 = poly2mask(x, y, 560, 560); %560=size of whole mask

%Choose section to analyse
x=[0 240 280]; %3 values for x
y=[320 0 280]; %3 values for y

%Turn into a mask
ThetaMask16a = poly2mask(x, y, 560, 560); %560=size of whole mask

%Multiply mask by mask by anulus matrix
Anulus16=(ThetaMask16.*ThetaMask16a).*AnulusFull;

%Choose section to analyse
x=[520 560 280]; %3 values for x
y=[0 520 280]; %3 values for y

%Turn into a mask
ThetaMask73 = poly2mask(x, y, 560, 560); %560=size of whole mask

%Choose section to analyse
x=[560 320 280]; %3 values for x
y=[240 560 280]; %3 values for y

%Turn into a mask
ThetaMask73a = poly2mask(x, y, 560, 560); %560=size of whole mask

```

```

%Multiply mask by mask by anulus matrix
Anulus73=(ThetaMask73.*ThetaMask73a).*AnulusFull;

Anulus16=Anulus16+Anulus73;

%Average the mask
ANULUS16=sum(Anulus16);
ANULUS16=sum(ANULUS16/(nnz(Anulus16)));
%
%
%Choose section to analyse
x=[50 0 280]; %3 values for x
y=[560 50 280]; %3 values for y

%Turn into a mask
ThetaMask17 = poly2mask(x, y, 560, 560); %560=size of whole mask

%Choose section to analyse
x=[0 230 280]; %3 values for x
y=[330 0 280]; %3 values for y

%Turn into a mask
ThetaMask17a = poly2mask(x, y, 560, 560); %560=size of whole mask

%Multiply mask by mask by anulus matrix
Anulus17=(ThetaMask17.*ThetaMask17a).*AnulusFull;

%Choose section to analyse
x=[500 560 280]; %3 values for x
y=[0 500 280]; %3 values for y

%Turn into a mask
ThetaMask74 = poly2mask(x, y, 560, 560); %560=size of whole mask

%Choose section to analyse
x=[560 340 280]; %3 values for x
y=[220 560 280]; %3 values for y

%Turn into a mask
ThetaMask74a = poly2mask(x, y, 560, 560); %560=size of whole mask

%Multiply mask by mask by anulus matrix
Anulus74=(ThetaMask74.*ThetaMask74a).*AnulusFull;

Anulus17=Anulus17+Anulus74;

%Average the mask
ANULUS17=sum(Anulus17);
ANULUS17=sum(ANULUS17/(nnz(Anulus17)));
%
%
%Choose section to analyse
x=[60 0 280]; %3 values for x
y=[560 60 280]; %3 values for y

%Turn into a mask
ThetaMask18 = poly2mask(x, y, 560, 560); %560=size of whole mask

```

```

%Choose section to analyse
x=[0 210 280]; %3 values for x
y=[340 0 280]; %3 values for y

%Turn into a mask
ThetaMask18a = poly2mask(x, y, 560, 560); %560=size of whole mask

%Multiply mask by mask by anulus matrix
Anulus18=(ThetaMask18.*ThetaMask18a).*AnulusFull;

%Choose section to analyse
x=[480 560 280]; %3 values for x
y=[0 480 280]; %3 values for y

%Turn into a mask
ThetaMask75 = poly2mask(x, y, 560, 560); %560=size of whole mask

%Choose section to analyse
x=[560 360 280]; %3 values for x
y=[200 560 280]; %3 values for y

%Turn into a mask
ThetaMask75a = poly2mask(x, y, 560, 560); %560=size of whole mask

%Multiply mask by mask by anulus matrix
Anulus75=(ThetaMask75.*ThetaMask75a).*AnulusFull;

Anulus18=Anulus18+Anulus75;

%Average the mask
ANULUS18=sum(Anulus18);
ANULUS18=sum(ANULUS18/(nnz(Anulus18)));
% _____ %

%Choose section to analyse
x=[80 0 280]; %3 values for x
y=[560 80 280]; %3 values for y

%Turn into a mask
ThetaMask19 = poly2mask(x, y, 560, 560); %560=size of whole mask

%Choose section to analyse
x=[0 190 280]; %3 values for x
y=[360 0 280]; %3 values for y

%Turn into a mask
ThetaMask19a = poly2mask(x, y, 560, 560); %560=size of whole mask

%Multiply mask by mask by anulus matrix
Anulus19=(ThetaMask19.*ThetaMask19a).*AnulusFull;

%Choose section to analyse
x=[460 560 280]; %3 values for x
y=[0 460 280]; %3 values for y

%Turn into a mask
ThetaMask76 = poly2mask(x, y, 560, 560); %560=size of whole mask

```

```

%Choose section to analyse
x=[560 380 280]; %3 values for x
y=[180 560 280]; %3 values for y

%Turn into a mask
ThetaMask76a = poly2mask(x, y, 560, 560); %560=size of whole mask

%Multiply mask by mask by anulus matrix
Anulus76=(ThetaMask76.*ThetaMask76a).*AnulusFull;

Anulus19=Anulus19+Anulus76;

%Average the mask
ANULUS19=sum(Anulus19);
ANULUS19=sum(ANULUS19/(nnz(Anulus19)));

%


---


%Choose section to analyse
x=[100 0 280]; %3 values for x
y=[560 100 280]; %3 values for y

%Turn into a mask
ThetaMask20 = poly2mask(x, y, 560, 560); %560=size of whole mask

%Choose section to analyse
x=[0 170 280]; %3 values for x
y=[380 0 280]; %3 values for y

%Turn into a mask
ThetaMask20a = poly2mask(x, y, 560, 560); %560=size of whole mask

%Multiply mask by mask by anulus matrix
Anulus20=(ThetaMask20.*ThetaMask20a).*AnulusFull;

%Choose section to analyse
x=[440 560 280]; %3 values for x
y=[0 440 280]; %3 values for y

%Turn into a mask
ThetaMask77 = poly2mask(x, y, 560, 560); %560=size of whole mask

%Choose section to analyse
x=[560 400 280]; %3 values for x
y=[160 560 280]; %3 values for y

%Turn into a mask
ThetaMask77a = poly2mask(x, y, 560, 560); %560=size of whole mask

%Multiply mask by mask by anulus matrix
Anulus77=(ThetaMask77.*ThetaMask77a).*AnulusFull;

Anulus20=Anulus20+Anulus77;

%Average the mask
ANULUS20=sum(Anulus20);
ANULUS20=sum(ANULUS20/(nnz(Anulus20)));

```

```

subplot(2,4,5)
imshow(Anulus20,[min(Anulus20(:)) max(Anulus20(:))]);
drawnow;
caption = sprintf('64 degrees');
title(caption);
axis square;
%
%
%Choose section to analyse
x=[120 0 280]; %3 values for x
y=[560 120 280]; %3 values for y

%Turn into a mask
ThetaMask21 = poly2mask(x, y, 560, 560); %560=size of whole mask

%Choose section to analyse
x=[0 150 280]; %3 values for x
y=[400 0 280]; %3 values for y

%Turn into a mask
ThetaMask21a = poly2mask(x, y, 560, 560); %560=size of whole mask

%Multiply mask by mask by anulus matrix
Anulus21=(ThetaMask21.*ThetaMask21a).*AnulusFull;

%Choose section to analyse
x=[420 560 280]; %3 values for x
y=[0 420 280]; %3 values for y

%Turn into a mask
ThetaMask78a = poly2mask(x, y, 560, 560); %560=size of whole mask

%Choose section to analyse
x=[560 420 280]; %3 values for x
y=[140 560 280]; %3 values for y

%Turn into a mask
ThetaMask78 = poly2mask(x, y, 560, 560); %560=size of whole mask

%Multiply mask by mask by anulus matrix
Anulus78=(ThetaMask78.*ThetaMask78a).*AnulusFull;

Anulus21=Anulus21+Anulus78;

%Average the mask
ANULUS21=sum(Anulus21);
ANULUS21=sum(ANULUS21/(nnz(Anulus21)));
%
%
%Choose section to analyse
x=[140 0 280]; %3 values for x
y=[560 140 280]; %3 values for y

%Turn into a mask
ThetaMask22 = poly2mask(x, y, 560, 560); %560=size of whole mask

```

```

%Choose section to analyse
x=[0 130 280]; %3 values for x
y=[420 0 280]; %3 values for y

%Turn into a mask
ThetaMask22a = poly2mask(x, y, 560, 560); %560=size of whole mask

%Multiply mask by mask by anulus matrix
Anulus22=(ThetaMask22.*ThetaMask22a).*AnulusFull;

%Choose section to analyse
x=[400 560 280]; %3 values for x
y=[0 400 280]; %3 values for y

%Turn into a mask
ThetaMask79 = poly2mask(x, y, 560, 560); %560=size of whole mask

%Choose section to analyse
x=[560 440 280]; %3 values for x
y=[120 560 280]; %3 values for y

%Turn into a mask
ThetaMask79a = poly2mask(x, y, 560, 560); %560=size of whole mask

%Multiply mask by mask by anulus matrix
Anulus79=(ThetaMask79.*ThetaMask79a).*AnulusFull;

Anulus22=Anulus22+Anulus79;

%Average the mask
ANULUS22=sum(Anulus22);
ANULUS22=sum(ANULUS22/(nnz(Anulus22)));
%

```

```

%Choose section to analyse
x=[160 0 280]; %3 values for x
y=[560 160 280]; %3 values for y

%Turn into a mask
ThetaMask23 = poly2mask(x, y, 560, 560); %560=size of whole mask

%Choose section to analyse
x=[0 110 280]; %3 values for x
y=[440 0 280]; %3 values for y

%Turn into a mask
ThetaMask23a = poly2mask(x, y, 560, 560); %560=size of whole mask

%Multiply mask by mask by anulus matrix
Anulus23=(ThetaMask23.*ThetaMask23a).*AnulusFull;

%Choose section to analyse
x=[380 560 280]; %3 values for x
y=[0 380 280]; %3 values for y

%Turn into a mask

```

```

ThetaMask80 = poly2mask(x, y, 560, 560); %560=size of whole mask

%Choose section to analyse
x=[560 460 280]; %3 values for x
y=[100 560 280]; %3 values for y

%Turn into a mask
ThetaMask80a = poly2mask(x, y, 560, 560); %560=size of whole mask

%Multiply mask by mask by anulus matrix
Anulus80=(ThetaMask80.*ThetaMask80a).*AnulusFull;

Anulus23=Anulus23+Anulus80;

%Average the mask
ANULUS23=sum(Anulus23);
ANULUS23=sum(ANULUS23/(nnz(Anulus23)));
%
%
%Choose section to analyse
x=[180 0 280]; %3 values for x
y=[560 180 280]; %3 values for y

%Turn into a mask
ThetaMask24 = poly2mask(x, y, 560, 560); %560=size of whole mask

%Choose section to analyse
x=[0 90 280]; %3 values for x
y=[460 0 280]; %3 values for y

%Turn into a mask
ThetaMask24a = poly2mask(x, y, 560, 560); %560=size of whole mask

%Multiply mask by mask by anulus matrix
Anulus24=(ThetaMask24.*ThetaMask24a).*AnulusFull;

%Choose section to analyse
x=[360 560 280]; %3 values for x
y=[0 360 280]; %3 values for y

%Turn into a mask
ThetaMask81a = poly2mask(x, y, 560, 560); %560=size of whole mask

%Choose section to analyse
x=[560 480 280]; %3 values for x
y=[80 560 280]; %3 values for y

%Turn into a mask
ThetaMask81 = poly2mask(x, y, 560, 560); %560=size of whole mask

%Multiply mask by mask by anulus matrix
Anulus81=(ThetaMask81.*ThetaMask81a).*AnulusFull;

Anulus24=Anulus24+Anulus81;

%Average the mask
ANULUS24=sum(Anulus24);
ANULUS24=sum(ANULUS24/(nnz(Anulus24)));

```

```

%
%
%Choose section to analyse
x=[200 0 280]; %3 values for x
y=[560 200 280]; %3 values for y

%Turn into a mask
ThetaMask25 = poly2mask(x, y, 560, 560); %560=size of whole mask

%Choose section to analyse
x=[0 70 280]; %3 values for x
y=[480 0 280]; %3 values for y

%Turn into a mask
ThetaMask25a = poly2mask(x, y, 560, 560); %560=size of whole mask

%Multiply mask by mask by anulus matrix
Anulus25=(ThetaMask25.*ThetaMask25a).*AnulusFull;

%Choose section to analyse
x=[340 560 280]; %3 values for x
y=[0 340 280]; %3 values for y

%Turn into a mask
ThetaMask82 = poly2mask(x, y, 560, 560); %560=size of whole mask

%Choose section to analyse
x=[560 500 280]; %3 values for x
y=[60 560 280]; %3 values for y

%Turn into a mask
ThetaMask82a = poly2mask(x, y, 560, 560); %560=size of whole mask

%Multiply mask by mask by anulus matrix
Anulus82=(ThetaMask82.*ThetaMask82a).*AnulusFull;

Anulus25=Anulus25+Anulus82;

%Average the mask
ANULUS25=sum(Anulus25);
ANULUS25=sum(ANULUS25/(nnz(Anulus25)));
%
%
%Choose section to analyse
x=[220 0 280]; %3 values for x
y=[560 220 280]; %3 values for y

%Turn into a mask
ThetaMask26 = poly2mask(x, y, 560, 560); %560=size of whole mask

%Choose section to analyse
x=[0 50 280]; %3 values for x
y=[500 0 280]; %3 values for y

%Turn into a mask
ThetaMask26a = poly2mask(x, y, 560, 560); %560=size of whole mask

%Multiply mask by mask by anulus matrix

```

```

Anulus26=(ThetaMask26.*ThetaMask26a).*AnulusFull;

%Choose section to analyse
x=[320 560 280]; %3 values for x
y=[0 320 280]; %3 values for y

%Turn into a mask
ThetaMask83 = poly2mask(x, y, 560, 560); %560=size of whole mask

%Choose section to analyse
x=[560 520 280]; %3 values for x
y=[40 560 280]; %3 values for y

%Turn into a mask
ThetaMask83a = poly2mask(x, y, 560, 560); %560=size of whole mask

%Multiply mask by mask by anulus matrix
Anulus83=(ThetaMask83.*ThetaMask83a).*AnulusFull;

Anulus26=Anulus26+Anulus83;

%Average the mask
ANULUS26=sum(Anulus26);
ANULUS26=sum(ANULUS26/(nnz(Anulus26)));
%
%
%
%
%Choose section to analyse
x=[240 0 280]; %3 values for x
y=[560 240 280]; %3 values for y

%Turn into a mask
ThetaMask27 = poly2mask(x, y, 560, 560); %560=size of whole mask

%Choose section to analyse
x=[0 30 280]; %3 values for x
y=[520 0 280]; %3 values for y

%Turn into a mask
ThetaMask27a = poly2mask(x, y, 560, 560); %560=size of whole mask

%Multiply mask by mask by anulus matrix
Anulus27=(ThetaMask27.*ThetaMask27a).*AnulusFull;

%Choose section to analyse
x=[300 560 280]; %3 values for x
y=[0 300 280]; %3 values for y

%Turn into a mask
ThetaMask84a = poly2mask(x, y, 560, 560); %560=size of whole mask

%Choose section to analyse
x=[560 540 280]; %3 values for x
y=[20 560 280]; %3 values for y

%Turn into a mask
ThetaMask84 = poly2mask(x, y, 560, 560); %560=size of whole mask

```

```

%Multiply mask by mask by anulus matrix
Anulus84=(ThetaMask84.*ThetaMask84a).*AnulusFull;

Anulus27=Anulus27+Anulus84;

%Average the mask
ANULUS27=sum(Anulus27);
ANULUS27=sum(ANULUS27/(nnz(Anulus27)));
%
%%%%%%%%%%%%%%%%%%%%%%%%%%%%%%%%%%%%%%%%%%%%%%%%%%%%%%%%%%%%%%%%%%%%%%%%%%%%%%

%Choose section to analyse
x=[260 0 280]; %3 values for x
y=[560 260 280]; %3 values for y

%Turn into a mask
ThetaMask28 = poly2mask(x, y, 560, 560); %560=size of whole mask

%Choose section to analyse
x=[0 10 280]; %3 values for x
y=[540 0 280]; %3 values for y

%Turn into a mask
ThetaMask28a = poly2mask(x, y, 560, 560); %560=size of whole mask

%Multiply mask by mask by anulus matrix
Anulus28=(ThetaMask28.*ThetaMask28a).*AnulusFull;

%Choose section to analyse
x=[280 560 280]; %3 values for x
y=[0 280 280]; %3 values for y

%Turn into a mask
ThetaMask85a = poly2mask(x, y, 560, 560); %560=size of whole mask

%Choose section to analyse
x=[560 560 280]; %3 values for x
y=[0 560 280]; %3 values for y

%Turn into a mask
ThetaMask85= poly2mask(x, y, 560, 560); %560=size of whole mask

%Multiply mask by mask by anulus matrix
Anulus85=(ThetaMask85.*ThetaMask85a).*AnulusFull;

Anulus28=Anulus28+Anulus85;

%Average the mask
ANULUS28=sum(Anulus28);
ANULUS28=sum(ANULUS28/(nnz(Anulus28)));
%
%%%%%%%%%%%%%%%%%%%%%%%%%%%%%%%%%%%%%%%%%%%%%%%%%%%%%%%%%%%%%%%%%%%%%%%%%%%%%%

%Choose section to analyse
x=[280 0 280]; %3 values for x
y=[560 280 280]; %3 values for y

%Turn into a mask
ThetaMask29 = poly2mask(x, y, 560, 560); %560=size of whole mask

```

```

%Choose section to analyse
x=[10 0 280]; %3 values for x
y=[560 10 280]; %3 values for y

%Turn into a mask
ThetaMask29a = poly2mask(x, y, 560, 560); %560=size of whole mask

%Multiply mask by mask by anulus matrix
Anulus29=(ThetaMask29.*ThetaMask29a).*AnulusFull;

%Choose section to analyse
x=[260 560 280]; %3 values for x
y=[0 260 280]; %3 values for y

%Turn into a mask
ThetaMask86a = poly2mask(x, y, 560, 560); %560=size of whole mask

%Choose section to analyse
x=[540 560 280]; %3 values for x
y=[0 540 280]; %3 values for y

%Turn into a mask
ThetaMask86= poly2mask(x, y, 560, 560); %560=size of whole mask

%Multiply mask by mask by anulus matrix
Anulus86=(ThetaMask86.*ThetaMask86a).*AnulusFull;

Anulus29=Anulus29+Anulus86;

%Average the mask
ANULUS29=sum(Anulus29);
ANULUS29=sum(ANULUS29/(nnz(Anulus29)));
% _____ %

%Choose section to analyse
x=[300 0 280]; %3 values for x
y=[560 300 280]; %3 values for y

%Turn into a mask
ThetaMask30 = poly2mask(x, y, 560, 560); %560=size of whole mask

%Choose section to analyse
x=[30 0 280]; %3 values for x
y=[560 30 280]; %3 values for y

%Turn into a mask
ThetaMask30a = poly2mask(x, y, 560, 560); %560=size of whole mask

%Multiply mask by mask by anulus matrix
Anulus30=(ThetaMask30.*ThetaMask30a).*AnulusFull;

%Choose section to analyse
x=[240 560 280]; %3 values for x
y=[0 240 280]; %3 values for y

%Turn into a mask
ThetaMask87 = poly2mask(x, y, 560, 560); %560=size of whole mask

```

```

%Choose section to analyse
x=[520 560 280]; %3 values for x
y=[0 520 280]; %3 values for y

%Turn into a mask
ThetaMask87a = poly2mask(x, y, 560, 560); %560=size of whole mask

%Multiply mask by mask by anulus matrix
Anulus87=(ThetaMask87.*ThetaMask87a).*AnulusFull;

Anulus30=Anulus30+Anulus87;

%Average the mask
ANULUS30=sum(Anulus30);
ANULUS30=sum(ANULUS30/(nnz(Anulus30)));

subplot(2,4,6)
imshow(Anulus30,[min(Anulus30(:)) max(Anulus30(:))]);
drawnow;
caption = sprintf('96 degrees');
title(caption);
axis square;
%
%%%%%%%%%%%%%%%%%%%%%%%%%%%%%%%%%%%%%%%%%%%%%%%%%%%%%%%%%%%%%%%%%%%%%%%%%%%%%%
%Choose section to analyse
x=[320 0 280]; %3 values for x
y=[560 320 280]; %3 values for y

%Turn into a mask
ThetaMask31 = poly2mask(x, y, 560, 560); %560=size of whole mask

%Choose section to analyse
x=[50 0 280]; %3 values for x
y=[560 50 280]; %3 values for y

%Turn into a mask
ThetaMask31a = poly2mask(x, y, 560, 560); %560=size of whole mask

%Multiply mask by mask by anulus matrix
Anulus31=(ThetaMask31.*ThetaMask31a).*AnulusFull;

%Choose section to analyse
x=[220 560 280]; %3 values for x
y=[0 220 280]; %3 values for y

%Turn into a mask
ThetaMask88= poly2mask(x, y, 560, 560); %560=size of whole mask

%Choose section to analyse
x=[500 560 280]; %3 values for x
y=[0 500 280]; %3 values for y

%Turn into a mask
ThetaMask88a = poly2mask(x, y, 560, 560); %560=size of whole mask

%Multiply mask by mask by anulus matrix
Anulus88=(ThetaMask88.*ThetaMask88a).*AnulusFull;

```

```

Anulus31=Anulus31+Anulus88;

%Average the mask
ANULUS31=sum(Anulus31);
ANULUS31=sum(ANULUS31/(nnz(Anulus31)));
%
%
%Choose section to analyse
x=[340 0 280]; %3 values for x
y=[560 340 280]; %3 values for y

%Turn into a mask
ThetaMask32 = poly2mask(x, y, 560, 560); %560=size of whole mask

%Choose section to analyse
x=[60 0 280]; %3 values for x
y=[560 60 280]; %3 values for y

%Turn into a mask
ThetaMask32a = poly2mask(x, y, 560, 560); %560=size of whole mask

%Multiply mask by mask by anulus matrix
Anulus32=(ThetaMask32.*ThetaMask32a).*AnulusFull;

%Choose section to analyse
x=[200 560 280]; %3 values for x
y=[0 200 280]; %3 values for y

%Turn into a mask
ThetaMask89 = poly2mask(x, y, 560, 560); %560=size of whole mask

%Choose section to analyse
x=[480 560 280]; %3 values for x
y=[0 480 280]; %3 values for y

%Turn into a mask
ThetaMask89a = poly2mask(x, y, 560, 560); %560=size of whole mask

%Multiply mask by mask by anulus matrix
Anulus89=(ThetaMask89.*ThetaMask89a).*AnulusFull;

Anulus32=Anulus32+Anulus89;

%Average the mask
ANULUS32=sum(Anulus32);
ANULUS32=sum(ANULUS32/(nnz(Anulus32)));
%
%
%Choose section to analyse
x=[360 0 280]; %3 values for x
y=[560 360 280]; %3 values for y

%Turn into a mask
ThetaMask33 = poly2mask(x, y, 560, 560); %560=size of whole mask

%Choose section to analyse
x=[80 0 280]; %3 values for x

```

```

y=[560 80 280]; %3 values for y

%Turn into a mask
ThetaMask33a = poly2mask(x, y, 560, 560); %560=size of whole mask

%Multiply mask by mask by anulus matrix
Anulus33=(ThetaMask33.*ThetaMask33a).*AnulusFull;

%Choose section to analyse
x=[180 560 280]; %3 values for x
y=[0 180 280]; %3 values for y

%Turn into a mask
ThetaMask90a = poly2mask(x, y, 560, 560); %560=size of whole mask

%Choose section to analyse
x=[460 560 280]; %3 values for x
y=[0 460 280]; %3 values for y

%Turn into a mask
ThetaMask90 = poly2mask(x, y, 560, 560); %560=size of whole mask

%Multiply mask by mask by anulus matrix
Anulus90=(ThetaMask90.*ThetaMask90a).*AnulusFull;

Anulus33=Anulus33+Anulus90;

%Average the mask
ANULUS33=sum(Anulus33);
ANULUS33=sum(ANULUS33/(nnz(Anulus33)));
%
_____
%

%Choose section to analyse
x=[380 0 280]; %3 values for x
y=[560 380 280]; %3 values for y

%Turn into a mask
ThetaMask34 = poly2mask(x, y, 560, 560); %560=size of whole mask

%Choose section to analyse
x=[100 0 280]; %3 values for x
y=[560 100 280]; %3 values for y

%Turn into a mask
ThetaMask34a = poly2mask(x, y, 560, 560); %560=size of whole mask

%Multiply mask by mask by anulus matrix
Anulus34=(ThetaMask34.*ThetaMask34a).*AnulusFull;

%Choose section to analyse
x=[160 560 280]; %3 values for x
y=[0 160 280]; %3 values for y

%Turn into a mask
ThetaMask91a = poly2mask(x, y, 560, 560); %560=size of whole mask

%Choose section to analyse

```

```

x=[440 560 280]; %3 values for x
y=[0 440 280]; %3 values for y

%Turn into a mask
ThetaMask91 = poly2mask(x, y, 560, 560); %560=size of whole mask

%Multiply mask by mask by anulus matrix
Anulus91=(ThetaMask91.*ThetaMask91a).*AnulusFull;

Anulus34=Anulus34+Anulus91;

%Average the mask
ANULUS34=sum(Anulus34);
ANULUS34=sum(ANULUS34/(nnz(Anulus34)));
%
%
%Choose section to analyse
x=[400 0 280]; %3 values for x
y=[560 400 280]; %3 values for y

%Turn into a mask
ThetaMask35 = poly2mask(x, y, 560, 560); %560=size of whole mask

%Choose section to analyse
x=[120 0 280]; %3 values for x
y=[560 120 280]; %3 values for y

%Turn into a mask
ThetaMask35a = poly2mask(x, y, 560, 560); %560=size of whole mask

%Multiply mask by mask by anulus matrix
Anulus35=(ThetaMask35.*ThetaMask35a).*AnulusFull;

%Choose section to analyse
x=[140 560 280]; %3 values for x
y=[0 140 280]; %3 values for y

%Turn into a mask
ThetaMask92 = poly2mask(x, y, 560, 560); %560=size of whole mask

%Choose section to analyse
x=[420 560 280]; %3 values for x
y=[0 420 280]; %3 values for y

%Turn into a mask
ThetaMask92a= poly2mask(x, y, 560, 560); %560=size of whole mask

%Multiply mask by mask by anulus matrix
Anulus92=(ThetaMask92.*ThetaMask92a).*AnulusFull;

Anulus35=Anulus35+Anulus92;

%Average the mask
ANULUS35=sum(Anulus35);
ANULUS35=sum(ANULUS35/(nnz(Anulus35)));
%
%

```

```

%Choose section to analyse
x=[420 0 280]; %3 values for x
y=[560 420 280]; %3 values for y

%Turn into a mask
ThetaMask36 = poly2mask(x, y, 560, 560); %560=size of whole mask

%Choose section to analyse
x=[140 0 280]; %3 values for x
y=[560 140 280]; %3 values for y

%Turn into a mask
ThetaMask36a = poly2mask(x, y, 560, 560); %560=size of whole mask

%Multiply mask by mask by anulus matrix
Anulus36=(ThetaMask36.*ThetaMask36a).*AnulusFull;

%Choose section to analyse
x=[120 560 280]; %3 values for x
y=[0 120 280]; %3 values for y

%Turn into a mask
ThetaMask93 = poly2mask(x, y, 560, 560); %560=size of whole mask

%Choose section to analyse
x=[400 560 280]; %3 values for x
y=[0 400 280]; %3 values for y

%Turn into a mask
ThetaMask93a = poly2mask(x, y, 560, 560); %560=size of whole mask

%Multiply mask by mask by anulus matrix
Anulus93=(ThetaMask93.*ThetaMask93a).*AnulusFull;

Anulus36=Anulus36+Anulus93;

%Average the mask
ANULUS36=sum(Anulus36);
ANULUS36=sum(ANULUS36/(nnz(Anulus36)));
%
%
%Choose section to analyse
x=[440 0 280]; %3 values for x
y=[560 440 280]; %3 values for y

%Turn into a mask
ThetaMask37 = poly2mask(x, y, 560, 560); %560=size of whole mask

%Choose section to analyse
x=[160 0 280]; %3 values for x
y=[560 160 280]; %3 values for y

%Turn into a mask
ThetaMask37a = poly2mask(x, y, 560, 560); %560=size of whole mask

%Multiply mask by mask by anulus matrix
Anulus37=(ThetaMask37.*ThetaMask37a).*AnulusFull;

```

```

% Choose section to analyse
x=[100 560 280]; %3 values for x
y=[0 100 280]; %3 values for y

%Turn into a mask
ThetaMask94 = poly2mask(x, y, 560, 560); %560=size of whole mask

% Choose section to analyse
x=[380 560 280]; %3 values for x
y=[0 380 280]; %3 values for y

%Turn into a mask
ThetaMask94a = poly2mask(x, y, 560, 560); %560=size of whole mask

%Multiply mask by mask by anulus matrix
Anulus94=(ThetaMask94.*ThetaMask94a).*AnulusFull;

Anulus37=Anulus37+Anulus94;

%Average the mask
ANULUS37=sum(Anulus37);
ANULUS37=sum(ANULUS37/(nnz(Anulus37)));
%
%
%Choose section to analyse
x=[460 0 280]; %3 values for x
y=[560 460 280]; %3 values for y

%Turn into a mask
ThetaMask38 = poly2mask(x, y, 560, 560); %560=size of whole mask

%Choose section to analyse
x=[180 0 280]; %3 values for x
y=[560 180 280]; %3 values for y

%Turn into a mask
ThetaMask38a = poly2mask(x, y, 560, 560); %560=size of whole mask

%Multiply mask by mask by anulus matrix
Anulus38=(ThetaMask38.*ThetaMask38a).*AnulusFull;

%Choose section to analyse
x=[80 560 280]; %3 values for x
y=[0 80 280]; %3 values for y

%Turn into a mask
ThetaMask95a = poly2mask(x, y, 560, 560); %560=size of whole mask

%Choose section to analyse
x=[360 560 280]; %3 values for x
y=[0 360 280]; %3 values for y

%Turn into a mask
ThetaMask95 = poly2mask(x, y, 560, 560); %560=size of whole mask

%Multiply mask by mask by anulus matrix
Anulus95=(ThetaMask95.*ThetaMask95a).*AnulusFull;

```

```

Anulus38=Anulus38+Anulus95;

%Average the mask
ANULUS38=sum(Anulus38);
ANULUS38=sum(ANULUS38/(nnz(Anulus38)));
%
%
%Choose section to analyse
x=[480 0 280]; %3 values for x
y=[560 480 280]; %3 values for y

%Turn into a mask
ThetaMask39 = poly2mask(x, y, 560, 560); %560=size of whole mask

%Choose section to analyse
x=[200 0 280]; %3 values for x
y=[560 200 280]; %3 values for y

%Turn into a mask
ThetaMask39a = poly2mask(x, y, 560, 560); %560=size of whole mask

%Multiply mask by mask by anulus matrix
Anulus39=(ThetaMask39.*ThetaMask39a).*AnulusFull;

%Choose section to analyse
x=[60 560 280]; %3 values for x
y=[0 60 280]; %3 values for y

%Turn into a mask
ThetaMask96a = poly2mask(x, y, 560, 560); %560=size of whole mask

% Choose section to analyse
x=[340 560 280]; %3 values for x
y=[0 340 280]; %3 values for y

%Turn into a mask
ThetaMask96 = poly2mask(x, y, 560, 560); %560=size of whole mask

%Multiply mask by mask by anulus matrix
Anulus96=(ThetaMask96.*ThetaMask96a).*AnulusFull;

Anulus39=Anulus39+Anulus96;

%Average the mask
ANULUS39=sum(Anulus39);
ANULUS39=sum(ANULUS39/(nnz(Anulus39)));
%
%
%Choose section to analyse
x=[500 0 280]; %3 values for x
y=[560 500 280]; %3 values for y

%Turn into a mask
ThetaMask40a = poly2mask(x, y, 560, 560); %560=size of whole mask

%Choose section to analyse
x=[220 0 280]; %3 values for x

```

```

y=[560 220 280]; %3 values for y

%Turn into a mask
ThetaMask40 = poly2mask(x, y, 560, 560); %560=size of whole mask

%Multiply mask by mask by anulus matrix
Anulus40=(ThetaMask40.*ThetaMask40a).*AnulusFull;

%Choose section to analyse
x=[40 560 280]; %3 values for x
y=[0 40 280]; %3 values for y

%Turn into a mask
ThetaMask97a = poly2mask(x, y, 560, 560); %560=size of whole mask

%Choose section to analyse
x=[320 560 280]; %3 values for x
y=[0 320 280]; %3 values for y

%Turn into a mask
ThetaMask97 = poly2mask(x, y, 560, 560); %560=size of whole mask

%Multiply mask by mask by anulus matrix
Anulus97=(ThetaMask97.*ThetaMask97a).*AnulusFull;

Anulus40=Anulus40+Anulus97;

%Average the mask
ANULUS40=sum(Anulus40);
ANULUS40=sum(ANULUS40/(nnz(Anulus40)));

subplot(2,4,7)
imshow(Anulus40,[min(Anulus40(:)) max(Anulus40(:))]);
drawnow;
caption = sprintf('128 degrees');
title(caption);
axis square;

%


---


%
%Choose section to analyse
x=[520 0 280]; %3 values for x
y=[560 520 280]; %3 values for y

%Turn into a mask
ThetaMask41a = poly2mask(x, y, 560, 560); %560=size of whole mask

%FIVEFOURTY Choose section to analyse
x=[240 0 280]; %3 values for x
y=[560 240 280]; %3 values for y

%Turn into a mask
ThetaMask41 = poly2mask(x, y, 560, 560); %560=size of whole mask

%Multiply mask by mask by anulus matrix
Anulus41=(ThetaMask41.*ThetaMask41a).*AnulusFull;

%Choose section to analyse

```

```

x=[20 560 280]; %3 values for x
y=[0 20 280]; %3 values for y

%Turn into a mask
ThetaMask98a = poly2mask(x, y, 560, 560); %560=size of whole mask

%Choose section to analyse
x=[300 560 280]; %3 values for x
y=[0 300 280]; %3 values for y

%Turn into a mask
ThetaMask98 = poly2mask(x, y, 560, 560); %560=size of whole mask

%Multiply mask by mask by anulus matrix
Anulus98=(ThetaMask98.*ThetaMask98a).*AnulusFull;

Anulus41=Anulus41+Anulus98;

%Average the mask
ANULUS41=sum(Anulus41);
ANULUS41=sum(ANULUS41/(nnz(Anulus41)));
%
%%%%%%%%%%%%%%%%%%%%%%%%%%%%%%%%%%%%%%%%%%%%%%%%%%%%%%%%%%%%%%%%%%%%%%%%%%
%

%Choose section to analyse
x=[540 0 280]; %3 values for x
y=[560 540 280]; %3 values for y

%Turn into a mask
ThetaMask42a = poly2mask(x, y, 560, 560); %560=size of whole mask

%Choose section to analyse
x=[260 0 280]; %3 values for x
y=[560 260 280]; %3 values for y

%Turn into a mask
ThetaMask42 = poly2mask(x, y, 560, 560); %560=size of whole mask
%Multiply mask by mask by anulus matrix
Anulus42=(ThetaMask42.*ThetaMask42a).*AnulusFull;

%Choose section to analyse
x=[0 560 280]; %3 values for x
y=[0 0 280]; %3 values for y

%Turn into a mask
ThetaMask99a = poly2mask(x, y, 560, 560); %560=size of whole mask

%Choose section to analyse
x=[280 560 280]; %3 values for x
y=[0 280 280]; %3 values for y

%Turn into a mask
ThetaMask99 = poly2mask(x, y, 560, 560); %560=size of whole mask

%Multiply mask by mask by anulus matrix
Anulus99=(ThetaMask99.*ThetaMask99a).*AnulusFull;

Anulus42=Anulus42+Anulus99;

```

```

%Average the mask
ANULUS42=sum(Anulus42);
ANULUS42=sum(ANULUS42/(nnz(Anulus42)));
%
%
%Choose section to analyse
x=[560 0 280]; %3 values for x
y=[560 560 280]; %3 values for y

%Turn into a mask
ThetaMask43a = poly2mask(x, y, 560, 560); %560=size of whole mask

% Choose section to analyse
x=[280 0 280]; %3 values for x
y=[560 280 280]; %3 values for y

%Turn into a mask
ThetaMask43 = poly2mask(x, y, 560, 560); %560=size of whole mask

%Multiply mask by mask by anulus matrix
Anulus43=(ThetaMask43.*ThetaMask43a).*AnulusFull;

%Choose section to analyse
x=[0 540 280]; %3 values for x
y=[20 0 280]; %3 values for y

%Turn into a mask
ThetaMask100a = poly2mask(x, y, 560, 560); %560=size of whole mask

%Choose section to analyse
x=[260 560 280]; %3 values for x
y=[0 260 280]; %3 values for y

%Turn into a mask
ThetaMask100 = poly2mask(x, y, 560, 560); %560=size of whole mask

%Multiply mask by mask by anulus matrix
Anulus100=(ThetaMask100.*ThetaMask100a).*AnulusFull;

Anulus43=Anulus43+Anulus100;

%Average the mask
ANULUS43=sum(Anulus43);
ANULUS43=sum(ANULUS43/(nnz(Anulus43)));
%
%
%Choose section to analyse
x=[560 20 280]; %3 values for x
y=[540 560 280]; %3 values for y

%Turn into a mask
ThetaMask44a = poly2mask(x, y, 560, 560); %560=size of whole mask

% Choose section to analyse
x=[300 0 280]; %3 values for x
y=[560 300 280]; %3 values for y

```

```

%Turn into a mask
ThetaMask44 = poly2mask(x, y, 560, 560); %560=size of whole mask

%Multiply mask by mask by anulus matrix
Anulus44=(ThetaMask44.*ThetaMask44a).*AnulusFull;

%Choose section to analyse
x=[0 520 280]; %3 values for x
y=[40 0 280]; %3 values for y

%Turn into a mask
ThetaMask101 = poly2mask(x, y, 560, 560); %560=size of whole mask

%Choose section to analyse
x=[240 560 280]; %3 values for x
y=[0 240 280]; %3 values for y

%Turn into a mask
ThetaMask101a = poly2mask(x, y, 560, 560); %560=size of whole mask

%Multiply mask by mask by anulus matrix
Anulus101=(ThetaMask101.*ThetaMask101a).*AnulusFull;

Anulus44=Anulus44+Anulus101;

%Average the mask
ANULUS44=sum(Anulus44);
ANULUS44=sum(ANULUS44/(nnz(Anulus44)));
%
%
%Choose section to analyse
x=[560 40 280]; %3 values for x
y=[520 560 280]; %3 values for y

%Turn into a mask
ThetaMask45a = poly2mask(x, y, 560, 560); %560=size of whole mask

%Choose section to analyse
x=[320 0 280]; %3 values for x
y=[560 320 280]; %3 values for y

%Turn into a mask
ThetaMask45 = poly2mask(x, y, 560, 560); %560=size of whole mask

%Multiply mask by mask by anulus matrix
Anulus45=(ThetaMask45.*ThetaMask45a).*AnulusFull;

%Choose section to analyse
x=[0 500 280]; %3 values for x
y=[60 0 280]; %3 values for y

%Turn into a mask
ThetaMask102a = poly2mask(x, y, 560, 560); %560=size of whole mask

%Choose section to analyse
x=[220 560 280]; %3 values for x
y=[0 220 280]; %3 values for y

```

```

%Turn into a mask
ThetaMask102 = poly2mask(x, y, 560, 560); %560=size of whole mask

%Multiply mask by mask by anulus matrix
Anulus102=(ThetaMask102.*ThetaMask102a).*AnulusFull;

Anulus45=Anulus45+Anulus102;

%Average the mask
ANULUS45=sum(Anulus45);
ANULUS45=sum(ANULUS45/(nnz(Anulus45)));
%
%
%Choose section to analyse
x=[560 60 280]; %3 values for x
y=[500 560 280]; %3 values for y

%Turn into a mask
ThetaMask46a = poly2mask(x, y, 560, 560); %560=size of whole mask

%Choose section to analyse
x=[340 0 280]; %3 values for x
y=[560 340 280]; %3 values for y

%Turn into a mask
ThetaMask46 = poly2mask(x, y, 560, 560); %560=size of whole mask

%Multiply mask by mask by anulus matrix
Anulus46=(ThetaMask46.*ThetaMask46a).*AnulusFull;

%Choose section to analyse
x=[0 480 280]; %3 values for x
y=[80 0 280]; %3 values for y

%Turn into a mask
ThetaMask103 = poly2mask(x, y, 560, 560); %560=size of whole mask

%Choose section to analyse
x=[200 560 280]; %3 values for x
y=[0 200 280]; %3 values for y

%Turn into a mask
ThetaMask103a = poly2mask(x, y, 560, 560); %560=size of whole mask

%Multiply mask by mask by anulus matrix
Anulus103=(ThetaMask103.*ThetaMask103a).*AnulusFull;

Anulus46=Anulus46+Anulus103;

%Average the mask
ANULUS46=sum(Anulus46);
ANULUS46=sum(ANULUS46/(nnz(Anulus46)));
%
%
%Choose section to analyse
x=[560 80 280]; %3 values for x
y=[480 560 280]; %3 values for y

```

```

%Turn into a mask
ThetaMask47a= poly2mask(x, y, 560, 560); %560=size of whole mask

%Choose section to analyse
x=[360 0 280]; %3 values for x
y=[560 360 280]; %3 values for y

%Turn into a mask
ThetaMask47 = poly2mask(x, y, 560, 560); %560=size of whole mask

%Multiply mask by mask by anulus matrix
Anulus47=(ThetaMask47.*ThetaMask47a).*AnulusFull;

%Choose section to analyse
x=[0 460 280]; %3 values for x
y=[100 0 280]; %3 values for y

%Turn into a mask
ThetaMask104a = poly2mask(x, y, 560, 560); %560=size of whole mask

%Choose section to analyse
x=[180 560 280]; %3 values for x
y=[0 180 280]; %3 values for y

%Turn into a mask
ThetaMask104 = poly2mask(x, y, 560, 560); %560=size of whole mask

%Multiply mask by mask by anulus matrix
Anulus104=(ThetaMask104.*ThetaMask104a).*AnulusFull;

Anulus47=Anulus47+Anulus104;

%Average the mask
ANULUS47=sum(Anulus47);
ANULUS47=sum(ANULUS47/(nnz(Anulus47)));
%


---


%Choose section to analyse
x=[560 100 280]; %3 values for x
y=[460 560 280]; %3 values for y

%Turn into a mask
ThetaMask48a = poly2mask(x, y, 560, 560); %560=size of whole mask

%Choose section to analyse
x=[380 0 280]; %3 values for x
y=[560 380 280]; %3 values for y

%Turn into a mask
ThetaMask48 = poly2mask(x, y, 560, 560); %560=size of whole mask

%Multiply mask by mask by anulus matrix
Anulus48=(ThetaMask48.*ThetaMask48a).*AnulusFull;

%Choose section to analyse
x=[0 440 280]; %3 values for x
y=[120 0 280]; %3 values for y

```

```

%Turn into a mask
ThetaMask105 = poly2mask(x, y, 560, 560); %560=size of whole mask

%Choose section to analyse
x=[160 560 280]; %3 values for x
y=[0 160 280]; %3 values for y

%Turn into a mask
ThetaMask105a = poly2mask(x, y, 560, 560); %560=size of whole mask

%Multiply mask by mask by anulus matrix
Anulus105=(ThetaMask105.*ThetaMask105a).*AnulusFull;

Anulus48=Anulus48+Anulus105;

%Average the mask
ANULUS48=sum(Anulus48);
ANULUS48=sum(ANULUS48/(nnz(Anulus48)));
%
%
%Choose section to analyse
x=[560 120 280]; %3 values for x
y=[440 560 280]; %3 values for y

%Turn into a mask
ThetaMask49a= poly2mask(x, y, 560, 560); %560=size of whole mask

% Choose section to analyse
x=[400 0 280]; %3 values for x
y=[560 400 280]; %3 values for y

%Turn into a mask
ThetaMask49 = poly2mask(x, y, 560, 560); %560=size of whole mask

%Multiply mask by mask by anulus matrix
Anulus49=(ThetaMask49.*ThetaMask49a).*AnulusFull;

%Choose section to analyse
x=[0 420 280]; %3 values for x
y=[140 0 280]; %3 values for y

%Turn into a mask
ThetaMask106a = poly2mask(x, y, 560, 560); %560=size of whole mask

%Choose section to analyse
x=[140 560 280]; %3 values for x
y=[0 140 280]; %3 values for y

%Turn into a mask
ThetaMask106 = poly2mask(x, y, 560, 560); %560=size of whole mask

%Multiply mask by mask by anulus matrix
Anulus106=(ThetaMask106.*ThetaMask106a).*AnulusFull;

Anulus49=Anulus49+Anulus106;

%Average the mask
ANULUS49=sum(Anulus49);

```

```

ANULUS49=sum(ANULUS49/(nnz(Anulus49)));
%
%
%Choose section to analyse
x=[560 140 280]; %3 values for x
y=[420 560 280]; %3 values for y

%Turn into a mask
ThetaMask50a = poly2mask(x, y, 560, 560); %560=size of whole mask

%Choose section to analyse
x=[420 0 280]; %3 values for x
y=[560 420 280]; %3 values for y

%Turn into a mask
ThetaMask50= poly2mask(x, y, 560, 560); %560=size of whole mask

%Multiply mask by mask by anulus matrix
Anulus50=(ThetaMask50.*ThetaMask50a).*AnulusFull;

%Choose section to analyse
x=[0 400 280]; %3 values for x
y=[160 0 280]; %3 values for y

%Turn into a mask
ThetaMask107a = poly2mask(x, y, 560, 560); %560=size of whole mask

%Choose section to analyse
x=[120 560 280]; %3 values for x
y=[0 120 280]; %3 values for y

%Turn into a mask
ThetaMask107 = poly2mask(x, y, 560, 560); %560=size of whole mask

%Multiply mask by mask by anulus matrix
Anulus107=(ThetaMask107.*ThetaMask107a).*AnulusFull;

Anulus50=Anulus50+Anulus107;

%Average the mask
ANULUS50=sum(Anulus50);
ANULUS50=sum(ANULUS50/(nnz(Anulus50)));

subplot(2,4,8)
imshow(Anulus50,[min(Anulus50(:)) max(Anulus50(:))]);
drawnow;
caption = sprintf('160 degrees');
title(caption);
axis square;
%
%
%Choose section to analyse
x=[560 160 280]; %3 values for x
y=[400 560 280]; %3 values for y

%Turn into a mask
ThetaMask51 = poly2mask(x, y, 560, 560); %560=size of whole mask

```

```

%Choose section to analyse
x=[440 0 280]; %3 values for x
y=[560 440 280]; %3 values for y

%Turn into a mask
ThetaMask51a = poly2mask(x, y, 560, 560); %560=size of whole mask

%Multiply mask by mask by anulus matrix
Anulus51=(ThetaMask51.*ThetaMask51a).*AnulusFull;

%Choose section to analyse
x=[0 380 280]; %3 values for x
y=[180 0 280]; %3 values for y

%Turn into a mask
ThetaMask108 = poly2mask(x, y, 560, 560); %560=size of whole mask

%Choose section to analyse
x=[100 560 280]; %3 values for x
y=[0 100 280]; %3 values for y

%Turn into a mask
ThetaMask108a = poly2mask(x, y, 560, 560); %560=size of whole mask

%Multiply mask by mask by anulus matrix
Anulus108=(ThetaMask108.*ThetaMask108a).*AnulusFull;

Anulus51=Anulus51+Anulus108;

%Average the mask
ANULUS51=sum(Anulus51);
ANULUS51=sum(ANULUS51/(nnz(Anulus51)));
%
%
%
%
%Choose section to analyse
x=[560 180 280]; %3 values for x
y=[380 560 280]; %3 values for y

%Turn into a mask
ThetaMask52 = poly2mask(x, y, 560, 560); %560=size of whole mask

%Choose section to analyse
x=[460 0 280]; %3 values for x
y=[560 460 280]; %3 values for y

%Turn into a mask
ThetaMask52a = poly2mask(x, y, 560, 560); %560=size of whole mask

%Multiply mask by mask by anulus matrix
Anulus52=(ThetaMask52.*ThetaMask52a).*AnulusFull;

%Choose section to analyse
x=[0 360 280]; %3 values for x
y=[200 0 280]; %3 values for y

%Turn into a mask
ThetaMask109 = poly2mask(x, y, 560, 560); %560=size of whole mask

```

```

%Choose section to analyse
x=[80 560 280]; %3 values for x
y=[0 80 280]; %3 values for y

%Turn into a mask
ThetaMask109a = poly2mask(x, y, 560, 560); %560=size of whole mask

%Multiply mask by mask by anulus matrix
Anulus109=(ThetaMask109.*ThetaMask109a).*AnulusFull;

Anulus52=Anulus52+Anulus109;

%Average the mask
ANULUS52=sum(Anulus52);
ANULUS52=sum(ANULUS52/(nnz(Anulus52)));
%

```

```

%Choose section to analyse
x=[560 200 280]; %3 values for x
y=[360 560 280]; %3 values for y

%Turn into a mask
ThetaMask53 = poly2mask(x, y, 560, 560); %560=size of whole mask

%Choose section to analyse
x=[480 0 280]; %3 values for x
y=[560 480 280]; %3 values for y

%Turn into a mask
ThetaMask53a = poly2mask(x, y, 560, 560); %560=size of whole mask

%Multiply mask by mask by anulus matrix
Anulus53=(ThetaMask53.*ThetaMask53a).*AnulusFull;

%Choose section to analyse
x=[0 340 280]; %3 values for x
y=[220 0 280]; %3 values for y

%Turn into a mask
ThetaMask110a = poly2mask(x, y, 560, 560); %560=size of whole mask

%Choose section to analyse
x=[60 560 280]; %3 values for x
y=[0 60 280]; %3 values for y

%Turn into a mask
ThetaMask110 = poly2mask(x, y, 560, 560); %560=size of whole mask

%Multiply mask by mask by anulus matrix
Anulus110=(ThetaMask110.*ThetaMask110a).*AnulusFull;

Anulus53=Anulus53+Anulus110;

%Average the mask
ANULUS53=sum(Anulus53);
ANULUS53=sum(ANULUS53/(nnz(Anulus53)));
%

```

```

%Choose section to analyse
x=[560 220 280]; %3 values for x
y=[340 560 280]; %3 values for y

%Turn into a mask
ThetaMask54 = poly2mask(x, y, 560, 560); %560=size of whole mask

%Choose section to analyse
x=[500 0 280]; %3 values for x
y=[560 500 280]; %3 values for y

%Turn into a mask
ThetaMask54a= poly2mask(x, y, 560, 560); %560=size of whole mask

%Multiply mask by mask by anulus matrix
Anulus54=(ThetaMask54.*ThetaMask54a).*AnulusFull;

%Choose section to analyse
x=[0 320 280]; %3 values for x
y=[240 0 280]; %3 values for y

%Turn into a mask
ThetaMask111 = poly2mask(x, y, 560, 560); %560=size of whole mask

%Choose section to analyse
x=[40 560 280]; %3 values for x
y=[0 40 280]; %3 values for y

%Turn into a mask
ThetaMask111a = poly2mask(x, y, 560, 560); %560=size of whole mask

%Multiply mask by mask by anulus matrix
Anulus111=(ThetaMask111.*ThetaMask111a).*AnulusFull;

Anulus54=Anulus54+Anulus111;

%Average the mask
ANULUS54=sum(Anulus54);
ANULUS54=sum(ANULUS54/(nnz(Anulus54)));
%
%
%
%
%Choose section to analyse
x=[560 240 280]; %3 values for x
y=[320 560 280]; %3 values for y

%Turn into a mask
ThetaMask55 = poly2mask(x, y, 560, 560); %560=size of whole mask

%Choose section to analyse
x=[520 0 280]; %3 values for x
y=[560 520 280]; %3 values for y

%Turn into a mask
ThetaMask55a = poly2mask(x, y, 560, 560); %560=size of whole mask

%Multiply mask by mask by anulus matrix
Anulus55=(ThetaMask55.*ThetaMask55a).*AnulusFull;

```

```

%Choose section to analyse
x=[0 300 280]; %3 values for x
y=[260 0 280]; %3 values for y

%Turn into a mask
ThetaMask112 = poly2mask(x, y, 560, 560); %560=size of whole mask

% Choose section to analyse
x=[20 560 280]; %3 values for x
y=[0 20 280]; %3 values for y

%Turn into a mask
ThetaMask112a = poly2mask(x, y, 560, 560); %560=size of whole mask

%Multiply mask by mask by anulus matrix
Anulus112=(ThetaMask112.*ThetaMask112a).*AnulusFull;

Anulus55=Anulus55+Anulus112;

%Average the mask
ANULUS55=sum(Anulus55);
ANULUS55=sum(ANULUS55/(nnz(Anulus55)));
%
%
pause(1);
print Figure1;

%create the centre circle
%create a mask for the central region in the same way as above
%r is the only element to change and note < changes to >.
r=7;
[x,y]=meshgrid(-(cx-1):(ix-cx),-(cy-1):(iy-cy));
Centre=(x.^2+y.^2)<=r^2);

%Mask the Image
Circle=Centre.*SUB;

%Average making
ImageC=sum(Circle);
ImageC=sum(ImageC/(nnz(Circle)));
%
%
ANULUS0=ImageC-ANULUS0;
ANULUS1=ImageC-ANULUS1;
ANULUS2=ImageC-ANULUS2 ;
ANULUS3=ImageC-ANULUS3;
ANULUS4=ImageC-ANULUS4 ;
ANULUS5=ImageC-ANULUS5;
ANULUS6=ImageC-ANULUS6 ;
ANULUS7=ImageC-ANULUS7 ;
ANULUS8=ImageC-ANULUS8 ;
ANULUS9=ImageC-ANULUS9 ;
ANULUS10=ImageC-ANULUS10 ;
ANULUS11=ImageC-ANULUS11 ;
ANULUS12=ImageC-ANULUS12 ;
ANULUS13=ImageC-ANULUS13 ;
ANULUS14=ImageC-ANULUS14 ;
ANULUS15=ImageC-ANULUS15 ;

```

```

ANULUS16=ImageC-ANULUS16 ;
ANULUS17=ImageC-ANULUS17 ;
ANULUS18=ImageC-ANULUS18 ;
ANULUS19=ImageC-ANULUS19 ;
ANULUS20=ImageC-ANULUS20;
ANULUS21=ImageC-ANULUS21;
ANULUS22=ImageC-ANULUS22;
ANULUS23=ImageC-ANULUS23;
ANULUS24=ImageC-ANULUS24;
ANULUS25=ImageC-ANULUS25 ;
ANULUS26=ImageC-ANULUS26 ;
ANULUS27=ImageC-ANULUS27 ;
ANULUS28=ImageC-ANULUS28;
ANULUS29=ImageC-ANULUS29;
ANULUS30=ImageC-ANULUS30;
ANULUS31=ImageC-ANULUS31;
ANULUS32=ImageC-ANULUS32;
ANULUS33=ImageC-ANULUS33;
ANULUS34=ImageC-ANULUS34 ;
ANULUS35=ImageC-ANULUS35 ;
ANULUS36=ImageC-ANULUS36 ;
ANULUS37=ImageC-ANULUS37;
ANULUS38=ImageC-ANULUS38;
ANULUS39=ImageC-ANULUS39;
ANULUS40=ImageC-ANULUS40;
ANULUS41=ImageC-ANULUS41;
ANULUS42=ImageC-ANULUS42;
ANULUS43=ImageC-ANULUS43;
ANULUS44=ImageC-ANULUS44;
ANULUS45=ImageC-ANULUS45;
ANULUS46=ImageC-ANULUS46;
ANULUS47=ImageC-ANULUS47;
ANULUS48=ImageC-ANULUS48;
ANULUS49=ImageC-ANULUS49;
ANULUS50=ImageC-ANULUS50;
ANULUS51=ImageC-ANULUS51;
ANULUS52=ImageC-ANULUS52;
ANULUS53=ImageC-ANULUS53;
ANULUS54=ImageC-ANULUS54;
ANULUS55=ImageC-ANULUS55;

%Collect into vectors
tbow=0:3.25:180;
arbow=[ANULUS0 ANULUS1 ANULUS2 ANULUS3 ANULUS4 ANULUS5 ANULUS6 ANULUS7
ANULUS8 ANULUS9 ANULUS10 ANULUS11 ANULUS12 ANULUS13 ANULUS14 ANULUS15
ANULUS16 ANULUS17 ANULUS18 ANULUS19 ANULUS20 ANULUS21 ANULUS22 ANULUS23
ANULUS24 ANULUS25 ANULUS26 ANULUS27 ANULUS28 ANULUS29 ANULUS30 ANULUS31
ANULUS32 ANULUS33 ANULUS34 ANULUS35 ANULUS36 ANULUS37 ANULUS38 ANULUS39
ANULUS40 ANULUS41 ANULUS42 ANULUS43 ANULUS44 ANULUS45 ANULUS46 ANULUS47
ANULUS48 ANULUS49 ANULUS50 ANULUS51 ANULUS52 ANULUS53 ANULUS54 ANULUS55];
% Then, we locate the min:
Low = find(arbow == min(arbow));

% Do the same for the max:
High = find(arbow == max(arbow));

ANULUS=[tbow(High) tbow(Low) arbow(High) arbow(Low)];

```

Program Name: Normality

```
function normality(x)
%Function returns the following parameters:
% Range of the data
% Mean of the data and the bootstrapped errors associated with this
% Median of the data and the bootstrapped errors associated with this
% Mode of the data and the bootstrapped error associated with this
% The Standard deviation of the data
% The 95th and 65th percentiles of the data
% The kurtosis coefficient of the data: Kurtosis is a measure of how
% outlier-prone a distribution is. The kurtosis of the normal
% distribution is 3. Distributions that are more outlier-prone than
% the normal distribution have kurtosis greater than 3; distributions
% that are less outlier-prone have kurtosis less than 3.
% The Skewness of the data: Skewness is a measure of the asymmetry of the
% data around the sample mean. If skewness is negative, the data are
% spread out more to the left of the mean than to the right. If
% skewness is positive, the data are spread out more to the right.
% The skewness of the normal distribution (or any perfectly symmetric
% distribution) is zero.
% The Shapiro-Wilk parametric hypothesis test and associated P-value:
% Shapiro-Wilk test to determine if the null hypothesis of
% composite normality is a reasonable assumption regarding the
% population distribution of a random sample X.
% The KS test and associated P-value: The one-sample Kolmogorov-Smirnov
% test is a nonparametric hypothesis test that evaluates the
difference
% between the empirical cdf of the data and the cdf of the
hypothesized
% distribution over the range of x in the data set.
% The AD test and associated P-value: The Anderson-Darling test returns
% a test decision for the null hypothesis that the data in vector x
% is from a population with a normal distribution.
%Function also plots a fixed 10 bin histogram, a Q-Q plot, a Boxplot and a
% P-P plot separately and on the same figure for a snap shot of the data.

X={'Range';'Mean';'MeanErrorLow';'MeanErrorHigh';'Median';'MedianErrorLow';
'MedianErrorHigh';'Mode';
'ModeErrorHigh';'ModeErrorLow';'StDev';'95thPercentile';'65thPercentile';'K
urtosis';'Skewness';'ShapiroH';'ShapiroPval';'KSH';'KSPval'};
a=max(x)-min(x);
b=mean(x);
c=bootci(1000,@mean,x);
d=median(x);
e=bootci(1000,@median,x);
f=kurtosis(x);
g=skewness(x);
[h,i]=swtest(x);
[j,k]=kstest(x);
l=std(x);
m=mode(x);
n=bootci(1000,@mode,x);
o=prctile(x,95);
p=prctile(x,65);
Y=[a b c(1) c(2) d e(1) e(2) m n(1) n(2) l o p f g h i j k]';

Data=dataset(X,Y)
```

```

figure;hist(x);
xlabel('Data Range')
ylabel('Frequency')
figure;qqplot(x);
figure;boxplot(x,'notch','on');
ylabel('Data Range')
figure;probplot(x);

figure;
subplot(2,2,1);
hist(x,10);
xlabel('Data Range');
ylabel('Frequency');
drawnow;
caption = sprintf('Histogram');
title(caption);

subplot(2,2,2);
qqplot(x);
drawnow;
caption = sprintf('Q-Q Plot');
title(caption);

subplot(2,2,3);
boxplot(x,'notch','on');
ylabel('Data Range')
drawnow;
caption = sprintf('Boxplot');
title(caption);

subplot(2,2,4);
probplot(x);
drawnow;
caption = sprintf('Probability Plot');
title(caption);

end

```

Appendix 3

The statistical analyses used in this thesis

Range – The difference between the lowest and highest numbers in a data set.

Mean – The average of a data set.

Median – The middle value of a data set, when the data are lined up in ascending numerical order.

Mode – The most frequently occurring value within a data set.

Standard deviation – A value for the data set which shows how much variation from the mean exists.

Percentile – A percentile indicates the value at which a certain percentage of the data fall below, for example, the 10th percentile is the value of which 10% of the data fall below.

Kurtosis – A measurement of the shape of the distribution, the 'peakedness'. Platykurtic distributions have values below 3 and are described as flat and broad. Leptokurtic distributions have values above 3 and are described as narrow and peaky.

Skewness – A measurement of the asymmetry of the distribution. A negative skewed distribution has a longer or fatter tail to the left of the mean and vice versa.

Quantile-Quantile plot – A plot where the quantiles of one distribution are plotted against the quantiles of another distribution, in this case a standard normal distribution. Quantiles are equal divisions of a distribution, quantiles where the distribution is divided into 100 equal parts are called percentiles.

empirical Probability Density Function – A histogram which has been normalised to an area of 1. This method of data display means that histograms containing varying numbers of N can be compared visually.

Pchip - $y_i = \text{pchip}(x,y,x_i)$ returns vector y_i containing elements corresponding to the elements of x_i and determined by piecewise cubic interpolation within vectors x and y . The vector x specifies the points at which the data y is given. If y is a matrix, then the interpolation is performed for each column of y and y_i is $\text{length}(x_i)$ -by- $\text{size}(y,2)$.

Appendix 4.

Growth phenotype screening of *Schizosaccharomyces pombe* using a Lensless microscope

Lynsey A. Penwill, Gwendoline E. Batten, Stefania Castagnetti, Andrew M. Shaw

Biosensors and Bioelectronics, Volume 54, 15 April 2014, Pages 345-350.